

# Dissertation

*submitted to the*

Combined Faculties of the Natural Sciences and Mathematics  
of the Ruperto-Carola University of Heidelberg, Germany

*for the degree of*

Doctor of Natural Sciences

*Put forward by*

Felix Paul Gerhard Ziegler

*born in:* Stuttgart, Germany

Oral examination: July 23rd, 2019

# Towards finite density properties and real-time dynamics in strongly correlated systems

Referees: Prof. Dr. Jan M. Pawłowski  
Prof. Dr. Joerg Jaeckel

## **Zu den Eigenschaften bei endlicher Dichte und Realzeitdynamik in stark korrelierten Systemen**

In der vorliegenden Arbeit untersuchen wir stark korrelierte Quantensysteme unter extremen Temperatur- und Dichtebedingungen. Ein bekanntes Beispiel dafür ist das Quark-Gluon Plasma, welches in ultra-relativistischen Schwerionenkollisionen erzeugt wird. Da die Freiheitsgrade der zu betrachtenden Systeme einer starken Kopplung unterliegen, ist der Einsatz von nicht-perturbativen Methoden erforderlich. Hierzu verwenden wir Gitterfeldtheorie, die es erlaubt, physikalische Größen mit hoher Präzision aus ersten Prinzipien zu bestimmen. Die Methode basiert auf Monte Carlo Simulationen. Wir untersuchen QCD-ähnliche Theorien bei endlicher Dichte. Letztere verursacht das sogenannte Vorzeichenproblem auf dem Gitter, das die Anwendung von Simulationsalgorithmen basierend auf Importance Sampling unterbindet. Zu vielversprechenden Methoden, die das Vorzeichenproblem umgehen bzw. mildern können zählen die Komplexe Langevingleichung sowie Lefschetz Thimbles. In dieser Arbeit schlagen wir neuartige Algorithmen in beiden Zugängen vor. Diese werden einerseits anhand von einfachen Modellen mit einem Vorzeichenproblem sowie andererseits in Gittereichtheorien erprobt. Weiterhin untersuchen wir Realzeiteigenschaften von Quantensystemen bei endlicher Temperatur. Dies ist für die Berechnung von Transportkoeffizienten erforderlich. Dazu führen wir Gittersimulationen in imaginärer Zeit durch mit dem Ziel, die spektrale Rekonstruktion thermischer Eigenschaften zu verbessern. Weiterhin betrachten wir Simulationen direkt in Realzeit. Dazu wird die Komplexe Langevingleichung mittels Variablentransformationen modifiziert.

## **Towards finite density properties and real-time dynamics in strongly correlated systems**

In this thesis we study strongly correlated quantum systems in extreme temperature and density conditions. A prominent example is the quark-gluon plasma produced in ultra-relativistic heavy-ion collisions. Since the degrees of freedom in the systems of interest are strongly coupled the use of non-perturbative methods is required. Our working method is lattice field theory allowing for high precision ab-initio calculations of physical quantities based on Monte Carlo simulations. We study QCD-like theories at finite density. This introduces the sign problem to the lattice preventing the applicability of importance sampling algorithms. Promising methods to tackle the sign problem are the Complex Langevin evolution on the one hand and Lefschetz Thimbles on the other hand. In this work we propose novel algorithmic ideas to both approaches which are put to work in simple models with a sign problem as well as in lattice gauge theories. Moreover, we investigate real-time properties of quantum systems at finite temperature which is necessary for the computation of transport coefficients. To that end we conduct lattice simulations in imaginary time which are aimed at improving the spectral reconstruction of thermal features. Moreover, we study simulations directly in real-time by means of the Complex Langevin evolution equipped with variable transformations.

# Contents

<b>1. Introduction</b>	<b>7</b>
1.1. Motivation . . . . .	7
1.2. Publications . . . . .	10
1.3. Outline of the thesis . . . . .	11
<b>2. Basic concepts</b>	<b>13</b>
2.1. Thermal field theory . . . . .	13
2.1.1. Imaginary time formalism . . . . .	13
2.1.2. The Schwinger-Keldysh contour . . . . .	14
2.2. Quantum Chromodynamics . . . . .	16
2.2.1. Basics . . . . .	16
2.2.2. Finite temperature QCD . . . . .	16
2.3. Aspects of lattice QCD . . . . .	17
2.3.1. Basics . . . . .	17
2.3.2. The sign problem . . . . .	18
2.4. The Complex Langevin evolution . . . . .	19
2.4.1. Stochastic quantization . . . . .	19
2.4.2. Complex stochastic dynamics . . . . .	20
2.5. Lefschetz thimbles . . . . .	21
2.6. Spectral reconstruction . . . . .	23
<b>3. Colored Noise Cooling</b>	<b>25</b>
3.1. Motivation and overview . . . . .	25
3.2. Stochastic quantization with colored noise . . . . .	26
3.3. Lattice QFT with colored noise . . . . .	28
3.4. Scalar field theory . . . . .	29
3.4.1. Lattice formulation . . . . .	29
3.4.2. Observables . . . . .	31
3.5. Colored Noise and the Renormalization Group . . . . .	32
3.6. Numerical Results . . . . .	34
3.6.1. Colored Noise: incomplete blocking . . . . .	34
3.6.2. Colored noise: complete blocking at tree level . . . . .	36
3.7. Applications . . . . .	42
3.8. Summary . . . . .	47
<b>4. Reweighting Lefschetz Thimbles</b>	<b>49</b>
4.1. Challenges for simulations . . . . .	49
4.2. Finding thimbles . . . . .	50
4.2.1. Axis scan . . . . .	50
4.2.2. Thimble cooling . . . . .	52

4.3.	Monte Carlo simulations on Lefschetz thimbles . . . . .	54
4.3.1.	Standard reweighting on thimbles . . . . .	54
4.3.2.	Computing the partition function weights . . . . .	55
4.4.	Applications . . . . .	55
4.4.1.	One-site $z^4$ model . . . . .	56
4.4.2.	$U(1)$ one link model . . . . .	57
4.5.	Summary . . . . .	59
<b>5.</b>	<b>Lefschetz thimbles in gauge theories</b>	<b>62</b>
5.1.	$U(1)$ lattice gauge theory . . . . .	62
5.1.1.	Theory and properties . . . . .	62
5.1.2.	Thimble decomposition . . . . .	63
5.1.3.	Sampling on thimbles . . . . .	65
5.1.4.	Application 1: One-link model . . . . .	67
5.1.5.	Application 2: $U(1)$ gauge theory in 1+1 dim. . . . .	68
5.1.6.	Tangent space simulation . . . . .	70
5.2.	Real-time scalar fields in $0 + 1$ dimensions . . . . .	74
5.2.1.	Sampling à la $\text{Im}(S) = \text{const.}$ . . . . .	74
5.2.2.	Takagi decomposition . . . . .	76
5.2.3.	Range of applicability of the local thimble algorithm . . . . .	77
5.3.	Summary . . . . .	78
<b>6.</b>	<b>Real-time properties at finite temperature</b>	<b>80</b>
6.1.	The analytic continuation problem . . . . .	80
6.2.	Correlators at general frequencies . . . . .	81
6.2.1.	Original proposal . . . . .	81
6.2.2.	Application to non-abelian gauge theory . . . . .	82
6.2.3.	Need for a reformulation . . . . .	84
6.2.4.	The double path-integral . . . . .	85
6.3.	Spectral representation . . . . .	90
6.4.	Numerical setup . . . . .	95
6.5.	Probing the kernel . . . . .	95
6.5.1.	Single exponential fits . . . . .	97
6.5.2.	Multiple exponential fits . . . . .	97
6.6.	Thermal information in the data . . . . .	98
6.7.	Summary . . . . .	100
<b>7.</b>	<b>Variable Transformations</b>	<b>102</b>
7.1.	Transformations in simple models . . . . .	102
7.2.	Schwinger-Keldysh on the lattice . . . . .	103
7.3.	Assessment and perspectives . . . . .	105
<b>8.</b>	<b>Summary and Outlook</b>	<b>107</b>
<b>A.</b>	<b>Technicalities on Colored Noise</b>	<b>110</b>
A.1.	Fourier transformation on the Lattice . . . . .	110
A.2.	Observables . . . . .	111
A.3.	Spacetime correlation function of colored noise . . . . .	113

A.4. Aspects of colored noise . . . . .	114
A.4.1. Fokker-Planck equation . . . . .	114
A.4.2. Alternative regularization functions . . . . .	117
A.5. Stochastic regularization and the FRG . . . . .	119
A.6. Gradient flow vs. colored noise . . . . .	120
<b>B. Lefschetz Thimbles and CLE</b>	<b>121</b>
B.1. Partition function weights . . . . .	121
B.2. Mapping integration ranges . . . . .	121
B.3. Combining the CLE and Lefschetz thimbles . . . . .	122
B.3.1. Variable transformations . . . . .	122
B.3.2. Lefschetz cooling . . . . .	123
B.3.3. Advanced Lefschetz cooling . . . . .	124
<b>C. Imaginary times</b>	<b>128</b>
C.1. Quantum mechanical anharmonic oscillator . . . . .	128
C.1.1. Harmonic oscillator . . . . .	128
C.1.2. Anharmonic oscillator and energy eigenspace . . . . .	129
C.1.3. Quantum statistics for the QM-AHO . . . . .	131
<b>Acknowledgments</b>	<b>135</b>
<b>Bibliography</b>	<b>136</b>

# 1. Introduction

Strongly correlated systems play a crucial role in a variety of modern scientific disciplines. In physics prominent examples are states of matter under extreme conditions. Amongst those rank ultra-cold atoms at  $T \approx 10^{-9}\text{K}$  [1] as well as the hot and dense quark-gluon plasma (QGP) accessible in heavy-ion collisions at  $T \approx 10^{12}\text{K}$  [2]. Remarkably, these systems at opposite extremes on the temperature scale share universal properties. For example both ultra-cold quantum gases and the QGP are almost ideal fluids [3]. For both experimental and theoretical research an essential task is to gain insight on the phases of such systems. Besides exploring static thermodynamic quantities such as equations of states a challenge for theory is the description of dynamical quantities from first principles. This involves transport properties in the medium such as viscosities or diffusion coefficients.

The work presented in this thesis is inspired by exploring the thermodynamic properties of Quantum Chromodynamics (QCD) at finite temperature and density. QCD describes the strong interactions between quarks and gluons. For the major part of the phase diagram, especially the yet unknown regions at finite density quarks and gluons are strongly coupled. Both for experiments and theory this provides challenges. On the theory side the use of non-perturbative methods is required. A successful framework is lattice field theory allowing for ab-initio computations of QCD. However, at finite density and in real-time standard lattice methods are hampered by the numerical sign problem. In this thesis we propose novel algorithms aiming at improvements of existing lattice methods designed to tackle the sign problem. Our ideas are probed in application to both QCD-like theories and models at finite density as well as field theories in real-time.

## 1.1. Motivation

There are four known fundamental forces in nature, the electromagnetic, weak and the strong interactions as well as gravity. The modern theoretical description in terms of quantum field theories has led to the development of the standard model of particle physics which comprises all the mentioned forces but gravity. The standard model has shown remarkable predictive successes throughout the last decades. An outstanding achievement was the 2012 discovery of the Higgs boson [4, 5]. In this thesis neither the electro-weak sector nor extensions of the standard model, see e.g. [6], will be discussed. Instead the motivation behind the work of this thesis is the strong sector. The latter describes the dynamics of quarks and gluons within QCD, being an  $SU(3)$  gauge theory. The gluons mediate the strong force between the quarks. Both quarks and gluons carry color charge. Hence, in contrast to electrodynamics the gluons interact among themselves. This is a consequence of the non-abelian nature of the theory. The pure gauge part of QCD is Yang-Mills theory [7]. A remarkable property of QCD is asymptotic freedom which means that with increasing energy the strong coupling tends to zero [8, 9]. In contrast, at low-energies QCD is strongly coupled.

In the following we briefly introduce aspects of QCD at finite temperature  $T$  and density  $n$  or chemical potential  $\mu$  which is expected to exhibit a rich phase structure, see [10–12]. Large parts of the phase diagram that is for intermediate to large densities are still unknown.

### Confinement, deconfinement and QGP

The low-energy sector of QCD comprises two important phenomena: confinement and chiral symmetry breaking. The former entails that at low temperature  $T$  and chemical potentials  $\mu$  quarks and gluons are bound into color-neutral hadrons. A direct consequence of confinement is the impossibility to observe free quarks or gluons in nature. Only color-neutral bound states can be measured where prominent examples are the proton, the neutron or the pions. With increasing temperature and density the bound states dissolve and quarks and gluons become the dominant degrees of freedom. They form the quark-gluon plasma and the corresponding phase is called deconfined phase. To see how the two phases are connected consider the limit of infinitely heavy quarks. Those decouple from the dynamics and one is left with the pure gauge theory. For  $SU(3)$  the deconfinement transition is of first order which has been investigated using lattice simulations in [13]. On the other hand in QCD with dynamical quarks there is no sharp phase transition but an analytic cross-over between the confined and the deconfined phase. The so-called pseudo-critical temperature of  $T_c \approx 155$  MeV has been determined on the lattice, see [14–16]. This has also been reviewed in [17, 18].

Experimentally, the QGP is produced and investigated by means of ultra-relativistic heavy-ion collisions at the ALICE experiment at the Large Hadron Collider (LHC) as well as at the Relativistic Heavy Ion Collider (RHIC). In tiny reaction volumes strongly interacting matter is created at high temperatures and low to intermediate densities. These conditions also characterize the state of the early universe. Due to the extremely short lifetime of the QGP it is only indirectly possible to measure its properties by investigating the re-hadronized products arriving in the detector. Since the quark-gluon plasma is strongly coupled it provides also a challenge for theoretical descriptions. For overviews addressing both experiment and theory see [19–24].

### Chiral symmetry breaking

The second important phenomenon of QCD is chiral symmetry breaking. From it the largest part of the mass in the visible universe originates. For vanishing quark masses the classical QCD Lagrangian exhibits chiral symmetry. In the full quantum theory this symmetry is spontaneously broken at low temperature which explains the largest part of the mass of the hadron's constituents. For increasing temperature a phase transition to the chirally restored phase occurs. However, for finite quark masses chiral symmetry is explicitly broken and instead of a phase-transition there is also a cross-over. The chiral and the deconfinement cross-over transitions occur at the same temperature as found in lattice simulations [25]. On the functional method side the two phenomena were studied e.g. in [26].

### Phase structure and experiments

For low temperatures and larger chemical potentials a first-order phase transition separates the quark-gluon plasma phase from the hadronic phase. It is conjectured that this first-order transition line is separated from the cross-over by a critical end-point corresponding to a second-order phase transition, see [27]. Experimentally detecting and theoretically determining the latter from first principles is an important goal of many research groups around the world. Moreover, at high densities and low temperature as, for instance, present in dense and cold stellar objects such as neutron stars, a color superconducting phase is expected [10, 28].

Complementary to the experiments mentioned above the unknown areas at intermediate temperatures and high density will be explored in the Compressed Baryonic Matter (CBM) experiment at the Facility for Antiproton and Ion Research (FAIR) as well as at NICA at JINR. These experiments aim at providing insight on the location and character of the deconfinement and chiral transition as well as on the critical end-point. For an overview on experimental efforts on the QCD phase diagram see also [29].

### Theoretical tools, non-perturbative methods

Regarding theoretical investigations perturbation theory has been applied successfully to QCD. Its use is however restricted to the high-energy region of the phase diagram where quarks and gluons are weakly interacting due to asymptotic freedom. Both the confinement as well as the chiral transition occur in energy regimes  $\approx \Lambda_{\text{QCD}}$  where the coupling between quarks and gluons is strong necessitating the use of non-perturbative methods. A well-established and powerful method allowing for first principle computations is lattice field theory. It has been applied to many areas of physics ranging from condensed matter systems to quantum gravity. Lattice gauge theory was pioneered by Wegner [30] and in 1974 Wilson formulated QCD on the lattice [31]. The Euclidean time path integral of QCD is discretized on a finite space-time lattice by sampling field configurations in Monte Carlo simulations. During the last decades it has shown remarkable success for instance in predicting the hadronic spectrum [32] or in determining the mass difference between the proton and the neutron to high accuracy [33]. Also at finite temperature lattice simulations yield robust predictions of experimental data obtained in collision experiments at  $T \geq 0$ , see, for instance [24, 34, 35]. However, lattice simulations are restricted to vanishing and small chemical potentials  $\mu/T \leq 1$ . Larger values of  $\mu$  cause lattice methods to break down due to the sign problem [36]. The finite chemical potential  $\mu$  renders the Euclidean action of QCD complex. This prohibits the use of conventional Monte Carlo methods based on importance sampling. This situation has triggered a plethora of work in this direction, for a recent review see [37]. Two candidates that have shown promising progress in tackling the sign problem are the Complex Langevin method [38] and Lefschetz thimbles [39, 40].

Other promising non-perturbative methods which are free of the sign problem are functional methods such as the functional renormalization group (FRG) [41–45] and Dyson-Schwinger equations [46].

### Real-time physics

While the computation of static quantities such as the QCD equation of state has been successfully determined by lattice computations, see [47–49] a robust computation of dy-

namical quantities such as transport coefficients is still under development, see e.g. [50] for a study on the shear viscosity of the QGP. Direct simulations in real-time are prohibitive due to the sign problem being most severe in this case. One is left with numerical analytic continuation from imaginary time correlator data. This comes with the problem of solving an ill-conditioned inverse problem. In addition, the thermal information in the data suffers from an exponentially decaying signal-to-noise ratio. A large part of this thesis is dedicated to tackling this problem.

Complementary to approaches carried out on classical computers there is intense research on quantum computing technologies to simulate real-time quantum systems reaching back to a proposal by Feynman [51]. For works on lattice gauge theories simulated with ultracold atoms in optical lattices see e.g. [52–54]. The goal of this approach is to simulate the stages of heavy-ion collisions in real-time.

### Contribution of this thesis

In this thesis we focus on QCD-like theories at finite density and also real-time properties in thermal field theory. Thereby our working framework is the non-perturbative lattice formulation. We both devise new methods and further develop existing algorithms for lattice simulations. To study strongly correlated systems at finite density those are applied to simple models in parameter regions that have been inaccessible before. Towards computing real-time properties of the quark-gluon plasma our working ground is a pure gauge theory. The long-term goal is to apply these methods to computing transport coefficients in the QGP or QCD at finite density. We remark that the methods studied here are still partially under development.

## 1.2. Publications

This thesis has been compiled solely by the author. Most of the research presented here has been conducted in joint work with my collaborators. A large part of this work is published. Text and figures taken from the publications are not indicated explicitly. In the list below as well as in the beginning of the corresponding chapters we note where the content from the publications is used.

**[55] Cooling Stochastic Quantization with Colored Noise**

J. M. Pawłowski, I.-O. Stamatescu and F. P. G. Ziegler

Published in Phys. Rev. D96 (2017) no. 11, 114505

e-Print: arXiv:1705.06231 [hep-lat]

Remark: This article is incorporated into Chapter 3 and Appendix A.

**[56] Reweighting Lefschetz Thimbles**

S. Bluecher, J. M. Pawłowski, M. Scherzer, M. Schlosser, I.-O. Stamatescu, S. Syrkowski and F. P. G. Ziegler

Published in SciPost Phys. 5 (2018) no.5, 044

e-Print: arXiv:1803.08418 [hep-lat]

Remark: Chapter 4 and Appendix B contain this article.

Moreover, there is a recent paper available as preprint on spectral reconstruction using deep neural networks which contains work from a side project by the author. It is therefore

not included in this thesis.

**[57] Spectral Reconstruction with Deep Neural Networks**

L. Kades, J. M. Pawłowski, A. Rothkopf, M. Scherzer, J. M. Urban, S. J. Wetzel,  
N. Wink and F. P. G. Ziegler

e-Print: arXiv:1905.04305[physics.comp-ph]

There are also proceedings on my contribution to the lattice conference in 2018 containing part of the work of [56].

**[58] Reweighting Lefschetz Thimbles**

S. Bluecher, J. M. Pawłowski, M. Scherzer, M. Schlosser, I.-O. Stamatescu, S. Syrkowski  
and F. P. G. Ziegler

Proceedings for the 36th Annual Symposium of Lattice Field Theory, East Lansing,  
USA, 2018

e-Print: arXiv:1901.05187 [hep-lat]

Remark: Parts of the proceedings are used in Chapter 4.

The remaining part of this thesis is based on unpublished work in progress with my collaborators.

- Topic: Novel algorithms for Lefschetz thimble simulations in field theories  
Collaborators: J. M. Pawłowski, M. Scherzer, C. Schmidt, I.-O. Stamatescu and  
F. Ziesché  
Remark: The current state of the collaborative research is presented in Chapter 5.  
A publication is in preparation [59].
- Topic: Real-time quantities on the lattice by improved imaginary time simulations  
Collaborators: D. Michels, J. M. Pawłowski, A. Rothkopf, N. Wink  
Remark: Chapter 6 summarizes the research results. Technicalities are explained in  
Appendix C.
- Topic: Real-time simulations using the Complex Langevin evolution in combination  
with variable transformations  
Collaborator: Jan M. Pawłowski  
Remark: The research originates from a recent project and is presented in Chapter  
7.

## 1.3. Outline of the thesis

The content of this thesis is organized as follows. In Chapter 2 we recapitulate basic concepts of Quantum Chromodynamics at finite temperature and density as well as lattice field theory. Moreover, we introduce Stochastic Quantization and Lefschetz Thimbles. This chapter only serves to provide some ingredients such as notation needed in later chapters. It may thus be skipped by the experienced reader. In Chapter 3 we present a novel smoothing method to improve precision calculations of physical quantities on the lattice. The method is based on Stochastic Quantization with a ultra-violet momentum cutoff giving rise to a colored noise. This allows to control short distance fluctuations. After discussing the properties and applications of the colored noise method we emphasize its interpretation in terms of the Wilsonian renormalization group. In Chapter 4 we

consider simple QCD-like models with a sign problem by means of the Lefschetz thimble method. We develop a novel method suited for lattice simulations on thimbles and discuss its viability. Chapter 5 contains work on the Lefschetz thimble approach applied to higher dimensional field theories including real-time and gauge theories. Algorithmic ideas for accessing Monte Carlo simulations on thimbles are presented. In Chapter 6 we address the computation of dynamical quantities such as transport properties of the QGP from lattice simulations. While the sign problem prohibits a direct access in real-time we consider correlation functions in imaginary time. Our method is based on a novel proposal on enhancing the thermal information content in imaginary time correlators aimed at facilitating the numerical analytic continuation problem [60]. We extend the proposal to gauge theories and furthermore assess its viability. In Chapter 7 we study real-time field theories with a severe sign problem. First results using the Complex Langevin evolution modified by variable transformations are shown. Promising aspects and issues of this approach are discussed.

## 2. Basic concepts

In this chapter we summarize a few basics of thermal field theory, QCD in the continuum and its lattice regularization. This is followed by a brief discussion of transport properties in the quark-gluon plasma. In the second part of the chapter we introduce the sign problem on the lattice and discuss a few candidate methods to handle it.

This thesis does not claim to represent a complete introduction to those topics. The chapter at hand only provides the notation as well as the bigger context for the research results presented in later chapters. For further reading on quantum field theoretical topics addressed here we refer to standard textbooks such as [61–63]. For thermal field theories see [64–66]. We work with the following units  $\hbar = 1 = c = k_B$ .

### 2.1. Thermal field theory

#### 2.1.1. Imaginary time formalism

Thermal information on a many-body quantum system is contained in the statistical mechanical partition function and the correlation functions derived thereof. For simplicity we consider a quantum mechanical particle with Hamilton operator  $\hat{H}$  coupled to a heat-bath with inverse temperature  $\beta = 1/T$ . The partition function reads

$$Z = \text{tr}(e^{-\beta\hat{H}}). \quad (2.1)$$

We can express this in quantum field theoretical language as follows [64]. The quantum mechanical system can be described as a  $0 + 1$  dimensional scalar field theory with the classical Lagrangian  $\mathcal{L}_M$ . Define the imaginary or Euclidean time  $\tau = it$  and Wick-rotate the phase in the real-time path-integral

$$\exp\left(i \int dt \mathcal{L}_M\right) \xrightarrow{t \rightarrow -i\tau} \exp\left(- \int_0^\beta d\tau \mathcal{L}_E\right) \quad (2.2)$$

where  $\mathcal{L}_E = -\mathcal{L}_M(\tau = it)$ . Importantly, the imaginary time is restricted to a compact interval  $\tau \in [0, \beta]$ . Moreover, periodicity in the field is required on the imaginary time path  $\phi(0) = \phi(\beta)$ . In terms of the path-integral the partition function (2.1) can be written as follows

$$Z = \int_{\phi(0)=\phi(\beta)} \mathcal{D}\phi e^{-S_E[\phi]}. \quad (2.3)$$

Here  $S_E = \int_0^\beta d\tau \mathcal{L}_E$  denotes the Euclidean action. Note that the trace in (2.1) demands the periodicity of the field. Because at finite temperature the imaginary time domain is compact the field can be expressed as a Fourier series over discrete frequencies, the so-called Matsubara frequencies [67]. For bosonic fields those read  $\omega_n = 2\pi Tn$ ,  $n \in \mathbb{Z}$ . The imaginary time formalism can also be easily extended to field theories.

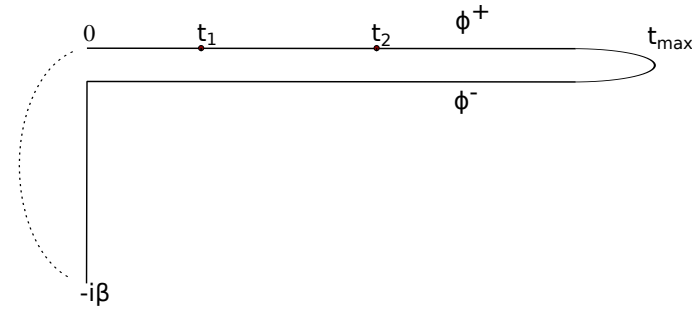


Figure 2.1.: The Schwinger-Keldysh contour. The dashed line indicates that the last point at  $-i\beta$  is identified with  $t = 0$  which corresponds to closing the trace.

### 2.1.2. The Schwinger-Keldysh contour

Static thermodynamic quantities such as the energy density can be calculated easily from (2.3). However, to extract dynamical information of the system we need to consider thermal correlation functions in real-time. This is put on formal grounds by the so-called Schwinger-Keldysh contour [68, 69]. Consider again a real scalar field theory. Bosonic operators fulfill the Heisenberg picture time evolution [61]

$$\hat{O}(\vec{x}, t) = e^{i\hat{H}t} \hat{O}(\vec{x}, 0) e^{-i\hat{H}t}. \quad (2.4)$$

Now we are interested in quantum statistical expectation values of time ordered products of these operators

$$\langle \hat{O}(\vec{x}_n, t_n) \dots \hat{O}(\vec{x}_1, t_1) \rangle = \text{Tr}(\hat{\rho}^{(0)} \hat{O}(\vec{x}_n, t_n) \dots \hat{O}(\vec{x}_1, t_1)). \quad (2.5)$$

Here,  $\hat{\rho}^{(0)} = \exp(-\beta\hat{H})/Z$  is the density matrix characterizing thermal equilibrium and  $Z$  is given in (2.1). For the scope of this thesis we are only interested in the time-ordering  $t_{\max} > t_n > \dots > t_1 > 0$  where  $t_{\max}$  denotes the maximum real-time extent. Next, consider the two-point correlation function of two field operators at times  $t_2$  and  $t_1$ . The expression can be rewritten in terms time evolution operators by using (2.4) and inserting unity  $\mathbb{1} = \exp(i\hat{H}t_{\max}) \exp(-i\hat{H}t_{\max})$

$$\begin{aligned} \langle \hat{\phi}(t_2) \hat{\phi}(t_1) \rangle &= \frac{1}{Z} \text{Tr}(e^{-\beta\hat{H}} \hat{\phi}(t_2) \hat{\phi}(t_1)) \\ &= \frac{1}{Z} \text{Tr}(e^{-\beta\hat{H}} e^{i\hat{H}t_{\max}} e^{-i\hat{H}(t_{\max}-t_2)} \hat{\phi}(0) e^{-i\hat{H}(t_2-t_1)} \hat{\phi}(0) e^{-i\hat{H}t_1}). \end{aligned} \quad (2.6)$$

We start at zero time and evolve to time  $t_1$  where the operator  $\hat{\phi}$  is evaluated. Next, this is further evolved to time  $t_2$  where  $\hat{\phi}$  is evaluated again. The time evolution goes on to  $t_{\max}$  and from there back to zero. Next, we evolve by  $-i\beta$  downwards into imaginary time<sup>1</sup> and close the trace. This is visualized in Fig. 2.1 depicting the Schwinger-Keldysh contour. Note that by inserting another unity in terms of time evolution operators the real-time part of the contour can be formally extended to infinity.

<sup>1</sup>Since we are in equilibrium the density matrix can be interpreted as a time evolution in imaginary time from 0 to  $-i\beta$ .

The partition function can also be expressed using path-integrals [70, 71]. To that end we rewrite the trace in (2.1) by integrating over a complete set of field states at time  $t_0 = 0$ . Following the notation in [70] the integral measure reads

$$[d\phi_0^\pm] = \prod_{\vec{x}} d\phi^\pm(\vec{x}, 0). \quad (2.7)$$

The superscript  $\pm$  will become clear in a few lines. The completeness relation holding at any time  $t$  reads

$$\int [d\phi_t] |\phi, t\rangle \langle \phi, t| = \mathbb{1}. \quad (2.8)$$

We use the notation  $|\phi, t\rangle \equiv |\phi_t\rangle$ . Thus, the partition function is rewritten as

$$Z = \int [d\phi_0^+] [d\phi_0^-] \langle \phi_0^+ | e^{-\beta \hat{H}} | \phi_0^- \rangle \langle \phi_0^- | \phi_0^+ \rangle. \quad (2.9)$$

We now insert unity in form of a complete set of states evolved to the final time  $t_{\max}$  and obtain

$$Z = \int [d\phi_{t_{\max}}] [d\phi_0^+] [d\phi_0^-] \langle \phi_0^+ | e^{-\beta \hat{H}} | \phi_0^- \rangle \langle \phi_0^- | \phi_{t_{\max}} \rangle \langle \phi_{t_{\max}} | \phi_0^+ \rangle. \quad (2.10)$$

We can now use the path-integral representation of transition amplitudes between initial and final states which yields

$$Z = \int [d\phi_{t_{\max}}] [d\phi_0^+] [d\phi_0^-] \langle \phi_0^+ | e^{-\beta \hat{H}} | \phi_0^- \rangle \times \int_{\phi^+(t=0)=\phi_0^+}^{\phi^+(t=t_{\max})=\phi_{t_{\max}}} \tilde{\mathcal{D}}\phi^+ e^{iS_M[\phi^+]} \int_{\phi^-(t=t_{\max})=\phi_{t_{\max}}}^{\phi^-(t=0)=\phi_0^-} \tilde{\mathcal{D}}\phi^- e^{-iS_M[\phi^-]}. \quad (2.11)$$

Here, the path-integral measure reads  $\tilde{\mathcal{D}}\phi^\pm = \prod_{\vec{x}, t \in (0, t_{\max})} d\phi^\pm(\vec{x}, t)$  where the times 0 and  $t_{\max}$  are excluded. The matrix element containing the density matrix corresponds to the initial conditions for the quantum evolution on the forward path going from 0 to  $t_{\max}$  for the fields  $\phi^+$  as well as on the backward bath from  $t_{\max}$  back to 0 for the fields  $\phi^-$ <sup>2</sup>. The partition function can be further rewritten plugging in the path integral for the matrix element containing the density matrix. Finally, we arrive at the following expression for the partition function

$$Z = \int [d\phi_{t_{\max}}] [d\phi_0^+] [d\phi_0^-] \underbrace{\int_{\phi_E(0)=\phi_0^-}^{\phi_E(\beta)=\phi_0^+} \tilde{\mathcal{D}}\phi_E e^{-S_E[\phi_E]}}_{\text{therm. initial cond.}} \times \underbrace{\int_{\phi^+(t=0)=\phi_0^+}^{\phi^+(t=t_{\max})=\phi_{t_{\max}}} \tilde{\mathcal{D}}\phi^+ e^{iS_M[\phi^+]} \int_{\phi^-(t=t_{\max})=\phi_{t_{\max}}}^{\phi^-(t=0)=\phi_0^-} \tilde{\mathcal{D}}\phi^- e^{-iS_M[\phi^-]}}_{\text{quantum dynamics}}. \quad (2.12)$$

In the measure  $\tilde{\mathcal{D}}\phi_E$  the integration is omitted over the field values at  $\tau = 0$  and  $\tau = \beta$ . For the correlator (2.6) the derivation is analogous. (2.12) describes an initial value problem. The density matrix provides the initial conditions for the quantum time evolution along the forward and the backward path. This formulation can also be used to describe non-equilibrium phenomena, see e.g. [70]. In this thesis non-equilibrium phenomena will not be discussed.

<sup>2</sup>The phase factor  $e^{-iS_M[\phi^-]}$  has a minus sign because the time evolution runs backward from  $t_{\max}$  to 0.

## 2.2. Quantum Chromodynamics

In this section we review a few basic concepts on quantum chromodynamics summarized from textbooks [61–63]. We work in Euclidean space-time where the metric is  $\delta_{\mu\nu}$ .

### 2.2.1. Basics

Quantum Chromodynamics (QCD) describes the strongly interacting sector of the standard model. The Lagrangian of QCD reads

$$\mathcal{L} = \frac{1}{4} F_{\mu\nu}^a F_{\mu\nu}^a + \sum_f \bar{\psi}^f (\gamma_\mu D_\mu + m^{(f)}) \psi^f. \quad (2.13)$$

The gauge group is  $SU(N_c)$  with  $N_c = 3$  representing the number of colors in QCD. The fermion (quark) fields  $\psi^{(f)}$  are in the fundamental representation of the color group. The index  $f$  sums over the different quark flavours, i.e.  $f = u, d, c, s, t, b$ . The index  $a = 1, \dots, N_c^2 - 1$  sums over the generators  $t^a$  of the gauge group. The gauge (gluon) field reads  $A_\mu = A_\mu^a t^a$ , hence it lives in the Lie-algebra  $\mathfrak{su}(N_c)$ . The covariant derivative is  $D_\mu = \partial_\mu - ig A_\mu^a t^a$ . The field strength tensor is given by  $F_{\mu\nu}^a = \partial_\mu A_\nu^a - \partial_\nu A_\mu^a + g f^{abc} A_\mu^b A_\nu^c$ . Here  $f^{abc}$  are the structure constants of the gauge group  $SU(N_c)$ . QCD is a non-abelian gauge theory. Therefore non-linear terms in the gauge field appear in the pure gauge part. This means that the gluons interact among themselves which is in contrast to  $U(1)$  gauge theory in QED. With  $U(x) \in SU(N_c)$  an important symmetry of (2.13) is the local gauge symmetry

$$\begin{aligned} \psi(x) &\rightarrow U(x)\psi(x) \\ A_\mu(x) &\rightarrow U(x)A_\mu(x)U(x)^\dagger + \frac{i}{g}U(x)\partial_\mu U(x)^{-1}. \end{aligned} \quad (2.14)$$

### 2.2.2. Finite temperature QCD

At low temperatures quarks and gluons are confined into color-neutral hadrons. Increasing the temperature a transition to quark-gluon plasma occurs where the bound states dissolve and quarks and gluons form a strongly coupled state of matter.

#### Deconfinement transition

In the limit of infinitely heavy quark masses the quarks decouple from the dynamics and one is left with the pure  $SU(3)$  gauge theory. We consider a static quark-anti-quark pair. At large separations the potential increases linearly implying a constant force. Hence, to separate the pair an infinite amount of energy is needed. Instead, in a realistic situation with finite quark masses, two quark-anti-quark pairs are created if the corresponding energy is reached. In the deconfined phase the potential is of Coulomb type. In  $SU(3)$  gauge theory the order parameter for the confinement-deconfinement transition is the Polyakov loop  $L(\vec{x})$ . Its correlator is related to the free energy  $F_{q\bar{q}}(r)$  as follows [37]

$$\langle L(\vec{x})L^\dagger(\vec{y}) \rangle = e^{-F_{q\bar{q}}(r)/T} \quad (2.15)$$

where  $T$  denotes the temperature and  $r = |\vec{x} - \vec{y}|$  is the separation of the quark-anti-quark pair. As we let  $r \rightarrow \infty$  the correlator reduces to  $|\langle L \rangle|^2$ . In the confined phase the free

energy diverges with increasing distance implying that  $\langle L \rangle = 0$ . On the other hand in the deconfined phase the free energy stays finite and hence  $\langle L \rangle \neq 0$ . With finite quark masses the first-order phase transition turns into an analytic cross-over.

### Transport properties

Finding robust estimates for transport properties in the quark-gluon plasma is subject to intense research [42, 50, 72–74]. A prominent quantity is the shear viscosity  $\eta/s$ . It is related to the spatial part of the energy-momentum tensor correlator via the Kubo relation [75]

$$\eta(T) = \pi \left. \frac{d\rho(\omega)}{d\omega} \right|_{\omega=0}. \quad (2.16)$$

The spectral function is related to the real-time correlator as follows

$$\rho(\omega) = \int \frac{d^4x}{(2\pi)^4} e^{-i\omega t + i\vec{p}\cdot\vec{x}} \langle [T_{12}(x), T_{12}(0)] \rangle \Big|_{\vec{p}=0}. \quad (2.17)$$

Numerical simulations of relativistic viscous hydrodynamics and kinetic theory yield an upper bound for the shear viscosity over entropy of  $\eta/s \leq 0.4$  [76]. A lower bound to the shear viscosity  $\eta/s \geq 1/4\pi$  was estimated in calculations of  $\mathcal{N} = 4$  super Yang-Mills theory, see [77].

## 2.3. Aspects of lattice QCD

At low-energies the coupling constant of QCD is large requiring the use of non-perturbative methods. Lattice field theory was pioneered by Wegner [30] and Wilson who proposed to discretize QCD action on a finite space-time lattice [31]. The lattice has the volume  $\Omega = N_s^3 N_\tau$  where  $N_s$  denotes the number of spatial lattice points in  $x, y, z$  direction each and  $N_\tau$  indicates the number of lattice points in temporal direction. Usually periodic boundary conditions are chosen in all directions which minimizes effects from the finite volume. The periodicity in the compact time direction implies that in frequency space correlation functions are defined on the discrete Matsubara frequencies introduced in Section 2.1. We leave technicalities coming along with fermions on the lattice aside since this is not needed throughout this thesis. For those and further reading we refer to standard textbooks such as [78–82]. Moreover, for an introduction to finite density QCD we recommend [37].

### 2.3.1. Basics

In lattice QCD the algebra-valued gauge fields are replaced by group valued degrees of freedom which are placed on the links between the lattice sites on which the fermions sit. Those link variables are defined as  $U_\mu(x) = e^{iaA_\mu(x)}$ .

#### The Wilson action

The pure gauge action also called the Wilson plaquette action reads

$$S_G[U] = \frac{\beta}{N_c} \sum_{x,\mu<\nu} \text{tr} \left( \mathbb{1} - \frac{1}{2} \left( U_{\mu\nu}(x) + U_{\mu\nu}(x)^{-1} \right) \right). \quad (2.18)$$

Here the inverse gauge coupling  $\beta = 2N_c/g^2$  has been defined. Moreover, the plaquette is defined as an elementary loop containing four links

$$U_{\mu\nu}(x) = U_\mu(x)U_\nu(x + \hat{\mu})U_\mu(x + \hat{\nu})^{-1}U_\nu(x)^{-1}. \quad (2.19)$$

In the limit  $a \rightarrow 0$  the Wilson action reduces to the classical Euclidean action of the continuum theory related to (2.13).

### Monte Carlo simulations

The partition function reads

$$Z = \int \mathcal{D}U e^{-S_G[U]}. \quad (2.20)$$

Since the latter represents a high dimensional integral evaluating observables in lattice QCD requires Monte Carlo simulations. This was pioneered by Creutz, see e.g. [83]. The main Monte Carlo methods we use in this thesis are the Metropolis algorithm [84], the heat-bath method [85] as well as the Langevin algorithm [86]. Those methods sample field configurations  $\{U\}$  distributed according to the Boltzmann factor  $e^{-S_G[U]}$ . Observable estimates are then calculated as sample expectation values on a set of measurements taken during the Monte Carlo trajectory. For statistical data analysis solid advice is provided in [87].

### The continuum limit

In the full quantum theory, the continuum limit is taken by studying the parameter regions where the lattice theory becomes critical and approaches a second order phase transition. Usually the thermodynamic limit has to be performed before taking the continuum limit to obtain a well-defined result. The two limits do not commute. For further details, see the following textbook [88] or [89].

#### 2.3.2. The sign problem

For a finite temperature and chemical potential the partition function reads  $Z = \text{tr}(e^{-\beta(H-\mu N)})$ . The chemical potential is coupled to the particle number which is a conserved charge. Now, according to [90, 91] this is implemented on the lattice by changing the temporal hopping terms in the fermionic part of the action to  $\bar{\psi}_x U_{x,0} e^{a\mu} \gamma_0 \psi_{x+\hat{0}} - \bar{\psi}_{x+\hat{0}} U_{x,0}^\dagger e^{-a\mu} \gamma_0 \psi_x$ . Obviously this adds an imaginary part to the gauge field in temporal direction, see [37] for details. Consequently, the action of lattice QCD becomes complex. This entails that the Boltzmann weight is replaced by a highly oscillatory function. When tackling such an integrand via importance sampling precise cancellations of contributions of the same order of magnitude have to be taken care of. This also holds for configurations in the exponentially suppressed tail of the distribution. Those configurations become equally important. In QCD the sampling effort increases exponentially with increasing space-time volume. This is the numerical sign problem. A measure of its severity is the average phase. Thereto consider an oscillating function  $f$  representing the integrand of a system at finite density and a positive-definite function  $g$ . Let the partition function of the system be  $Z = \int dx f(x)$ . An observable expectation value computed with respect to  $f$  can now

be written as an expectation value with respect to  $g$

$$\langle \mathcal{O} \rangle_f = \frac{\int dx \mathcal{O}(x) f(x)}{\int dx f(x)} = \frac{\int dx \mathcal{O}(x) \frac{f(x)}{g(x)} g(x)}{\int dx \frac{f(x)}{g(x)} g(x)} = \frac{\langle \mathcal{O} \frac{f}{g} \rangle_g}{\langle \frac{f}{g} \rangle_g}. \quad (2.21)$$

This is called reweighting. If  $g = |f|$  a measure for the average phase is simply [36]

$$\left\langle \frac{f}{g} \right\rangle_g = \frac{Z_f}{Z_g} = e^{-\Omega \Delta f}. \quad (2.22)$$

Here  $\Delta f$  is the free energy density between the system described by  $f$  and the one described by  $g$ . Because  $Z_f \leq Z_g$  it follows  $\Delta f \geq 0$ . Hence, the average sign decreases with the space-time volume exponentially to zero.

Since the sign problem prohibits standard Monte Carlo methods this severely limits the access to the largest part of the QCD phase diagram. By now, there are many approaches towards a solution of the sign problem. Overviews addressing developments in finite density QCD over the last years can e.g. be found in [36, 92–96]. Amongst those are Taylor expansions [97], simulations at imaginary chemical potential [98, 99], reweighting [100], the density of states method [101], dual formulations [94], the Complex Langevin method [38, 102–109] and the Lefschetz thimble method [39, 40]. So far none of those methods have been able to give reliable results for  $\mu/T \gtrsim 1$ .

## 2.4. The Complex Langevin evolution

Over a decade the Complex Langevin evolution (CLE) has been an active area of research within lattice field theory. On the one hand mathematical aspects of the method have been studied by assessing its viability regarding convergence to the correct results. On the other hand the method has been applied to a variety of theories with a sign problem including full QCD at finite chemical potential [103, 110]. In this section we summarize a few key points on the Complex Langevin evolution.

### 2.4.1. Stochastic quantization

For simplicity consider a Euclidean real scalar field theory with the action  $S = S[\phi]$  where we drop the subscript  $E$ . Stochastic Quantization is based on describing a Euclidean quantum field theory by a classical statistical mechanical system in thermal equilibrium with a heat reservoir [86, 111]. This is formulated in terms of a stochastic process with a stationary distribution  $\exp(-S[\phi])/Z$ , where

$$Z = \int \mathcal{D}\phi \exp(-S[\phi]) \quad (2.23)$$

denotes the partition function. The stochastic process<sup>3</sup> evolves the fields according to the corresponding Langevin equation in a Langevin-time  $\tau$ <sup>4</sup>

$$\frac{\partial \phi(x, \tau)}{\partial \tau} = -\frac{\delta S}{\delta \phi(x, \tau)} + \eta(x, \tau). \quad (2.24)$$

<sup>3</sup>For an introductory textbook on Stochastic Quantization see [112] and for a general introduction to stochastic processes see [113, 114].

<sup>4</sup>The latter should not be confused with the imaginary time  $\tau$  introduced in Section 2.1. The Langevin time is a fictitious time that can also be thought of as a computer time.

Here,  $\phi(x, \tau)$  denotes the  $\tau$ -dependent scalar field and  $\eta(x, \tau)$  is the white noise field representing the quantum fluctuations. With vanishing noise the solution of the Langevin evolution converges to a solution of the classical equations of motion. The white noise is characterized by Gaussian distributed random numbers with

$$\begin{aligned}\langle \eta(x, \tau) \rangle &= 0, \\ \langle \eta(x, \tau) \eta(y, \tau') \rangle &= 2 \delta^{(d)}(x - y) \delta(\tau - \tau').\end{aligned}\tag{2.25}$$

In the limit  $\tau \rightarrow \infty$  thermal equilibrium is reached and the equal Langevin-time correlation functions of the statistical mechanical system converge to the Green's functions of the Euclidean quantum field theory. The real Langevin evolution (2.24) can be applied as an updating algorithm in lattice simulations to sample field configurations from the Boltzmann distribution.

For a given Langevin equation there is an associated Fokker-Planck equation. The latter describes the Langevin-time evolution of a probability distribution function  $P(\phi, \tau)$  and reads

$$\frac{\partial P(\phi, \tau)}{\partial \tau} = \int d^d x \frac{\delta}{\delta \phi(x, \tau)} \left( \frac{\delta S}{\delta \phi(x, \tau)} + \frac{\delta}{\delta \phi(x, \tau)} \right) P(\phi, \tau).\tag{2.26}$$

One can verify that the Boltzmann distribution  $\exp(-S[\phi])$  is therefore the stationary distribution of (2.26) with  $\partial_\tau P(\phi, \tau) = 0$ . More generally, if the action is real and positive semi-definite a stationary distribution of the Fokker-Planck equation exists which equals  $\exp(-S[\phi])$  and the solution converges exponentially fast [86, 115]. In summary, Stochastic Quantization provides an alternative to the standard quantization approach based on the path integral formalism.

### 2.4.2. Complex stochastic dynamics

Complex Langevin is a promising contender to tackle the sign problem because it does not rely on a positive probability measure. Instead the stochastic process wanders the complexified field space. For the original ideas see [116–119] and for recent reviews see [37, 115]. For simplicity we consider a holomorphic action  $S : \mathbb{R} \rightarrow \mathbb{C}, x \mapsto S(x)$  of one variable. Some complex parameter renders the action complex. In the Langevin equation the latter gives rise to a complex drift term which pushes the field variable  $x$  into the complex plane. With the fields being complexified by  $x \rightarrow x + iy$  the complex Langevin equation reads

$$\begin{aligned}\frac{\partial x}{\partial \tau} &= -\operatorname{Re} \left. \frac{\partial S}{\partial x} \right|_{x \rightarrow x+iy} + \eta_R \\ \frac{\partial y}{\partial \tau} &= -\operatorname{Im} \left. \frac{\partial S}{\partial x} \right|_{x \rightarrow x+iy} + \eta_I.\end{aligned}\tag{2.27}$$

The equilibrium distribution of the stochastic process (2.27) on the complexified field space is a positive measure  $P(x, y) dx dy$ . Complex Langevin yields correct expectation values of holomorphic observables with respect to the distribution  $P(x, y)$  if they agree with the ones determined by the complex density  $e^{-S}$  on the real manifold. This is put on formal grounds in [120, 121]. Therein it has also been identified that the decay properties of  $P(x, y)$  are relevant for the approach to work. If the decay is not sufficient, slower than

exponential, boundary terms cause the failure of Complex Langevin. This has also been studied recently in [122]. For the noise terms  $\eta_R$  and  $\eta_I$  are independent Gaussian random variables, thus

$$\begin{aligned}\langle \eta_R(\tau) \rangle &= 0 = \langle \eta_I(\tau) \rangle, \\ \langle \eta_{R(I)}(\tau) \eta_{R(I)}(\tau') \rangle &= 2N_{R(I)} \delta(\tau - \tau'), \\ \langle \eta_R(\tau) \eta_I(\tau') \rangle &= 0.\end{aligned}\tag{2.28}$$

Here it holds  $N_I \geq 0$  and  $N_R = N_I + 1$ . For simulations of the complex Langevin equation it is useful set  $N_I = 0$ . A finite  $N_I$  may cause slow decay in imaginary direction in  $P(x, y)$ . This has been analyzed in detail in [121].

Two main issues come with the complex Langevin equation

1. Convergence of the Langevin evolution to incorrect results.
2. Stability of the complex stochastic process.

The first issue is associated with the above mentioned boundary terms which may falsify the results. In the presence of poles in the drift force, an example being the contribution from fermion determinant in QCD this has been investigated in [105]. The second issue has been noticed in gauge theories. The complexified gauge group is the non-compact group  $SL(N, \mathbb{C})$ . The original unitary manifold  $SU(N)$  is non-attractive under the drift force which causes field configurations to wander off into imaginary directions. A method proposed to control this is gauge cooling [123]. It uses gauge transformations in  $SL(N, \mathbb{C})$  which are chosen such that they minimize the distance of link configurations in  $SL(N, \mathbb{C})$  to  $SU(N)$ . As we see later, the CLE and the Lefschetz thimbles are closely related. Studies investigating the interplay and the connection between the two approaches can be found in [124, 125].

## 2.5. Lefschetz thimbles

In the following we briefly revisit the Lefschetz thimble method. For simplicity we consider a complex action  $S(x)$  of a real variable that we extend to the complex plane  $x \rightarrow z = x + iy$ . The Lefschetz thimbles [39, 40] are the paths of steepest descent  $D_\sigma \in \mathbb{C}$  of the real part of the action and are obtained from the flow equation

$$\frac{\partial z}{\partial \tau} = -\overline{\frac{\partial S}{\partial z}}.\tag{2.29}$$

The thimbles end in the critical points  $z_\sigma \in \mathbb{C}$  of the action which are the stationary solutions to the right-hand side of (2.29) that is

$$\left. \frac{\partial S}{\partial z} \right|_{z=z_\sigma} = 0.\tag{2.30}$$

In the context of Lefschetz thimbles we sometimes use the terms critical point and stationary point synonymously. Along the thimble the real part of the action decreases and it is

minimal at the critical point  $z_\sigma$ . Importantly, the imaginary part of the action is constant along each thimble which can ameliorate the sign problem. The partition function can be rewritten as an integral over the union of the thimbles whose anti-thimbles (path of steepest ascent of  $\text{Re}[S]$ ) cross the real axis. If the critical points are non-degenerate this holds by continuously deforming the original real integration contour into the thimbles<sup>5</sup> [39]. The union of the thimbles is homotopy equivalent to the original integration domain. Hence, for the partition function we have

$$Z = \int_I dx e^{-S(x)} = \sum_\sigma n_\sigma e^{-i\text{Im}[S(z_\sigma)]} \int_{D_\sigma} dz e^{-\text{Re}[S(z)]} \quad (2.31)$$

where we define the sub-partition function on every thimble according to

$$Z_\sigma := \int_{D_\sigma} dz e^{-\text{Re}[S(z)]}. \quad (2.32)$$

Here,  $I \subset \mathbb{R}$  denotes the original real integration domain.  $n_\sigma$  counts the number of intersections of a given anti-thimble with  $I$ . The latter is also called the unstable thimble since the action is not bounded from below. Observables are obtained from the expression

$$\langle \mathcal{O} \rangle = \frac{1}{Z} \sum_\sigma n_\sigma e^{-i\text{Im}[S(z_\sigma)]} \int_{D_\sigma} dz \mathcal{O} e^{-\text{Re}[S(z)]} = \frac{\sum_\sigma n_\sigma e^{-i\text{Im}[S(z_\sigma)]} Z_\sigma \langle \mathcal{O} \rangle_\sigma}{\sum_\sigma n_\sigma e^{-i\text{Im}[S(z_\sigma)]} Z_\sigma}, \quad (2.33)$$

where we have defined

$$\langle \mathcal{O} \rangle_\sigma := \frac{1}{Z_\sigma} \int_{D_\sigma} dz e^{-\text{Re}[S(z)]} \mathcal{O}. \quad (2.34)$$

Monte Carlo simulations on the thimbles have been first proposed in [40]. For lattice theories defined as integrals over  $N$ -dimensional real manifolds (e.g.  $\mathbb{R}^N$  for scalar or  $U(1)^N$  for an abelian gauge theory) the thimble structure and numerical parametrizations are hard to determine. There are two basic algorithmic frameworks [40, 127] providing recipes for Monte Carlo simulations on the Lefschetz thimbles. The first employs Monte Carlo simulations directly on the thimbles. The latter continuously deforms the original integration path close to the actual thimbles to lessen the sign problem. In Euclidean space-time the Lefschetz thimble approach has been applied to bosonic theories as well as to (low-dimensional) QCD in [40, 128–132]. Recent applications to fermionic theories (such as the Thirring model) can be found in [127, 133]. Moreover, field theories in Minkowski space-time formulated on the Schwinger-Keldysh contour have been studied using the thimble formalism in [134]. Algorithmic improvements to the holomorphic gradient flow method were proposed in [135]. Recent contributions in the field more generally involve complex manifolds close to Lefschetz thimbles that are optimized such that they ameliorate the sign problem, see e.g. [136–139].

<sup>5</sup> One has to be careful if there are paths of steepest descent that connect two critical points which spoils the uniqueness of the thimble decomposition, see [39, 40, 126]. This is also known as Stokes phenomenon.

## 2.6. Spectral reconstruction

Here, we introduce a few technical aspects extract spectral properties from lattice data. The determination of the shear viscosity  $\eta$  in (2.16) requires the the computation of the spectral function corresponding to the energy-momentum tensor correlation function in real-time. The spectral function is related to the real-time correlator by a Fourier transformation followed by taking the imaginary part.

$$\rho(\omega) = \text{Im} \left[ \int dt e^{i\omega t} G(t) \right]. \quad (2.35)$$

The correlator is defined by the quantum statistical expectation value (2.6).

Since so far no direct real-time computation using non-perturbative methods have been possible we can however exploit the analytic continuation to imaginary times. Thermal correlators calculated in imaginary time are related to the spectral function via analytic continuation of (2.35)

$$G_\beta(\tau) = \int_0^\infty d\mu \frac{\cosh(\mu(\tau - \beta/2))}{\sinh(\beta\mu/2)} \rho(\mu). \quad (2.36)$$

However, finding the solution  $\rho(\mu)$  represents an ill- conditioned inverse problem. This is best understood examining the zero temperature limit of (2.36), see also [140]. which yields the Laplace transform of the vacuum spectral function

$$\lim_{\beta \rightarrow \infty} G_\beta(\tau) = \int_0^\infty d\mu e^{-\mu\tau} \rho_{\text{vac}}(\mu). \quad (2.37)$$

By Lerch's theorem the solution to the inverse problem is unique provided that  $\rho(\mu)$  is continuous [141, 142]. However, the inverse process - reconstructing  $\rho$  from a given  $G$  - is not continuous [143]. This means small perturbations in  $G$  can cause large changes in  $\rho$  which renders the inverse problem ill-conditioned. By means of the example of the energy-momentum tensor correlator whose  $\sim \omega^4$  part in the ultra-violet<sup>6</sup> contributes more than 90% to the integral (2.36) the authors of [144] illustrate the severity of the ill-conditioned problem. Two spectral functions completely differing in the infra-red regime with associated shear viscosities differing by a factor 10 correspond to only marginally different correlators. There is a high loss of information in the integral transform.

For practical purposes a numerical treatment of (2.36) requires the discretization of the integral usually by means of a trapezoidal rule. The numerical extraction of  $\rho$  thus reduces to solving the linear algebra problem  $G_i = K_{ij}\rho_j$ . Because we aim at extracting a continuous spectral function it holds  $\dim(\rho) > \dim(G)$  rendering the problem ill-posed, see [145]. Additionally, input data  $G_\beta$  usually obtained in lattice simulations contains noise. Over the last years a plethora of method tackling the inverse problem has been developed. A prominent class are Bayesian methods such as the Maximum Entropy Method (MEM) [146, 147] and the more recent Bayesian reconstruction (BR) method [148]. Those methods aim at estimating the most probable spectral reconstruction  $\rho$  given the data  $G_\beta$ . Key element to this is Bayes' rule and the most probable solution to the inverse problem is defined by the maximum of the posterior distribution. The latter defines the probability

<sup>6</sup>This can be shown in the hard-thermal loop formalism [50].

distribution of obtaining a certain  $\rho$  given the data  $G_\beta$ . Importantly, the above mentioned non-uniqueness of the problem requires regularization which the Bayesian methods provide by incorporating prior knowledge on  $\rho$  such as assumptions on smoothness or positivity, see [146, 148] for details. Amongst further reconstruction methods rank Tikhonov regularization, see [149] for a recent study of lattice vacuum correlators of the gauge sector as well as the Backus-Gilbert method used for spectral reconstructions of the energy-momentum tensor correlator in [150].

## 3. Colored Noise Cooling

### 3.1. Motivation and overview

Extracting physical quantities in lattice field theories at finite temperature and density with high precision requires smoothing of the field configurations which is also called cooling. Cooling algorithms, see e.g. [151], are set-up to eliminate configurations that carry large ultraviolet fluctuations. They are based on the assumption that physics scales can be safely separated from the ultraviolet scales where cooling is applied. Then, cooling simply improves the signal-to-noise ratio without altering the physics under investigation. To illustrate this we consider topological properties in Yang-Mills theory or QCD, see [78] for details. Here, cooling has been applied successfully to compute observables such as the action density or the topological charge density. In practice cooling methods for lattice gauge theories are iterative procedures that replace a link  $U_\mu(x)$  by a gauge group element constructed such that it minimizes the local action. Thereby all other links remain fixed, see [152] for details. Thus, if cooling is not stopped it produces classical configurations for a large number of iterations or cooling times. Hence, the crucial question is that after a well-defined stopping time. This stopping time can be related to the physical scale of the cooled theory of interest, see e.g. [153]. The same intricacy also is present for the gradient flow cooling [154–159], for further applications see [160, 161]. A comparison of the two approaches can be found in [152].

In this chapter we propose a cooling method based on Stochastic Quantization cooled with colored noise. This combines the Langevin equation (2.24) with the gradient flow. To that end we first notice that the Langevin equation without noise simply is the gradient flow. Hence, removing the noise for high momentum modes above a UV cutoff scale  $\Lambda$  leaves us with a gradient flow for these modes. Then, the related colored noise Langevin evolution completely removes the momentum modes with  $p^2 > \Lambda^2$ . In summary, a Langevin equation with such a colored noise introduces a UV momentum cutoff  $\Lambda$  to the path integral. By varying the cutoff  $\Lambda$  we interpolate between the full quantum evolution characterized by the Langevin equation with Gaussian white noise ( $\Lambda \rightarrow \infty$ ) and the classical evolution characterized by the gradient flow ( $\Lambda = 0$ ). This approach is closely related to the concept of stochastic regularization [162, 163]. For extended studies on gauge theories by this group, see [164–166].

Our approach is put to work in a scalar theory and numerical results are presented in two dimensions. Colored noise is also related to standard Kadanoff block spin steps [167], as well as to the realization of the latter within the functional renormalization group, for reviews see e.g. [41, 168–172]. We show that a large regime of ultraviolet fluctuations can be removed without altering the physics content of the theory. Hence, cooling with colored noise can significantly reduce the numerical costs of lattice simulations done within Stochastic Quantization.

The chapter is organized as follows. In Section 3.2 we introduce the concept of stochastic

regularization and discuss colored noise in the continuum. The lattice field theory formulation of the Langevin equation with colored noise is described in Section 3.3. In Section 3.4 we review real scalar field theory on the lattice providing a suitable testbed for our numerical studies. This is followed by the discussion of the relation between colored noise and the renormalization group in Section 3.5. In Section 3.6 we discuss numerical results from simulations with colored noise. Applications of the approach and the relation to the functional renormalization group is discussed in Section 3.7. For the largest part of this chapter text and figures are taken from the author's publication [55].

## 3.2. Stochastic quantization with colored noise

In the Langevin formulation the noise containing the quantum fluctuations can be regularized in the ultraviolet by introducing a cutoff parameter  $\Lambda$  [163]. The modified stochastic process in terms of the Langevin equation with a colored noise kernel then reads

$$\frac{\partial \phi(x, \tau)}{\partial \tau} = -\frac{\delta S}{\delta \phi(x, \tau)} + r_\Lambda(\Delta_x) \eta(x, \tau), \quad (3.1)$$

where the dimensionless regularization function  $r_\Lambda(\Delta_x)$  is a function of the ratio  $\Delta_x/\Lambda^2$  of the Laplace operator and the square of the cutoff  $\Lambda$ . Using a short-hand notation for the functional derivatives, see Appendix A.4, the associated Fokker-Planck equation is

$$\frac{\partial P(\phi, \tau)}{\partial \tau} = \int d^d x \frac{\delta}{\delta \phi_x} \left( \frac{\delta S}{\delta \phi_x} + r_\Lambda^2(\Delta_x) \frac{\delta}{\delta \phi_x} \right) P(\phi, \tau). \quad (3.2)$$

Note, that with  $r_\Lambda(\Delta_x) \rightarrow 1$  in the limit  $\Lambda \rightarrow \infty$  the full quantum theory is recovered. For a detailed derivation of the Fokker-Planck equation from the Langevin equation with a noise kernel see Appendix A.4. Note, that the regularization function can be chosen in different ways. A simple and intuitive choice of the regularization function is a sharp cutoff in momentum space

$$r_\Lambda(p^2) = \theta(\Lambda^2 - p^2). \quad (3.3)$$

Using (3.3) in the Fokker-Planck equation (3.2) allows for a simple relation of Stochastic Quantization with colored noise with functional renormalization group equations, for reviews see [41, 168–172]. A solution of the fixed point equation  $\partial_\tau P = 0$  in momentum space is given by

$$P_\Lambda(\phi, \tau) = \exp(-S - \Delta S_\Lambda), \quad (3.4)$$

with the cutoff term

$$\Delta S_\Lambda[\phi] = \frac{1}{2} \int_p \phi_p \Lambda^2 \left( \frac{1}{r_\Lambda(p^2)} - 1 \right) \phi_{-p}. \quad (3.5)$$

Inserting (3.4) with (3.5) into (3.2) we are led to the fixed point equation

$$\left[ \left( 1 - r_\Lambda(p^2) \right) \frac{\delta S}{\delta \phi_p} - r_\Lambda(p^2) \frac{\delta \Delta S_\Lambda}{\delta \phi_p} \right] P_\Lambda(\phi, \tau) = 0. \quad (3.6)$$

Both terms in the square brackets in (3.6) vanish for  $p^2 < \Lambda^2$  as they are proportional to  $1 - r_\Lambda(p^2)$ . Note that in the second term this comes from  $r_\Lambda(1/r_\Lambda - 1) = 1 - r_\Lambda$ . In turn,

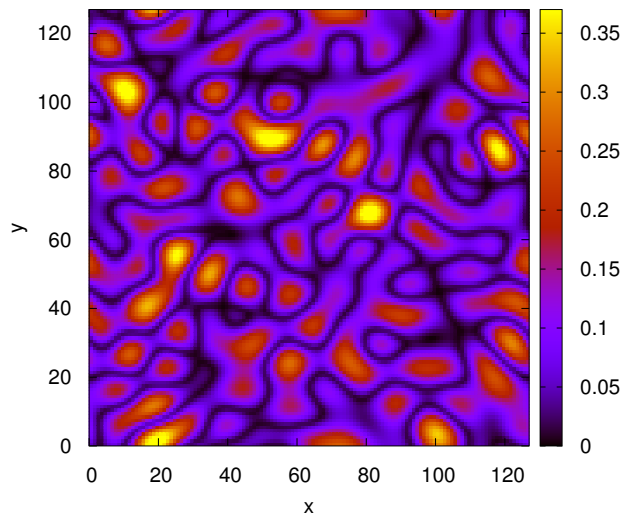


Figure 3.1.: Heat map plot of the absolute value of colored noise on a  $128 \times 128$  lattice for momentum cutoff  $s_\Lambda = 8$  (see Sec. 3.3 for the definition of the lattice cutoff). In contrast to the white noise picture described in (2.25) non-delta like spatially correlated structures extending over several lattice spacings are visible. The arrangement of the structures however appears to be random for we require the UV-modified stochastic process to remain Markovian.

for  $p^2 > \Lambda^2$  the measure  $P(\phi, \tau)$  vanishes and hence (3.6) is satisfied for all fields and momenta. In summary, this entails that the ultraviolet modes satisfy the classical equations of motion and no quantum effects are taken into account. For more details on the connection between the kerneled Fokker-Planck equation and the functional renormalization group see Appendix A.5.

The regularization function (3.3) defines the colored noise field

$$\eta_{\text{col}}(p, \tau) := \eta(p, \tau) \theta(\Lambda^2 - p^2), \quad (3.7)$$

with the space-time representation

$$\eta_{\text{col}}(x, \tau) = \frac{1}{(2\pi)^d} \int d^d p \eta_{\text{col}}(p, \tau) e^{-ip \cdot x}. \quad (3.8)$$

This leads us to the Langevin equation with colored noise

$$\frac{\partial \phi(x, \tau)}{\partial \tau} = -\frac{\delta S}{\delta \phi(x, \tau)} + \eta_{\text{col}}(x, \tau). \quad (3.9)$$

A visualization of the colored noise  $\eta_{\text{col}}(x, \tau)$  in (3.8) with the sharp cutoff (3.7) is illustrated in Fig. 3.1.

### 3.3. Lattice QFT with colored noise

In this section we present the implementation of our method for lattice simulations of Euclidean quantum field theories. We consider finite isotropic space-time lattices in  $d$  dimensions setting  $N_s = N_\tau = N$  lattice points in each direction. Hence, the physical volume is  $a^d \Omega = (aN)^d$ . Then, the allowed lattice momenta on the dual momentum lattice are given by

$$p_\mu = \frac{2\pi}{aN} n_\mu, \quad \text{with} \quad \mu = 1, \dots, d, \quad (3.10)$$

where  $n_\mu = -N/2 + 1, \dots, N/2$ . In the thermodynamic limit  $N \rightarrow \infty$  the  $d$ -dimensional Brillouin zone is given by the interval  $(-\pi/a, \pi/a]^d$ .

In lattice simulations using the Langevin equation with colored noise we work with the sharp regulator (3.3) introduced in the previous section. Similarly as in the continuum, colored noise is generated by cutting off the noise modes on the momentum lattice followed by a discrete Fourier transformation<sup>1</sup> back to the real space lattice which leads to

$$\eta_{\text{col}}(x, \tau) = \frac{1}{\Omega} \sum_p e^{ip \cdot x} r_\Lambda(p^2) \eta(p, \tau). \quad (3.11)$$

The discretized Langevin equation with colored noise thus reads

$$\phi(x, \tau_{n+1}) = \phi(x, \tau_n) - \frac{\delta S}{\delta \phi(x, \tau_n)} \Delta\tau + \sqrt{\Delta\tau} \eta_{\text{col}}(x, \tau_n) \quad (3.12)$$

with the Langevin time step  $\Delta\tau$ . In our implementation we retain noise modes with  $p^2 \leq \Lambda^2$  and remove larger modes, see Fig. 3.2. Modes are being removed as the decreasing cutoff  $\Lambda$  sweeps over the discrete lattice momenta. Note that the lattice theory only changes at the discrete values  $\Lambda = s_\Lambda \pi/a$  with

$$s_\Lambda = \max \left( \frac{1}{\sqrt{d}} \sqrt{n_\mu^2} \right) \quad \text{with} \quad p^2(n_\mu) \leq \Lambda^2. \quad (3.13)$$

For the  $\Lambda$ -dependence see Fig. 3.3. For these values the cutoff  $\Lambda$  sweeps over the discrete momentum values, see Fig. 3.2 for a two-dimensional dual lattice. We also notice that integer values of  $s_\Lambda$  indicate a standard cubic momentum lattice of non-zero quantum fluctuations. Moreover  $s_\Lambda = N/2$  corresponds to the standard Langevin evolution with Gaussian white noise. For  $s_\Lambda = 0$  only the zero-momentum mode contributes to the colored noise. For the simulation with the gradient flow we use the Langevin equation with the noise term set to zero.

For the further discussion it is useful to split the full field in momentum space in a classical and quantum contribution,

$$\phi(p) = \phi_{\text{cl}}(p) + \delta\phi_{\text{qu}}(p), \quad (3.14)$$

with

$$\delta\phi_{\text{qu}}(p) = 0 \quad \text{for} \quad p^2 > s_\Lambda^2. \quad (3.15)$$

<sup>1</sup>The conventions for the Fourier transformation on the lattice used in this thesis are summarized in Appendix A.1.

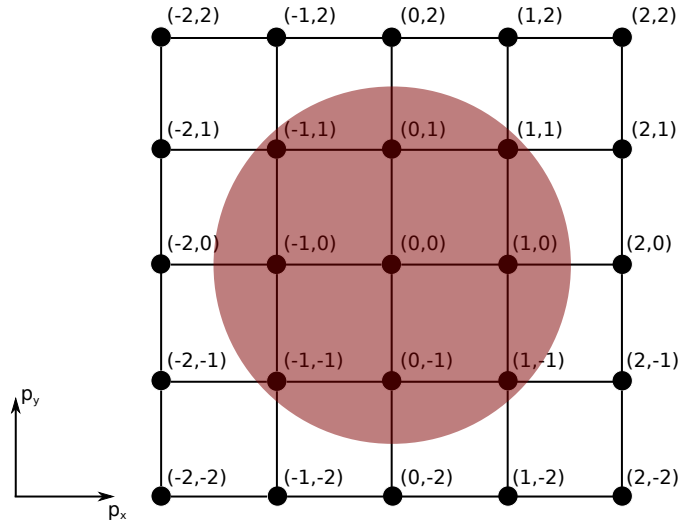


Figure 3.2.: Schematic illustration of the dual lattice in  $d = 2$  describing our implementation of the cutoff. The radius of the red shaded circle corresponds to the cutoff  $\Lambda$ . Noise modes outside of the circle have zero weight in the Langevin evolution. Colored noise only receives finite contributions for momentum modes from inside the red circle.

Note that the field  $\delta\phi_{\text{qu}}$ , that carries the quantum fluctuations, lives on the momentum lattice defined by  $p^2 \leq s_\Lambda^2$ . Henceforth we call this generically smaller lattice the *quantum* lattice. In turn, the classical field  $\phi_{\text{cl}}$  lives on the full momentum lattice which we therefore call the *classical* lattice. In position space this translates into a fine classical lattice and a coarser quantum lattice.

## 3.4. Scalar field theory

### 3.4.1. Lattice formulation

Scalar field theories on the lattice have been investigated in numerous works over the recent decades and their applications range over a broad spectrum of topics involving particle, statistical and condensed matter physics. Here, we consider a Euclidean real single-component scalar field theory in  $d$  dimensions with lattice action

$$S = \sum_x a^d \left[ \frac{1}{2} \sum_{\mu=1}^d \frac{(\phi_0(x + a\hat{\mu}) - \phi_0(x))^2}{a^2} + \frac{m_0^2}{2} \phi_0^2 + \frac{g_0}{4!} \phi_0^4 \right], \quad (3.16)$$

where  $\hat{\mu}$  denotes the unit vector in  $\mu$ -direction. The subscript 0 indicates bare quantities, i.e. the bare mass  $m_0$ , the bare coupling  $g_0$  and the bare field  $\phi_0$  in the action. For numerical simulations the action is cast in the following dimensionless form

$$S = \sum_x \left[ -2\kappa \sum_{\mu=1}^d \phi(x)\phi(x + \hat{\mu}) + (1 - 2\lambda) \phi(x)^2 + \lambda \phi(x)^4 \right]. \quad (3.17)$$

The parameter  $\kappa$  is the so-called hopping parameter and  $\lambda$  describes the quartic coupling

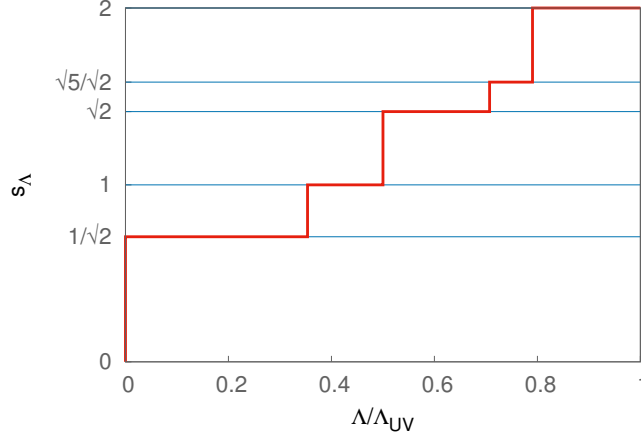


Figure 3.3.:  $s_\Lambda(\Lambda)$  for  $N = 4$  in two dimensions. The integer values of  $s_\Lambda$  characterize the standard cubic momentum lattices. The latter will be used in the further analysis.

of the theory. Note that here, the parameters  $\kappa$  and  $\lambda$  are positive. They are related to the bare mass, bare coupling and the lattice spacing in the following way

$$\begin{aligned} a^{\frac{d-2}{2}} \phi_0 &= (2\kappa)^{1/2} \phi, \\ (am_0)^2 &= \frac{1-2\lambda}{\kappa} - 2d, \\ a^{-d+4} g_0 &= \frac{6\lambda}{\kappa^2}, \end{aligned} \quad (3.18)$$

where we have introduced the dimensionless field  $\phi$ . The white noise Langevin update step ( $\tau_n \rightarrow \tau_{n+1}$ ) of a field variable at lattice point  $x$  is given by

$$\phi(x, \tau_{n+1}) = \phi(x, \tau_n) + K[\phi(x, \tau_n)]\Delta\tau + \sqrt{\Delta\tau} \eta(x, \tau_n), \quad (3.19)$$

where the drift term  $K[\phi(x)] = -\delta S[\phi]/\delta\phi(x)$  explicitly reads

$$K[\phi(x)] = 2\kappa \sum_{\mu=1}^d [\phi(x + \hat{\mu}) + \phi(x - \hat{\mu})] + 2\phi(x) (2\lambda(1 - \phi(x)^2) - 1). \quad (3.20)$$

The process (3.19) can be solved iteratively by using an explicit Euler-Maruyama discretization scheme. Higher order Runge-Kutta schemes are possible as well and are discussed in [86, 173, 174].

Let us consider the case  $d \geq 2$ . If the action contains no explicit symmetry breaking term for each value of  $\lambda$ , there exists a critical value of the hopping parameter  $\kappa_c$  at which the system undergoes a second order phase transition. The  $\mathbb{Z}_2$  symmetry of the system becomes spontaneously broken above the critical point. The phase transition for the case of  $d = 2$  is illustrated in Fig. 3.4. Classically, the broken phase is characterized by a negative mass term  $(am_0)^2 < 0$ , leading to two degenerated minima in the potential. Within the dimensionless formulation these minima are at  $\pm\phi_{\min}$  with

$$\phi_{\min} = \left[ \frac{1}{2\lambda} (2d\kappa - 1 + 2\lambda) \right]^{1/2}. \quad (3.21)$$

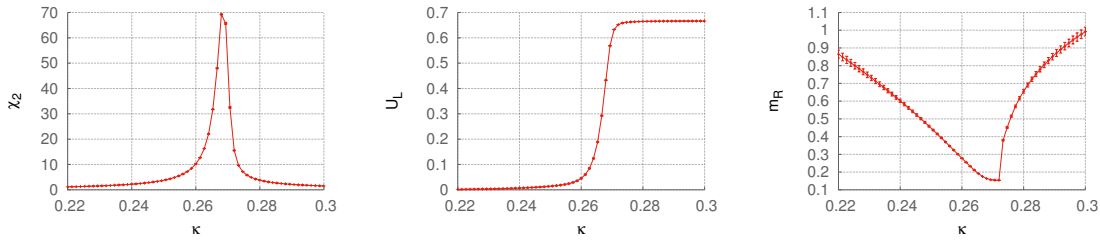


Figure 3.4.: The phase diagram of  $O(1)$  scalar field theory on the lattice characterized by three of the main observables, here at (fixed) coupling  $\lambda = 0.02$  for a  $32 \times 32$  lattice. (Left) The plot on the left-hand side shows the susceptibility as a function of the hopping parameter  $\kappa$ . (Middle) The central figure depicts the Binder cumulant. The critical value is given by  $\kappa_c \approx 0.27$ . The range for  $\kappa \leq \kappa_c$  describes the symmetric phase. For values of  $\kappa$  larger than the critical point the theory is in the phase with spontaneously broken symmetry. (Right) The figure on the right-hand side shows the renormalized mass  $m_R$  in lattice units. The results were produced using the Langevin equation with white noise taking  $10^6$  measurements in equilibrium  $\tau \rightarrow \infty$ . The data points are connected by lines to guide the eye.

The critical value for the hopping parameter in the classical theory can be determined by requiring the mass term to vanish, leading to

$$\kappa_c(\lambda) = \frac{1 - 2\lambda}{2d}. \quad (3.22)$$

### 3.4.2. Observables

We now discuss some of the main observables to explain the properties of the theory. Those are useful in the analysis of the effects of colored noise. The vacuum expectation value of the field also called the magnetization reads

$$\langle M \rangle := \left\langle \frac{1}{\Omega} \sum_x \phi(x) \right\rangle. \quad (3.23)$$

It is zero in the symmetric phase of the theory and takes a finite value in the broken phase. Note that  $\Omega$  is given by the number of lattice points since we consider the dimensionless formulation. The connected two-point correlation is defined as

$$G_c(x, y) = \langle \phi(x)\phi(y) \rangle_c \equiv \langle \phi(x)\phi(y) \rangle - \langle \phi(x) \rangle \langle \phi(y) \rangle. \quad (3.24)$$

From this we can compute the two-point correlation function of time slices where we denote the Euclidean time by  $t$  in this chapter. To that end we evaluate the spatial Fourier transform of  $G_c(x, y)$  at vanishing spatial momentum

$$G_c(t) = \frac{1}{V} \sum_{\vec{x}} G_c(x, 0). \quad (3.25)$$

It measures the decay of correlations over the time extent of the lattice. The mass is related to the inverse correlation length. Moreover, (3.25) is related to the connected

susceptibility by

$$\chi_2 = V \sum_t G_c(t) = \Omega (\langle M^2 \rangle - \langle M \rangle^2). \quad (3.26)$$

Hence, the susceptibility is the (d-dimensional) Fourier transform of the correlator (3.24) evaluated at zero momentum. The susceptibility measures the Gaussian fluctuations of the magnetization. The fourth-order cumulant or Binder cumulant [175] quantifies the kurtosis of the fluctuations. It can be used to study phase transitions and to determine critical exponents. The Binder cumulant reads

$$U_L = 1 - \frac{1}{3} \frac{\langle M^4 \rangle}{\langle M^2 \rangle^2}. \quad (3.27)$$

It vanishes in the symmetric phase and assumes the value 2/3 in the phase with broken symmetry. The second moment is defined by

$$\mu_2 := dV \sum_t t^2 G(t)_c. \quad (3.28)$$

From (3.26) and (3.28) the renormalized mass can be computed according to

$$m_R^2 = \frac{2d\chi_2}{\mu_2}. \quad (3.29)$$

This is derived in more detail in Appendix A.2. In Fig. 3.4 the behaviour of the connected susceptibility, the Binder cumulant and the renormalized mass as a function of  $\kappa$  for constant  $\lambda = 0.02$  are shown across the phase transition.

### 3.5. Colored Noise and the Renormalization Group

Colored noise introduces a UV cutoff  $s_\Lambda$ . The change of the theory with an infinitesimal change of the cutoff is governed by the renormalization group. In terms of our lattice setup colored noise leads to the separation into the classical and the quantum lattice (3.14). The momentum space quantum lattice (3.15) contains only field modes with  $|p| \leq s_\Lambda$ . Those receive a non-zero contribution to fluctuations from the colored noise term in the Langevin equation (3.12). The remaining contribution encoded in the drift term is purely classical and applies to all field modes. Let  $s_{\Lambda, \max}$  denote the maximum cutoff on the lattice with  $N^d$  points. In general, for a given cutoff  $s_\Lambda \leq s_{\Lambda, \max}$  the quantum lattice in momentum space has less points than the classical lattice. In the limit  $\tau \rightarrow \infty$  the field modes with  $|p| > s_\Lambda$  assume their classical value according to the limit of the gradient flow. The fewer points of the quantum momentum lattice translate into a coarser quantum real space lattice as compared to the classical real space lattice, see Fig. 3.5. With this in mind we study the relation of the colored noise Langevin evolution to the renormalization group in more detail. We investigate if the effect of the cutoff  $s_\Lambda$  may be compensated by varying the lattice spacing  $a$ , thus tuning the coarseness of the quantum real space lattice (3.15). To this end we compare a simulation with white noise at  $s_\Lambda = s_{\Lambda, \max}$  on a coarse lattice with spacing  $a_1$  with a colored noise simulation at cutoff  $s_\Lambda < s_{\Lambda, \max}$  on a fine lattice with spacing  $a_2 < a_1$ .

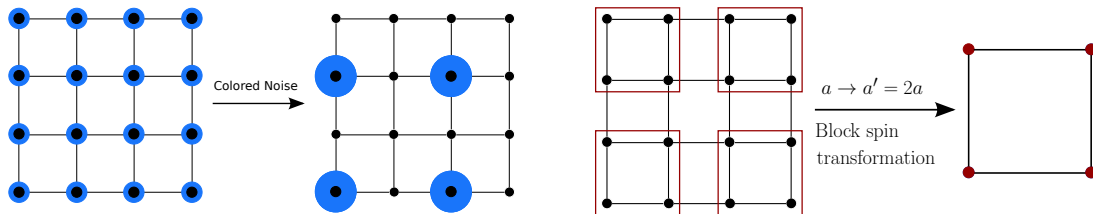


Figure 3.5.: (Left) Illustration of the classical and the quantum lattice in two-dimensional real space (blue figure). The two lattices agree for the Langevin equation with white noise where  $s_\Lambda = s_{\Lambda,\max}$ , see the left lattice sketch. Using a sharp regulator only field modes with  $|p| \leq s_\Lambda$  receive a non-vanishing contribution from the colored noise term. This leads to a coarser quantum lattice (blue circles) compared to its classical counterpart (black points) which is unaffected by the cutoff.

(Right) A typical block spin transformation in two dimensions is illustrated (red figure). A possible choice of the transformation is to define the blocked field variables by averages over the four fields inside the red squares. This leads to a coarser lattice with double the lattice spacing and a quarter of the original lattice points. The illustrations point out the analogy between colored noise coarsening the quantum lattice and standard block spin transformations.

Our procedure is to introduce scale factors for the following parameters

$$a \rightarrow a' = s^{-1}a, \quad N \rightarrow N' = sN, \quad p \rightarrow p' = sp, \quad (3.30)$$

where  $s \geq 1$  and  $a, a'$  are the original coarse and the fine lattice spacing. Correspondingly, the lattice size  $N$  as well as the lattice momenta  $p$  are transformed. The physical volume  $(aN)^d$  is thereby kept constant. The cutoff is transformed according to

$$s_\Lambda(a, N) \rightarrow s_\Lambda'(a', N') = s^{-1}s_\Lambda(a', N'). \quad (3.31)$$

To give an explicit example of our transformation logic we consider the case  $N = 4, s = 2$ . Let the cutoff on the coarse lattice be  $s_\Lambda(a, N = 4) \equiv s_{\Lambda,\max}(a, 4) = 2$ . This corresponds to the white noise case. The transformed cutoff reads  $s_\Lambda'(s^{-1}a, sN) = 2 = s_{\Lambda,\max}(a/2, 8) / 2$ . This corresponds to a colored noise simulation at half the maximum cutoff on the finer lattice.

The above scaling transformations result in a change of the parameters  $\kappa$  and  $\lambda$  in the scalar theory introduced in Sec. 3.4. From now on we explicitly consider the two-dimensional theory. To derive the tree-level renormalization group equations for the parameters  $\kappa$  and  $\lambda$  we fix the bare parameters  $m_0, g_0$ , see (3.18) in Sec. 3.4. The first expression of (3.30) yields

$$\begin{aligned} (am_0)^2 &\rightarrow s^{-2}(am_0)^2, \\ a^2g_0 &\rightarrow s^{-2}a^2g_0. \end{aligned} \quad (3.32)$$

Next we use the definition (3.18) in (3.32) leading to

$$\begin{aligned} s^{-2} \left[ \frac{1 - 2\lambda}{\kappa} - 4 \right] &= \frac{1 - 2\lambda'}{\kappa'} - 4 \\ s^{-2} \frac{6\lambda}{\kappa^2} &= \frac{6\lambda'}{\kappa'^2}. \end{aligned} \quad (3.33)$$

These equations can be solved for  $\kappa'$  and  $\lambda'$  used in the colored noise simulation with cutoff  $s_\Lambda'$ . We remark, that the equations (3.33) are akin with standard block-spinning equations [167, 176]. Under a complete block spin transformation the partition function is invariant. This requires an adjustment of the couplings of the theory which completes the renormalization group step. The right-hand side of Fig. 3.5 shows a typical block spin transformation on a two-dimensional lattice. Field variables are organized into blocks by local averaging which reduces the number of lattice points and renders the lattice coarser. The physical volume thereby remains fixed. For the correlation length this entails

$$2\xi(N^B = N/2, \kappa^B, \lambda^B) = \xi(N, \kappa, \lambda), \quad (3.34)$$

where  $N^B, \kappa^B, \lambda^B$  are the number of lattice points and the adjusted couplings on the blocked lattice. Our procedure is therefore analogous to block spinning since decreasing the cutoff  $s_\Lambda$  generates the local averaging and the coarsening of the quantum lattice.

## 3.6. Numerical Results

In this section, we present numerical results for the scalar theory in two dimensions. All simulations in this work have been carried out using the sharp regulator function defined in (3.3) and a fixed Langevin time step  $\Delta\tau = 10^{-2}$ . For a comparison of different regularization choices see App. A.4.2. In the first part of this section we study the effect of the sliding cutoff scale  $s_\Lambda$  by means of the observables introduced in Sec. 3.4. Our simulation with maximal  $s_\Lambda$  (white noise) reproduces the results in [177]. In the second part we focus on the relation between colored noise and the real space renormalization group.

### 3.6.1. Colored Noise: incomplete blocking

A first check of our colored noise approach is shown in Fig. 3.6. The expectation value of the absolute magnetization measured on a  $32 \times 32$  lattice is plotted as a function of the cutoff  $s_\Lambda$ . Here, for the parameter choice ( $\kappa = 0.26, \lambda = 0.02$ ) the classical theory is in the broken phase and the full quantum theory is in the symmetric phase. The white noise result ( $s_\Lambda = 16$ ) is indicated by the blue dashed line. We find that colored noise (red data) allows for a consistent interpolation between the full quantum theory and the classical theory.

Next the interpolation between the two phases is investigated further by considering the fluctuation content of the theory. Thereto, we analyze the susceptibility, the Binder cumulant and the renormalized mass shown in Fig. 3.7. The parameters are the same as for Fig. 3.6. Cutting off ultraviolet modes gradually moves the susceptibility (left) and the Binder cumulant (middle) across the phase transition. This confirms the effects of colored noise observed in Fig. 3.6. The right plot in Fig. 3.7 shows the renormalized mass

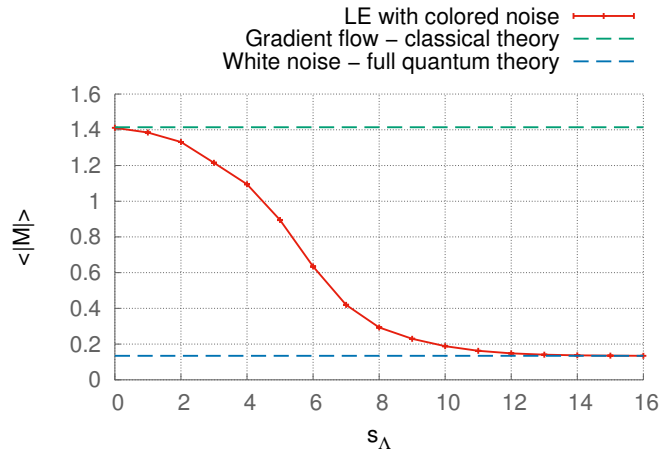


Figure 3.6.: Magnetization  $\langle |M| \rangle$  as a function of the cutoff  $s_\Lambda$  for  $\kappa = 0.26$ ,  $\lambda = 0.02$  and  $N = 32$ . For these external parameters  $(\kappa, \lambda)$  the minima of the classical potential are located at  $\pm\phi_{\min}$  with  $\phi_{\min} = \sqrt{2}$  as given by (3.21). We find a consistent interpolation between the classical and the full quantum theory using our colored noise setup.

calculated from the second moment and the connected susceptibility. The mass decreases with lowering the cutoff which means that the correlation length (in lattice units) increases. Beyond the critical point we expect the renormalized mass to increase again. However, for  $s_\Lambda < 4$  the sharp regulator induces oscillations in the correlation function of time slices. Then,  $m_R$  as defined in (3.29) shows a delayed transition from the symmetric to the broken phase. This problem can be resolved with the application of a smooth regulator function. In Appendix A.4.2 we analyze the behaviour of the correlation function of time slices comparing two different regularization choices. From this we can draw conclusions on the behaviour of  $m_R$  for any  $s_\Lambda$ . In summary we find that the susceptibility, the Binder cumulant and the renormalized mass represent quantities that are sensitive to the application of colored noise if all bare parameters  $(\kappa, \lambda)$  and the lattice size  $N$  are kept fixed.

To continue our analysis we investigate the susceptibility as a function of  $\kappa$  for different cutoffs  $s_\Lambda$  as shown in Fig. 3.8. Here, the results were produced on a  $64 \times 64$  lattice where  $\lambda = 0.02$  is kept fixed. The violet curve depicts the white noise result. Our observations are: The peak position corresponding to  $\kappa_c$  is successively shifted towards lower values of  $\kappa$  with decreasing cutoff. This is consistent with the previous results in this section. Colored noise removes quantum fluctuations rendering the theory more classical. In the limit of the pure gradient flow the peak of the susceptibility would lie directly on the tree-level value of  $\kappa_c^{(\text{cl})} = 0.24$  according to (3.22). The stepwise UV regularized theory shows its critical behaviour in ranges of  $\kappa$  where the full quantum theory ( $s_\Lambda = s_{\Lambda, \text{max}}$ ) lives in the symmetric phase.

Moreover, in the situations studied here the peak height shrinks when lowering the cutoff below  $s_\Lambda = 4$ . This suggests that the momentum fluctuations below this characteristic momentum scale given by  $s_\Lambda = 4$  are relevant for the physics observed. Removing these momenta with a lower cutoff therefore modifies the theory. In turn, the momentum fluctuations above this scale are physically irrelevant.

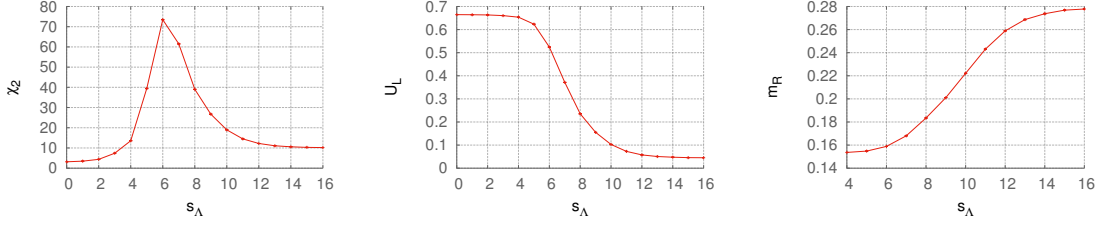


Figure 3.7.: The phase transition of the theory is shown by means of its characteristic observables as a function of the cutoff  $s_\Lambda$ . The parameters  $N = 32$ ,  $\kappa = 0.26$  and  $\lambda = 0.02$  are fixed. (Left) The susceptibility shows a peak indicating that the quantum theory *moves* from the symmetric to the broken phase where the classical theory lives as ultraviolet modes are being removed successively. (Middle) The Binder cumulant confirms this effect of colored noise. (Right) The renormalized mass  $m_R$  smoothly decreases towards the phase transition as the cutoff is lowered from  $s_\Lambda = 16$  to  $s_\Lambda = 4$ . For  $s_\Lambda < 4$ ,  $m_R$  as defined in (3.29) shows a delayed phase transition from the symmetric to the broken phase. Moreover, below  $s_\Lambda = 4$  the sharp cutoff imprints artifacts on the correlation function. For a detailed illustration of this behaviour see also Appendix A.4.2.

### 3.6.2. Colored noise: complete blocking at tree level

In this section we relate the effects of colored noise to the real space renormalization group. Following the procedure outlined in Sec. 3.5 we set up the white noise reference simulation ( $s = 1$ ,  $s_\Lambda = s_{\Lambda, \max}$ ) on an  $8 \times 8$  lattice. The parameters are chosen to be  $\lambda = \lambda^{(1)} = 0.02$  and  $0.22 \leq \kappa = \kappa^{(1)} \leq 0.32$  with lattice spacing  $a = a^{(1)}$ . This determines the full quantum theory we want to compare our colored noise results with. We proceed by setting  $s = 2, 4, 8$  and perform colored noise simulations with finer lattice spacings  $a^{(s)}$  on  $N^{(s=2)} \times N^{(s=2)} = 16 \times 16$ ,  $N^{(s=4)} \times N^{(s=4)} = 32 \times 32$  and  $N^{(s=8)} \times N^{(s=8)} = 64 \times 64$  lattices at the corresponding cutoffs  $s^{-1} s_{\Lambda, \max}(a^{(s)}, N^{(s)})$ . Table 3.1 summarizes the lattice spacings  $a^{(s)}$  and cutoffs  $s_\Lambda$  used in the simulations. Accordingly, the transformed parameters are determined from (3.33). The resulting parameters ( $\kappa^{(s)}$ ,  $\lambda^{(s)}$ ) are plotted in Fig. 3.9.

Fig. 3.10 shows the Gaussian fluctuations by means of the volume rescaled connected susceptibility  $\chi_2/V$  plotted as a function of the untransformed hopping parameter  $\kappa^{(1)}$  at fixed  $\lambda^{(1)} = 0.02$ . That is we consider  $(\chi_2/V)[\kappa^{(s)}(\kappa^{(1)}, \lambda^{(1)}), \lambda^{(s)}(\kappa^{(1)}, \lambda^{(1)})]$ . Analogously, the Binder cumulant  $U_L$  as well as the rescaled renormalized mass  $Nm_R$  are presented in Fig. 3.11 and Fig. 3.12. The violet curve represents the full quantum theory produced on the  $8 \times 8$  lattice with white noise. We find that the colored noise results (blue for  $N^{(s=2)} = 16$ , red for  $N^{(s=4)} = 32$  and dark yellow for  $N^{(s=8)} = 64$ ) are in close agreement with the results for the full theory. This meets the expectations of our construction. Although the classical lattices for different  $s$  do not coincide in size, the quantum lattices are the same due to the rescaling (3.32). However, a few deviations are clearly visible.

The correlation function of time slices for the choice  $\kappa^{(1)} = 0.22$ ,  $\lambda^{(1)} = 0.02$  and the transformed parameters  $\kappa^{(s)}$ ,  $\lambda^{(s)}$  thereof are shown in Fig. 3.13. The sharp regulator affects the colored noise correlators at small Euclidean times and causes oscillations for larger times as already mentioned in Sec. 3.6. However, the results seem to agree well if we rescale the Euclidean time axis for the  $s = 1, 2, 4$  cases to the time extent of the

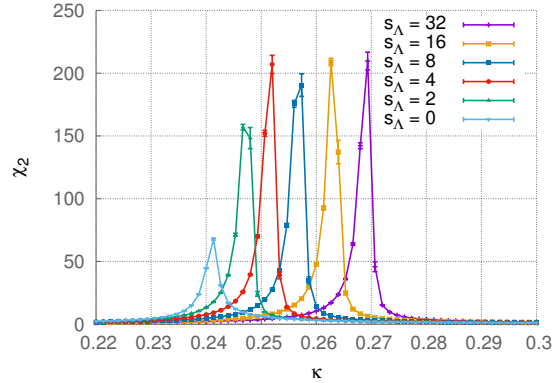


Figure 3.8.: The susceptibility  $\chi_2$  as a function of  $\kappa$  for  $N = 64$  and fixed  $\lambda = 0.02$  for different cutoffs  $s_\Lambda$ . As the cutoff is lowered the peak of the susceptibility is being shifted towards smaller values of  $\kappa$  and approaches the classical critical value  $\kappa_c^{(cl)} = 0.24$ . For the lowest cutoffs the peak height shrinks. Note that the white noise result is represented by the violet curve for  $s_{\Lambda, \max} = 32$ .

$N$	lattice spacing	$s_\Lambda$	$\sqrt{d} (2\pi/a^{(s)}N) s_\Lambda$
8	$a^{(s=1)} = a$	$s_{\Lambda, \max} = 4$	$\sqrt{2} \frac{\pi}{a}$
16	$a^{(s=2)} = a/2$	$s_{\Lambda, \max}/2 = 4$	$\sqrt{8} \frac{\pi}{a}$
32	$a^{(s=4)} = a/4$	$s_{\Lambda, \max}/4 = 4$	$\sqrt{32} \frac{\pi}{a}$
64	$a^{(s=8)} = a/8$	$s_{\Lambda, \max}/8 = 4$	$\sqrt{128} \frac{\pi}{a}$

Table 3.1.: Lattice scales for the RG transformation (3.32) in two dimensions. The last column shows the lattice cutoff with reinstated lattice spacing.

$N^{(s=8)} = 64$  lattice. The shape of the correlator hints also the behaviour of the correlation length regardless of the artifacts from the sharp cutoff. In agreement with (3.34) we find that the correlation lengths in lattice units fulfill  $\xi(N^{(s)}, \kappa^{(s)}, \lambda^{(s)}) \approx s \xi(N, \kappa^{(1)}, \lambda^{(1)})$ . The correlation length increases which is consistent with the requirement  $a \rightarrow a^{(s)} = a/s$ . This is moreover in agreement with the concept of the block spin transformation (here in a kind of reverted sense) as discussed in Sec. 3.5. Accordingly, from investigating the renormalized mass in Fig. 3.12 we find that  $m_R(N, \kappa^{(1)}, \lambda^{(1)}) \approx s m_R(N^{(s)}, \kappa^{(s)}, \lambda^{(s)})$ .

In Fig. 3.14 the order parameter  $\langle |M| \rangle$  is plotted as a function of  $\kappa^{(1)}$ . The colored noise results seem to converge with increasing lattice size to the dark-yellow curve for  $N^{(s=8)} = 64$ .

There are several error sources that have to be taken into account. The deviations in the critical region are influenced by critical slowing down, see Fig. 3.10 and Fig. 3.12. The latter poses a hard issue for a local updating algorithm such as the Langevin equation. Furthermore, finite size effects are a possible error source for the mismatch of our data in the critical region. Those are also clearly visible in the order parameter in Fig. 3.14.

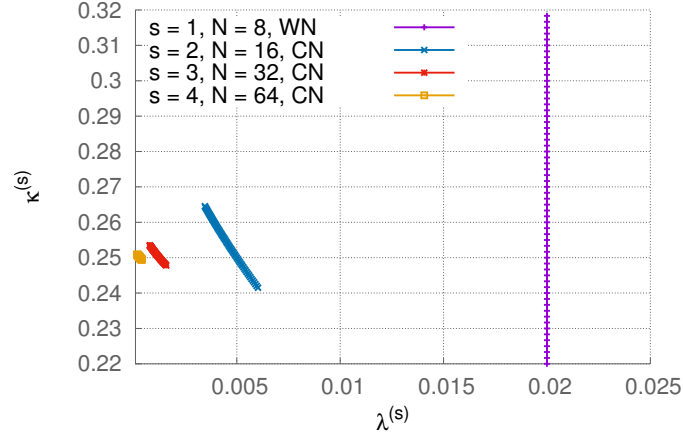


Figure 3.9.: Transformed values for  $\kappa^{(s)}$  and  $\lambda^{(s)}$  used in simulations. The violet line represents the parameter range used for the  $s = 1$  white noise simulation.

Moreover, the deviations from the full quantum theory observed in our data indicate that our compensation procedure might be incomplete. One reason is that our naive renormalization group transformation is based on the tree-level relations (3.33). With increasing  $s$  the deviation from the tree-level relations should increase as well due to the running of  $m_0^2$  and  $g_0$  affecting  $\kappa$  and  $\lambda$ . A further reason is that the number of blocking steps is limited on a finite lattice. Here, only for the first RG step our procedure seems to yield correct results.

To cope with the finite size effects, we repeat our analysis considering larger lattices. We proceed analogously as before but in contrast to the discussion above we carry out the  $s = 1$  simulation using white noise on a larger  $24 \times 24$  lattice and set the scale factors for the colored noise simulations to  $s = 2, 3, 4$ . The parameter set for the full theory is again given by  $0 \leq \kappa^{(1)} \leq 0.22$  and  $\lambda^{(1)} = 0.02$ . Note, that the lattice sizes for the simulations with colored noise at half, third and quarter the maximum cutoff are now  $N^{(s=2)} \times N^{(s=2)} = 48 \times 48$ ,  $N^{(s=3)} \times N^{(s=3)} = 72 \times 72$  and  $N^{(s=4)} \times N^{(s=4)} = 96 \times 96$ .

From the susceptibility shown in Fig. 3.15 and the Binder cumulant in Fig. 3.16 we find that by halving the lattice spacing the results from the  $N^{(s=1)} = 24$  and the  $N^{(s=2)} = 48$  simulations are in good agreement. In the critical regime the results for larger lattices however deviate from the white noise reference result.

The renormalized mass in Fig. 3.17 shows that the  $N^{(s=1)} = 24$  and the  $N^{(s=2)} = 48$  data agree well over the whole range in the hopping parameter in spite of the deviation caused by the (remaining) finite size effect around the critical point. The larger lattices however, indicate that the masses differ from the white noise result. We remark that the simulations are plagued by a bad signal-to-noise ratio, visible in the correlator for parameters sufficiently far in the symmetric or broken phase respectively. The magnetization for the larger lattices in Fig. 3.18 shows an analogous behaviour as observed on the small lattices. We conclude, that except for the renormalized mass our renormalization procedure gives the same result on large and small lattices.

The results in this section have been produced from  $10^6$  measurements of time slice configurations for each lattice size. Between two measurements we have performed 100 subsequent Langevin update sweeps corresponding to a Langevin time  $\tau = 1$  without

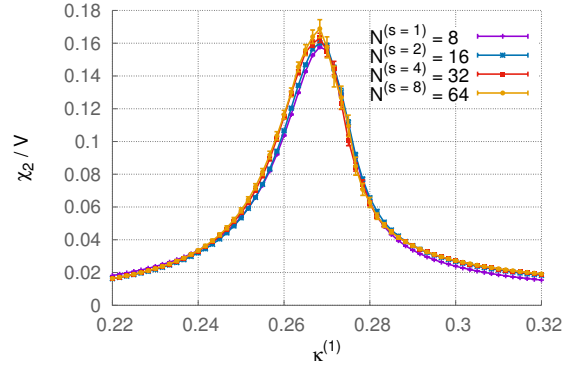


Figure 3.10.: The connected two-point susceptibility rescaled by the volume as a function of  $\kappa^{(1)}$  for different cutoff scales  $s_\Lambda$ . The violet curve represents the white noise reference result on the smallest and coarsest lattice. All of the remaining curves for  $s = 2, 4, 8$  were produced by means of colored noise with couplings adjusted according to the RG transformation (3.33).

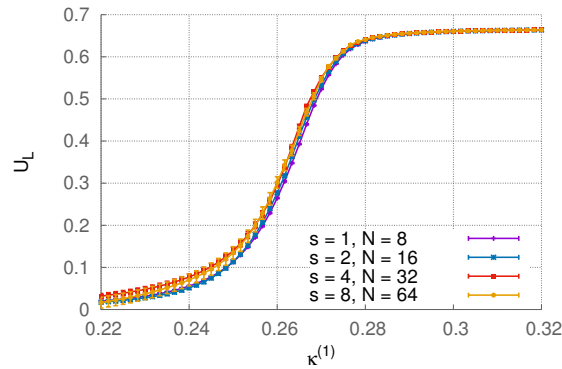


Figure 3.11.: The Binder cumulant  $U_L$  as a function of  $\kappa^{(1)}$  for different cutoff scales  $s_\Lambda$ . The violet curve represents the white noise result.

measurement to reduce the autocorrelation of the observables. After a standard data blocking check we find that this is not enough, especially in the case of the large and fine lattices. The data is more severely correlated. For example at  $\kappa^{(1)} = 0.26$  for an  $N = 96$  lattice a block must have a minimum length of 5000 which we have used for a standard blocked Jackknife error analysis.

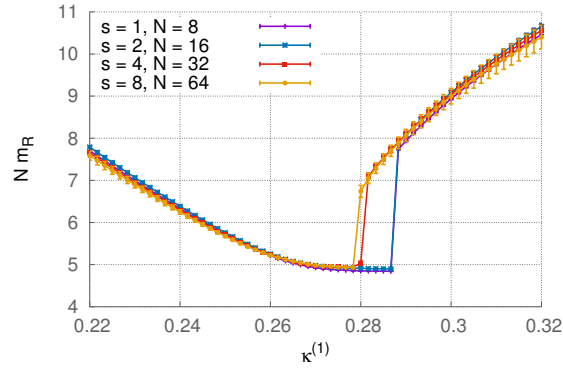


Figure 3.12.: The rescaled renormalized mass  $Nm_R$  as a function of  $\kappa^{(1)}$  for different cutoff scales  $s_\Lambda$ . The violet curve represents the white noise result.

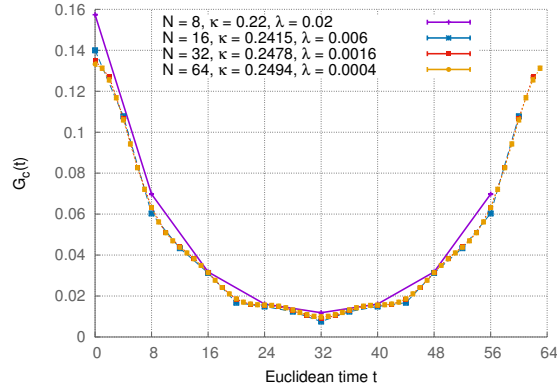


Figure 3.13.: The correlation function of time slices  $G_c(t)$  for different lattice sizes  $N^{(s)}$  and transformed couplings  $(\kappa^{(s)}, \lambda^{(s)})$ . The violet curve represents the white noise result.

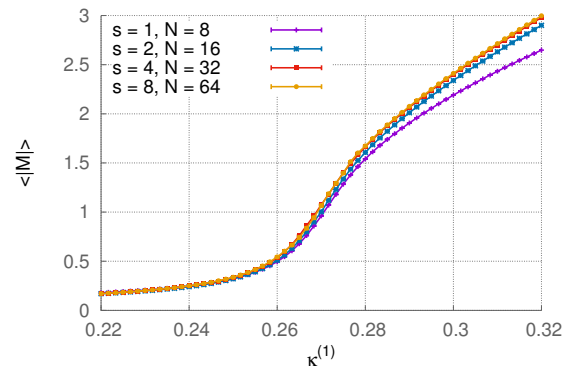


Figure 3.14.: The magnetization as a function of  $\kappa^{(1)}$  for different cutoff scales  $s_\Lambda$ . The violet curve represents the white noise result.

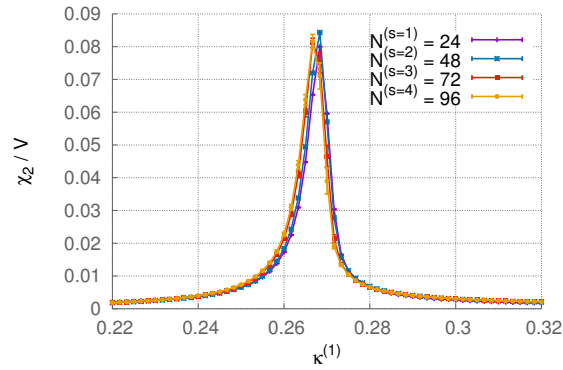


Figure 3.15.: The susceptibility rescaled by the volume as a function of  $\kappa^{(1)}$  for different cutoffs  $s_\Lambda$  on large lattices. The violet curve represents the white noise result.

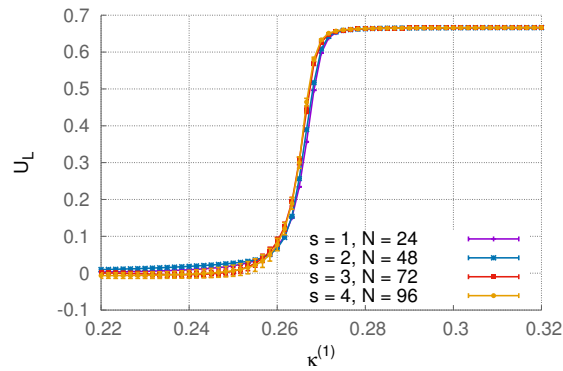


Figure 3.16.: The Binder cumulant as a function of  $\kappa^{(1)}$  for different cutoff scales  $s_\Lambda$ . The violet curve represents the white noise result.

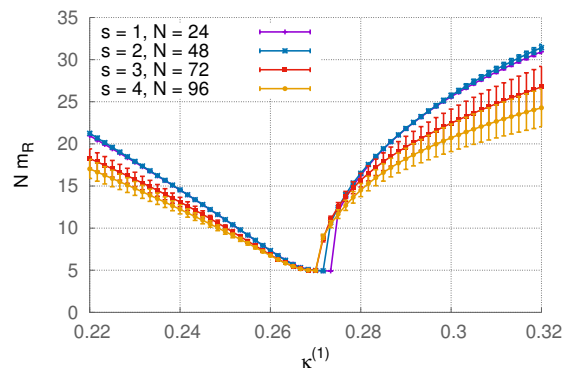


Figure 3.17.: The rescaled renormalized mass  $Nm_R$  as a function of  $\kappa^{(1)}$  for different cutoff scales  $s_\Lambda$ . The violet curve represents the white noise result.

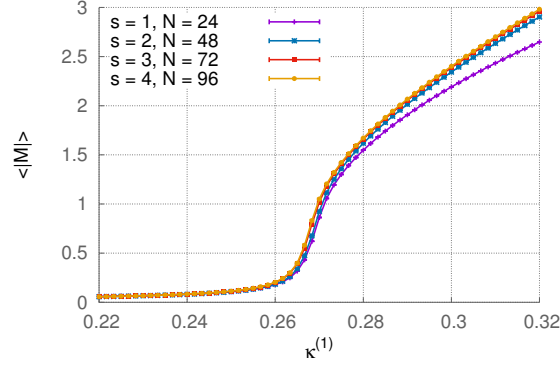


Figure 3.18.: The magnetization as a function of  $\kappa^{(1)}$  for different cutoff scales  $s_\Lambda$ . The violet curve represents the white noise result.

### 3.7. Applications

In the previous sections we have shown that the cutoff can be decreased stepwise without changing the physics content of the theory if the cutoff is still sufficiently large. The complementary Wilsonian picture is that of integrating out degrees of freedom: with colored noise the path integral measure  $P_\Lambda[\phi]$  only involves modes with  $p^2 \leq \Lambda^2$ . Accordingly, let us consider the colored stochastic process (3.1), (3.2) with  $S \rightarrow S_{\text{eff},\Lambda}$ , where the latter already contains the quantum effects of fields with  $p^2 > \Lambda^2$ ,

$$e^{-S_{\text{eff},\Lambda}[\phi]} = \int d\phi_{p^2 > \Lambda^2} e^{-S[\phi]}, \quad (3.35)$$

This leads us to

$$\frac{\partial \phi(x, \tau)}{\partial \tau} = -\frac{\delta S_{\text{eff},\Lambda}}{\delta \phi(x, \tau)} + r_\Lambda(\Delta_x) \eta(x, \tau), \quad (3.36a)$$

with

$$\frac{\partial P_{\text{eff},\Lambda}}{\partial \tau} = \int d^d x \frac{\delta}{\delta \phi_x} \left( \frac{\delta S_{\text{eff},\Lambda}}{\delta \phi_x} + r_\Lambda^2(\Delta_x) \frac{\delta}{\delta \phi_x} \right) P_{\text{eff},\Lambda}. \quad (3.36b)$$

The stochastic process (3.36) gives the full correlation functions for momenta  $p^2 \leq \Lambda^2$ . The related generating functional is that of the full theory

$$Z = \int d\phi_{p^2 \leq \Lambda^2} e^{-S_{\text{eff},\Lambda}[\phi]} = \int d\phi e^{-S[\phi]}, \quad (3.37)$$

with the classical action  $S[\phi]$  used in the original Langevin evolution. The Wilsonian effective action  $S_{\text{eff},\Lambda}$  can be also understood in terms of an improved or perfect lattice action if an additional block spinning transformation is applied.

In summary the following picture emerges: if the ultraviolet cutoff is asymptotically large, lowering the cutoff only changes the bare couplings  $\kappa_\Lambda, \lambda_\Lambda$  in the classical lattice action to accommodate the RG-running of the theory. Effectively this defines a scale  $\Lambda_{\text{phys}}$ , and for  $\Lambda \gg \Lambda_{\text{phys}}$  the above statement holds. Higher order operators are suppressed by UV power counting with powers of  $\Lambda_{\text{phys}}/\Lambda$  and can be safely dropped. This leads us to

$$S_{\text{eff},\Lambda \gg \Lambda_{\text{phys}}} \simeq S[\kappa_\Lambda, \lambda_\Lambda], \quad (3.38)$$

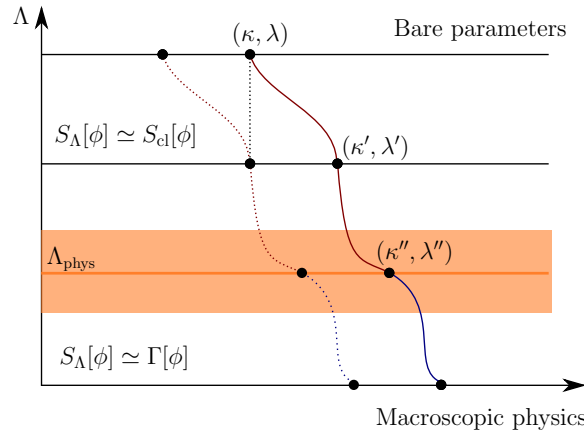


Figure 3.19.: Sketch of colored noise cooling. Each point on a horizontal line represents a pair of couplings  $(\kappa, \lambda)$ . The vertical axis denotes the cutoff scale  $\Lambda$ . The upper horizontal line depicts the white noise limit, and the curves constitute lines of constant physics. The couplings of UV-irrelevant operators are also generated during the RG flow. The corresponding axes are perpendicular to the plane in the plot, and are dropped.

For  $\Lambda \gg \Lambda_{\text{phys}}$  we have  $S_{\text{eff},\Lambda} = S[\kappa_\Lambda, \lambda_\Lambda]$ , see (3.38), depicted by the dark-red straight and dashed lines. Changing  $\Lambda$  at fixed couplings effectively changes the physics content, see vertical black dashed line and also the observables in Fig. 3.7.

The scale  $\Lambda_{\text{phys}}$  and the orange band denote the bound below which the action in the colored noise simulation must be described by the full quantum effective action.

see also Fig. 3.19. In turn, for small cutoffs,  $\Lambda \lesssim \Lambda_{\text{phys}}$ , physical fluctuations are removed from the lattice. Then, RG-transformations of the bare parameters in the classical lattice action do not suffice to keep the physics constant. Still, the latter can be achieved by RG transformations leading to improved or perfect actions,

$$S_{\text{eff},\Lambda \lesssim \Lambda_{\text{phys}}} \neq S[\kappa_\Lambda, \lambda_\Lambda]. \quad (3.39)$$

This idea is depicted in Fig. 3.19. It also suggests a systematic way to use the Wilsonian picture in terms of the (lattice) functional renormalization group (FRG) for improved lattice computations as well as for effectively determining  $\Lambda_{\text{phys}}$ . In contrast to the previous section we shall consider RG transformations beyond tree-level on lattices of fixed size and lattice spacing. These transformations are encoded in the flow equation for the Wilsonian effective action  $S_{\text{eff},\Lambda}$ . In the present work we concentrate on the sharp cutoff, a more general analysis also including smooth cutoffs will be presented elsewhere.

For the sharp cutoff  $S_{\text{eff},\Lambda}$  satisfies the Wegner-Houghton equation [178]. For the sake of computational convenience we formulate it for the 1PI effective action, the Legendre transform of  $S_{\text{eff},\Lambda}$  (where the cutoff term is subtracted [41, 168–172]),

$$\partial_\Lambda \Gamma_\Lambda[\bar{\phi}] = \frac{1}{2} \text{Tr} \langle \phi(p) \phi(-p) \rangle_c \Lambda^2 \partial_\Lambda \left( \frac{1}{r_\Lambda(p^2)} - 1 \right), \quad (3.40)$$

where the subscript  $_c$  stands for the connected part of the two-point function similarly as introduced in Sec. 3.4. The trace  $\text{Tr}$  stands for the sum over momenta in the Brillouin zone,

and  $\bar{\phi} = \langle \phi \rangle$ . In the continuum limit it turns into the standard momentum integration  $\int d^d p / (2\pi)^d$ . In (3.40) a suitable smoothing of the sharp cutoff is assumed and mandatory on the lattice. The propagator is the inverse of the second derivative of  $\Gamma_\Lambda$  w.r.t. the fields,  $\Gamma_\Lambda^{(2)} = \delta^2 / \Gamma_\Lambda \delta \phi^2$ , and hence (3.40) is a closed equation for  $\Gamma_\Lambda$ . In the continuum it takes the simple form

$$\Lambda \partial_\Lambda \Gamma_\Lambda[\bar{\phi}] = \frac{1}{2} \text{Tr} \log \left( \Gamma_\Lambda^{(2)}[\bar{\phi}] \right) (p^2 = \Lambda^2). \quad (3.41)$$

In the UV regime with  $\Lambda \gg \Lambda_{\text{phys}}$  the effective action is given by the classical action, see (3.38). Then the flow equation is a closed equation for  $\kappa(t)$  and  $\lambda(t)$  with  $t = \log \Lambda / \Lambda_{\text{UV}}$ , where  $\Lambda_{\text{UV}}$  is a normalization scale, typically the initial UV scale. In the present case this is the maximal momentum on the classical lattice. Another convenient definition originates in  $\Lambda / \Lambda_{\text{UV}} = s_\Lambda / s_{\Lambda_{\text{UV}}}$ . Since  $s_\Lambda$  is already dimensionless we drop the normalization and use

$$t = \log s_\Lambda. \quad (3.42)$$

For  $\Lambda \lesssim \Lambda_{\text{phys}}$  the simple closed flows for  $\kappa(t)$  and  $\lambda(t)$  do not hold anymore, and the higher operators will be important. By comparing the full flows with the simplified ones the physical scale  $\Lambda_{\text{phys}}$  can be defined as the scale below which the correlation functions computed from the stochastic processes with either  $S$  and  $S_{\text{eff}}$  show significant deviations. Note that this procedure is less costly than the blocking procedure which involves decreasing the lattice spacing while simultaneously increasing the number of lattice points.

A full analysis of this framework goes beyond the scope of the present work. Here we want to provide some first simple practical computations that also give indications of the precision needed in fully quantitative analyses. To that end we approximate the lattice RG transformations by the functional RG flow equations in the continuum theory (3.41). In the asymptotic UV regime with  $\Lambda \gg \Lambda_{\text{phys}}$  the effective action  $\Gamma_\Lambda$  is given by the classical action, to wit

$$\Gamma_\Lambda[\phi] \simeq \int d^d x \left\{ \frac{1}{2} \phi (-\partial^2 + m^2) \phi + \frac{g}{4!} \phi^4 \right\}, \quad (3.43)$$

for  $m^2 \geq 0$ . Taking two and four field derivatives at  $\phi = 0$  and  $p = 0$  we are lead to the flows

$$\partial_\Lambda m = F_m(m, g), \quad \partial_\Lambda g = F_g(m, g), \quad (3.44)$$

for the mass and the coupling.

The derivation of the flows of the couplings is straightforward and standard textbook knowledge, thus not explained here. We refer the reader to chapter 2 in [179] as well as to [88].

The latter can be converted to flows for the dimensionless lattice parameters  $\kappa, \lambda$  using the relations (3.18). Note that the flow of  $g$  runs like  $1/\Lambda^2$  for large  $\Lambda$  up to logarithmic corrections. Hence, at leading order only  $m^2$  and  $\kappa$  run logarithmically proportional to  $\log(\Lambda)$  and  $1/\log(\Lambda)$  for large  $\Lambda$ . Accordingly, for  $\Lambda \rightarrow 1/2\Lambda$  the mass squared shifts by an amount proportional to  $\log(2)$ . The prefactor can be computed from (3.44). In explicit form, the dimensionful continuum flow equations for the mass  $m$  and the coupling  $g$  read

$$\Lambda \partial_\Lambda m^2 = -\frac{g}{4\pi} \frac{1}{1 + m^2/\Lambda^2}, \quad (3.45)$$

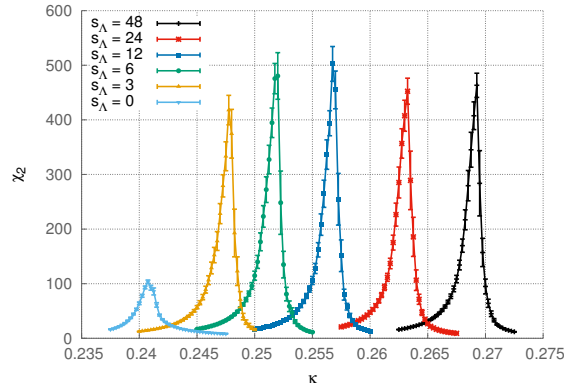


Figure 3.20.: Susceptibility  $\chi_2$  as a function of the hopping parameter  $\kappa$  for different cutoffs  $s_\Lambda$ . The coupling is fixed to  $\lambda = 0.02$ . The results shown here have been computed using a  $96 \times 96$  lattice. The white noise result corresponds to  $s_\Lambda = 48$ .

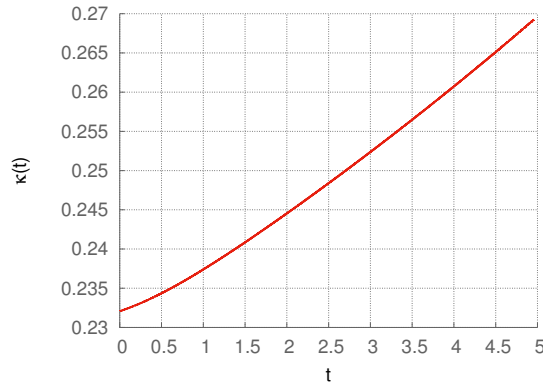


Figure 3.21.: Scale dependence of the hopping parameter  $\kappa$  from integrating the flow (3.47).

and

$$\Lambda \partial_\Lambda g = \frac{3}{4\pi} \frac{g^2}{\Lambda^2} \frac{1}{(1 + m^2/\Lambda^2)^2}. \quad (3.46)$$

The flow equations are cast into dimensionless form by multiplying both sides with the fixed square lattice spacing  $a^2$ . The dimensionless cutoff reads  $a\Lambda$  and the flow time is defined by  $t := \log(a\Lambda)$ . Using the relations (3.18) leads to the flow equations for the lattice parameters.

$$\begin{aligned} \partial_t \kappa(t) &= \frac{3}{2} \frac{\lambda(t)}{\pi} \kappa(t) \frac{e^{2t}}{1 + 2\lambda(t)} \\ &\times \frac{\kappa(t) (e^{2t} - 4) - 8\lambda(t) + 1}{[\kappa(t) (e^{2t} - 4) - 2\lambda(t) + 1]^2}, \end{aligned} \quad (3.47)$$

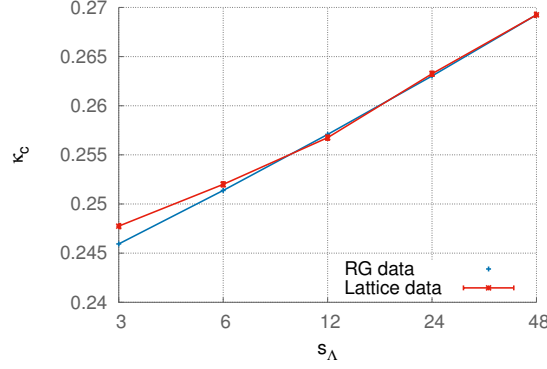


Figure 3.22.: Predictions for the critical hopping parameter  $\kappa_c$  from the functional RG flow equations (blue) in comparison with colored noise simulations on the lattice (red).

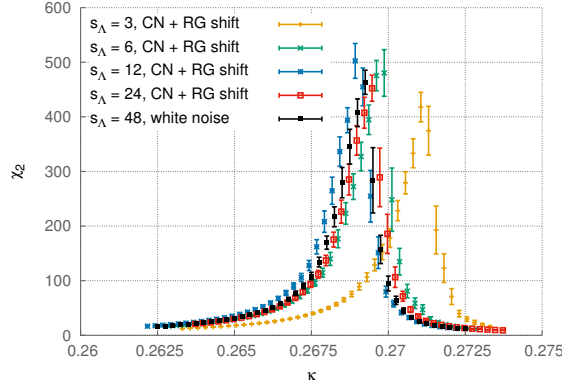


Figure 3.23.: Shift of the susceptibility peaks according to the results for  $\kappa$  and  $\lambda$  from the flow equations (3.47) and (3.48).

$$\begin{aligned} \partial_t \lambda(t) &= \frac{3}{2} \frac{\lambda(t)^2}{\pi} \frac{e^{2t}}{1 + 2\lambda(t)} \\ &\times \frac{2\kappa(t)(e^{2t} - 4) - 10\lambda(t) + 5}{[\kappa(t)(e^{2t} - 4) - 2\lambda(t) + 1]^2}. \end{aligned} \quad (3.48)$$

For a quantitative comparison between the continuum RG and colored noise cooling on the lattice we consider the peak positions  $\kappa_c$  of the susceptibilities for different  $s_\Lambda$  as shown in Fig. 3.20. The data stems from simulations on a  $96 \times 96$  lattice. The coupling  $\lambda = 0.02$  is fixed as in the previous sections. For the comparison we take into account the data for  $s_\Lambda = 3, 6, 12, 24, 48$ . The flow equations (3.47) and (3.48) are initialized at the maximum flow time  $t_{\max} = \log(a \Lambda_{\max})$  using the parameters  $\lambda(t_{\max}) = 0.02$  and  $\kappa(t_{\max}) = \kappa_{c, \text{WN}}$ . Here,  $\kappa_{c, \text{WN}}$  indicates the critical hopping parameter obtained from the simulation with white noise ( $s_{\Lambda, \max} = 48$ ). Moreover, the continuum cutoff translates into its lattice counterpart with  $a \Lambda_{\max} = \sqrt{2\pi} C$ , where  $C$  is a free RG-parameter. The running hopping parameter  $\kappa(t)$  is depicted in Fig. 3.21. To compute the remaining critical hopping parameters  $\kappa_c$  from the RG flow corresponding to lower values of  $s_\Lambda$  we evaluate  $\kappa(t)$  at scales  $t_{\max} - n \log(2)$ , where  $n = 1, 2, 3, 4$ . The red data points in Fig. 3.22 show

the critical values  $\kappa_c$  as a function of  $s_\Lambda$  from the lattice simulations. The blue points denote the values of  $\kappa_c$  obtained from the RG flow (3.47).

We find that at large cutoff scales the critical values  $\kappa_c$  measured on the lattice coincide with those calculated from the flow equations. In contrast, for small cutoff momenta a deviation is visible. This indicates that at lower momentum scales the stochastic process in terms of the classical action fails to describe the full theory. There the classical action needs to be replaced by an effective action as mentioned above. We conclude that for the model considered in this work colored noise cooling is applicable at scales between the UV and a specific IR scale. In the case investigated here this IR scale lies between  $s_{\Lambda,\max}/4$  and  $s_{\Lambda,\max}/8$ . This is also supported by the shifted susceptibility in Fig. 3.23. Here, the peaks have been translated by the difference between  $\kappa_{c,\text{WN}}$  and the values of  $\kappa_c$  from the RG prediction, see Fig. 3.22. While the agreement between the curves is quite good up to  $s_\Lambda = 12$  (blue curve), for lower cutoffs the results deviate from the full theory, see the green and yellow curves.

There are a few caveats to mention. Firstly, we work at fixed  $\lambda$  in our lattice simulations. When lowering  $s_\Lambda$ ,  $\lambda$  should be adjusted properly. Secondly, we approximate RG transformations of the lattice parameters by the continuum functional RG. For a more exact comparison between the RG transformations and the lattice results, we need to solve the flow equations (3.45) and (3.46) on the lattice. This however comes with a few technical complications since the flow is only defined at the discrete lattice momenta.

### 3.8. Summary

In this chapter we have investigated lattice theories with Stochastic Quantization with UV-regularized colored noise. Cooling the Langevin evolution by removing field configurations in the UV may be a promising candidate to optimize lattice simulations of systems with a clear scale separation between the relevant physics and the asymptotic UV regime. There are two possible interpretations of our method. The first is that the colored noise Langevin equation can be applied in the traditional sense of smoothing out UV-fluctuations. The alternative interpretation is to sample smooth configurations directly from the UV-regularized Langevin evolution.

Here we have exploited the latter interpretation which also can be connected directly to the renormalization group. The scale of the smooth fields is set by using an external cutoff parameter  $\Lambda$ . By varying  $\Lambda$  the colored noise Langevin equation interpolates between the full quantum theory accessible in a standard white noise simulation and the classical theory.

Our approach has been put to work within a real scalar field theory in two dimensions using a sharp momentum cutoff. We have shown, that for sufficiently large cutoff scales  $\Lambda$  no relevant physics is cut off. In Sec. 3.7 we have analyzed the viability of the colored noise cooling by sampling configurations with colored noise on lattices of fixed size. Thereby the form of the classical action is kept unchanged. This procedure is only valid for  $\Lambda \gg \Lambda_{\text{phys}}$ . In turn, for  $\Lambda \lesssim \Lambda_{\text{phys}}$  deviations grow large. At this point a description by means of an effective action might be necessary. Furthermore finite size and volume effects on the lattice certainly also play a rôle and prohibit the use of the continuum approximation for small UV cutoffs. Hence, a refined analysis may even lower the cooling range.

Even without the refined analysis we have shown that a remarkably large regime of ultraviolet fluctuations can be removed without altering the physics content of the theory.

The next step is to probe the maximal colored cooling by identifying the lowest possible cutoff scale at which the use of the classical action is still valid. Thereto, we compute the parameters  $\kappa$  and  $\lambda$  from the associated RG flows at a desired scale  $\Lambda$  and use them in the lattice simulation. This is left to future studies.

Moreover, in our ongoing work we use a (Symanzik) improved action and study the flow of the couplings of operators with dimension larger than  $O(a^2)$ . Further perspectives of the method are to explore the effects of regulator functions different from the sharp cutoff beyond the effects shown in Appendix [A.4.2](#).

Applications of the method to  $SU(N_c)$  gauge theories and to finite density models are also work in progress. In theories with a complex action induced e.g. by a finite chemical potential, the Complex Langevin evolution might be optimized by colored noise cooling.

## 4. Reweighting Lefschetz Thimbles

In this chapter we study toy models for finite density QCD which exhibit a sign problem by means of Lefschetz thimbles. One of the main challenges with Monte Carlo simulations on Lefschetz thimbles is to determine the weights of the thimbles relative to each other. This difficulty arises as the original path integral is decomposed into a sum of integrals over multiple thimbles (2.33). We show that this difficulty can be overcome by a standard Monte Carlo determination of the ratios of the real partition functions on the thimbles. This is facilitated by a novel reweighting procedure which is generally applicable to field theories. In this chapter we assume prior knowledge on a parametrization of the contributing thimbles. To find such a parametrization we present recipes for finding parametrizations of thimbles and anti-thimbles applicable to simple models. However, the reweighting procedure does not rely on knowing a parametrization. Our ideas are put to work in simple models, i.e. ordinary integrals. Among those we consider a one-site quartic model with a  $\frac{\lambda}{4}z^4$  term as well as a  $U(1)$  one-link model.

This chapter is organized as follows. We start by briefly recapitulating a few challenges with simulations on Lefschetz thimbles in Section 4.1. In Sec. 4.2 we propose two algorithms to find thimbles and their parametrizations necessary for Monte Carlo integration. In Sec. 4.3 we present our idea of sampling on multiple thimbles taking into account the relative weights of different thimbles. Sec. 4.4 introduces the toy models we use for numerical investigations together with our results. During the research for this part of the author and his collaborators have also developed many ideas to combine the Complex Langevin evolution and the Lefschetz Thimble method. While none of those approaches lead to generally applicable algorithms, they still provide some useful insight into the structure of the models, hence we give some of those ideas and corresponding results in App. B.3.

For the largest part of this chapter text and figures are taken from the author's publication [56] as well as from the proceedings [58].

### 4.1. Challenges for simulations

For an overview we recall the formula (2.33) for the expectation value of an observable in the thimble decomposition

$$\langle \mathcal{O} \rangle = \frac{\sum_{\sigma} n_{\sigma} e^{-i\text{Im}S(z_{\sigma})} Z_{\sigma} \langle \mathcal{O} \rangle_{\sigma}}{\sum_{\sigma} n_{\sigma} e^{-i\text{Im}S(z_{\sigma})} Z_{\sigma}}. \quad (4.1)$$

To fully evaluate this quantity observable expectation values have to be computed on each contributing thimble. This approach has two practical challenges:

1. For Monte Carlo sampling on (at least the main contributing) thimbles with partition functions

$$Z_{\sigma} = \int_{D_{\sigma}} dz e^{-\text{Re}[S(z)]} \quad (4.2)$$

it is necessary to find a numerical parametrization of the integration domain  $D_\sigma$  implicitly or explicitly. In some cases the contributing thimbles all have (approximately) the same weight. An example is  $U(1)$  gauge theory on the lattice in real-time. This will be discussed in more detail in Chapter 5. For higher dimensional integrals and field theory finding parametrizations becomes costly.

2. In most realistic theories multiple thimbles contribute to the partition function. Hence, we need to determine the relative weights of the sub-partition functions  $Z_\rho/Z_\sigma$  where  $\rho \neq \sigma$  in (4.1).

Numerical cost and complexity of the above tasks increase with the dimensionality of the considered theory. So far there has not been a general solution capturing both problems. However, the first difficulty can be tackled by the holomorphic flow equations continuously deforming the original integration contour towards the thimbles [127]. Another approach addresses the second problem by means of a semi-classical approximation [131]. In the following we propose novel general solutions to both problems which do not rely on approximations. We test these solutions in application to simple models which are represented by one-dimensional integrals with a complex integrand. In all scenarios considered in this chapter the determination of the intersection numbers  $n_\sigma$  is trivial. They can be simply read off from plotting the thimble curves in the complex plane, see Sec. 4.4.1 and 4.4.2. The application of our solution to the second problem to field theories is subject to the discussion in chapter 5.

## 4.2. Finding thimbles

In this section we propose two algorithms which can be used to systematically find contributing thimbles. The first algorithm presented in Sec. 4.2.1 scans the real axis in search of intersecting anti-thimbles. From there it determines the position of the stationary point used to solve the flow equation for the thimble. The second algorithm discussed in Sec. 4.2.2 takes the information on the stationary points as input. It projects points in the complex plane onto thimbles, in order to determine a numerical parametrization. Both methods are put to work in simple one-dimensional integrals. They apply also to higher dimensional theories, however the numerical costs may rise exponentially with the number of lattice points.

### 4.2.1. Axis scan

Since the only contributing thimbles are those with non-zero intersection number of the anti-thimble with the original manifold, one can find all contributing fixed points by scanning the manifold for such intersections. This can be a challenging problem in higher dimensional theories where the thimbles are surfaces as can be their intersections with  $\mathbb{R}^N$ . However a remedy might be provided by using the prior knowledge from Monte Carlo sampling in parameter regions without a sign problem or in the phase quenched theory where reweighting is applicable. These results might give already a good starting points for the searches or one could rely on extrapolations to parameter regions where the sign problem is more severe. In the following we describe the searching algorithm for the case of simple integrals where the original manifold is an interval  $[a, b] \in \mathbb{R}$ . The algorithm is the following [181],

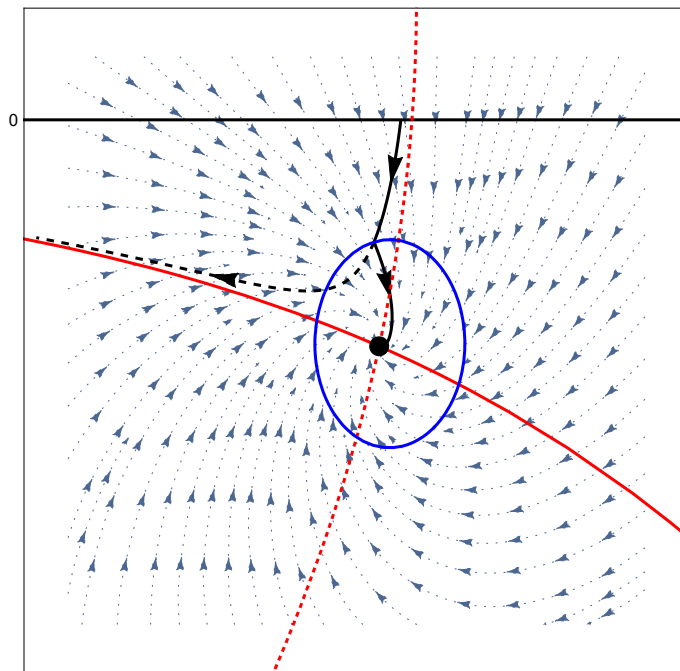


Figure 4.1.: Visualization of the fixed point search via an axis scan. The red lines indicate the thimble (solid) and the anti-thimble (dashed). The steepest ascent equation (4.3) is solved using a starting point on the real axis close to the anti-thimble. As the trajectory approaches the fixed point the modulus of the derivative of the action tends to zero. The region where it is smaller or equal to a value  $\delta > 0$  is indicated by the blue circle. Here, the flow is switched depending on the stability properties of the fixed point which is summarized in (4.6). It is then guided towards the fixed point (solid black arrows) where it ends. The steepest ascent without switching close to the fixed point will asymptotically approach the thimble (black dashed arrow). Note that the latter property of the steepest ascent flow is the main ingredient behind the method of flowed manifolds [180].

1. Choose a starting point on the real axis.
2. Solve the steepest ascent equation

$$\frac{\partial z}{\partial \tau} = \frac{\overline{\partial S}}{\partial z} \Big/ \left| \frac{\overline{\partial S}}{\partial z} \right|, \quad (4.3)$$

using the starting point as an initial condition.

3. If the derivative of the action becomes small

$$\left| \frac{\overline{\partial S}}{\partial z} \right| < \delta, \quad (4.4)$$

the flow is close to a fixed point of the action.

4. Depending on the structure of the fixed point, one can now reach it by looking at the flow determined by the negative gradient of the action which in analogy to the

Langevin evolution we here refer to as Langevin flow (LF)

$$\dot{z} = -\frac{\partial S}{\partial z}, \quad (4.5)$$

and changing the sign according to the following prescription

$$\dot{z} = \begin{cases} -\frac{\partial S}{\partial z} & \text{FP attractive under LF} \\ +\frac{\partial S}{\partial z} & \text{FP repulsive under LF} \\ \pm e^{i\pi/2} \frac{\partial S}{\partial z} & \text{FP circular under LF} \end{cases}. \quad (4.6)$$

All those cases have to be tested, and one of them will end in the fixed point.

This algorithm is visualized in Fig. 4.1. Once the fixed points are known, the numerical parametrization of the thimbles can be computed. In the case of one-dimensional integrals, this boils down to solving one-dimensional ordinary differential equations. We do so by solving the normalized steepest descent equation

$$\frac{\partial z}{\partial \tau} = -\frac{\overline{\partial S}}{\partial z} \bigg/ \left| \frac{\overline{\partial S}}{\partial z} \right|, \quad (4.7)$$

with opposite sign starting close to the fixed point [124]. In other words we let the steepest descent flow "run backwards" which flows points arbitrarily close to the stationary point outwards along the thimble. The reason for the normalization with the modulus will be clarified later when we address the computation of the relative weights in the thimble decomposition. For now it is sufficient to remark that the normalization helps with numerical stability when solving the steepest descent equation. Note that this normalization is simply a rescaling of the flow parameter  $\tau$ .

#### 4.2.2. Thimble cooling

In this section we propose a straight-forward algorithm to find parametrizations of all thimbles and anti-thimbles for a given complexified action  $S : \mathbb{C} \rightarrow \mathbb{C}$  where the only required information is the knowledge about the fixed points. We show results for the  $z^4$  model introduced and discussed in more detail in Sec. 4.4.1 with parameters  $\sigma = 1, \lambda = 1, h = 1 + i$ . The idea is to minimize the distance of any set of points in the complex plane to curves on which the imaginary part of the action is constant. This leads to the following definition.

$$M_\sigma(x, y) = |\text{Im}S(x + iy) - \text{Im}S(z_\sigma)|^2, \quad (4.8)$$

where  $\sigma$  labels the stationary points. We call  $M_\sigma(x, y)$  the cooling function in analogy to cooling in the sense of smoothing field configurations by driving them towards the minimum of the classical action as discussed in the beginning of Chapter 3. The numerical minimization procedure is facilitated by the following gradient equations

$$\begin{aligned} \dot{x} &= -\frac{\partial M_\sigma(x, y)}{\partial x}, \\ \dot{y} &= -\frac{\partial M_\sigma(x, y)}{\partial y}. \end{aligned} \quad (4.9)$$

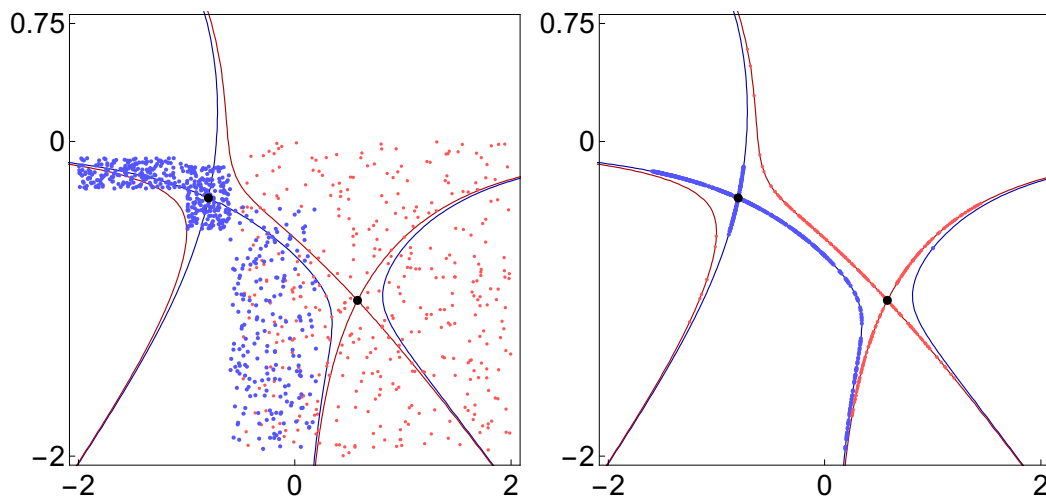


Figure 4.2.: Complex plane with the solutions to the gradient equations (4.9) for a given grid of initial conditions for the left thimble (blue) and the right thimble (red). In the left plot we show a possible choice of initial conditions for the gradient equations. The right plot depicts the resulting distribution of points lying on the thimble and anti-thimble. Moreover other curves not passing through the fixed point on which the imaginary part of the action is constant are hit by the algorithm.

By construction the gradient equations orthogonally project a given point on a curve with constant imaginary part of the action. As initial conditions for (4.9) we use a grid of points in the complex plane. This is shown in the left plot in Fig. 4.2. The choice of a random grid is arbitrary. We could have also chosen a regular grid. In the right plot of Fig. 4.2 we show the result of the solution to the gradient equations. The procedure works well for a large box of initial conditions (red) as shown for the right fixed point (black). The resulting set of points lies on the thimble, the anti-thimble and an additional curve on the left without physical relevance. This curve obviously has the same imaginary part and asymptotically connects the blue thimble and anti-thimble corresponding to the other fixed point. Alternatively, we can start with a small rectangle around the fixed point, see the blue points in the left plot. From the resulting points flowed to thimble and anti-thimble we can choose the next set of initial conditions along e.g. the thimble and repeat the procedure iteratively. Note that also from looking at the flow lines of (4.9) we can determine suitable areas for initial conditions.

This method provides a useful tool to find parametrizations to the thimbles (and anti-thimbles) by interpolating the flowed set of points. Moreover, by knowing each anti-thimble we can map out if it intersects with the original integration manifold thus enabling us to determine whether and how much the corresponding thimble contributes.

Thimble cooling has the potential advantage over the procedure in Sec. 4.2.1 that one does not have to solve the holomorphic gradient flow in many directions but one directly flows to the (anti-)thimbles. The cooling method put forward here can also be used to reduce numerical discretizations artifacts (see Sec. 4.4) in the thimble parametrization.

We remark, that a generalization of thimble cooling to higher dimensional integrals may in general prove difficult due to the dimensionality of the hyper-surface parametrized by

$\text{Im}[S(z)] = \text{const}$ . There, it is a priori not clear how the method proposed here can single out the (anti-)thimble from the other surfaces that are of no relevance to the path-integral. In App. B.3.3 we propose a combination of Lefschetz thimble and complex Langevin, which samples around all thimbles. This could also be used as a starting point for thimble cooling.

### 4.3. Monte Carlo simulations on Lefschetz thimbles

The previous section has dealt with finding parametrizations for the thimbles. In this section we present an algorithm for a Monte Carlo simulation on Lefschetz thimbles, assumed that we know a parametrization of all contributing thimbles. The method is divided up into two steps. First we discuss how to compute the expectation value of a given observable on a single thimble  $D_\sigma$  according to (2.34). In the second step we demonstrate how the ratios of partition functions determining the relative weights of the thimbles can be computed within the Monte Carlo simulation. With both steps completed the full observable expectation value (4.1) can be calculated.

#### 4.3.1. Standard reweighting on thimbles

For the first step let  $[a, b] \subset \mathbb{R} \rightarrow D_\sigma : \tau \mapsto z(\tau)$  be a (numerical) parametrization of the thimble  $D_\sigma$ . Its associated partition function reads

$$Z_\sigma = \int_{D_\sigma} dz e^{-\text{Re}[S(z)]} = \int_a^b d\tau e^{-\text{Re}[S_\sigma(\tau)]} J_\sigma(z(\tau)). \quad (4.10)$$

Here  $S_\sigma(\tau) = S(z(\tau))$  denotes the action evaluated on  $D_\sigma$ . Moreover, the complex Jacobian  $J_\sigma(\tau) := \partial z(\tau)/\partial \tau$  on  $D_\sigma$  measuring the deviation of inclination of the complex volume element  $dz$  from the real one has been introduced. We define

$$\langle \mathcal{O} \rangle_\sigma^r = \frac{1}{Z_\sigma^r} \int_a^b d\tau e^{-\text{Re}[S_\sigma(\tau)]} \mathcal{O}, \quad (4.11)$$

as well as

$$Z_\sigma^r = \int_a^b d\tau e^{-\text{Re}[S_\sigma(\tau)]}. \quad (4.12)$$

Thus, to calculate an observable on a single thimble we sample  $\tau$  distributed according to the probability distribution

$$p_\sigma(\tau) = e^{-\text{Re}[S_\sigma(\tau)]} / Z_\sigma^r. \quad (4.13)$$

We take into account the Jacobian via conventional reweighting

$$\langle \mathcal{O} \rangle_\sigma = \frac{\langle \mathcal{O} J_\sigma \rangle_\sigma^r}{\langle J_\sigma \rangle_\sigma^r}. \quad (4.14)$$

The phase of the Jacobian gives rise to the so-called residual sign problem. The expectation value of an observable reads

$$\langle \mathcal{O} \rangle = \frac{\sum_\sigma n_\sigma e^{-i\text{Im}[S(z_\sigma)]} Z_\sigma^r \langle \mathcal{O} J_\sigma \rangle_\sigma^r}{\sum_\sigma n_\sigma e^{-i\text{Im}[S(z_\sigma)]} Z_\sigma^r \langle J_\sigma \rangle_\sigma^r}. \quad (4.15)$$

It is obvious that in the case of a single contributing thimble (4.15) reduces to (4.14). Note that in (4.15) the thimbles are weighted with their partition functions which is subject to the following discussion.

### 4.3.2. Computing the partition function weights

In the second step we capture the weights from the partition functions  $Z_\sigma^r$  from within the Monte Carlo simulation. For simplicity we consider (4.15) with only two contributing thimbles, i.e.  $\sigma = 1, 2$ . Without loss of generality we choose the second thimble and factor out  $Z_2^r$  in the numerator as well as in the denominator. This thimble is referred to as the "master thimble". Hence in this example the expectation value to calculate reads

$$\langle \mathcal{O} \rangle = \frac{n_1 e^{-i\text{Im}[S(z_1)]} \frac{Z_1^r}{Z_2^r} \langle \mathcal{O} J_1 \rangle_1^r + n_2 e^{-i\text{Im}[S(z_2)]} \langle \mathcal{O} J_2 \rangle_2^r}{n_1 e^{-i\text{Im}[S(z_1)]} \frac{Z_1^r}{Z_2^r} \langle J_1 \rangle_1^r + n_2 e^{-i\text{Im}[S(z_2)]} \langle J_2 \rangle_2^r}. \quad (4.16)$$

We are left with computing the ratio of the partition functions  $Z_1^r$  and  $Z_2^r$  which can be straightforwardly written in terms of the expectation value (4.11) of the ratio of the associated Boltzmann factors

$$\frac{Z_1^r}{Z_2^r} = \left\langle e^{\text{Re}[S_2 - S_1]} \right\rangle_2^r. \quad (4.17)$$

This means that we determine the relative weights in (4.15) by reweighting with respect to the master thimble. For a derivation of (4.17) see App. B.1. We remark that for (4.17) to hold (a) the integrals over the thimbles have the same parameter interval  $[a, b]$  and (b) the parameters  $\tau$  on both thimbles must be identified. In case the latter does not hold we need to take into account an additional Jacobian. For the example integrals considered in this work (a) can be realized by suitable variable transformations see also App. B.2. (b) can be achieved by normalizing the steepest descent equation as shown in (4.3) in Sec. 4.2.1 when determining the numerical parametrizations.

In conclusion, we can compute the relative weights of the contributing thimbles (4.17) within the Monte Carlo simulation by reweighting with respect to the master thimble which completes the list of ingredients for (4.15). The reweighting method might also be useful in addressing higher dimensional integrals for field theories since it does not rely on an explicit (numerical) parametrization of the thimble. We will come back to this point in chapter 5.

## 4.4. Applications

Now, we investigate different sign problem plagued models with varying complexity to test our algorithms presented in Sec. 4.2 and 4.3. However, in this section we will focus mainly on the reweighting procedure for the relative weights proposed in Sec. 4.3.2. In the first step we consider a one-site  $z^4$  model in Sec. 4.4.1. Two parameter scenarios are examined. For the first only one thimble contributes. This situation serves as a good test case for setting up the Monte Carlo sampling of (4.13) discussed in Sec. 4.3.1. In the second scenario two thimbles contribute. Their flow parameters run over the same interval  $\tau \in (-\infty, \infty)$  which facilitate a straightforward check of our novel reweighting method for the relative weights described in Sec. 4.3.2. In the second step in Sec. 4.4.2 we investigate a U(1) one link model serving as a hard test case. It is a model for a gauge theory with fermions and has thimbles that end in poles. This model is quite general in the sense that it contains all features that are to be expected in more complicated cases such as field theories.

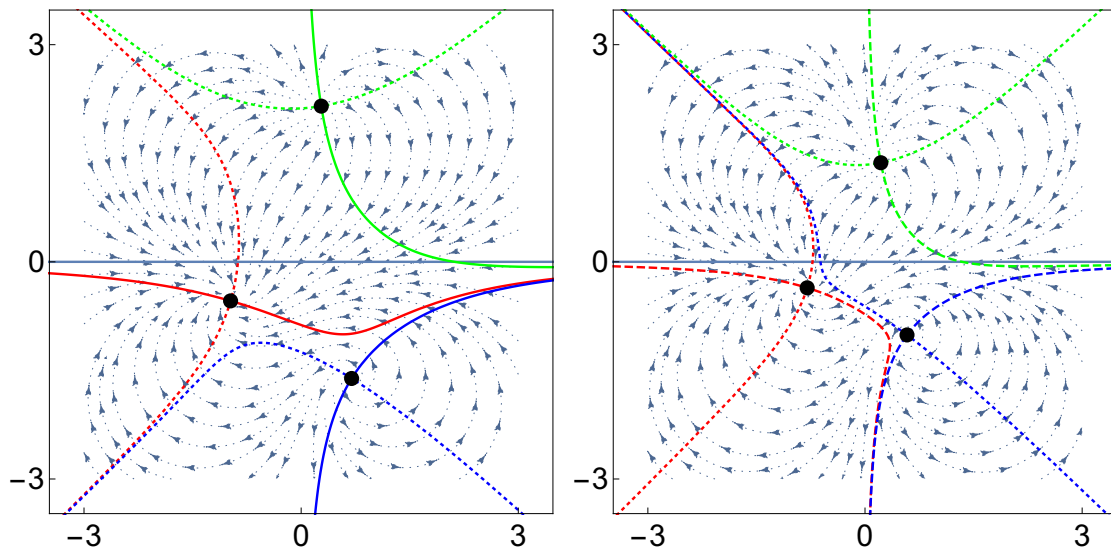


Figure 4.3.: Complex plane showing the thimble structures of the one-site  $z^4$  model corresponding to the two parameter sets described in the main text. Left: Scenario 1 with one contributing thimble (red full line). The corresponding anti-thimble (red dashed line) crosses the real axis. Right: Scenario 2 with two contributing thimbles (red and blue long dashed lines). The blue arrows in the background of each figure represent the drift force in the Complex Langevin evolution. The relation to the latter will be clarified in App. B.3.

#### 4.4.1. One-site $z^4$ model

The one-site  $z^4$  model generically consists of three thimbles, which end in different asymptotic regions at infinity. This structure makes the model a rather simple test case for the algorithms we propose. The model is given by the action

$$S(z) = \frac{\sigma}{2}z^2 + \frac{\lambda}{4}z^4 + hz, \quad (4.18)$$

for more details see e.g. [124]. The number of contributing thimbles characterized by the intersection number  $n_\sigma$  in the model can be adjusted by a suitable choice of the parameters. The following two scenarios are of interest.

1. For  $\sigma = 1$ ,  $\lambda = 1/3$  and  $h = 1 + i$  there is only one contributing thimble.
2. For  $\sigma = 1$ ,  $\lambda = 1$  and  $h = 1 + i$  there are two contributing thimbles.

Both cases are shown in Fig. 4.3. The stationary points are computed by solving the equation resulting from setting the gradient of (4.18) to zero. The numerical parametrization for the thimbles are obtained by solving the steepest ascent equation as described in Sec. 4.2 for an initial condition in an  $\varepsilon$  neighborhood around each stationary point where  $\varepsilon$  is usually of the order of  $10^{-7}$ .

For the Monte Carlo simulations in both scenarios the crucial objects are the probability distributions  $\exp(-\text{Re}[S(\tau)])$  for the parameter  $\tau$  from (4.13). For the case where two thimbles contribute the distributions are shown in Fig. 4.4. They have been mapped onto the interval  $[0, 1]$ , see App. B.2 for the choice of suitable variable transformation

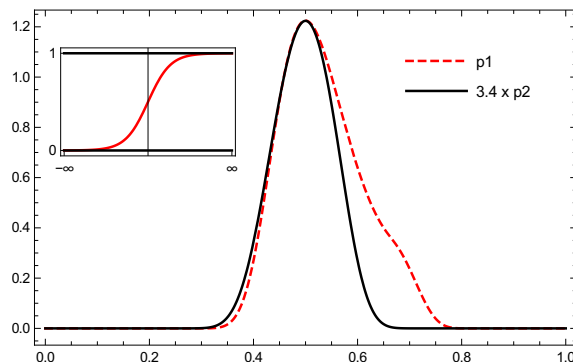


Figure 4.4.: For scenario 2 the Boltzmann factor  $\exp(-\text{Re}[S(\tau)])$  as a function of the flow parameter  $\tau$  on the contributing thimbles in the  $z^4$  model is shown. The integration ranges have been mapped from  $[-\infty, \infty]$  to  $[0, 1]$  and the compactifying transformation  $x \rightarrow x' = (1 + \tanh(\xi x))/2$  is visualized in the inlay. The free parameter in the transformation (B.4) is chosen to be  $\xi = 0.25$ . For details see App. B.2.

for the parameter  $\tau$ . However, this is not necessary for the simulation in this model, since the original domains (both  $\mathbb{R}$ ) already overlap. Moreover, both distributions fall off exponentially which guarantees numerically stable simulations. Numerical simulations have been carried out according to the recipe in (4.16). Results for the observable  $\langle z^2 \rangle$  (scenario 1 and 2) as well as the ratio of partition functions from (4.17) for scenario 2 are given in Table 4.1. For simplicity, the simulations have been performed without employing the variable transformation for the mapping to  $[0, 1]$ . For the simulations we have collected  $O(10^{10})$  data points. Errors have been estimated via a standard Jackknife analysis.

#### 4.4.2. U(1) one link model

In this section we put to work our reweighting algorithm by using a  $U(1)$  one-link model with a finite chemical potential  $\mu$

$$Z = \int_{-\pi}^{\pi} dx e^{-S(x)},$$

$$S(x) = -\beta \cos(x) - \log(1 + \kappa \cos(x - i\mu)). \quad (4.19)$$

Despite its simplicity the model shares general features with more complicated theories such as QCD at finite chemical potential. In the following we consider the case  $\beta = 1$ ,  $\kappa = 2$  and  $\mu = 2$ . The model has been studied using the Complex Langevin evolution in [38]. Its thimble structure has been investigated in [124, 135]. There are three contributing thimbles, see the red and black full lines in Fig. 4.5. The two red ones are related by symmetry and their partition functions are complex conjugates [124]. The second term in the effective action in (4.19) modeling a fermion determinant generates poles in the holomorphic flow (and equivalently in the Complex Langevin drift) in which the contributing thimbles end for finite flow time  $\tau$ . Due to the presence of these poles leading to a diverging drift the Complex Langevin evolution yields incorrect results for the given parameters above [124]. For the partition functions (4.12) associated with the contributing thimbles all integration ranges for the parameter  $\tau$  differ. This demands to transform these to the

$\langle \mathcal{O} \rangle$	numerical	exact
$z^4-1$ thimble		
$\text{Re}\langle z^2 \rangle$	0.73922(6)	0.73922
$\text{Im}\langle z^2 \rangle$	0.63006(4)	0.630089
$z^4-2$ thimbles		
$\text{Re}\langle z^2 \rangle$	0.509299(5)	0.509297
$\text{Im}\langle z^2 \rangle$	0.305819(3)	0.305815
$Z_2/Z_1 _{T_1}$	0.2253778(4)	0.2253779
$Z_1/Z_2 _{T_2}$	4.436(12)	4.437

Table 4.1.: Numerical results and exact values of the observable  $z^2$  and the relative weights with statistical errors for the one-site  $z^4$  model. The upper table corresponds to scenario 1. Here, only one thimble contributes. The lower table corresponds to scenario 2. Two thimbles contribute and besides the result for  $z^2$  the relative weights are shown. Numerical results have been obtained by sampling from the distributions  $p_\sigma(\tau)$  which for scenario 2 are shown in Fig. 4.4 and by applying the reweighting formula (4.17) to evaluate the full expectation value (4.16). What is denoted as exact results here is obtained by carrying out a standard numerical integration over the thimbles to evaluate the thimble decomposition for the observables as a cross-check. Possible deviations in the results are caused by numerical discretization errors, see the main text for a detailed remark.

same interval, here  $[0, 1]$ , yielding overlap of the distributions  $e^{-\text{Re}[S_\sigma(\tau)]}$  which facilitates the reweighting procedure for the relative weights (4.17). The remapped distributions are shown in Fig. 4.6 where details on the transformation mappings are provided in the inlay and in the caption. The central thimble (black) carries the largest weight. We choose it to be the master thimble. For a quantitative test of our method we compute the analogue of the Polyakov loop, its inverse, the plaquette and the density which are given in analytical form in [38]

$$\begin{aligned}
\langle U \rangle &= \langle e^{ix} \rangle, \\
\langle U^{-1} \rangle &= \langle e^{-ix} \rangle, \\
\langle P \rangle &= \langle \cos(x) \rangle, \\
\langle n \rangle &= \left\langle \frac{i\kappa \sin(x - i\mu)}{1 + \kappa \cos(x - i\mu)} \right\rangle.
\end{aligned} \tag{4.20}$$

The results of our Monte Carlo simulations are displayed in Table 4.2 in comparison with the exact results. This includes the relative weights for the contributing thimbles with respect to the master thimble of choice. For the simulation we have measured each observable  $O(10^9)$  times. The error estimates have been obtained by a standard Jackknife

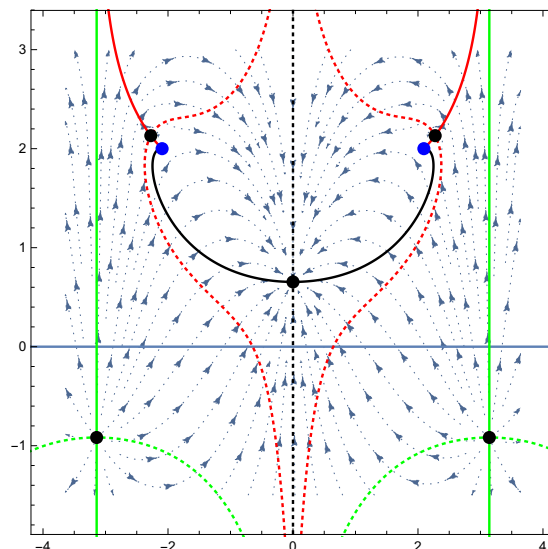


Figure 4.5.: Contributing thimbles (full lines) and anti-thimbles (dashed lines) for the  $U(1)$  one-link model. The critical points of the action are represented by the black dots and poles of the holomorphic flow are indicated by blue dots. The contributing thimbles all end in poles at finite flow times  $\tau$ . The blue arrows in the background represent the drift force in the Complex Langevin evolution. Due to the periodicity of the model the non-contributing thimbles (green) at the edges of the original integration domain  $[-\pi, \pi]$  coincide.

analysis. Systematic errors arise from numerical discretization artifacts along the thimble. In the simple cases at hand the latter can be quantified by comparing the exact solution with the result from integrating along the discretization obtained from the gradient flow (4.9). In the case of the observables given in (4.20) the deviation is of order  $10^{-6}$ . Therefore the systematic error is comparable to the statistical error. The ratio of partition functions seems to be particularly sensitive to this effect, see Table 4.2. However, combining the statistical and the systematic error we find that all quantities agree with the exact results. We remark that we obtained the same results within the combined errorbars for either choosing the central or the left (right) thimble as the master thimble.

## 4.5. Summary

We have proposed a new method based on Lefschetz thimbles for solving theories with a sign problem. This method works with two steps.

First we find all contributing fixed points by scanning the original manifold for intersecting anti-thimbles. We then project a grid of points in the complex plane onto the thimbles – which requires the knowledge of the fixed points – to obtain a numerical parametrization. However, this way of finding numerical parametrizations of the thimbles may be costly in higher dimensions.

We remark in addition to the discussion in Section 4.1 that the thimble decomposition (4.1) provides a third challenge, namely the determination of the intersection number  $n_\sigma$ .

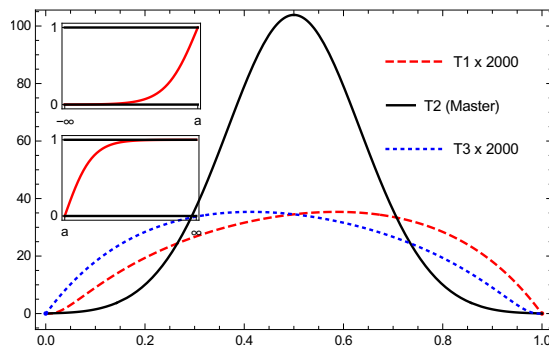


Figure 4.6.: Boltzmann factor  $\exp(-\text{Re}(S))$  vs. flow parameter  $\tau$  on the contributing thimbles in the  $U(1)$  one link model, where thimbles end in poles. Here it is necessary to transform integration ranges to maximize overlap. We chose to map all integration ranges to  $[0, 1]$ , which can be done by a linear transformation for a thimble on  $[a, b]$  or appropriate hyperbolic tangent transformations for intervals  $[-\infty, a]$  or  $[a, \infty]$ , see inlays and (B.2) and (B.3) for the latter two transformations (we chose the free parameter of the transformation as  $\xi = 1.5$ ). For details see App. B.2. This choice is not unique. Note that the curves have been rescaled for better visibility.

In one-dimensional integrals where it is straightforward to resolve the full thimble structure this issue is solvable, see also [133]. However, the intersection numbers represent global quantities. In higher dimensional theories this makes it highly non-trivial for local methods such as the here proposed axis scan to determine the contribution amount of the thimbles.

In the second step we have developed a novel reweighting procedure to determine the relative weights in the thimble decomposition. Our proposal has been illustrated by means of a one-site  $z^4$  model in Sec. 4.4.1. It has also successfully passed a hard test using a  $U(1)$  one-link model at finite density in Sec. 4.4.2. Numerical results for the expectation values of observables agree well with exact results within the combined statistical and systematic errors. Importantly, the reweighting method can be tuned such that there is no overlap problem.

Furthermore, the power of the reweighting procedure lies in the fact that it is generalizable to field theories and can be combined with other simulation algorithms for thimbles. This is current work in progress in application to field theories [59]. However, the extension to higher dimensional theories is challenging since Monte Carlo sampling on the thimble is required with or without having an explicit parametrization. Ideas to realize sampling on thimbles in this case, applied to gauge theories, are subject to the discussion in Chapter 5.

**Remark:**

The method presented here has emerged from discussions and investigations of the idea of simulating a complex Langevin evolution, that is directed to the Lefschetz thimbles. This procedure of a Lefschetz-cooled Langevin update has been partially, but not fully, successful. In our opinion such a combined approach still has its potential, more details can be found in App. B.3.

$\mathcal{O}$	numerical	exact
$\text{Re}\langle U \rangle$	0.315217(3)	0.315219
$\text{Re}\langle U^{-1} \rangle$	1.800941(3)	1.800939
$\text{Re}\langle P \rangle$	1.058079(3)	1.058079
$\text{Re}\langle n \rangle$	0.742861(1)	0.742860
$Z_2/Z_1 _{T_1} \times 10^{-3}$	2.99378(3)	2.99382
$Z_1/Z_2 _{T_2} \times 10^4$	3.34032(4)	3.34022
$Z_2/Z_3 _{T_3} \times 10^{-3}$	2.99377(3)	2.99382
$Z_3/Z_2 _{T_2} \times 10^4$	3.34026(9)	3.34022

Table 4.2.: Numerical results and exact values of observables for the U(1) model with statistical errors. Note that the imaginary parts for the observables are all consistent with zero within the statistical error. Possible deviations are caused by numerical discretization errors, see main text for a detailed discussion.

## 5. Lefschetz thimbles in gauge theories

In this chapter we explore novel simulation strategies inspired by studying Lefschetz thimbles for lattice field theories with a sign problem. Among those we consider examples where complementary methods to tackle the sign problem, in particular complex Langevin, fail. An essential difficulty with sampling thimbles in higher dimensions and field theories is that those are global objects. Unlike for the one-dimensional integrals considered in chapter 4 it is far from straightforward to obtain an analytical or a numerical parametrization of the thimbles<sup>1</sup>. Moreover, global updating techniques, most prominently the holomorphic gradient flow [180] come with high computational cost. Here, we are interested in devising local update rules that might allow for cheaper simulations. Our goal is to rewrite the path-integral in terms of local degrees of freedom which parametrize the thimble. This shifts the non-locality to the appearing Jacobian which might give rise to a potentially problematic residual sign problem. If this is under control, such local algorithms could in principle be completed with the reweighting technique developed in ch. 4 to account for the relative weights of the thimbles. Throughout this chapter we benchmark our results with analytical values where available. First, we construct an algorithm that allows to locally sample single thimbles by considering a  $U(1)$  gauge theory in  $1+1$  dimensions with a complex coupling in Section 5.1.3. In addition we discuss a complementary approach to the  $U(1)$  gauge theory based on locally sampling the tangent space in a  $U(1)$  one-link model, see Sec. 5.1.6. Secondly, we probe the local thimble algorithm by means of a free scalar field theory in real time in Sec. 5.2.3.

The content of this chapter summarizes joint research work with my collaborators as mentioned in the beginning of this thesis.

### 5.1. $U(1)$ lattice gauge theory

#### 5.1.1. Theory and properties

Pure  $U(1)$  gauge theory in  $1+1$  dimensions on the lattice serves as a suitable testbed. In particular it exhibits confinement, for a discussion see for instance [78]. First we consider the theory without a sign problem. The link variables are elements of the unit circle

$$U_{x,\mu} = e^{i\phi_{x,\mu}} \quad \text{with } \phi_{x,\mu} \in (-\pi, \pi] \quad (5.1)$$

and  $\mu = 1, 2$ . The Euclidean action is the Wilson plaquette gauge action introduced in ch. 2

$$S[U] = \beta \sum_{x,\mu < \nu} \left( 1 - \frac{1}{2} \left[ P_{x,\mu\nu}[U] + P_{x,\mu\nu}^{-1}[U] \right] \right) \quad (5.2)$$

where

$$P_{x,\mu\nu}[U] = U_{x,\hat{\mu}} U_{x+\hat{\mu},\hat{\nu}} U_{x+\hat{\nu},\hat{\mu}}^{-1} U_{x,\hat{\nu}}^{-1} \quad (5.3)$$

---

<sup>1</sup>Exceptions are special theories such as the free scalar field theory discussed in Sec. 5.2.3.

denotes the plaquette. Note that we have periodic boundary conditions. Let  $\Omega = N_\tau N_s$  denote the space-time volume of the lattice. For reasons of clarity we summarize the space-time and direction indices of the link variables into a single latin letter  $k = (x, \mu)$ . The path-integral of the theory reads

$$Z = \int_{U(1)^{2\Omega}} \prod_{k=1}^{2\Omega} dU_k e^{-S[U]} = \frac{1}{(2\pi)^{2\Omega}} \int_{[-\pi, \pi]^{2\Omega}} \prod_{k=1}^{2\Omega} d\phi_k e^{-S[U(\phi)]}. \quad (5.4)$$

In the thermodynamic limit the theory can be solved analytically integrating over plaquette degrees of freedom [78] yielding the following expression for Wilson loops

$$W(R, T) = \left( \frac{I_1(\beta)}{I_0(\beta)} \right)^{RT}. \quad (5.5)$$

Here  $R$  and  $T$  denote the spatial and the temporal extent of the Wilson loop respectively.

### 5.1.2. Thimble decomposition

Let  $\beta \in \mathbb{C}$  such that the action (5.2) becomes complex. We complexify the link variables  $U_k \in \mathbb{C}$ . Next, we analyze the structure of the critical points in this theory. Unlike the simple models studied in ch. 4 we are now faced with critical manifolds. The defining equation for the critical manifold is obtained by setting the derivative of the action to zero. In terms of the plaquettes containing the link  $U_k$  the derivative of the action with respect to the gauge field  $\phi_k$  reads

$$\frac{\partial S}{\partial \phi_k} = -\frac{i\beta}{2} (P_i - P_i^{-1} - P_j + P_j^{-1}). \quad (5.6)$$

$U_k$  is part of two differently oriented plaquettes. The first is denoted by  $P_i := U_k U_l U_m^{-1} U_n^{-1}$  being oriented counter-clockwise. The other,  $P_j^{-1}$  is oriented clockwise and results from taking the inverse of the counter-clockwise plaquette  $P_j := U_p U_q U_k^{-1} U_r^{-1}$ . Finding the stationary manifold on the level of the links could turn out to be intractable. Therefore, we examine the plaquettes in more detail using the representation

$$P_i = e^{i\phi_i} \quad \text{with} \quad \phi_i = \phi_i^R + i\phi_i^I. \quad (5.7)$$

It holds

$$P_i - P_i^{-1} = -2 \sinh(\phi_i^I) \cos(\phi_i^R) + 2i \cosh(\phi_i^I) \sin(\phi_i^R). \quad (5.8)$$

Setting the gradient (5.6) to zero we are thus left with

$$\begin{aligned} \sinh(\phi_i^I) \cos(\phi_i^R) &= \sinh(\phi_j^I) \cos(\phi_j^R) \\ \cosh(\phi_i^I) \sin(\phi_i^R) &= \cosh(\phi_j^I) \sin(\phi_j^R). \end{aligned} \quad (5.9)$$

There are two solutions to the previous set of equations, namely

$$\phi_i = \phi_j \pmod{2\pi} \quad (5.10)$$

$$\phi_i^R = \pi - \phi_j^R \pmod{2\pi} \text{ and } \phi_i^I = \phi_j^I. \quad (5.11)$$

$U(1)$  or  $\mathbb{C} \setminus \{0\}$  respectively are both abelian groups, thus the following rule for the plaquettes holds

$$\prod_{k=1}^{\Omega} P_k = 1. \quad (5.12)$$

Here it is important that we have specified periodic boundary conditions. To be on the stationary manifold all neighbouring plaquettes have to take values such that (5.6) is zero. Hence, it is useful to construct the stationary manifolds using plaquette configurations with values

$$P_i = \pm 1. \quad (5.13)$$

Because the product of all plaquettes is one, there can only be an even number of plaquettes with a flipped sign  $P_i = -1$ . Without loss of generality let  $\Omega$  be even. If we count all such possible configurations we obtain

$$\#\text{configurations with even number of flipped plaquettes} = \sum_{k=0}^{\Omega/2} \binom{\Omega}{2k}. \quad (5.14)$$

This is the number of disconnected critical manifolds which have  $\Omega/2 + 1$  different imaginary parts of the action. The latter can be easily calculated from (5.2). Assume we flip  $2k$  plaquettes then it holds

$$S_I := \text{Im}(S) = \beta_I(\Omega - ((\Omega - 2k) - 2k)) = 4k\beta_I, \quad k = 0, \dots, \Omega/2 \quad (5.15)$$

where  $\beta_I = \text{Im}(\beta)$ . As an example we consider a  $2 \times 2$  lattice. We have  $4/2 + 1 = 3$  different imaginary parts. The two stationary points where all plaquettes either assume the value  $+1$  ( $S_I = 0$ ) or  $-1$  ( $S_I = 8\beta_I$ ) are non-degenerate. By contrast the case where one half of the plaquettes differs in sign from the other half is six-fold degenerate ( $S_I = 4\beta_I$ ) because there are six ways to distribute this configuration on the  $2 \times 2$  lattice. We end up with 8 critical manifolds. Evaluating (5.14) yields [182]

$$\sum_{k=0}^{\Omega/2} \binom{\Omega}{2k} = 2^{\Omega-1}. \quad (5.16)$$

Hence the degeneracy of the stationary manifolds with respect to the imaginary part of the action grows exponentially with the lattice volume. For example for a  $2 \times 4$  lattice we have already 128 configurations corresponding to critical manifolds with 5 different imaginary parts of the action. Note that the path-integral (5.4) is written over link degrees of freedom. Gauge symmetry introduces an additional redundancy in characterizing the stationary manifolds in terms of link variables. The critical configurations connected by real gauge transformations form gauge orbits [39]. The gauge orbits are a sub-manifold to the critical manifold. We shall not discuss this further here because we consider plaquettes which are gauge invariant quantities. However, for a detailed discussion on the relation between the stationary manifolds and gauge symmetry see [126]. The thimble decomposition of the path-integral (5.4) reads

$$Z = \sum_{\sigma} n_{\sigma} e^{-iS_{I,\sigma}} \int_{\mathcal{J}_{\sigma}} d^{2\Omega} \phi e^{-S_R[\phi]} \quad (5.17)$$

where  $S_{I,\sigma}$  denotes the imaginary part of the action evaluated on the critical manifold  $\sigma$ . To each critical manifold a thimble is attached which has the same dimension as the original real integration domain, namely  $2\Omega$ . Note that for  $\beta_R > 0$  there is a hierarchy of thimbles regarding their weight in the partition function. The thimble for which  $S_I = 0$  also called the main thimble has the largest weight. Compared to the other thimbles it has the lowest real part of the action on its stationary manifold. Since the action is an extensive quantity the term corresponding to the weight of the main thimble proportional to  $e^{-S_R}$  in the partition function survives in the thermodynamic limit  $\Omega \rightarrow \infty$ . The terms corresponding to the sub-leading thimbles are exponentially suppressed relative to it. For  $\beta_R > 0$  the hope is that sampling the main thimble and a minimal number of the sub-leading thimbles is sufficient to compute observables. This should worsen when  $\beta_I$  is larger than  $\beta_R$ . In case  $\beta_R = 0, \beta_I > 0$  which corresponds to a pure real-time scenario all thimbles become equal in weight.

### 5.1.3. Sampling on thimbles

To realize a local Monte Carlo algorithm on the thimbles updating the links successively, we need to rewrite the thimble decomposition (5.17). Therein we integrate over the gauge field  $\phi_i$  along the thimbles. We are interested in a parametrization of the thimble of the form

$$\phi_i = \phi_i^R + i\phi_i^I \rightarrow \tilde{\phi}_i(\phi_i^R) := \phi_i^R + i\phi_i^I(\phi_i^R). \quad (5.18)$$

Crucially, the imaginary part of the field  $\phi_i$  becomes a function of the real part. The partition function on each thimble is expressed in terms of the real field variables  $\phi_i^R$  as follows

$$Z_\sigma = \frac{1}{\text{vol}(\mathcal{J}_\sigma)} e^{-iS_{I,\sigma}} \int_{\min(\phi_1^R)}^{\max(\phi_1^R)} d\phi_1^R \dots \int_{\min(\phi_{2\Omega}^R)}^{\max(\phi_{2\Omega}^R)} d\phi_{2\Omega}^R e^{-S_R[\tilde{\phi}(\phi^R)]} \det(J(\phi^R)). \quad (5.19)$$

The Jacobian is given by

$$J_{kl} = \frac{\partial \tilde{\phi}_k}{\partial \phi_l^R}. \quad (5.20)$$

The formally introduced integral boundaries in (5.19)  $\min(\phi_i^R)$  and  $\max(\phi_i^R)$  carry the dependence on the local plaquette configurations surrounding the link  $U_i$ . This will become relevant for determining the domain of the allowed  $\phi_i^R$  when we put to work this formulation in terms of a simulation prescription. Because the link variables are coupled inside the plaquettes and neighboring plaquettes are coupled as well the non-locality of the integral over a single thimble  $\mathcal{J}_\sigma$  is transferred to the Jacobian (5.19) which has to be a dense matrix. Monte Carlo updates are organized as usual as sweeps of Metropolis updates for the  $\phi_i^R$  over the lattice. Importantly, in order to stay on the thimble we need

1. to initialize the Monte Carlo simulation on the associated stationary manifold and
2. the updates have to preserve the imaginary part of the action.

Observables on the thimbles are computed via standard reweighting with respect to the Jacobian (5.20). The reweighting procedure presented in Section 4.3.2 yields the relative weights between the different contributing thimbles. Now, we derive the local thimble

algorithm on a more technical level. For the updates to preserve the imaginary part of the action the following constraint must hold

$$\text{Im}(S) = \text{const} . \quad (5.21)$$

Hence, a change in the action  $\Delta S$  produced by a local update has to have a vanishing imaginary part

$$\text{Im}(\Delta S) = 0 . \quad (5.22)$$

Since we are doing local updates it is sufficient to consider the local action. We have

$$S_{\text{loc}}[U_k] = \beta \left( 2 - \frac{1}{2}(U_k(V_i + V_j^{-1})) + U_k^{-1}(V_j + V_i^{-1}) \right) . \quad (5.23)$$

Here,  $V_i$  and  $V_j$  are the staples surrounding the link  $U_k$ . It is useful to define the staple sum as follows

$$V_{ij} = \frac{1}{2}(V_i + V_j^{-1}) . \quad (5.24)$$

Next making a local proposal  $U_k \rightarrow U'_k$  the action difference yields

$$\Delta S = S[U'] - S[U] = \beta(V_{ij}(U_k - U'_k) + V_{ji}(U_k^{-1} - U'^{-1}_k)) . \quad (5.25)$$

With  $U_k = e^{i\phi_k}$  the proposal link can be written as

$$U'_k = \Delta U_k U_k = e^{i\Delta\phi_k} e^{i\phi_k} = e^{i\Delta\phi_k} U_k . \quad (5.26)$$

For the plaquettes surrounding  $U_k$  we can define similarly as for the staples

$$P_{ij} = \frac{1}{2}(P_i + P_j^{-1}) . \quad (5.27)$$

With that the action difference becomes

$$\Delta S = \beta(P_{ij}(1 - \Delta U_k) + P_{ji}(1 - \Delta U_k^{-1})) . \quad (5.28)$$

In accordance with the parametrization (5.18) we split the quantity  $\Delta U_k$  into a radial and a phase factor

$$\Delta U_k = |\Delta U_k| e^{i\Delta\phi_k^R}, \quad \text{where } |\Delta U_k| = e^{-\Delta\phi_k^I} . \quad (5.29)$$

Plugging this into the constraint equation (5.22)

$$\text{Im}(S) = \text{Im}[\beta(P_{ij} + P_{ji})] - |\Delta U_k| \text{Im}[\beta P_{ij} e^{i\Delta\phi_k^R}] - |\Delta U_k|^{-1} \text{Im}[\beta P_{ji} e^{-i\Delta\phi_k^R}] = 0 . \quad (5.30)$$

Upon multiplication with  $-|\Delta U_k|$  we end up with a quadratic equation for  $|\Delta U_k|$  with the solution

$$|\Delta U_k| = \frac{\text{Im}[\beta(P_{ij} + P_{ji})] \pm \sqrt{\text{Im}[\beta(P_{ij} + P_{ji})]^2 - 4\text{Im}[\beta P_{ij} e^{i\Delta\phi_k^R}]\text{Im}[\beta P_{ji} e^{-i\Delta\phi_k^R}]}}{2\text{Im}[\beta P_{ij} e^{i\Delta\phi_k^R}]} . \quad (5.31)$$

With this equation we have a local parametrization of the surface with  $S_I = \text{const}$  in terms of the real part of the angle  $\Delta\phi^R$ . In order to determine the correct proposal for  $|\Delta U_k|$  we need to examine formula (5.31) closer. We need to require  $|\Delta U_k| > 0$  per definition. Moreover the term under the square-root can become negative characterizing a forbidden

region for the  $\Delta\phi_k^R$ . This restricts the range of possible proposals for  $\Delta\phi^R$ . An update is completed by a Metropolis accept-reject step involving the difference of the real part of the local action  $\Delta S_{\text{loc},R}$ . The last remaining ingredient for computing observables is the Jacobian for which it holds

$$\frac{\partial \tilde{\phi}_k}{\partial \phi_l^R} = \frac{\partial(\phi_k^R + i\phi_k^I(\phi^R))}{\partial \phi_l^R} = \delta_{kl} + i \frac{\partial \phi_k^I(\phi^R)}{\partial \phi_l^R}. \quad (5.32)$$

We can use the following identity for a smooth function  $f : \mathbb{R} \rightarrow \mathbb{R}$  to compute the derivative corresponding to the imaginary part of (5.32)

$$\begin{aligned} f(x+h) &= f(x) + h \frac{\partial f}{\partial x} + O(h^2) \\ \Rightarrow \frac{\partial(f(x+h) - f(x))}{\partial h} \Big|_{h=0} &= \frac{\partial f}{\partial x}. \end{aligned} \quad (5.33)$$

Hence this yields

$$\frac{\partial \phi_k^I(\phi^R)}{\partial \phi_l^R} = \frac{\partial \Delta \phi_k^I(\Delta \phi^R)}{\partial \Delta \phi_l^R} \Big|_{\Delta \phi_l^R=0}, \quad \Delta \phi_k^I = -\log |\Delta U_k|. \quad (5.34)$$

#### 5.1.4. Application 1: One-link model

A simple benchmark for the method described in the previous section is a one-link model whose action reads

$$S = -\frac{\beta}{2}(U + U^{-1}) = -\beta \cos(\phi). \quad (5.35)$$

where  $U = e^{i\phi}$  and  $\phi \in (-\pi, \pi]$ . Note that this is the gauge part of the action of the one-link model (4.19) discussed in chapter 4. The partition function reads

$$Z = \frac{1}{2\pi} \int_{-\pi}^{\pi} d\phi e^{\beta \cos(\phi)} = I_0(\beta), \quad (5.36)$$

where  $I_0(\beta)$  is a modified Bessel function of the first kind [38]. The action (5.35) is a special case of the Wilson action (5.2) with only a single link whose surrounding staples are set to one. This greatly simplifies the sampling algorithm on the thimbles. The thimble structure of the model is depicted in Fig. 5.1 for three scenarios of  $\beta$ . The critical points are located  $\phi_{c,1} = 0$  and  $\phi_{c,2} = \pi$  because the derivative of the action with respect to  $\phi$  is proportional to  $\sin(\phi)$ . There are two thimbles one corresponding to  $U(\phi_{c,1}) = +1$  and the other to  $U(\phi_{c,2}) = -1$ . For  $\beta_R > 0$  the real part of the action  $S_R$  is lower than on the second. Hence it carries the larger weight in the partition sum and is therefore the main thimble. However, for  $\beta_R = 0$ , corresponding to a pure real-time scenario the thimbles are congruent and contribute equally to the partition sum, see also the right-hand side of Fig. 5.1. We restrict our simulation to the main thimble. Sampling is performed according to the recipe in the last section. Observables are computed via conventional reweighting with respect to the Jacobian reading here

$$\frac{\partial \tilde{\phi}_k}{\partial \phi_l^R} = 1 + i \frac{\text{Re}[\beta(U - U^{-1})]}{\text{Im}[\beta(U - U^{-1})]}. \quad (5.37)$$

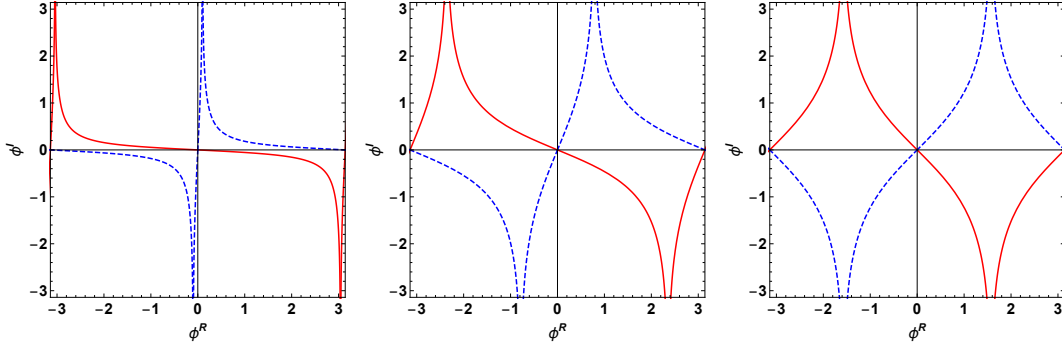


Figure 5.1.: Thimble structure for the  $U(1)$  one-link model for different values of  $\beta = 1 + 0.1i$  (left),  $1 + i$  (center), and  $i$  (right). The critical points of the action are  $0$  and  $\pi$  (being equivalent to  $-\pi$ ). Red full lines describe thimbles and blue dashed lines the associated anti-thimbles. The main thimble having the largest weight in the partition sum for  $\beta_R > 0$  is the one passing through the origin. If  $\beta \in \mathbb{R}$  the main thimble coincides with the interval  $(-\pi, \pi]$ . Note also that if  $\beta_R = 0$  and  $\beta_I \neq 0$  both thimbles contribute equally. This situation corresponds to the gauge theory in real-time.

We consider the scenario  $\beta = 3 + i$ . Within the statistical error sampling results for the link expectation value are in agreement with the results from numerically integrating along the main thimble

$$\begin{aligned} \langle e^{i\phi} \rangle_{\text{sampling}} &= 0.840(5) + 0.060(15)i, \\ \langle e^{i\phi} \rangle_{\text{num. int.}} &= 0.839 + 0.064i. \end{aligned}$$

The parametrizations of the thimbles used for the numerical integration are discussed in Sec. 5.1.6. Moreover, we investigate how much the main thimble contributes relative to the full result given by (5.36). To that end we consider the expectation value

$$\frac{1}{2} \langle U + U^{-1} \rangle = \frac{I_1(\beta)}{I_0(\beta)}. \quad (5.38)$$

which is the analogue of the plaquette expectation value. Note that it coincides with the plaquette expectation value for the full  $U(1)$  gauge theory in the thermodynamic limit as mentioned in Sec. 5.1.1. Fig. 5.2 shows the comparison between the result evaluated on the main thimble via numerical integration and the analytical result for fixed  $\beta_I = 0.5$  (left) and  $\beta_I = 3$  (right). Both results show that for  $\beta_R \rightarrow \infty$  the main thimble solely determines the result. For small  $\beta_R$  the contribution of the sub-leading thimble is relevant and it should be included into simulations. Moreover, we consider the  $\beta_I$  dependence of the plaquette expectation value for fixed  $\beta_R = 0.5$  and  $\beta_I \in [0.5, 12]$ , see Fig. 5.3. Here, no agreement between the result of the main thimble and the full result is found. This indicates that in a situation close to the real-time scenario  $\beta_R = 0$  the weights of the thimbles become equally important.

### 5.1.5. Application 2: $U(1)$ gauge theory in 1+1 dim.

The local sampling algorithm described in Sec. 5.1.3 has been probed for  $U(1)$  gauge theory in 1 + 1 dimensions. For comparisons at complex  $\beta$  we only have an analytical

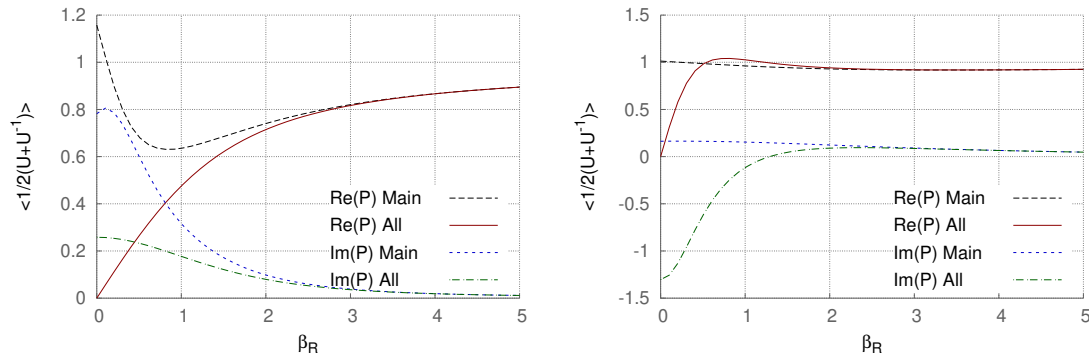


Figure 5.2.:  $\beta_R$  dependence of the plaquette expectation value computed on the main thimble in comparison with the analytical result (5.38), the latter being equivalent to include all thimbles. Left: For fixed  $\beta_I = 0.5$  the main thimble's contribution to the result becomes dominant for  $\beta_R \gtrsim 2$ . Right: For fixed  $\beta_I = 3$  the main thimble's contribution to the result becomes dominant for  $\beta_R \gtrsim 1.5$ . Both results show that asymptotically for  $\beta_R \rightarrow \infty$  only the main thimble determines the result.

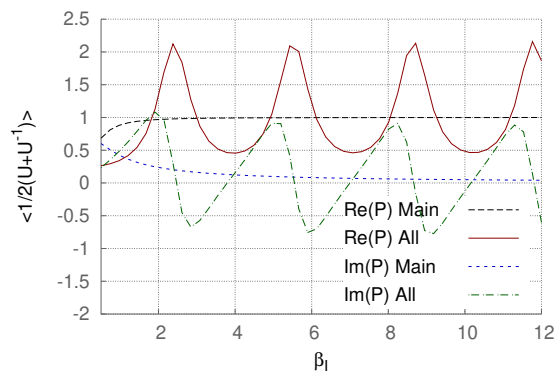


Figure 5.3.: Dependence of the plaquette expectation value on  $\beta_I \in [0.5, 12]$  for fixed  $\beta_R = 0.5$ . The result from integrating along the main thimble is compared to the analytical result (5.38). Here, the main thimble result completely deviates from the full result. This suggests that both thimbles become equally important.

result in the thermodynamic limit, see Sec. 5.1.1. As long as  $\beta_R > 0$  the main thimble carries the largest weight. Thus in the thermodynamic limit  $\Omega \rightarrow \infty$  it solely determines the partition function. Hence, we restrict our discussion to the main thimble for which  $S_I = 0$ . The simulation is initialized on the critical manifold. A simple choice is to set all links to one,  $U_i = 1 \forall i$ . For the lattices and couplings  $\beta$  considered the algorithm suffers from numerical instabilities prohibiting the extraction of results.

We characterize the problems with the algorithm by means of the following example. Consider an  $N_\tau = 8, N_s = 8$  lattice at  $\beta = 3 + 3i$ . We let the system thermalize over a sequence of  $O(10^4)$  Metropolis sweeps. Initially the real part of the global action  $S_R$  is positive. At a point that depends on the initial seed for the random number generator it decreases towards zero and becomes negative. It then diverges to minus infinity. To understand this we have monitored the unitarity norm<sup>2</sup> [123], the individual links as well as the real part of the local action  $S_{R,\text{loc}}$ . Right from the start the unitarity norm rises monotonously. Applying a special variant of gauge cooling, the increase rate of the unitarity norm can be slowed down. Importantly, the constraint  $S_I = 0$  is fulfilled numerically during the thermalization allowing to stay on the stationary manifold and the thimble in principle. However, consistent with the rising unitarity norm we observe large fluctuations over several orders of magnitude in the real and imaginary parts of the individual links causing the  $S_{R,\text{loc}}$  to become negative. This leads to self-enhancing destabilizing effect, since negative local actions fuel the acceptance rate such that every candidate that makes  $S_R$  more negative is accepted. By definition, on the thimble the real part of the global action is larger or equal to zero. Thus a negative real part hints that the sampled configuration inevitably leave the thimble and settle on the anti-thimble or other surfaces in  $\mathbb{C}^{2\Omega}$  on which  $S_I = 0$ . The latter are connected with the thimble and the stationary manifold. Thus, a large fluctuation in a single link may kick the entire configuration over to that other surface. This is also consistent with our finding that the configuration where  $S_R$  crosses zero is not gauge equivalent to the stationary manifold. Remarkably, for  $\beta_I > \beta_R$  the numerical instabilities are somewhat milder and  $S_R$  diverges to minus infinity much more slowly. To diagnose the problems with the simulation algorithm we apply it to a simple field theory without gauge degrees of freedom and a trivial thimble structure in Section 5.2.3.

### 5.1.6. Tangent space simulation

We wish to keep the concept of a local sampling strategy for  $U(1)$  gauge theory in  $1 + 1$  dimensions at a complex  $\beta$ . Instead of sampling the thimble by keeping  $\text{Im}(S)$  constant, see Sec. 5.1.3, here we aim at generate configurations on different manifolds immersed in  $\mathbb{C}^{2\Omega}$  which integrated over leave the path integral invariant. In other words they have to be homotopy equivalent to the original manifold  $U(1)^{2\Omega}$ . The manifold we have in mind here consists of the product of the tangent spaces to the critical points in the one-link model. Local updates for the individual links are determined by the tangent space structure of the one-link model. The latter is sketched in Fig. 5.4 for the case  $\beta = 1 + i$ . Recall that in the one-link model the critical points are indicated by  $U = \pm 1$ . The thimbles can be

<sup>2</sup>The unitarity norm measures the distance between of a given configuration in  $\mathbb{C}^{2\Omega}$  from the unitary manifold  $U(1)^{2\Omega}$ .

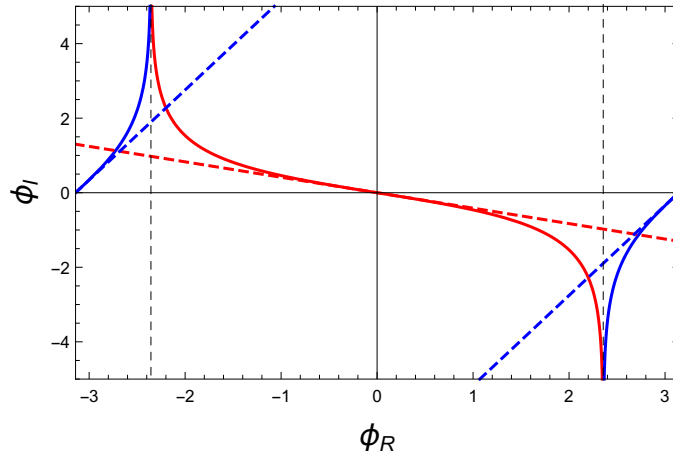


Figure 5.4.: Thimble and tangent structure to the critical points in the  $U(1)$  one-link model for  $\beta = 1 + i$ . The dashed black lines mark the boundaries of the thimbles (full lines).

parametrized by solving  $\text{Im}(S[U]) = \mp\beta_I$  for  $|\Delta U|$  where  $U = |\Delta U|e^{i\phi_R}$ . This yields

$$|U(\phi_R)| = \frac{\pm\beta_I \pm |\beta| \sin(\phi_R)}{\beta_I \cos(\phi_R) + \beta_R \sin(\phi_R)}. \quad (5.39)$$

The plus sign corresponds to the main thimble and the minus sign to the sub-leading thimble at  $\pi$ . In Fig. 5.4 the boundaries of the thimbles are displayed by the black vertical dashed lines. The boundaries are computed as follows. The right boundary  $\phi_{R,+}$  of the thimbles is set by the angle where the denominator vanishes and the numerator is different from zero. The point where the numerator vanishes and the denominator is non-zero determines the left boundary  $\phi_{R,-}$  which is the right boundary mirrored at the origin. This means

$$\begin{aligned} \phi_{R,+} &= \arctan 2(-\beta_I, \beta_R) + \pi \\ \phi_{R,-} &= -\arctan 2(-\beta_I, \beta_R) - \pi. \end{aligned} \quad (5.40)$$

Now, we discuss the tangent space algorithm. The link is updated such that its surrounding plaquettes lie on the main tangent within specified boundaries. As we take into account also the tangent at the sub-leading critical point, the intersection points of the tangents determine the boundaries of the single tangents. The total product tangent space manifold is homotopy equivalent to  $U(1)^{2\Omega}$ . Its structure is simple. The residual sign problem reduces to a constant for each factor corresponding to the slope of each tangent in the one-link model. Locally the tangents are continuously connected at their intersection points. Sampling is then facilitated by applying the reweighting procedure for the relative weights of the contributing integration paths. For the preliminary results shown here, we only consider the tangents to the main critical point and leave the inclusion of the sub-leading tangents as well as the reweighting to future work. The boundaries we assign to the main tangent are those of the thimble in (5.40). The simulation is initialized by setting all links to one, i.e.  $U_i = 1 \forall i$ . The local Metropolis update to sample a single thimble is divided into the following steps:

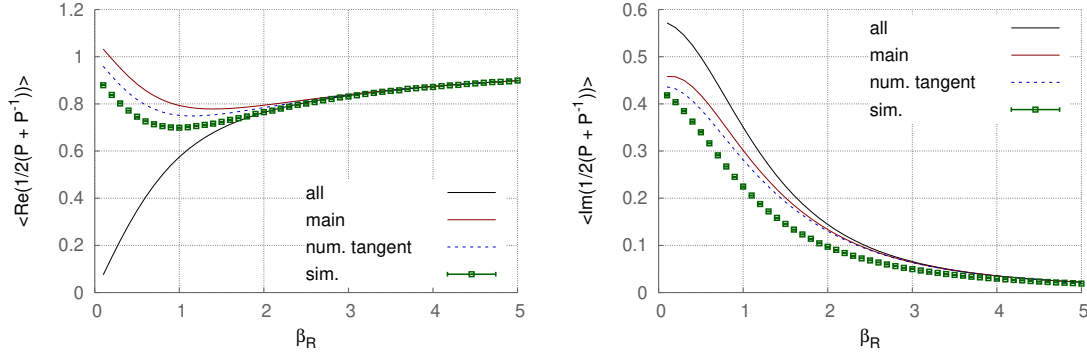


Figure 5.5.: Numerical results for the real (left) and imaginary part (right) of the plaquette expectation value from the tangent space simulation for varying  $\beta_R$ . The main tangent only is considered. The simulations have been carried out on a  $16 \times 16$  lattice at fixed  $\beta_I = 1$  (green). The analytical result (black, label "all") is given by (5.38). The simulation data is compared to numerically integrating along the parametrizations of the main thimble (5.39) (red) and the main tangent (blue). For large  $\beta_R$  the main thimble contributes most and all results converge. The simulation on the tangent space manifold also shows the same trend as the main thimble over the total range of  $\beta_R$  considered.

1. Choose a link to be updated and determine the phases of its surrounding plaquettes  $\phi_{R,i} = \arg(P_i)$  and  $\phi_{R,j} = \arg(P_j)$ .
2. Draw a uniform random number  $\xi_R \in (a, b)$ , where  $a = -\min(|\phi_{R,i} - \phi_{R,-}|, |\phi_{R,j} - \phi_{R,-}|)$  and  $b = \min(|\phi_{R,i} - \phi_{R,+}|, |\phi_{R,j} - \phi_{R,+}|)$ .
3. Calculate  $\xi_I := \gamma \xi_R$ . with  $\gamma = (-1/\beta_I)(|\beta| - \beta_R)$  being the tangent's slope corresponding to the main critical point.
4. Calculate a proposal for the link  $U' \rightarrow e^{i\xi} U$  and perform a Metropolis accept-reject step using the real part of the action difference  $\text{Re}(S_{\text{loc}}[U'] - S_{\text{loc}}[U])$ .

First numerical results for the tangent space simulation have been obtained on a  $16 \times 16$  lattice using  $O(10^3)$  configurations. The left-hand side of Fig. 5.5 shows the real part of the plaquette expectation value as a function of  $\beta_R$  at fixed  $\beta_I = 1$ . For large  $\beta_R$  the results from numerically integrating the main thimble as well as the main tangent of the one-link model agree with the simulation data and the analytical result. For small  $\beta_R$  the inclusion of the sub-leading tangents is required. For small  $\beta_R$  the same trend in the simulation data and in the results from numerically integrating along the main thimble and the tangent is visible. This is plausible, since in the thermodynamic the  $U(1)$  gauge theory coincides with the one-link model. It is also plausible that the simulation result is closer to the numerical integration along the tangent. A similar result is shown by the imaginary part of the plaquette on the right-hand side of Fig. 5.5. In Fig. 5.6 the same observables are shown as a function of  $\beta_I$  for fixed  $\beta_R = 1$ . As noted above, we have only simulated the product manifold of the main tangents. The inclusion of the sub-leading tangents is work in progress. Since the total tangent manifold is homotopy equivalent to the original manifold, this algorithm could turn out promising. While the values for the

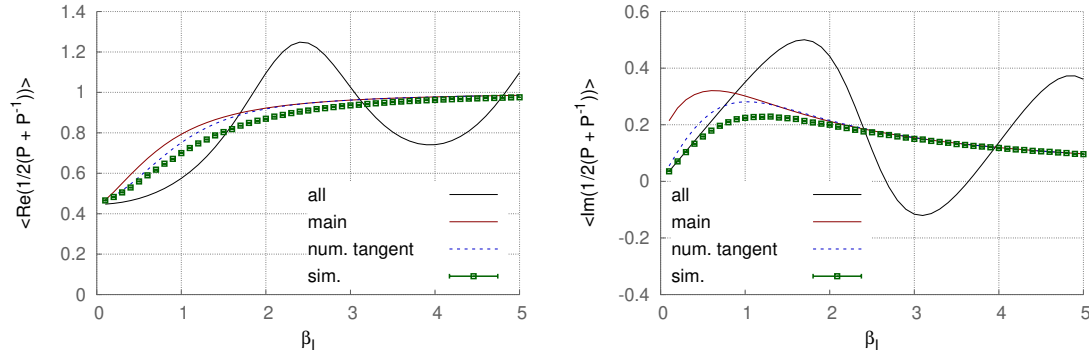


Figure 5.6.: Numerical results for the real (left) and imaginary part (right) of the plaquette expectation value from the tangent space simulation for varying  $\beta_I$ . The main tangent only is considered. The simulations have been carried out on a  $16 \times 16$  lattice at fixed  $\beta_R = 1$  (green). Similarly as in Figure 5.5 the tangent space simulation produces results close to the main thimble. However, as already seen when discussing the one-link model by means of the local thimble algorithm for increasing  $\beta_I$  the thimbles become equal in weight. Hence we need to include the sub-leading tangents as well.

plaquettes are constrained to the tangent at the origin in the one-link model, the individual links can again assume arbitrary values. We find an increasing unitarity norm throughout the simulation which can be controlled by applying the above mentioned variant of gauge cooling.

**Remark:** We have experimented with simulations on other complex manifold for instance the one resulting from taking the product of the thimbles in the  $U(1)$  one-link model, see Fig. 5.1. Each link lives on the thimble structure of the one-link model where the two thimbles need to be connected at the boundaries  $\phi_{R,+}$  and  $\phi_{R,-}$ . Local updates are performed with respect to the real part of the action. Observables are computed via standard reweighting with the phase  $e^{-iS_I}$ . However, we find that for the interesting parameter ranges  $\beta_I \leq \beta_R$  the average phase is small indicating a poor choice for the manifold to sample on.

## 5.2. Real-time scalar fields in 0 + 1 dimensions

In this section, we take a step back to probe the local sampling algorithm on the thimble keeping  $\text{Im}(S)$  fixed by means of integrals in low dimensions. To that end we consider a free real scalar field in 0 + 1 dimensions with a complex action. First, we formulate the sampling recipe applied to this example and discuss numerical results. Secondly, using the Takagi decomposition allows to determine a range of validity for the local thimble algorithm. Moreover, the Takagi decomposition itself gives rise to a sampling method.

### 5.2.1. Sampling à la $\text{Im}(S) = \text{const.}$

We consider the action of a free real scalar field theory in real-time.

$$S = -i \sum_{j=1}^{N_t} a \left( \frac{(\phi_{j+1} - \phi_j)^2}{2a^2} - \frac{m^2}{2} \phi_j^2 \right). \quad (5.41)$$

Moreover, we choose  $N_t = 2$  and define dimensionless quantities  $\tilde{\phi} = a^{-1/2}\phi$  as well as  $\tilde{m} = am$ . Dropping the tilde we can write the action as follows

$$S = \frac{1}{2} \sum_{j,l} \phi_j K_{jl} \phi_l \quad \text{where } K = \begin{pmatrix} -2i(1 - \frac{m^2}{2}) & 2i \\ 2i & -2i(1 - \frac{m^2}{2}) \end{pmatrix} \quad (5.42)$$

with  $j, l = 1, 2$ . The partition function is a Gaussian integral which can be easily evaluated

$$Z = \int_{\mathbb{R}^2} d\phi_1 d\phi_2 e^{-S} = \frac{2\pi}{\sqrt{\det(K)}}. \quad (5.43)$$

Note that it is not defined for  $m = 2$  which can be seen by computing the determinant of  $K$ . In this section we consider only mass parameters for which  $m^2 > 4$ . Note that for  $m^2 < 4$  the local sampling algorithm is inapplicable, see Sec. 5.2.3 for a detailed discussion. A suitable quantity for testing the sampling algorithm is given by the expectation value of the squared field

$$\langle \phi^2 \rangle := \left\langle \frac{\phi_1^2 + \phi_2^2}{2} \right\rangle = i \frac{\partial}{\partial m^2} \log(Z) = -\frac{i}{2} \left( \frac{1}{m^2} + \frac{1}{m^2 - 4} \right). \quad (5.44)$$

Next, we consider the thimble structure of the model. The complexified field variables live in  $\mathbb{C}^2 \simeq \mathbb{R}^4$ . Since the action is quadratic in the fields there is a single critical point  $\phi_1 = 0 = \phi_2$  and the thimble and the anti-thimble are two-dimensional orthogonal hyperplanes. The constraint  $\text{Im}(S) = 0$  gives rise to a three dimensional hyper-surface immersed in  $\mathbb{R}^4$ . A cut through the  $\text{Im}(\phi_2) = 0$  plane reveals that this surface is given by a double cone whose apex touches the critical point. In this picture the (anti-)thimble is given by a ray along the two cones passing through the origin.

We locally sample the thimble following the strategy presented in Sec. 5.1.3. Similarly as shown in (5.19) the path-integral is reparametrized in terms of the real parts of the field variables. Proposals for new candidates  $\phi_j \rightarrow \phi'_j = \phi_j + \Delta\phi_j^R + i\Delta\phi_j^I$  ( $\Delta\phi_j^R$ ) are calculated from demanding that  $\Delta S_I = 0$ . Without loss of generality we consider the field  $\phi_1$  to be

updated. Setting the imaginary part of the action difference to zero yields a quadratic equation for  $\Delta\phi_1^I$  with solutions

$$\Delta\phi_1^I(\Delta\phi_1^R) = \frac{-\eta\phi_1^I - 2\phi_2^I \pm \sqrt{(\eta\phi_1^I + 2\phi_2^I)^2 + \eta(\eta(\Delta\phi_1^R)^2 + 2\eta\Delta\phi_1^R\phi_1^R + 4\Delta\phi_1^R\phi_2^R)}}{\eta} \quad (5.45)$$

where  $\eta := m^2 - 2$ . The update algorithm now works as follows:

1. Depending on the current field configuration  $\{\phi_1, \phi_2\}$  check if the term under the square-root in (5.45) can become negative. If yes, determine its zeros  $\delta_-$  and  $\delta_+$ . Possible values of  $\Delta\phi_1^R$  can now be drawn from  $(-\infty, \delta_-]$  and  $[\delta_+, \infty)$ . If the term under the square-root is strictly positive set both  $\delta_-$  and  $\delta_+$  to the position of its minimum.
2. Choose randomly if a step in  $\Delta\phi_1^R$  is taken to the left or to the right.
3. Draw a Gaussian random number of unit variance  $x$ . If the step is to the left set  $\Delta\phi_1^R = \delta_- - \varepsilon|x|$ . If it is to the right set  $\Delta\phi_1^R = \delta_+ + \varepsilon|x|$ .
4. Determine  $\Delta\phi_1^I$  as follows. If the step  $\Delta\phi_1^R$  is to the left, the solution with the plus sign in (5.45) is chosen. If it is to the right the solution with the minus sign is chosen<sup>3</sup>.
5. Set  $\phi_1 \rightarrow \phi_1 + \Delta\phi_1$  and close the update by a Metropolis accept-reject step involving the real part of the local action.
6. Proceed with the field  $\phi_2$  analogously.

In Fig. 5.7 we show the algorithm put to work for  $m^2 = 6$ . The sampled configurations lie on the thimble (red). Our updates are guaranteed to sample the thimble by choosing the sign in front of the square-root in (5.45) accordingly. The simulation is stable against small fluctuations and we find that  $\text{Re}(S) \geq 0$  confirming that we sample the thimble. To compute observables it remains to take into account for the Jacobian  $\partial\phi_k/\partial\phi_l^R$ . The latter is a complex  $2 \times 2$  matrix and it can be shown that the diagonal elements are  $1 \pm i$  depending on whether in the associated update step  $\Delta\phi_l^R$  is larger than  $\delta_+$  or smaller than  $\delta_-$ . Representing the off-diagonal elements consider

$$J_{12} = \frac{\partial\Delta\phi_1^I}{\partial\Delta\phi_2^R} = \frac{4\phi_2^R}{\sqrt{(4\phi_1^I + 2(m^2 - 2)\phi_2^I)^2}} \quad (5.46)$$

which corresponds to the solution with the minus sign in (5.45). Fig. 5.8 shows a Monte Carlo time history of this off-diagonal element. Clearly visible are the large spikes originating from small values of the denominator in (5.46). Those lead to numerical instabilities hampering a reliable computation of observables.

<sup>3</sup>The choice of the solution is determined by looking at the real part of the local action as a function of  $\Delta\phi_1^R$  given by (5.45) evaluated at the starting point of the simulation, i.e.  $\phi_1 = 0 = \phi_2$ . For  $\Delta\phi_1^R < 0$   $S_{R,\text{loc}}$  evaluated in terms of the solution with the plus sign is positive. On the other hand if  $\Delta\phi_1^R > 0$   $S_{R,\text{loc}}$  evaluated in terms of the solution with the minus sign is positive. We state without proof that this also holds for all other configurations of  $\phi_1$  and  $\phi_2$ .

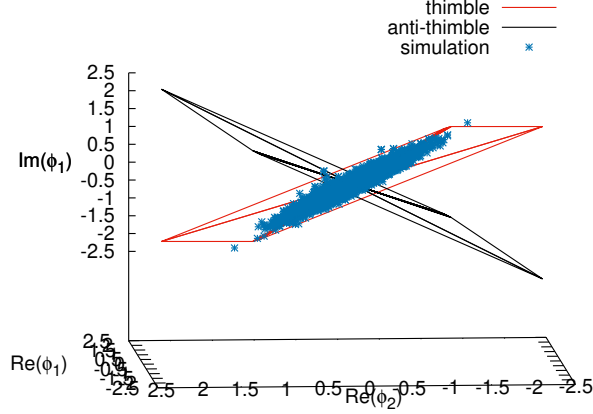


Figure 5.7.: Scatter plot of configurations sampled using the local thimble algorithm for  $m^2 = 6$  (blue points). Thimble and anti-thimble are two-dimensional orthogonal planes intersecting at the origin. The sampled configurations populate the thimble. We find that on average  $\text{Im}(S)$  is numerically zero with the fluctuation being of  $O(10^{-14})$ . There are some outliers scattering around the thimble plane which are part of or close to other surfaces with  $\text{Im}(S) = 0$ . Moreover  $\text{Re}(S) > 0$  during sampling confirms that we sample the thimble. The sampling algorithm appears to be stable with the thimble being attractive.[59]

### 5.2.2. Takagi decomposition

Although the local thimble sampling algorithm can be applied successfully for  $m^2 > 4$  the Jacobian suffers from numerical instabilities. A complementary approach to sample the thimble and to extract observables is to consider the Takagi vectors spanning the tangent space of the thimble at the critical point  $\phi = 0$  see [40] for technical details. The latter are defined by solving the eigenvalue problem

$$\overline{H}\vec{z} = \lambda\vec{z} \quad \text{where } \lambda \in \mathbb{R}. \quad (5.47)$$

Here,  $H$  denotes the Hessian evaluated at the critical point which coincides with the matrix  $K$  in (5.42) that is

$$H := \left( \frac{\partial^2 S}{\partial \phi_k \partial \phi_l} \right)_{k,l=1,2} = -i \begin{pmatrix} (2 - m^2) & -2 \\ -2 & (2 - m^2) \end{pmatrix}. \quad (5.48)$$

For the Takagi vectors we obtain  $\vec{z}_l = c_l \vec{v}_l$  with

$$\vec{v}_1 = \begin{pmatrix} 1 \\ 1 \end{pmatrix} \quad \text{and} \quad \vec{v}_2 = \begin{pmatrix} 1 \\ -1 \end{pmatrix} \quad (5.49)$$

as well as

$$c_1 = e^{-i\pi/4} \quad \text{and} \quad c_2 = e^{i\text{sign}(4-m^2)\pi/4} = \begin{cases} e^{i\pi/4} & m < 2 \\ e^{-i\pi/4} & m > 2 \end{cases} \quad (5.50)$$

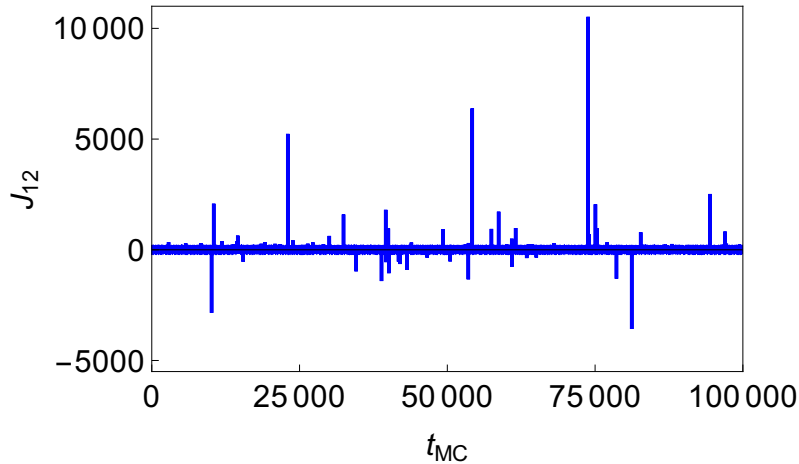


Figure 5.8.: Monte Carlo time history of the off-diagonal element  $J_{12}$  of the Jacobian for the free scalar theory in real-time on a two-site lattice with  $m^2 = 6$ . While oscillating most of the time between  $+1$  and  $-1$  the Jacobian shows large numerical values at some times. Those spikes occur when the denominator in (5.46) becomes small spoiling the computation of observables.

A complex vector on the tangent space can be parametrized according to

$$\begin{pmatrix} \phi_1 \\ \phi_2 \end{pmatrix} = r\vec{z}_1 + s\vec{z}_2 = \begin{pmatrix} e^{-i\pi/4}r + e^{i\text{sign}(4-m^2)\pi/4}s \\ e^{-i\pi/4}r - e^{i\text{sign}(4-m^2)\pi/4}s \end{pmatrix}, \quad r, s \in \mathbb{R}. \quad (5.51)$$

Plugging this parametrization into the action in (5.42) shows that the action on the tangent space is real and positive for all  $r, s$ . This shows that at the case at hand the tangent space coincides with the thimble. Moreover, we can analytically calculate the partition function and correlation functions by plugging in the Takagi parametrization into the path integral in (5.43). The expectation value of the squared field reads

$$\langle \phi^2 \rangle = -i \frac{|4 - m^2| - \text{sign}(4 - m^2)m^2}{2m^2|4 - m^2|}. \quad (5.52)$$

Note that for  $m = 2$  the expression diverges which is in agreement with our observation for the partition function. Moreover in this case the critical point  $\phi = 0$  is degenerate because only one Takagi vector is defined there. Using a standard Metropolis algorithm with respect to the coefficients  $r, s$  allows to sample the thimble within the tangent space parametrization. Numerical results are shown in comparison with the analytical formula (5.52) in Fig. 5.9

### 5.2.3. Range of applicability of the local thimble algorithm

As stated above for  $m^2 < 4$  the local thimble algorithm is not applicable. Using the parametrization of the thimble by means of the Takagi vectors we can give a formal proof. Sampling the thimble requires that the local updates are in directions of vectors that span the thimble at the critical point. These also generate the tangent space as we have seen in the previous section. We update site after site thus the two vectors have the form

$$\vec{w}_1 = \begin{pmatrix} \Delta\phi_1^R + i\Delta\phi_1^I \\ 0 \end{pmatrix} \quad \text{and} \quad \vec{w}_2 = \begin{pmatrix} 0 \\ \Delta\phi_2^R + i\Delta\phi_2^I \end{pmatrix}. \quad (5.53)$$

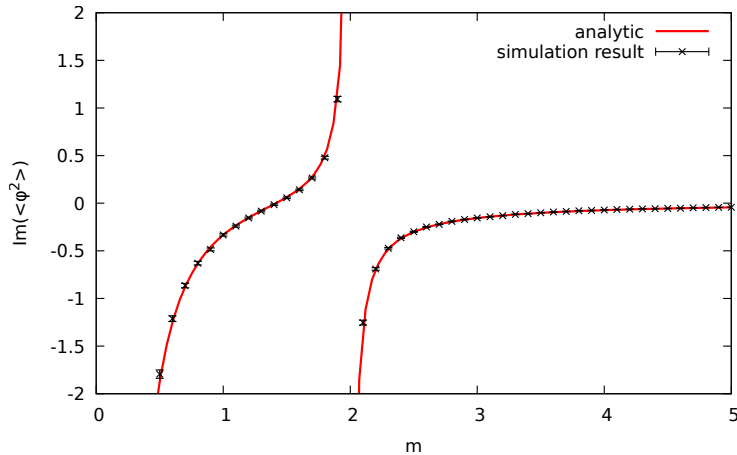


Figure 5.9.: Comparison of numerical results using a Metropolis algorithm for the Takagi parametrization of the thimble with the analytical formula for the expectation value of the squared field (5.52). Note that for  $m = 2$  the partition function is undefined leading to the critical point becoming degenerate.

They have to be a linear combination of the Takagi vectors

$$\vec{w}_k = r_k \vec{z}_1 + s_k \vec{z}_2 \quad \text{with } r_k, s_k \in \mathbb{R}, k = 1, 2 \quad (5.54)$$

where the coefficients are real. For  $m > 2$  the coefficients  $c_1, c_2$  are equal and the associated system of equations can be easily solved yielding  $r_1 = s_1$  and  $r_2 = -s_2$ . If  $m < 2$  the coefficients  $c_1, c_2$  are not equal which leads to a system of equation where the only solution is given by  $r = 0 = s$ . We conclude that the local thimble algorithm is only applicable for  $m > 2$ .

### 5.3. Summary

In this chapter we have put forward local update algorithms for lattice simulations on Lefschetz thimbles in a gauge theory with a hard sign problem. The general strategy is to first sample on a single thimble or a suitable manifold with a sufficiently large average phase. The next step which is still work in progress is to extend the sampling to sub-leading thimbles and apply the reweighting procedure introduced in the precedent chapter.

We have attempted to sample the main thimble in  $U(1)$  lattice gauge theory by means of enforcing the constraint  $\text{Im}(S) = \text{const.}$  locally. For this theory comparisons with analytical results are only possible in the thermodynamic limit. We have found that setting up the local thimble algorithm comes with difficulties. The first price to pay is that the candidate proposal for a link becomes intricate to choose because the range where the formula (5.31) for the  $|\Delta U_k|$  is well-defined non-trivially determines the range of possible  $\Delta \phi_k^R$ . The second concerns the numerical cost when determining the determinant of the dense Jacobi matrix corresponding to the parametrization in terms of the variables  $\phi_k^R$ . Moreover, an explanation for the failure of the local thimble algorithm in the  $U(1)$  lattice gauge theory is given by the fact that when sampling the surface with  $\text{Im}(S) = \text{const.}$  the

configurations can hop from the stationary manifold or the thimble to parts of the surface where the real part of the action is unbounded from below causing numerical instabilities.

A promising algorithm we have shown is the tangent space method. It comes with the advantage that the Jacobian is trivial. The inclusion of the sub-leading thimbles can be performed by considering the configurations of an even number of flipped plaquettes. Those are highly degenerated as we have derived in the beginning of this chapter. This has to be considered when applying reweighting with respect to the main thimble.

## 6. Real-time properties at finite temperature

In this chapter we propose novel simulation strategies for thermal field theories on the lattice. The aim is to optimize spectral reconstructions from Euclidean time correlator data which is generally subject to intense research motivated by extracting thermal features in the spectra such as transport properties. The original idea behind the research presented here is based on the approach proposed in [60]. This chapter contains results from joint research with my collaborators on applying the original proposal to gauge theories at finite temperature. In addition modifications and viability tests of the method are presented. A large part of the technical work regarding derivations and numerical simulations has been carried out in collaboration with a Master's student [183].

The methods considered here are aimed at providing an exponential enhancement in the thermal information content present in the correlator measured on a new non-compact time path compared to a standard imaginary time correlator in conventional lattice simulations. The chapter is organized as follows. After discussing the main problem with the spectral reconstruction of thermal properties in Sec. 6.1 we review the original idea behind the novel simulation strategy in Sec. 6.2. This is followed by presenting the main results from applying the original formulation to finite temperature gauge theory. We have found that the method needs to be modified to provide for sufficient thermal information in the correlator data. To that end we give a formal derivation. In Section 6.3 we complete this by studying the spectral representation of correlation functions on the non-compact time path. Moreover, in Section 6.6 we analyze the thermal information content based on simulation data. We find evidence that the reformulation does not yield a thermal information content extending that of the conventional Matsubara correlator.

### 6.1. The analytic continuation problem

Extracting dynamical properties such as transport coefficients in a strongly correlated quantum system is a challenging task. Regarding QCD a prominent example is the shear viscosity  $\eta$  of the quark-gluon plasma as introduced in Section 2.2.2. In order to determine  $\eta$  according to (2.16) knowledge on the infra-red part of the spectral function is required. The latter corresponds to the energy-momentum tensor correlation function. We recall the relation between the finite temperature correlator in imaginary time and the spectral function

$$G_\beta(\tau) = \int_0^\infty d\mu \frac{\cosh(\mu(\tau - \beta/2))}{\sinh(\beta\mu/2)} \rho(\mu). \quad (6.1)$$

Unfolding the spectral function and its encoded thermal features comes at a price which is two-fold

1. (6.1) represents an ill-conditioned inverse problem.
2. The thermal information in the data  $G_\beta(\tau)$  suffers from an exponentially decaying signal-to-noise ratio.

The first issue has been explained in Section 2.6. We now argue that the second problem is the main difficulty. For over a decade it has provided a formidable challenge of determining a robust estimate for the shear viscosity over entropy ratio as a function of the temperature from first principle calculations, see [50, 72, 74]. The second issue concerns the exponential suppression of thermal information in the large time tail of the correlator. With this comes an exponentially decaying signal-to-noise ratio. To examine this further we consider frequency space where the inverse problem is formulated in terms of the Källén-Lehmann spectral representation

$$G(\omega_n) = \int_0^\infty d\mu \frac{2\mu}{\mu^2 + \omega_n^2} \rho(\mu). \quad (6.2)$$

The exponentially decaying signal-to-noise ratio manifests itself in the Matsubara correlator such that thermal information is effectively present in the first two Matsubara modes, i.e. up to  $\omega_1 = 2\pi T$ . For higher Matsubara frequencies the exponential suppression is already that large that the thermal correlator is indistinguishable from the vacuum correlator within the error. This renders the numerical unfolding problem exponentially hard. Simply making the lattice larger and finer will not remedy the suppression of thermal information. This only adds more Matsubara frequencies enlarging the ultra-violet range which is uninteresting for thermal properties. For computing  $\eta$  the physically relevant regime in  $G_\beta(\omega)$  is  $\omega \lesssim T$ . Therefore, a possible resolution to the second problem lies in an exponential enhancement of thermal information. The motivation behind the work presented here is to achieve this by generating correlator data at general frequencies "in between" the Matsubara modes. This has originally been proposed in [60] which will be reviewed briefly in Sec. 6.2.1.

## 6.2. Correlators at general frequencies

In this section we review the original formulation of the novel sampling strategy for thermal fields at general frequencies based on [60]. Moreover we present a few results of extending the method to finite temperature gauge theory. This is followed by identifying a key problem with the original use of the method. We argue for the need of a reformulation.

### 6.2.1. Original proposal

The strategy proposed in [60] starts with considering the thermal field theory formulated on the Schwinger-Keldysh contour (2.12), see also Figure 2.1. It is argued that at any finite time  $t$  the field on the forward branch  $\phi^+$  has no knowledge on the field on the backward branch  $\phi^-$  to which it is connected at infinite real time because all correlations become suppressed as  $t \rightarrow \infty$ . This allows to cut open the contour at infinite real time followed by analytic continuation of the forward branch to a non-compact imaginary time  $\tau$  in addition to the standard compact imaginary time interval  $[0, \beta]$ . The setup is illustrated in Fig. 6.1. To describe equilibrium physics taking into account correlations on the forward branch is completely sufficient. Therefore, the backward branch is discarded. The remaining compact and non-compact imaginary time paths are connected at  $\tau = 0$ . The paths are then discretized on time lattices respectively. The simulation setup is straightforward. On the compact imaginary time path the fields  $\phi_E$  are sampled via a standard simulation, indicated by the subscript E. Setting  $\phi_E(0) = \phi^+(0)$  carries the thermal initial conditions to the non-compact path representing quantum dynamics, compare (2.12). For

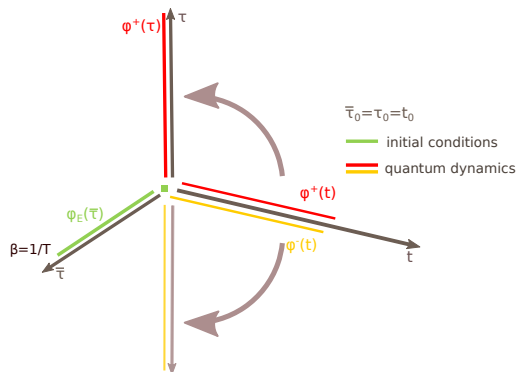


Figure 6.1.: Schematic illustration of the novel simulation strategy on the non-compact time path as originally formulated in [60]. As correlations at infinite real-time become suppressed, the contour can be cut open at  $t = \infty$  and the forward (red) and backward (yellow) real-time paths are analytically continued to non-compact imaginary time. The backward path is furthermore discarded because in thermal equilibrium correlation functions on the forward path already contain all physical information. The analytically continued forward path and the standard compact imaginary time piece (green) are connected at  $t_0$  which is chosen to be set to zero, see also the main text. Since the forward path extends to infinity it gives rise to continuous frequencies which are proposed to enhance the thermal information content needed for ameliorating the inverse problem (6.2).

$\tau > 0$  Monte Carlo sampling on the non-compact time path is performed with respect to  $e^{-S_E}$  where the action contains the initial condition. Increasing the number of lattice points on the non-compact path gives rise to an arbitrarily resolution in frequency space. The method has been applied to a quantum-mechanical anharmonic oscillator at zero temperature. The correlator at general frequencies interpolates the Matsubara frequencies for  $\omega > \omega_1$ . However, in the relevant small frequency regime  $[\omega_0, \omega_1]$  the general frequency result significantly deviates from the Matsubara correlator. The method has however correctly produced the vacuum spectral functions. So far the novel method has not alleviated the extraction of finite temperature features. This is subject to the discussion in the remainder of the chapter. The subsequent two sections summarize the results from the authors joint work with his collaborators. There are two underlying points of focus:

1. Extending the method to gauge theories with the aim to compute transport properties.
2. Probing the capability of the described proposal to enhance the thermal information content in the correlator measured on the non-compact time path.

### 6.2.2. Application to non-abelian gauge theory

The simulation method reviewed in the previous section is now extended to  $SU(2)$  gauge theory. The action of the theory is the Wilson action given in (2.18). We focus on the

deconfined phase where thermal effects should come into play.

The numerical setup is as follows. A standard simulation using heat-bath updates on the compact Euclidean time lattice produces gauge link configurations serving as thermal initial conditions for the non-compact time lattice. At  $\tau = 0$  the latter is initialized with the spatial and temporal links of the zero time-slice from the compact time lattice. The remaining links can be set to one. Next, heat-bath updates on the non-compact time lattice at  $\tau > 0$  are performed with the links at  $\tau = 0$  held fixed. After thermalization of the non-compact time lattice followed by a desired number of measurements the initial condition is replaced with a new link configuration from the Markov chain on the compact time lattice. This is followed again by updating and measurements on the non-compact time lattice. These steps are repeated for a desired number of initial conditions. In the end, the average over all measurements is calculated. For the observables shown below we have taken  $O(10^6)$  measurements on the non-compact path in total. A straightforward benchmark of the method is to compare the plaquette expectation value on the compact and the non-compact time lattice. This is shown in Figure 6.2 as a function of the non-compact imaginary time extent  $N_\tau$ . The inverse gauge coupling is set to  $\beta = 2.8$ . The spatial lattice size is  $8^3$  and the compact time lattice has 8 sites. The red line corresponds to the standard Matsubara (compact imaginary time) result. Blue points indicate the results obtained on the non-compact time lattice. We find that as  $N_\tau$  is increased the results converge. However, a statement on the thermal information is not possible here because the plaquette knows only about the physics at scales of the lattice spacing or the UV-cutoff respectively. The latter is dominated by the vacuum with thermal effects being effectively zero.

Instead to compare if thermal physics is sufficiently encoded in the configurations simulated on the non-compact time lattice requires the analysis of Wilson loops of the size of the lattice. In the work behind this thesis we have carried out an extensive study on Wilson loops. However, this observable has not shown sufficient imprints of thermal physics. The reasons are explained in the main text. With the modified approach introduced in Section 6.2.4 we have also analyzed Wilson loops. We have found no enhancement in the thermal information in the data compared to the standard Matsubara result. From the point of view of the analysis in Section 6.6 this is plausible. Note that for Wilson loops with large temporal extent the observable suffers again from an exponentially decaying signal-to-noise ratio hiding thermal properties at large Euclidean times.

Next, we investigate the energy-momentum tensor correlation function. The elements of the energy-momentum tensor are determined according to the clover discretization [79]. We measure the time-slices for the off-diagonal component  $T_{12}(\tau, \vec{p} = 0)$ , i.e. the zero spatial momentum component. This is analogous to the definition of the time-slices in Appendix A.2. We then calculate the correlator of time-slices. Under the assumption that time translation invariance holds on the non-compact path we can use it to boost our statistics. The energy-momentum tensor correlator is computed at inverse gauge coupling  $\beta = 3$  on a compact time lattice of size  $4^3 \times 8$  and on non-compact time lattices of sizes  $4^3 \times N_\tau$  with varying  $N_\tau$ . The parameters have been chosen to allow for comparisons with the results of [150] where a temperature of  $T \simeq 1.2T_c$  was used. In the setup at hand we need to take into account the substantial finite size effect associated with the small spatial

lattice size. Using the results of [184, 185] we roughly estimate our resulting temperature to  $T \simeq 1.5T_c$ . Numerical results are shown in Figure 6.3. On the left-hand side the result as a function of the general imaginary frequencies is shown. For increasing  $N_\tau$  the general frequency correlator appears to converge to the Matsubara correlator indicated by the black triangles. On the right-hand side the energy-momentum tensor correlator as a function of imaginary time is displayed. The vertical axis is scaled logarithmically. The correlator suffers from a quickly decaying signal-to-noise ratio. We have measured  $O(10^6)$  configurations. Data being statistically distinct from the noise is given up to a distance of three lattice spacings. Physical information on the system which is not hidden in the noise is present only in the ultra-violet regime of the correlator which effectively contains no thermal information due to exponential suppression. As a remark, the frequency correlator on the left shows tiny modulations which are not visible in the figure. The latter represent a remnant of the noisy tail of the correlator in imaginary time after taking the Fourier transformation. The small time behaviour which is exponentially larger than the large time tail is entirely responsible for the shape of the frequency correlator.

Moreover we have attempted to reconstruct the spectral functions by means of the BR method discussed in Section 2.6 from the data for the energy-momentum tensor. While the asymptotic  $\omega^4$  behaviour in the ultra-violet has been captured well in the reconstructed spectral function the data has not allowed to produce a statistically significant result for a transport peak at  $\omega = 0$  to reliably extract an estimate for the shear viscosity  $\eta^1$ . An aggravating effect is that the UV-behaviour of the spectral function dominates the inverse problem (6.2) by more than 90 per cent [74, 144].

In conclusion, the simulated data obtained here shows no sign of thermal information. To optimize the statistics in the correlator use of the multi-level algorithm should be made [74, 186–188]. In addition to the spectral reconstruction via the BR method we have also tried Padé fits to the data, see also related works in [140, 189]. The Padé approximant allows for a direct analytic continuation of the imaginary frequency correlator. It is however prone to noise in the data. Hence, from the data shown in Fig. 6.3 reliable results using the Padé approximation have not been possible.

### 6.2.3. Need for a reformulation

The data obtained from applying the original proposal for correlators at general frequencies has not shown an enhancement of thermal information so far. The root of the problem is the assumption of time translation invariance on the non-compact time path. We have used it to enhance the statistics of the correlator. However, this effectively corresponds to measuring the correlator on a compact time lattice where the thermal initial condition represents the boundary condition. In a time-translation invariant setup the physics should not depend on the boundary condition of the fields. Consequently, as the time extent  $N_\tau$  is increased we approach the zero temperature limit on the non-compact time lattice. In other words by assuming time-translation invariance, any thermal information is averaged out on the non-compact time path when computing correlation functions. We conclude that this requires a reformulation of the approach which is presented in the next subsection.

<sup>1</sup>This is also indicated by the large time behaviour of the energy-momentum correlator in Figure 6.3 (right) where noise hides infra-red information.

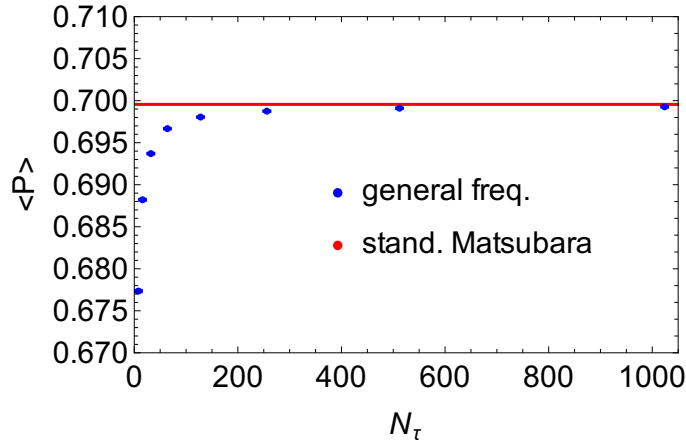


Figure 6.2.: Numerical results for the plaquette expectation value in the deconfined phase ( $\beta = 2.8$ ) calculated on the non-compact imaginary time path corresponding to an  $8^3 \times N_\tau$  lattice (blue points) in comparison to the result from the standard simulation on the compact time domain on an  $8^3 \times 8$  lattice (red line). For large non-compact imaginary time extents the results converge. Note that the plaquette contains only information on the physics at ultra-violet momentum scales of  $O(1/a)$ . Hence, the data shown represents vacuum physics.

#### 6.2.4. The double path-integral

In order to resolve the issue with the absence of thermal physics in the results presented above we need to discard time-translation invariance on the non-compact path. This section deploys a reformulation of the problem which guarantees the imprint of temperature effects in the correlation functions. To that end we start over from the Schwinger-Keldysh contour and perform the analytic continuation of the initial value problem step-by-step. The viability of the reformulation regarding enhanced thermal information compared to a standard imaginary time setup is compared in section 6.6. Note that in this section  $\beta$  refers to the inverse temperature.

#### Derivation

First we go back to the Schwinger-Keldysh contour, see Figure 2.1 where the partition function is given by (2.12). As explained in Section 6.2 for the full physical information in thermal equilibrium it suffices to consider correlation on the forward branch of the contour. Let  $0 \leq t_1 < t_2 < t_{\max}$  and we omit the spatial dependence of the fields in our

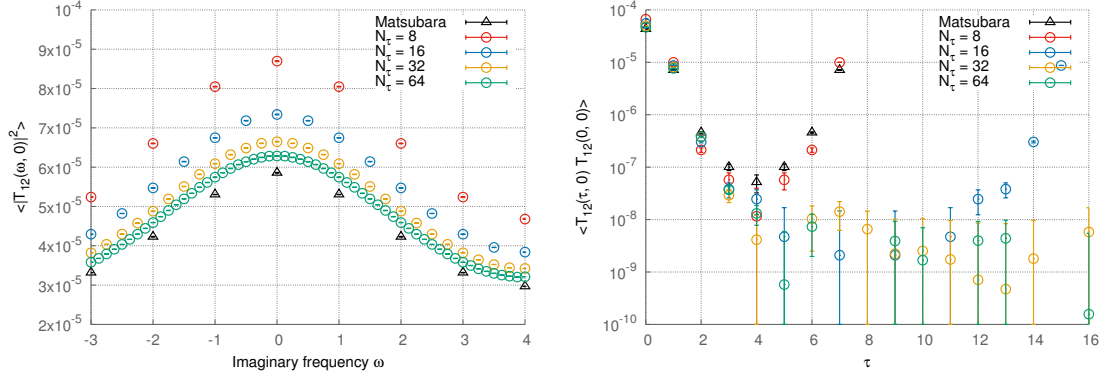


Figure 6.3.: Correlation function of the spatial off-diagonal elements of the energy-momentum tensor for different non-compact time extents  $N_\tau$ . The black triangles denote the standard Matsubara correlator. We simulate the deconfined phase with the bare inverse gauge coupling set to  $\beta = 3$  similarly as studied in [150]. Left: Correlator data as a function of the general frequency  $\omega$ . We find that the data converges to the Matsubara result as the extent of the non-compact imaginary time lattice increases. Right: The same data as on the left-hand side represented as a function of the imaginary time  $\tau$ . Note the logarithmic scale. The energy-momentum tensor correlator suffers from a quickly decaying signal-to-noise ratio. With the data shown here we have attempted to reconstruct the spectral function. However, from the data it has not been possible to reliably extract transport coefficients. This is plausible since the thermal information is exponentially suppressed in the noisy large time regime of the correlator. This is also discussed in the main text. The compact imaginary time correlator is symmetric around  $\beta/2$  obeying the periodicity introduced in Section 2.1.1. Moreover, here we have used periodic boundary conditions on the non-compact time path together with time translation invariance leading to an analogous behaviour.

notation in the following. The two-time correlator reads

$$\begin{aligned}
G^{++}(t_2, t_1) &:= \langle \hat{\phi}(t_2) \hat{\phi}(t_1) \rangle = \frac{1}{Z} \text{Tr} \left( e^{-\beta \hat{H}} \hat{\phi}(t_2) \hat{\phi}(t_1) \right) \\
&= \frac{1}{Z} \int [d\phi_{t_{\max}}] [d\phi_0^+] [d\phi_0^-] \langle \phi_0^+ | e^{-\beta \hat{H}} | \phi_0^- \rangle \langle \phi_0^- | \phi_{t_{\max}} \rangle \langle \phi_{t_{\max}} | \hat{\phi}(t_2) \hat{\phi}(t_1) | \phi_0^+ \rangle \\
&= \frac{1}{Z} \int [d\phi_{t_{\max}}] [d\phi_0^+] [d\phi_0^-] \int_{\phi_E(0)=\phi_0^-}^{\phi_E(\beta)=\phi_0^+} \tilde{\mathcal{D}}\phi_E e^{-S_E[\phi_E]} \times \\
&\quad \int_{\phi^+(t=0)=\phi_0^+}^{\phi^+(t=t_{\max})=\phi_{t_{\max}}} \tilde{\mathcal{D}}\phi^+ \phi^+(t_2) \phi^+(t_1) e^{iS_M[\phi^+]} \times \\
&\quad \int_{\phi^-(t=t_{\max})=\phi_{t_{\max}}}^{\phi^-(t=0)=\phi_0^-} \tilde{\mathcal{D}}\phi^- e^{-iS_M[\phi^-]}. \tag{6.3}
\end{aligned}$$

From this we derive the corresponding correlation function on an infinite time path in imaginary time on which the thermal fields from the standard compact imaginary time path enter as an initial condition. The hope is that the correlation function measured on the infinite path then contains exponentially more information than present on the standard compact imaginary time correlator. Starting from the partition function (2.12) we define the so-called weight function

$$W_-[\phi_0^+, \phi_{t_{\max}}] := \int [d\phi_0^-] \int_{\phi_E(0)=\phi_0^-}^{\phi_E(\beta)=\phi_0^+} \tilde{\mathcal{D}}\phi_E e^{-S_E[\phi_E]} \int_{\phi^-(t=t_{\max})=\phi_{t_{\max}}}^{\phi^-(t=0)=\phi_0^-} \tilde{\mathcal{D}}\phi^- e^{-iS_M[\phi^-]}. \quad (6.4)$$

This contains the full path-integral over the backward path as well as the thermal initial conditions. With this the partition function becomes

$$Z = \int [d\phi_{t_{\max}}] [d\phi_0^+] W_-[\phi_0^+, \phi_{t_{\max}}] \int_{\phi^+(t=0)=\phi_0^+}^{\phi^+(t=t_{\max})=\phi_{t_{\max}}} \tilde{\mathcal{D}}\phi^+ e^{iS_M[\phi^+]}. \quad (6.5)$$

Similarly the two-point correlation function in terms of the weight reads

$$G^{++}(t_2, t_1) = \frac{1}{Z} \int [d\phi_{t_{\max}}] [d\phi_0^+] W_-[\phi_0^+, \phi_{t_{\max}}] \int_{\phi^+(t=0)=\phi_0^+}^{\phi^+(t=t_{\max})=\phi_{t_{\max}}} \tilde{\mathcal{D}}\phi^+ \phi^+(t_2)\phi^+(t_1) e^{iS_M[\phi^+]}. \quad (6.6)$$

In order to found this into a sampling algorithm amenable to conventional lattice simulations we need to analytically continue the real-time path-integral on the forward branch in (6.6) to imaginary time. Let  $t_{\max} \rightarrow \infty$  and  $\tau = it$  denote the imaginary time which in the interval  $[0, \beta]$  describes the standard compact imaginary time physics. In contrast, in the interval  $[\beta, \infty)$  it corresponds to the analytically continued real-time evolution for the field  $\phi^+$  with initial conditions provided by the density matrix  $e^{-\beta\hat{H}}$ . For simplicity we consider correlations between 0 and a point  $\tau \in [0, \infty)$ , i.e. we set  $\tau_1 = 0$  and  $\tau_2 = \tau$ . Thus, we only need to perform the analytic continuation in one time argument. We restrict the following considerations only to the forward branch of the contour. For the field we make the following identifications obeying the periodicity relation

$$\phi(\tau) := \begin{cases} \phi_E(\tau), & 0 \leq \tau \leq \beta \quad \text{where } \phi_E(0) = \phi_E(\beta) = \phi^+(\beta) \\ \phi^+(\tau), & \beta \leq \tau < \infty. \end{cases} \quad (6.7)$$

Let  $G(\tau)$  denote the correlator on the non-compact time path. For a proper analytic continuation we propose the following requirements on the level of the correlation function.

1.  $G(\tau) := \langle \phi(\tau)\phi(0) \rangle = G_\beta(\tau)$  for  $0 \leq \tau \leq \beta$ .
2.  $\beta \leq \tau < \infty$ :  $\lim_{\tau \rightarrow \infty} G(\tau) = 0$ .

Here,  $\langle \cdot \rangle$  refers to taking expectation values on the analytically continued real-time path.  $G_\beta(\tau)$  denotes the correlator on the standard compact path. We will show the full expression for the correlator below. We propose the following ansatz for the weight function for  $\tau \in [0, \infty)$ .

$$W_-^{\text{IT}}[\phi_0, \phi^\infty] = \frac{1}{\nu} \delta(\phi(0) - \phi(\beta)) + \Theta(\tau - \beta) W_+^{\text{IT}}[\phi_0]. \quad (6.8)$$

Here the superscript IT stands for imaginary time and  $\phi_0 = \phi(\tau = 0)$ . The first term determines the correlation function to coincide with the standard compact imaginary time correlator for  $0 \leq \tau \leq \beta$ . Thereby it holds  $G_\beta(0) = G_\beta(\beta)$ . The normalization factor  $\nu$  correspondingly reads

$$\nu = \int_{\phi(\beta)=\phi(0)}^{\phi(\infty)=\phi^\infty} \mathcal{D}\phi e^{-S_E[\phi]}. \quad (6.9)$$

The second term relevant for the physics on the non-compact path  $[\beta, \infty)$  depends on the initial condition at  $\tau = \beta$  via the here introduced weight  $W_+^{\text{IT}}[\phi_0]$ . There is still a freedom left in choosing the weight  $W_+^{\text{IT}}[\phi_0]$  in order to uniquely determine the analytic continuation. For  $\tau > \beta$  the standard analytic continuation would be to realize periodicity in the correlator  $G(\tau) = G(\tau + n\beta)$  with  $n \in \mathbb{N}$  which is the Kubo-Martin-Schwinger (KMS) relation, see also [64]. In other words this means to periodically continue the standard compact imaginary time correlator ad infinitum. In this case the weight reads

$$W_+^{\text{IT}}[\phi_0] = \sum_{n \in \mathbb{N}} \frac{\delta(\phi(n\beta) - \phi((n+1)\beta))}{\int_{\phi(\beta)=\phi(0)} \mathcal{D}\phi e^{-S_E[\phi]}}. \quad (6.10)$$

This however is not providing us with more (thermal) information beyond the conventional Matsubara frequencies. Instead we choose a continuation that dampens the correlation to zero at infinite imaginary time. From a physical point of view this motivation is plausible since at infinity the initial thermal information should decay to zero. Hence, a choice which realizes both requirements is to set the weight  $W_+^{\text{IT}}[\phi_0]$  to zero, i.e.

$$W_+^{\text{IT}}[\phi_0] = 0. \quad (6.11)$$

With this choice for  $W_-^{\text{IT}}$  the two requirements are fulfilled. For  $0 \leq \tau \leq \beta$  we reproduce the compact imaginary time correlator  $G_\beta(\tau)$  with  $G_\beta(0) = G_\beta(\beta)$  and for  $\beta \leq \tau < \infty$  we ensure that the correlation function decays to zero. However, as shown in the previous section this comes at the price of discarding time-translation invariance on the non-compact path although it appears counter-intuitive since we consider thermal equilibrium. Recall that if we assumed time-translation invariance on the piece  $[\beta, \infty)$  regardless of the initial condition going in at  $\phi^+(\beta) = \phi_E(0)$  we would be left with a vacuum simulation.

The formally analytic continuation of the path-integral for the two-point correlator on the forward branch now reads

$$\begin{aligned}
 G^{++}(t, 0) &= \frac{1}{Z} \int [d\phi_{t_{\max}}] [d\phi_0^+] W_-[\phi_0^+, \phi_{t_{\max}}] \int_{\phi^+(t=0)=\phi_0^+}^{\phi^+(t=t_{\max})=\phi_{t_{\max}}} \tilde{\mathcal{D}}\phi^+ \phi^+(t)\phi^+(0) e^{iS_M[\phi^+]} \\
 &\xrightarrow{t \rightarrow -i\tau, \tau_{\max} \rightarrow \infty} \frac{1}{Z} \int [d\phi^\infty] [d\phi_0] W_-^{\text{IT}}[\phi_0, \phi^\infty] \int_{\phi_0=\phi_E(\beta)}^{\phi(\tau=\infty)=\phi^\infty} \tilde{\mathcal{D}}\phi \phi(\tau)\phi(0) e^{-S_E[\phi]} \\
 &= \frac{1}{Z} \int [d\phi^\infty] [d\phi_0] \frac{\delta(\phi(0) - \phi(\beta))}{\int_{\phi(\beta)=\phi(0)}^{\phi(\infty)=\phi^\infty} \mathcal{D}\phi e^{-S_E[\phi]}} \int_{\phi_0=\phi_E(\beta)}^{\phi(\tau=\infty)=\phi^\infty} \tilde{\mathcal{D}}\phi \phi(\tau)\phi(0) e^{-S_E[\phi]} \\
 &= \frac{\int_{\phi_E(0)=\phi_E(\beta)} \mathcal{D}\phi_E e^{-S_E[\phi_E]} \left( \frac{\int_{\phi(0)=\phi_E(\beta)}^{\phi(\infty)=0} \mathcal{D}\phi \phi(\tau)\phi(0) e^{-S_E[\phi]}}{\int_{\phi(0)=\phi_E(\beta)}^{\phi(\infty)=0} \mathcal{D}\phi e^{-S_E[\phi]}} \right)}{\int_{\phi_E(0)=\phi_E(\beta)} \mathcal{D}\phi_E e^{-S_E[\phi_E]}} \\
 &=: \langle \phi(\tau)\phi(0) \rangle. \tag{6.12}
 \end{aligned}$$

We refer to the last expression also as the double path-integral in the following. In the inner path integral the functional integration measure  $\mathcal{D}\phi$  includes an integration over the field at infinity while the integration over the field point at  $\tau = 0$  or equivalently  $\tau = \beta$  is omitted. In the lattice discretization the double path-integral is finite and contains the full thermal information encoded in the partition sum  $Z$  in correlation functions on the forward branch. Note that at a closer look we find that for  $0 \leq \tau \leq \beta$  we can factor out the product  $\phi(\tau)\phi(0)$  from the inner path-integral. The numerator and denominator in the inner path-integral cancel and we are left with the standard compact imaginary time correlator. The derivation shown above can be performed for arbitrary  $n$ -point correlation functions on the forward path. However, the analytic continuation gets more complicated. It is important to note that for the analytically continued two-point correlation function in (6.12) a spectral representation can be formulated which however differs from the usual Källén-Lehmann representation because of the infinitely extended imaginary time path. In Section 6.3 we derive a spectral representation relating the non-compact imaginary time correlator and the physical spectral function. Moreover, the thermal information content on the extended path is assessed in Section 6.6.

### A note on rigor

A rigorous proof that analytic continuation from (6.4) leads to the weight function (6.8) has not been found so far. When performing analytic continuations in the complex time plane one has to be careful not to hit any poles or branch cuts of the function to be continued. In the literature the information about defining an analytic continuation of real times larger than  $\beta$  is very scarce. At this point it has to be checked if the analytic continuation is well-defined. Also we have stated without proof that the correlation functions obtained from the double path integral represent the same thermal physics as in (2.6).

### Practical implications

In lattice simulations the double path-integral (6.12) is implemented as follows. The outer integral samples thermal initial conditions at imaginary times  $0 \leq \tau \leq \beta$  with periodic boundary conditions  $\phi_E(0) = \phi_E(\beta)$  which serve as input for the inner integral. This means we leave the simulation setup described in Section 6.2.1 where we simulated gauge fields unchanged. When we discuss our numerical results from sampling from the double path-integral in Section 6.5 we provide a step-by-step manual for the implementation. An essential difference to the simulation prescription before is that time-translation invariance cannot be used to enhance the statistics of measured correlation function on the non-compact time path. For example for noisy observables such as the energy-momentum tensor correlator this might turn out to be crucial. However, in principle the multi-level algorithm could also be of help here. Its only requirement to work is the locality of the action [186]. The propagation of the thermal initial condition to the non-compact imaginary time path is compatible with this. A direct simulation in imaginary frequencies as originally proposed by [60] is not possible because of the lack of time-translation invariance. This prevents us from simply going to Fourier space. However, it is possible to study the correlation functions by means of a Wigner transformation [183].

### 6.3. Spectral representation

In the following we derive a spectral representation for the two-point correlation function (6.12) based on the double path-integral introduced in the previous section. This is put to work by means of a quantum mechanical harmonic oscillator.

#### Derivation

We consider a simple field theory that is a free theory in  $0 + 1$  dimensions corresponding to the quantum-mechanical harmonic oscillator. Here the position  $x(t)$  plays the role of the field  $\phi(t)$ . Regarding the notation we stay as close as possible to field theory. The classical action in real-time reads

$$S[x] = \int_{t_a}^{t_b} dt \left( \frac{1}{2} (\partial_t x(t))^2 - \frac{m^2}{2} x(t)^2 \right). \quad (6.13)$$

After analytic continuation according to the procedure in Section 6.2.4 the correlation function on the non-compact imaginary time path reads

$$\langle x(\tau)x(0) \rangle = \frac{\int_{x_E(0) \equiv x_E(\beta)} \mathcal{D}x_E \frac{\int_{x(0) \equiv x_E(0)} \mathcal{D}x \frac{x(\tau)x(0) e^{-S_E[x]}}{\int_{x(0) \equiv x_E(0)} \mathcal{D}x e^{-S_E[x]}} e^{-S_E[x_E]}}{\int_{x_E(0) \equiv x_E(\beta)} \mathcal{D}x_E e^{-S_E[x_E]}}. \quad (6.14)$$

We assume the correlator in the extended imaginary time has a spectral representation

$$\langle x(\tau)x(0) \rangle = \int_0^\infty d\mu \rho(\mu, m) f(\mu, \tau, \beta). \quad (6.15)$$

Thereby  $f(\mu, \tau, \beta)$  is an unknown kernel function and  $\rho(\mu)$  is the physical spectral function for the problem at hand. For the harmonic oscillator we know the spectral function

analytically, see for example a standard textbook on thermal field theory such as [64]. This is also the spectral function for a free boson. It reads

$$\rho(\mu, m) = \frac{\pi}{2m} (\delta(\mu - m) - \delta(\mu + m)). \quad (6.16)$$

An explicit calculation of (6.14) can therefore reveal the kernel  $f(\mu, \tau, \beta)$  in the spectral representation – at least for the free theory. We might assume that by universality it should follow that this kernel holds for a large class of interacting theories. This however will turn out to be false for the case when the spectral function contains more than one state due to finite temperature excitations. We will show this numerically by providing an explicit counterexample in Section 6.5.2.

### The inner integral

For the evaluation of the double path integral (6.14) we first treat the inner integral in real-time for a fixed initial condition  $x_E(0)$ . This is facilitated by using the fluctuation expansion applied when evaluating path-integrals. To that end we need to recall a few ingredients from deriving path-integrals for transition amplitudes and correlation functions for the quantum mechanical harmonic oscillator.

We follow the detailed description presented in Kleinert's book on path-integrals [190]. The quantum mechanical transition amplitude from an initial state  $|x_a, t_a\rangle$  to a final state  $|x_b, t_b\rangle$  for a particle in a harmonic potential  $V(x) = \frac{m^2}{2}x^2$  can be expressed in terms of a path integral as follows

$$\langle x_b, t_b | x_a, t_a \rangle = \int_{x(t_a)=x_a}^{x(t_b)=x_b} \mathcal{D}x e^{iS[x]}. \quad (6.17)$$

To evaluate (6.17) we apply the fluctuation expansion. The paths  $x(t)$  are decomposed into a classical trajectory  $x_{\text{cl}}(t)$  and a fluctuating part  $\delta x(t)$ . Importantly, Dirichlet boundary conditions hold, i.e. at the boundaries of the time interval the fluctuations vanish

$$\delta x(t_a) = 0 = \delta x(t_b). \quad (6.18)$$

Because the action  $S$  is quadratic in  $x = x_{\text{cl}} + \delta x$  it can be written as a sum of a classical part and a fluctuating part

$$S = S_{\text{cl}} + S_{\text{fl}}, \quad (6.19)$$

where we have

$$S_{\text{cl}}[x] = \int_{t_a}^{t_b} dt \frac{1}{2} ((\dot{x}_{\text{cl}})^2 - m^2 x_{\text{cl}}^2) \quad (6.20)$$

and

$$S_{\text{fl}}[\delta x] = \int_{t_a}^{t_b} dt \frac{1}{2} [(\delta \dot{x})^2 - m^2 (\delta x)^2] \quad (6.21)$$

with  $\dot{x} \equiv \partial_t x$ . Because the fluctuations  $\delta x(t)$  vanish at the boundary of the interval  $[t_a, t_b]$  and  $x_{\text{cl}}$  fulfills the classical equations of motion mixed terms in  $\delta x(t)$  and  $x_{\text{cl}}$  are absent. The transition amplitude can be written as a product of a classical factor and a fluctuation amplitude  $A_{\text{fl}}$

$$\langle x_b, t_b | x_a, t_a \rangle = e^{iS_{\text{cl}}} \underbrace{\int_{\delta x(t_a)=0}^{\delta x(t_b)=0} \mathcal{D}(\delta x) e^{iS_{\text{fl}}[\delta x]}}_{=: A_{\text{fl}}(t_b - t_a)}. \quad (6.22)$$

The classical trajectory from initial time  $t_a$  to final time  $t_b$  reads

$$x_{\text{cl}}(t) = \frac{x_b \sin(\omega(t - t_a)) + x_a \sin(\omega(t_b - t))}{\sin(\omega(t_b - t_a))}. \quad (6.23)$$

The classical action is determined by integrating the Lagrangian and thereby using the equations of motion. The fluctuation factor is calculated by discretizing the interval  $[t_a, t_b]$  on a lattice and evaluating the appearing Gaussian integral using the Fourier decomposition. For details and the results see [190]. The next quantity we need to recall is the correlator of the fluctuating fields

$$\langle \delta x(t_2) \delta x(t_1) \rangle = i G_{\text{HO}}(t_2, t_1) \quad (6.24)$$

where

$$G_{\text{HO}}(t, t') = (-\partial_t^2 - m^2)^{-1} \delta(t - t'), \quad t, t' \in (t_a, t_b). \quad (6.25)$$

$G_{\text{HO}}$  is just the Green's function for the classical harmonic oscillator. Importantly, it has to obey the Dirichlet boundary conditions same as the fluctuating field  $\delta x(t)$  at  $t_a$  and  $t_b$ .

With these ingredients at hand we go back to the inner path-integral in (6.14). To that end we write down the expression for the two point correlator for the harmonic oscillator in real-time. We are only interested in the following time ordering  $t_b > t_2 > t_1 > t_a$ . By using the above listed knowledge on transition matrix elements we can compute the correlator by means of the fluctuation expansion. In the end we Wick rotate the expression back to imaginary time and evaluate the result for the thermal initial condition condition  $x_E$ . First, we consider the real-time transition matrix element for the inner path-integral

$$\begin{aligned} \frac{\langle x_b, t_b | \hat{x}(t_2) \hat{x}(t_1) | x_a, t_a \rangle}{\langle x_b, t_b | x_a, t_a \rangle} &= \frac{\int_{x(t_a)=x_a}^{x(t_b)=x_b} \mathcal{D}x \, x(t_2) x(t_1) e^{iS[x]}}{\int_{x(t_a)=x_a}^{x(t_b)=x_b} \mathcal{D}x \, e^{iS[x]}} \\ &= \frac{\int_{x(t_a)=x_a}^{x(t_b)=x_b} \mathcal{D}x \, (x_{\text{cl}}(t_2) + \delta x(t_2)) (x_{\text{cl}}(t_1) + \delta x(t_1)) e^{iS[x]}}{\int_{x(t_a)=x_a}^{x(t_b)=x_b} \mathcal{D}x \, e^{iS[x]}} \\ &= \frac{x_{\text{cl}}(t_1) x_{\text{cl}}(t_2) e^{iS_{\text{cl}}} A_{\text{fl}}(t_b - t_a)}{e^{iS_{\text{cl}}} A_{\text{fl}}(t_b - t_a)} + x_{\text{cl}}(t_2) \langle \delta x(t_1) \rangle + \langle \delta x(t_2) \rangle x_{\text{cl}}(t_1) \\ &+ \frac{e^{iS_{\text{cl}}} \int \mathcal{D}(\delta x) \, \delta x(t_2) \delta x(t_1) e^{iS_{\text{fl}}[\delta x]}}{e^{iS_{\text{cl}}} \int \mathcal{D}(\delta x) e^{iS_{\text{fl}}[\delta x]}} \\ &= x_{\text{cl}}(t_1) x_{\text{cl}}(t_2) + i G_{\text{HO}}(t_2, t_1). \end{aligned} \quad (6.26)$$

In the step from the third to the last equation we used

$$\langle \delta x(t) \rangle = \frac{\int \mathcal{D}(\delta x) \, \delta x(t) e^{iS_{\text{fl}}[\delta x]}}{\int \mathcal{D}(\delta x) e^{iS_{\text{fl}}[\delta x]}} = 0. \quad (6.27)$$

which is obvious by looking at the action (6.21) being quadratic in  $\delta x$ . In the last line, the two-point correlation functions for the fluctuations  $G_{\text{HO}}(t_2, t_1)$  (6.24) appears. At this

stage it is important to notice that the fluctuation term depends on the initial and the final time  $t_a$  and  $t_b$ . For the evaluation of the inner path-integral of (6.14) we need to take the limit of  $t_a \rightarrow -\infty$  and  $t_b \rightarrow +\infty$ . Recall that in the end we wish to measure correlations on an infinitely extended imaginary time path. The last missing ingredient is the Green's function  $G_{\text{HO}}$  for  $[t_a, t_b]$  extended to infinite size. As shown in [190] the two-point functions of the fluctuations for an infinite (real) time interval is given by

$$G_{\text{HO}}(t, t') = \frac{-i}{2m} e^{-im|t-t'|}. \quad (6.28)$$

The fluctuation part loses all information on the times  $t_a$  and  $t_b$  (or  $\tau_a$  and  $\tau_b$  respectively) as the time interval is extended to infinity. Obviously, the classical part carries the information about the initial condition at  $t_a$ . In the next step we analytically continue the result (6.26) to imaginary time  $t \rightarrow -i\tau$  and set  $x_a = x_E, x_B = 0, \tau_a = 0 = \tau_1, \tau_2 = \tau$ . Note that the boundary condition at the maximum time extent of the non-compact path is set to zero. We start with the classical part based on (6.23). It holds

$$\begin{aligned} x_{\text{cl}}(\tau) x_{\text{cl}}(0) &= x_E^2 \frac{\sinh(m(\tau_b - \tau)) \sinh(m\tau_b)}{\sinh^2(m\tau_b)} \\ &= x_E^2 \frac{e^{m(\tau_b - \tau)} - e^{-m(\tau_b - \tau)}}{e^{m\tau_b} - e^{-m\tau_b}} \xrightarrow{\tau_b \rightarrow \infty} x_E^2 e^{-m\tau}. \end{aligned} \quad (6.29)$$

Now, we consider the fluctuation part. If we analytically continue the two-point function we get

$$G_{\text{HO}}(\tau, 0) = \frac{-i}{2m} e^{-m\tau}. \quad (6.30)$$

This yields for the analytically continued inner path integral

$$\langle x(\tau)x(0) \rangle_{x_E} = \theta(\tau) \left( \underbrace{x_E^2 e^{-m\tau}}_{\text{thermal fluct.}} + \underbrace{\frac{1}{2m} e^{-m\tau}}_{\text{vacuum quantum fluct.}} \right). \quad (6.31)$$

### Kernel version 1

The outer path integral is now easily evaluated using the well-known result for the two-point function in the imaginary time formalism [64]. Hence, it holds

$$\langle x(\tau)x(0) \rangle = \theta(\tau) \frac{1}{2m} \left( \coth\left(\frac{\beta m}{2}\right) + 1 \right) e^{-m\tau} \stackrel{!}{=} \int_0^\infty d\mu \rho(\mu) f(\mu, \tau, \beta). \quad (6.32)$$

With (6.16) the kernel reads

$$f(\mu, \tau, \beta) = \frac{1}{\pi} \theta(\tau) \left( \coth\left(\frac{\beta \mu}{2}\right) + 1 \right) e^{-\mu\tau}. \quad (6.33)$$

Using  $\coth(x) + 1 = e^x / \sinh(x)$  this can be brought into the form

$$f(\mu, \tau, \beta) = \frac{1}{\pi} \theta(\tau) \frac{e^{(\beta/2 - \tau)\mu}}{\sinh(\frac{\beta \mu}{2})}. \quad (6.34)$$

In (6.31) the first term in the round brackets representing the classical trajectory depends on the thermal initial condition thus carrying thermal fluctuations from the outer path-integral. The second term has been labeled "vacuum quantum fluctuations" because there is no dependence on the thermal initial conditions.

### Kernel version 2

With the above noticed splitting of quantum and thermal fluctuations in mind the correlator of the quantum fluctuations  $G_{\text{HO}}(\tau, 0)$  can be expressed in terms of its Källén-Lehmann spectral representation and the zero temperature spectral function. The equation for the double path integral then reads

$$\begin{aligned} \langle x(\tau)x(0) \rangle &= \theta(\tau) \frac{1}{2m} \coth\left(\frac{\beta m}{2}\right) e^{-m\tau} + \int_0^\infty d\mu \rho_{\text{vac}}(\mu) \frac{\cosh((\tilde{\beta}/2 - \tau)\mu)}{\sinh(\frac{\tilde{\beta}\mu}{2})} \\ &\stackrel{!}{=} \int_0^\infty d\mu \rho_\beta(\mu) \tilde{f}(\mu, \tau, \beta) + \int_0^\infty d\mu \rho_{\text{vac}}(\mu) \frac{\cosh((\tilde{\beta}/2 - \tau)\mu)}{\sinh(\frac{\tilde{\beta}\mu}{2})} \end{aligned} \quad (6.35)$$

$$\underbrace{\rightarrow}_{\tilde{\beta} \rightarrow \infty} \int_0^\infty d\mu \rho_\beta(\mu) \tilde{f}(\mu, \tau, \beta) + \int_0^\infty d\mu \rho_{\text{vac}}(\mu) e^{-\mu\tau}. \quad (6.36)$$

Here we have defined  $\tilde{\beta}$  to be the time on the non-compact imaginary time path.  $\rho_{\text{vac}}(\mu)$  is the vacuum spectral function (6.16) and  $\rho_\beta(\mu)$  denotes the finite temperature piece of the spectral function. In a free theory moreover temperature does not play a role so if we set  $\rho_{\text{vac}}(\mu) = \rho_\beta(\mu)$  we have

$$f(\mu, \tau, \beta) = \tilde{f}(\mu, \tau, \beta) + \frac{\theta(\tau)}{\pi} e^{-\mu\tau}. \quad (6.37)$$

with  $f(\mu, \tau, \beta)$  given in (6.33).

### Concluding remark

For the sake of simplicity we consider the first version of the kernel (6.34) for further numerical studies in the next sections. In contrast to the standard quantum field theoretical derivation of the Källén-Lehmann representation in a fully interacting theory here we started with the non-interacting case. Note that we have made the assumption that the kernel has the same form also for interacting theories at finite temperature. However, below we show in an explicit example that convoluting the kernel (6.34) with an exactly known spectral function of an interacting theory at finite temperature does not reproduce the simulation data from the double path-integral. The conclusion is that the derivation of the kernel needs to be performed for each theory or class of theory separately. The universal form of the kernel similarly as for the Källén-Lehmann kernel is not available here. However, a non-perturbative derivation of the kernel for a strongly interacting theory at finite temperature might be a tedious task. Due to the lack of analytical methods a numerical determination of the kernel would be the only option. For example for an interacting scalar theory in  $0+1$  dimensions this might be realized by solving the inverse problem (6.2) for an unknown kernel function with the physical spectral function and the

double path-integral correlator data given as input. However, this leads to an ill-posed problem. The latter can be tackled using Bayesian methods. Thereby an ansatz for the kernel assuming it involves an exponential decay similarly as in (6.34) reads

$$f(\mu, \tau, \beta) = c(\beta, \mu)e^{-\mu\tau}. \quad (6.38)$$

Thereby, the function  $c(\beta, \mu)$  must be determined. In this work we have not further pursued this idea.

## 6.4. Numerical setup

We shortly describe the numerical lattice simulations we have carried out sampling fields from the double path integral (6.12). The method is applied to a quantum-mechanical anharmonic oscillator which has also been investigated in [60, 134, 191]. Our reference results are obtained by diagonalizing the Hamiltonian in the energy eigenbasis. From this we obtain the time evolution giving access to the correlation function and the spectral function. This is shown in detail in Appendix C.1. The lattice action used for sampling on the standard compact time path as well as on the non-compact time path reads

$$S_E = \sum_{j=0}^{N-1} a \left( -\frac{1}{2a^2} y_j (y_{j+1} + y_{j-1} - 2y_j) + \frac{1}{2} m^2 y_j^2 + \frac{\lambda}{24} y_j^4 \right), \quad (6.39)$$

where  $N = N_\beta, N_\tau$  and  $y = x_E, x$ . Note that as usual we have periodic boundary conditions on the standard compact imaginary time path, i.e.  $x_{E, N_\beta} = x_{E, 0}$ . On the non-compact imaginary time-path the setup is  $x_0 = x_{E, 0}$  and  $x_{N_\tau} = 0$ . The simulation recipe is as follows.

1. Initialize the simulation corresponding to the outer path-integral in (6.12) which is performed in standard compact imaginary time. Usually we choose a cold start  $x_j = 0 \forall j = 0, \dots, N_\beta - 1$ .
2. Let the simulation thermalize until equilibrium is reached.
3. Choose an initial condition  $x_{E, 0}$ .
  - a) Initialize the simulation on the non-compact path via a cold start.
  - b) Let the lattice thermalize until equilibrium is reached. Do further updates thereby measuring the observables of interest.
4. Perform updates on the compact path until a new decorrelated configuration is reached.
5. Repeat 3. and 4. a sufficient number of times for a good statistics.

## 6.5. Probing the kernel

Here, the kernel (6.34) corresponding to the spectral representation of a free theory on the non-compact time path is applied to interacting theories at vanishing and finite temperature. Before any attempt on reconstructions applied to an arbitrary quantum field theory

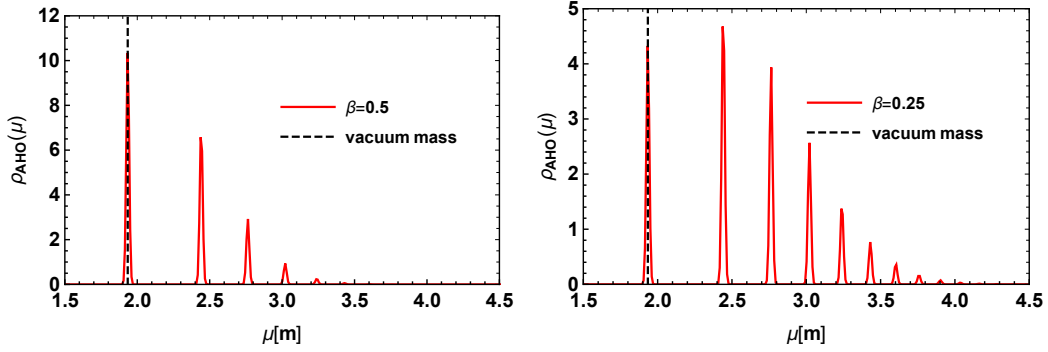


Figure 6.4.: Spectral functions computed from the Hamiltonian formulation for  $\beta = 0.5$  (left) and  $\beta = 0.25$  (right). The parameters are set to  $m = 1$ ,  $\lambda = 24$ . For illustrative reasons only the delta peaks have been replaced by peaks with a finite. Note that with increasing temperature the first excited mass state becomes more important than the ground state.

should be made it is important to verify if the correlators resulting from the convolution of the kernel with the physical spectral function match the simulation data. This is checked both for the vacuum as well as the finite temperature case. As mentioned in the previous section our testbed is a quantum-mechanical anharmonic oscillator whose Hamiltonian reads

$$\hat{H} = \hat{p}^2 + \frac{m^2}{2} \hat{x}^2 + \frac{\lambda}{24} \hat{x}^4. \quad (6.40)$$

Let  $\{|\phi_n\rangle\}$  and  $E_n$  denote the corresponding eigenstates and energy eigenvalues. The full temperature dependent result for the spectral function reads

$$\rho_{\text{AHO}}(\mu) = \frac{\pi}{Z} \sum_{n,l} e^{-\beta E_n} |\langle \phi_l | \hat{x} | \phi_n \rangle|^2 \left[ \delta(\mu - (E_l - E_n)) - \delta(\mu + E_l - E_n) \right]. \quad (6.41)$$

The detailed derivation of the latter expression using numerical diagonalization is presented in Appendix C.1. The expression (6.41) serves as a cross-check for the lattice results. The only error source thereby is a truncation in the space of energy eigenstates to be made which has negligible effects for the considerations throughout this work. The physical spectral function for this system is a sum of delta functions where the peak positions correspond to the excitation energies between the energy levels. In Figure 6.4 we show two spectral functions for  $\beta = 0.5$  (left) and  $\beta = 0.25$  (right) obtained by numerical diagonalization of the Hamiltonian. The parameters are set to  $m = 1$ ,  $\lambda = 24$ . For illustrative reasons we have replaced the delta peaks by peaks with a finite width. The convolution of the kernel (6.34) with the spectral function (6.41) now is of the form

$$g(\tau, \vec{c}, \vec{m}) = \sum_i c_i e^{-m_i \tau} \quad \text{with } c_i := a_i \frac{e^{m_i \beta / 2}}{\sinh\left(\frac{\beta m_i}{2}\right)}, \quad (6.42)$$

where the  $a_i$  carry information from the weights of each state in (6.41). As fit parameters we can choose the weights  $c_i$  only or both the weights  $c_i$  and the masses  $m_i$ .

### 6.5.1. Single exponential fits

First, we consider a free theory. Here, only the vacuum state contributes and finite temperature plays no role. In Fig. 6.5 we display the fit of (6.42) with a single exponential  $g(\tau) = ce^{-m\tau}$  to data simulated by means of the double path-integral (6.12). We have used the following parameters:  $m = 1$ ,  $\lambda = 24$ ,  $a = 1/16$ ,  $N_\beta = 8$ ,  $N_\tau = 64$ . The fit matches the data well and we find the correct vacuum mass  $m_{\text{fit}} = 1.01(1)$ . Hence, this confirms the correctness of constructing the kernel (6.34) from the double path-integral. Regarding the data at large imaginary times effects of the boundary condition as well as an exponentially decaying signal-to-noise ratio come into play. Therefore, regarding the simulation results in this chapter we show only a window of the first 30 points of the correlator data.

In Fig. 6.6 we show the simulated correlator on the non-compact path for the fully interacting theory. The parameters are  $m = 1$ ,  $\lambda = 24$ ,  $\beta = 2$ ,  $a = 1/16$ ,  $N_\beta = 32$ ,  $N_\tau = 64$ . This scenario is close to vanishing temperature hence higher excited states in (6.41) are sufficiently suppressed. We find that a single exponential fit corresponding to the vacuum state matches the data well. The fit result for the vacuum mass coincides with the result from the Hamiltonian formulation up to a few per mille in accuracy. For details see the caption of Fig. 6.6. Similarly as for the free theory, we find that the data is well described by the a single exponential confirming the usability of the kernel (6.34) in this case. Hence, simulations on the modified non-compact time path without time translation invariance pass the vacuum cross-check.

### 6.5.2. Multiple exponential fits

The situation dramatically changes as soon as we switch on temperature in the interacting theory. This is best illustrated by means of the following parameter scenario:  $\beta = 0.5$ ,  $m = 1$ ,  $\lambda = 24$ . The data is displayed in Fig. 6.7 for two different lattice spacings. In agreement with the corresponding spectral function in Fig. 6.4 we find that for  $\beta = 0.5$  three mass peaks are relevant among which the ground state and the first excited state dominate. Thus we can employ a double exponential fit to the data. We have also tried to fit three exponentials here which however has not produced reliable results. A reason is that the thermal information on the higher excited states is encoded in roughly the first eight data points (right plot in Fig. 6.7) that are distinguishable from the vacuum correlator. This is not enough data for a robust determination. The thermal information content in the correlators is subject to a detailed discussion in the next section.

#### Fixed mass parameters

First we consider a fit with the masses fixed to their physical values obtained from the Hamiltonian formulation. The coefficients  $c_i$  are used as fit parameters. The result from a double exponential fit to the data yields a ratio of the first excited to the vacuum state of  $c_2/c_1 = 0.004(6)$  for the lattice spacing  $a = 1/16$  and  $c_2/c_1 = 0.076(4)$  for  $a = 1/32$  which is too small. The semi-exact result from the Hamiltonian formulation for the ratio yields  $c_2/c_1 \approx 0.7$ .

#### Variable mass parameters

Secondly, considering a fit with both the  $c_i$  and masses  $m_i$  as fit parameters we obtain both coefficient ratios and masses which deviate significantly from the results by diagonalizing

the Hamiltonian for all considered parameter sets and lattice spacings. For instance for  $a = 1/16$  the coefficient ratios are of the order of  $10^{-3}$  for, similarly as in the first fit scenario. While the ground state mass is estimated quite well with a value of 1.92(1) the mass of the first excited is way off with yielding 4.8(3). Here, the semi-exact result gives a value of 2.44. In short, the kernel (6.34) has not delivered satisfactory results for multiple exponential contributions failing to capture both the correct weights and masses of the physical states.

## Conclusion

Because the form of the physical spectral function for an interacting theory at finite temperature on a finite lattice representing a sum of delta peaks is hard-wired, the only possible modification for the kernel is to introduce a time dependence in the coefficients in (6.42) in order to fit the weights.

$$g(\tau, \vec{m}) = \sum_i c_i(\tau) e^{-m_i \tau}. \quad (6.43)$$

In order to get more insight on the functional form of the coefficients  $c_i(\tau)$  a derivation of the kernel for the fully interacting theory at finite temperature is necessary. This might turn out to be highly non-trivial as pointed out in the end of Section 6.3. From the fits using the derived kernel only a reliable extraction of the vacuum physics of the correlators generated with the double path-integral has been possible. The information on higher excited states appears to be suppressed relative to the vacuum information in a higher manner than what is expected from the result obtained by numerical diagonalization of the Hamiltonian. Hence, the conclusion is two-fold. First, the kernel (6.34) appears not to be useful for finite temperature spectral reconstructions of data on the non-compact imaginary time path. Secondly, the analysis here suggests the necessity to examine the content of thermal information present in the non-compact time data. This is subject to the discussion in the next section.

Before closing this section we remark that we have also tried to fit the higher excited states using the standard Matsubara correlator. In compact imaginary time the latter corresponds to a sum of hyperbolic cosines. The larger the temperature the more difficult it is to extract information on higher excited states. The reason is that the excited states, see Fig. 6.4 for e.g.  $\beta = 0.5$ , lie relatively close together and their weights are of comparable size. This leads to a mixing of these states in the lattice correlator. Hence, when applying a double or triple cosh fit to the data, the resulting fit parameters for the first or second excited states will lie somewhere in between the values of the true masses. The mixing leads to a flattening of the Matsubara correlator prohibiting a separation of different mass regimes.

## 6.6. Thermal information in the data

In the previous section we have examined the correlator for the quantum-mechanical anharmonic oscillator at finite temperature by means of exponential fits. The results have shown that the thermal information on higher excited states appears to be suppressed relative to the vacuum correlator. How much the data is suppressed is answered here

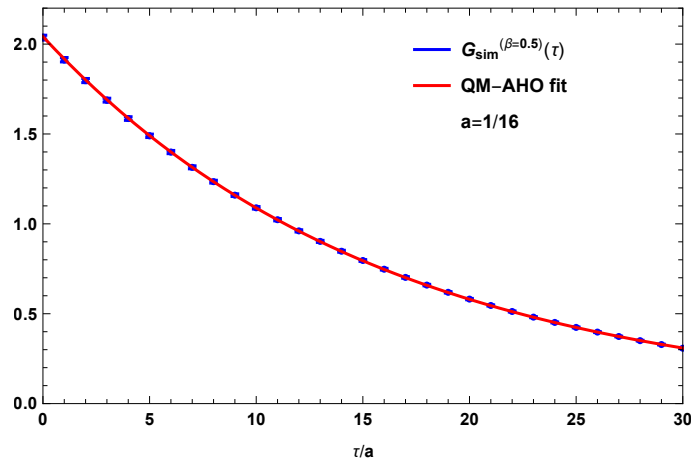


Figure 6.5.: Fitting a single exponential decaying function  $g(\tau) = c \exp(-m\tau)$  to the data obtained in a simulation for the free theory, i.e.  $m = 1, \lambda = 0$  with  $\beta = 0.5$ . The number of lattice points on the non-compact path amounts to  $N_\tau = 64$ . Here we only show the short to mid-time segment of the correlator for reasons mentioned in the main text. We observe that using the physical spectral function, the kernel (6.34) describes the data for the free theory correctly. Moreover, consistently temperature does not play a role for a free theory. The fitted mass here is  $m_{\text{fit}} = 1.01(1)$ .

based on the simulated data. In the same step this allows us to answer how much thermal information the correlator on the non-compact time path contains compared to the standard compact time correlator. To that end we compute the relative deviation of the finite temperature data with respect to the vacuum result corresponding to an inverse temperature  $\beta = 2$ . The latter has been shown to coincide with the vacuum correlator from using the Hamiltonian formulation, see also Figure 6.6. Note that again we fix  $m = 1, \lambda = 24$ . The following quantity measures the relative deviation between a correlator at inverse temperature  $\beta_1$  and a reference data set at inverse temperature  $\beta_2$

$$R(\tau, \beta_1, \beta_2) := \frac{|G_{\text{sim}}^{(\beta_1)}(\tau) - G_{\text{sim}}^{(\beta_2)}(\tau)|}{G_{\text{sim}}^{(\beta_2)}(\tau)}. \quad (6.44)$$

First we consider data simulated  $\beta = 0.5$  at two different lattice spacings  $a = 1/16$  and  $a = 1/32$ . The results are shown in Figure 6.7. For small times an effect induced by the thermal initial condition is visible in the blue data compared to the vacuum result (red). For larger times both data overlap within the error bars consistently showing that the thermal excitations decay into the vacuum. Next, we evaluate the relative deviation of the two correlators given by (6.44). This is shown in Figure 6.8. We find independent of the lattice spacing that for a physical time range smaller than around  $\beta/2$  thermal information persists in the data. For larger times no statistically significant difference compared to the vacuum data is found. This robustly indicates that the correlator on the non-compact time path contains at most as much thermal information as the standard compact time result.

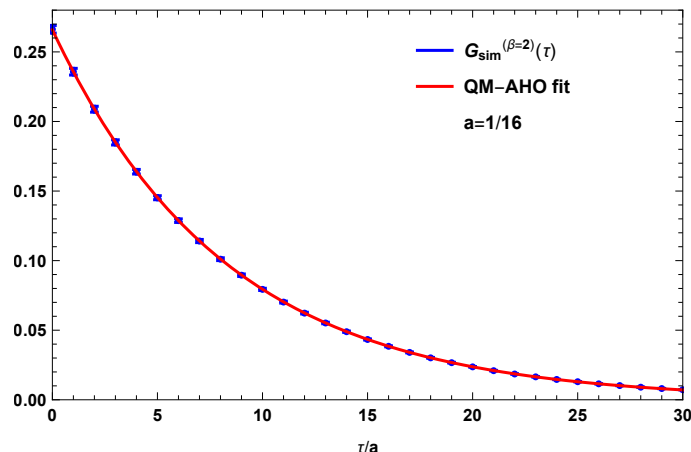


Figure 6.6.: Simulation data using the double path-integral for  $\beta = 2$ ,  $\lambda = 24$  and  $m = 1$ . This setting is close to zero temperature physics. The correlator on the non-compact path agrees with the vacuum result within the error bars. From the single exponential fit we extract the vacuum mass  $m_{\text{fit}} = 1.932(5)$  which matches the result  $m_{\text{vac}} = 1.934$ . The kernel (6.34) describes the simulation data correctly.

## 6.7. Summary

In this chapter we have investigated the novel simulation approach [60] which formulates the thermal initial value problem entirely in imaginary time. The extension of the method to non-abelian gauge theory at finite temperature has not revealed an exponential enhancement in thermal information. Nevertheless, we have shown by modifying the approach that the thermal information persists along the non-compact time path. To that end we have derived the double path integral. The formulation hence describes an analytically continued real-time system coupled to an external heat bath. To facilitate spectral reconstructions of data generated with the double path integral we have derived a spectral representation. Unfortunately, for the finite temperature theory this spectral representation is not valid.

Moreover, we have probed the data with respect to its thermal information content. To that end the relative deviation of finite temperature and vacuum data has been measured. We have found that over a physical time range which is approximately  $\beta/2$  thermal information in the correlator data is distinguishable from the vacuum physics within the errorbars. This behaviour persists in the continuum limit. Hence, the contribution from the finite temperature physics on the non-compact path decays in the same way as on the conventional compact imaginary time setup where the thermal decay length of the system is of the order of  $\beta/2$ . We have thus robustly shown that the formulation using the double path integral does not enhance the thermal information content in the two-point correlation function compared to the standard compact imaginary time simulation.

During the work behind this thesis we have made a variety of attempts to formulate a novel contour in imaginary time or to find different representations of the thermal real-time correlation function capable of providing the above mentioned enhancement of thermal information. This also includes direct simulations in real-time which is subject to the discussion in Chapter 7.

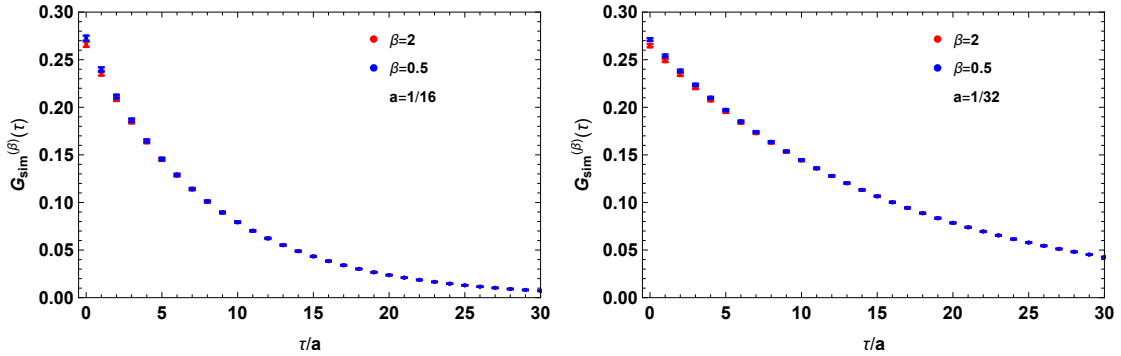


Figure 6.7.: Simulated correlators for two inverse temperatures  $\beta = 2$  and  $\beta = 0.5$  according to the double path integral (6.12). The mass and coupling parameters are set to  $m = 1$  and  $\lambda = 24$ . For both cases shown the non-compact imaginary time path has  $N_\tau = 64$  points. For better visibility of the excited states physics, we only show the small to medium times segments of the correlators. At large times the correlator decays to zero as demanded by the fixed boundary condition. Left: The lattice spacing is set to  $a = 1/16$  and  $N_\beta = 8$  (blue), 32 (red). Right: The lattice spacing is set to  $a = 1/32$  and  $N_\beta = 16$  (blue), 64 (red). Both scenarios confirm that for times larger than around  $\beta/2$  the two correlators overlap within the errorbars.

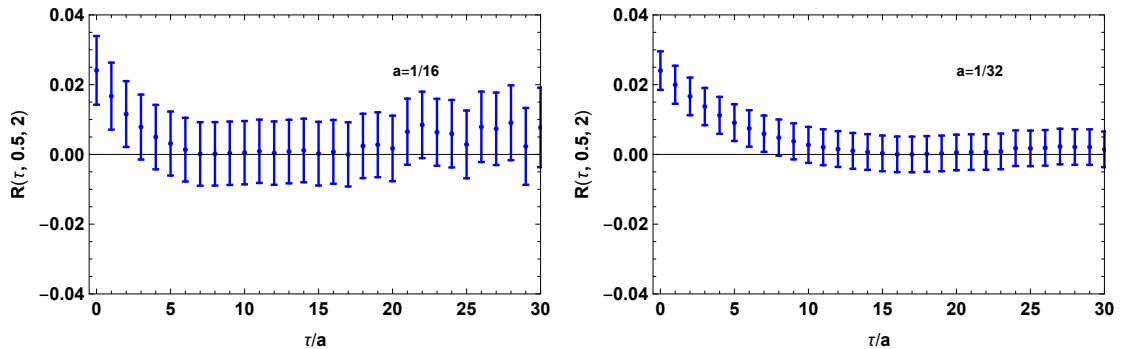


Figure 6.8.: Relative deviation of the simulated finite temperature correlator ( $\beta = 0.5$ ) with respect to the vacuum result ( $\beta = 2$ ) according to (6.44). On the left the lattice spacing is set to  $a = 1/16$  and  $N_\beta = 8$  whereas for the data on the right we have set  $a = 1/32$  and  $N_\beta = 16$ . The Hamiltonian formulation shows that for  $\beta = 0.5$  the thermally excited states become relevant, see Fig. 6.4. This is confirmed by the simulated data on the non-compact path. In comparison with the vacuum result we find that independent of the lattice spacing thermal information is present up to a time of around  $\beta/2$  corresponding to  $\tau/a = 4$  on the left and  $\tau/a = 8$  on the right. Beyond that the data on the finite temperature correlator is indistinguishable from the vacuum result. This demonstrates that the thermal information content in the finite temperature correlator at most as large as in standard compact time data. The errorbars have been obtained by standard error propagation based on the simulated data.

## 7. Variable Transformations

In this chapter we consider real-time quantum field theories on the lattice. The research presented here has emerged recently and is therefore summarized briefly. So far on the lattice real-time simulations have been rare. An implementation of a tilted Schwinger-Keldysh contour has been carried out by means of the Complex Langevin evolution in [191, 192]. The difficulty here is that the Langevin evolution only achieves converging results if the real-time extent  $t_{\max}$  is smaller or equal to the imaginary time extent  $\beta$ . For larger real-time the drift leads to instabilities by driving the fields into imaginary direction. Recently also the holomorphic flow method has shown promising results see [134, 193]. It has reached larger real-time extents than the Complex Langevin evolution. However it suffers from growing auto-correlation times with rising  $t_{\max}$ .

Here, we simulate real-time theories and toy models by using the Complex Langevin evolution. The goal is to improve the method such that it can simulate larger real-time extents. This is facilitated with the help of variable transformations [102]. The latter have shown promising effects on the stability and convergence of Complex Langevin in simple models.

The strategy to realize such real-time simulations imposes to requirements for the variable transformations:

1. Stability of the stochastic process must be ensured.
2. The average phase  $\langle e^{-iS_I} \rangle$  (which measures the strength of the sign problem) should be minimal.

### 7.1. Transformations in simple models

A simple model with a tunable sign problem is following version of the quartic model

$$S(x, \alpha) := e^{i\alpha} \left( \frac{\sigma}{2} x^2 + \frac{\lambda}{4} x^4 \right)$$

$$Z = \int_{\mathbb{R}} dx e^{-S(x, \alpha)}. \quad (7.1)$$

Here  $\sigma, \lambda \in \mathbb{R}^+$  and  $\alpha \in (-\pi, \pi]$ . The latter allows for interpolation between the Euclidean model and the Minkowski model. Now, we complexify the variable  $x \rightarrow z = x + iy$  and consider the variable transformation  $z(u) = e^u$ . The transformed action reads

$$S_{\text{eff}}(u) = S(e^u, \alpha) - \log(z'(u)) = e^{i\alpha} \left( \frac{\sigma}{2} e^{2u} + \frac{\lambda}{4} e^{4u} \right) - u. \quad (7.2)$$

The Complex Langevin equation reads

$$\frac{\partial u}{\partial \tau} = -\frac{\partial S_{\text{eff}}}{\partial u} + \eta = -e^{i\alpha} (\sigma e^{2u} + \lambda e^{4u}) + 1 + \eta. \quad (7.3)$$

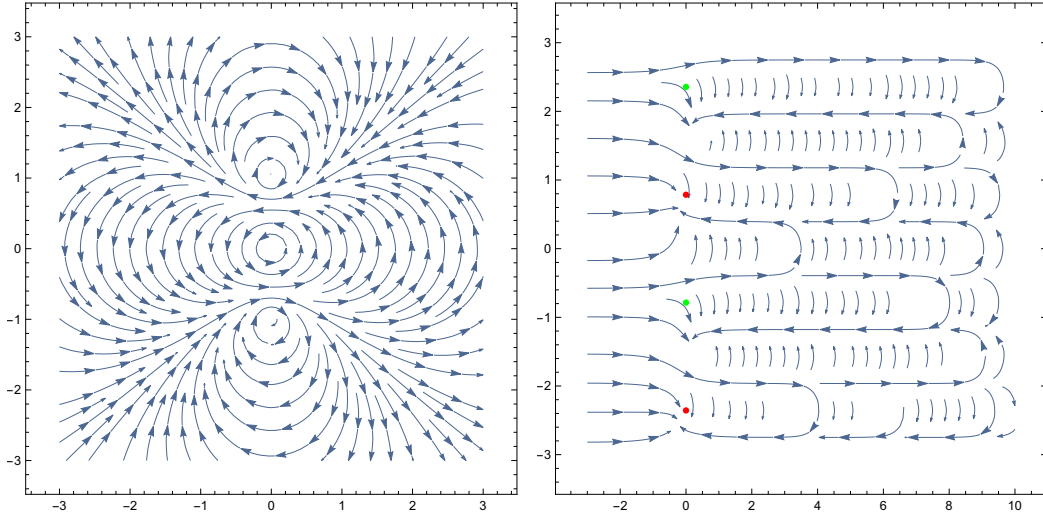


Figure 7.1.: Drift of the quartic model for  $\alpha = -\pi/2$ . On the left-hand side the drift for the original model is depicted. The fixed points sit at  $0, \pm i$ . On the right-hand side the transformed drift using the  $e^u$  transformation is shown. The transformation stabilizes the dynamics and introduces  $2\pi$  periodicity in imaginary direction.

Looking at the drift term of the original and the transformed theory for  $\alpha = \pi/2$  in Figure 7.1 we find that the  $e^u$  transformation fulfills the first requirement, i.e. stability.

Note that while for a real Langevin evolution a unique fixed determines the stochastic process in the complex case there can be several fixed points. Those influence the stochastic dynamics and the convergence of the method. We have found that for  $\alpha > \pi/4$  the transformation does not yield correct results. Close to the attractive fixed points which yield the correct result a partially attractive, partially circular fixed point emerges as  $\alpha > \pi/4$ . Although we use an adaptive step size in our Langevin evolution following [194] the second fixed point spoils the results.

## 7.2. Schwinger-Keldysh on the lattice

We consider a quantum mechanical anharmonic oscillator coupled to a heat-bath similarly as in Chapter 6. This corresponds to a real scalar field theory in 0+1 dimensions formulated on the Schwinger-Keldysh contour. We use the contour which goes from 0 to  $t_{\max}$ , then downwards to  $t_{\max} - i\beta/2$ , then backwards to  $-i\beta/2$  and then downwards again to  $-i\beta$ , see [71, 193] for details. The action reads

$$S_c = \sum_{l=0}^{N-1} a_l \left[ \frac{(\phi_{l+1} - \phi_l)^2}{2a_l^2} - \left( \frac{m^2}{2} \frac{\phi_l^2 + \phi_{l+1}^2}{2} + \frac{\lambda}{24} \frac{\phi_l^4 + \phi_{l+1}^4}{2} \right) \right] \quad (7.4)$$

where we take the same discretization convention as used in [191, 193]. Note that  $N = 2N_t + N_\beta$ . Moreover, periodic boundary conditions  $\phi_0 = \phi_N$  are used. For the complex

lattice spacings we have  $a_l = \xi_l a$  with

$$\xi_l = \begin{cases} 1 & 0 \leq l \leq N_t - 1 \\ -i & N_t \leq l \leq N_t + N_\beta/2 - 1 \\ -1 & N_t + N_\beta/2 \leq l \leq 2N_t + N_\beta/2 - 1 \\ -i & 2N_t + N_\beta/2 \leq l \leq 2N_t + N_\beta - 1 \end{cases} \quad (7.5)$$

### Variable transformations

A suitable variable transformation which stabilizes the dynamics is motivated by considering again the quartic model for the Minkowski scenario.  $z(u) = e^{i\pi/8}u$ <sup>1</sup> transforms the potential term

$$-i\frac{\lambda}{4}z^4 \rightarrow \frac{\lambda}{4}e^{4u}. \quad (7.6)$$

Hence, for large  $|u|$  the drift pushes the fields towards the origin rendering the stochastic process attractive. In the simple model this transformation solves the sign problem because the stochastic process is stable and samples around the fixed point at the origin. This is also related to the Lefschetz thimbles and deformed manifolds as follows. Note that the rotated real axis by  $\pi/8$  falls into the good regions [40] where the continuously deformed path-integral is convergent. The good region surrounds the thimble.

Applied to the field theory we have for the transformed fields

$$\phi_n \rightarrow \phi_n(u) = e^{i\theta_n}u_n, \quad i = 1, \dots, N. \quad (7.7)$$

The Jacobi matrix reads

$$(J(u))_{nk} := \frac{\partial \phi_n}{\partial u_k} = e^{i\theta_n} \delta_{nk}. \quad (7.8)$$

Moreover periodic boundary conditions, i.e.  $u_0 = u_N$  are employed.

Moreover, based on our preliminary considerations on stability in (7.6) the transformations on the forward, backward and downward pieces are chosen according to

$$\theta_l = \begin{cases} -\pi/8 & 0 \leq l \leq N_t - 1 \\ 0 & N_t \leq l \leq N_t + N_\beta/2 - 1 \\ \pi/8 & N_t + N_\beta/2 \leq l \leq 2N_t + N_\beta/2 - 1 \\ 0 & 2N_t + N_\beta/2 \leq l \leq 2N_t + N_\beta - 1 \end{cases} \quad (7.9)$$

Note that the field variables on the Euclidean time pieces are unmodified because the local drift at these points is already attractive (with respect to the quartic term). Naively this should guarantee stability also in the field theory. In particular it must be guaranteed in the limit  $|u| \rightarrow \infty$  and for large  $\lambda$  where the quartic term dominates the dynamics. The Jacobian is trivial since it is constant and its determinant equals one

$$\det J(u) = \prod_{l=0}^{N-1} e^{i\theta_l} = 1. \quad (7.10)$$

<sup>1</sup>Note the similarity to combining the Complex Langevin evolution and thimbles in the so-called Lefschetz cooling in Appendix B.3.

We rewrite the action in terms of dimensionless quantities (lattice units)

$$[\phi] = [u] = a^{1/2} \quad (7.11)$$

$$[m] = a^{-1} \quad (7.12)$$

$$[\lambda] = a^{-3} \quad (7.13)$$

$$\tilde{\phi} = a^{-1/2} \phi \quad (7.14)$$

$$\tilde{u} = a^{-1/2} u \quad (7.15)$$

$$\tilde{m} = am \quad (7.16)$$

$$\tilde{\lambda} = a^3 \lambda. \quad (7.17)$$

Now, the transformed action used here reads

$$S_c = \sum_{l=0}^{N-1} \left[ -e^{2i\theta_l} u_l \frac{(u_{l+1} + u_{l-1} - 2u_l)}{2\xi_l} - \xi_l \left( \frac{m^2}{2} \frac{e^{2i\theta_l} u_l^2 + e^{2i\theta_{l+1}} u_{l+1}^2}{2} + \frac{\lambda}{24} \frac{e^{4i\theta_l} u_l^4 + e^{4i\theta_{l+1}} u_{l+1}^4}{2} \right) \right], \quad (7.18)$$

where we have dropped the tilde. The path integral is simply given by

$$Z = \int_{\mathbb{R}^N} d^N u e^{-S[u]}, \quad (7.19)$$

where  $S[u] = -iS_c[u]$ .

### Numerical results

We have carried out numerical simulations of the Complex Langevin equation derived from (7.18) for the following parameters:  $N_t = 2, N_\beta = 4, a = 0.25, m = 1, \lambda = 24, \theta = \pi/8$ . A scatter plot of a thermalization trajectory is shown in Figure 7.2. We find from the stochastic trajectory that the fields are directed towards three different accumulation points. The field variables on the Euclidean time pieces of the contour flow towards the central attractive region on the real axis. On the other hand the fields living on the real-time paths are clustering around the accumulation points in the lower left as well as in the upper right corner. We have also measured the average sign in such a run which amounts to  $|\langle e^{-iS_I} \rangle| \approx 0.01$ . From this we conclude that the second requirement proposed in the beginning of this chapter is not fulfilled and we are still dealing with a sign problem here. This might also be related to the observed behaviour of the field variables clustering around different attractive points. Note also that the variable transformation based on (7.9) does not continuously connect the fields at the corners of the contour.

## 7.3. Assessment and perspectives

The variable transformation (7.9) applied to the Schwinger-Keldysh contour represents one of the simplest possible mappings fulfilling the stability condition. It corresponds to a rotation of the axes of the original integration manifold  $\mathbb{R}^N$ . The thimbles and the

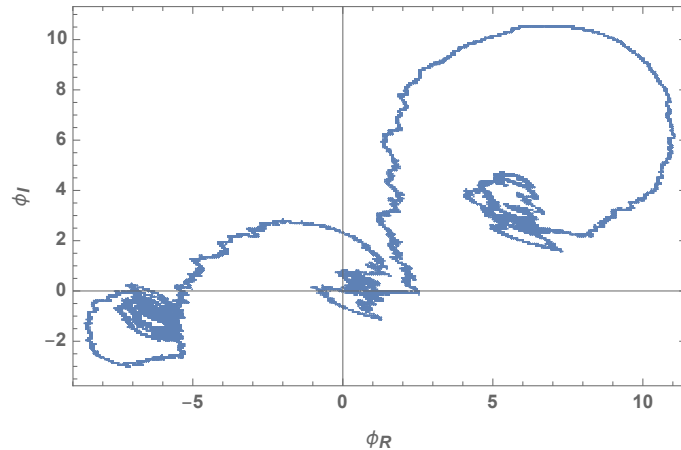


Figure 7.2.: Scatter plot of a Complex Langevin trajectory with  $O(10^5)$  steps at a step size of  $10^{-4}$  for the variable transformed action on the Schwinger-Keldysh contour with 8 lattice points in total. The parameters are given in the main text. There seem to be three stable attractive fixed points where the fields on disjoint lattice points flow to. The (local) drift gets modified differently depending if the field variable sits on a real-time or Euclidean time piece. It appears that the fields sitting on the imaginary time pieces flow to the attractive region on the real axis while the real-time fields are directed towards the two regions in the complex plane in the lower left and upper right.

Complex Langevin evolution are closely related [124]. For the Schwinger-Keldysh example the thimble represents a curved manifold immersed into  $\mathbb{C}^N$ . From this it might also imply that the variable transformation for the Complex Langevin evolution needs to carry non-local information. Constructing these transformations however is non-trivial and we leave it to future studies. A starting point is to map an integrand giving rise to a sign problem to a Gaussian probability distribution function for which the stochastic process is stable and trivial. The information on the original integral is carried entirely by the Jacobian. Furthermore one could try to combine an ansatz for a variable transformation fulfilling the stability requirement with path optimization techniques as proposed in [195] to find a numerical parametrization for the sampling.

## 8. Summary and Outlook

In this work we have put forward various ideas for novel methods usable in lattice simulations of strongly correlated systems at finite temperature and density. There are two main areas in which these algorithms can be applied. The first concerns QCD at finite density and the second real-time properties of quantum systems, a prominent example being transport coefficients for the quark-gluon plasma. In both areas the lattice suffers from the sign problem which is most severe in the second case.

### Colored noise

In Chapter 3 we have investigated lattice field theory with Stochastic Quantization and a UV-regularized colored noise. Cooling the Langevin evolution by removing field configurations in the UV may be a promising candidate to optimize lattice simulations of systems with a clear scale separation between the relevant physics and the asymptotic UV regime. The momentum cutoff in the regularization function serves as an external parameter determining the smoothness scale and allowing for a controlled removal of UV fluctuations. We sample smooth configurations directly from the UV-regularized Langevin evolution which is a potential advantage over the gradient flow [154]. Our approach has been put to work within a real scalar field theory in two dimensions using a sharp momentum cutoff. A large range of ultra-violet fluctuations can be removed without changing the physics content of the theory. As long as the cutoff is larger than the physical scale of the system the use of the classical action is valid. For even lower scales the RG-running of the couplings requires a Symanzik-improved action. Testing the approach using further parameter ranges in the scalar theory and incorporating improved actions is left to future studies. In many areas of lattice field theory physical quantities need to be determined with increasing precision. An example being the energy-momentum tensor correlator. Hence, smoothing methods are highly necessary. During the last years there has been intense research on the interplay between the gradient flow and the renormalization group [159, 196]. The work here presents an important step towards understanding the role of stochastic processes and the RG, see also [197] for a recent work.

### Lefschetz Thimbles

In Chapter 4 we have proposed a novel reweighting method to calculate the relative weights appearing in the thimble decomposition which is a promising candidate to ameliorate the sign problem in lattice theories with a complex action. The approach is successfully put to work by considering a  $U(1)$  one-link model representing a toy model for a gauge theory with fermions at finite density. Although its thimble structure is easy to parametrize numerically it provides a valuable testbed. The central prospect of the reweighting procedure is that it is generalizable to field theories. Moreover it can be combined with other simulation algorithms for thimbles.

In Chapter 5 we have extended our studies of Lefschetz thimbles to field theories. In

this case thimbles are objects immersed in a high dimensional space. This makes explicit numerical parametrizations hard to determine in practice. There exist global sampling algorithms such as the generalized Lefschetz thimble method [180]. However, those are computationally demanding. We propose a novel local sampling method on the thimbles which comes at low simulation cost. It has been applied successfully to simple models however in  $U(1)$  lattice gauge theory in two dimensions the local thimble algorithm fails. An explanation might be that there exists regions on the surface determined by the condition  $\text{Im}(S) = \text{const.}$  where the real part of the action is no longer bounded from below. This gives rise to numerical instabilities. Furthermore, we have tested the local sampling algorithm by means of a free scalar field theory in real time. Here, the algorithm is stable and samples the thimble. The situation has improved into a promising direction by employing a simulation on the product manifolds of the tangent spaces to the  $U(1)$  one-link model. So far this has been used to sample the contribution corresponding to the main thimble. The above proposed reweighting algorithm might be useful to compute the full result and to assess the method further.

### **Non-compact imaginary time**

In Chapter 6 we have studied real-time systems by means of an analytic continuation to a novel non-compact imaginary time path. The method has been applied to gauge theories. However, during the work of this thesis we have found that the method needs modifications to incorporate thermal physics in the observables. We have carried out further studies on a quantum mechanical anharmonic oscillator providing a good testing ground for assessing the thermal information in correlation functions. By analyzing the data we have found that the thermal information content on the non-compact imaginary time path does not exceed the one obtained in standard compact imaginary time simulations. Our findings indicate that the problem of exponentially suppressed thermal information persists.

### **Real-time via variable transformations**

In Chapter 7 we we have investigated a quantum mechanical system on the Schwinger-Keldysh contour discretized on the lattice. This comes with a hard sign problem we tackle by means of the complex Langevin simulation. The strategy is now two-fold. The first ingredient is stability preventing the stochastic trajectory to escape into imaginary directions. This can be achieved by a transformation of the form  $\phi_l(u) = e^{i\theta_l} u_l$  where the angles  $\theta_l$  are such that the drift force directs the fields towards the origin at large field values. This is determined according to the potential term in the action. The second point is to achieve a mild sign problem. Although in principle Complex Langevin circumvents the sign problem it is nevertheless important to ensure that the configurations being sampled are distributed according to the correct weight. We have found that enforcing the stability condition one has to pay the price of a low average phase. This is subject to ongoing research.

### **Conclusion**

By developing various approaches for tackling the sign problem in this thesis we have also gained insight how the different methods are related. This concerns for instance the convergence regions of the thimbles and the stability of the Complex Langevin evolution.

---

So far the phase structure of QCD especially at low temperatures and large densities has remained inaccessible due to numerical difficulties with the discussed algorithms. However, the sign problem is representation dependent. Applying suitable variable transformations to simple models, see Chapter 7, we could give a class of reparametrizations which solved the sign problem. In field theories however these representations are non-trivial. Therefore it is necessary to further investigate simple models and to use our findings from there for generalizations to higher dimensional theories. A promising step in this direction is the tangent space algorithm being a local sampling method for lattice gauge theories. The future work consists of analyzing simple models with non-abelian degrees of freedom with the aim to take the first steps towards full QCD.

# A. Technicalities on Colored Noise

## A.1. Fourier transformation on the Lattice

On the lattice the discrete Fourier transformation of the field  $\phi(x)$  reads

$$\phi(p) = \sum_x a^d e^{-ip \cdot x} \phi(x), \quad (\text{A.1})$$

where the momenta  $p$  are elements of the discrete Brillouin zone. The inverse Fourier transform of the field  $\phi(x)$  is correspondingly given by

$$\phi(x) = \frac{1}{a^d N^d} \sum_p e^{ip \cdot x} \phi(p), \quad (\text{A.2})$$

where the sum runs over all momenta in the Brillouin zone. In the thermodynamic limit  $N \rightarrow \infty$  the previous equation converges to

$$\phi(x) = \frac{1}{(2\pi)^d} \int_{-\pi/a}^{\pi/a} d^d p e^{ip \cdot x} \phi(p). \quad (\text{A.3})$$

For the remaining part of this section we work in the thermodynamic limit.

The  $O(a^2)$  discretized Euclidean Laplace operator has the form

$$\Delta_{x,y} = -\frac{1}{a^2} \sum_{\mu=1}^d (\delta_{x+\hat{\mu},y} - 2\delta_{x,y} + \delta_{x-\hat{\mu},y}). \quad (\text{A.4})$$

Let  $\Delta_{x,y}^{-1}$  denote the inverse lattice Laplacian obeying

$$\Delta_{x,y} \Delta_{y,z}^{-1} = \frac{\delta_{x,z}}{a^d}. \quad (\text{A.5})$$

Substituting the Fourier transform of the Laplacian according to (A.3) in the previous equation yields

$$\begin{aligned} \Delta_{x,y} & \left[ \frac{1}{(2\pi)^d} \int_{-\pi/a}^{\pi/a} d^d p e^{ip \cdot (y-z)} \Delta^{-1}(p) \right] \\ & = \frac{1}{(2\pi)^d} \int_{-\pi/a}^{\pi/a} d^d p e^{ip \cdot (x-z)}. \end{aligned} \quad (\text{A.6})$$

Evaluating this further leads to the lattice Laplacian in momentum space

$$\Delta(p) = \frac{4}{a^2} \sum_{\mu=1}^d \sin^2 \left( \frac{ap_\mu}{2} \right). \quad (\text{A.7})$$

The right-hand side of (A.7) appears in a similar fashion in the free propagator of a scalar field theory. It relates the physical momenta to the lattice momenta (3.10) by

$$\tilde{p}_\mu := \frac{2}{a} \sin \left( \frac{ap_\mu}{2} \right). \quad (\text{A.8})$$

## A.2. Observables

In this section we work in lattice units. Let  $V = N_s^{d-1}$  denote the spatial lattice volume and  $T = N_t$  the time extent of the lattice. Similarly as above we work with  $N_s = N = N_t$ . The total lattice volume is  $\Omega = VT$ . In the following we derive in more detail a few of the key observables of a real scalar field theory with the lattice action given in (3.17). We keep our notation close to [82].

The connected two-point susceptibility is defined as the integrated connected two-point correlation function (3.24). It can be formulated in terms of the magnetization  $M$  defined in (3.23) using that  $\langle \phi(x) \rangle = \langle \phi(0) \rangle = \langle M \rangle$ .

$$\begin{aligned}
\chi_2 &:= \sum_x G_c(x, 0) = \sum_x \langle \phi(x) \phi(0) \rangle_c \\
&= \sum_x (\langle \phi(x) \phi(0) \rangle - \langle \phi(x) \rangle \langle \phi(0) \rangle) \\
&= \sum_x \left( \frac{1}{\Omega} \left\langle \sum_y \phi(x+y) \phi(y) \right\rangle - \langle M \rangle^2 \right) \\
&= \frac{1}{\Omega} \left\langle \sum_{x,y} \phi(x+y) \phi(y) \right\rangle - \Omega \langle M \rangle^2 \\
&= \left\langle \sum_y M \phi(y) \right\rangle - \Omega \langle M \rangle^2 \\
&= \Omega (\langle M^2 \rangle - \langle M \rangle^2) = \Omega \langle M^2 \rangle_c.
\end{aligned} \tag{A.9}$$

In the step from the third to the fourth as well as from the fifth to the sixth equation translation invariance on the lattice has been used.

Moreover, we exploited the linearity of the (path integral) expectation value. Alternatively, the connected susceptibility is just the Fourier transform of the connected correlation function with momentum set to zero

$$\chi_2 \equiv \tilde{G}(p) \Big|_{p=0}. \tag{A.10}$$

Here, the momentum space correlator for small  $p$  has the form

$$\tilde{G}(p) = \frac{1}{2\kappa m_R^2 + p^2 + O(p^4)}. \tag{A.11}$$

From this, the second moment is determined according to

$$\mu_2 \equiv - \frac{\partial^2}{\partial p_\nu \partial p_\nu} \tilde{G}(p) \Big|_{p=0}. \tag{A.12}$$

Explicitly, for the susceptibility it holds

$$\chi_2 = \tilde{G}(0) = \frac{1}{2\kappa m_R^2}. \tag{A.13}$$

The evaluation of (A.12) for the second moment yields

$$\mu_2 = \frac{2d}{2\kappa m_R^4} \frac{Z_R}{m_R^4}. \tag{A.14}$$

Thus, the renormalized mass is given by

$$m_R^2 = 2d \frac{\chi_2}{\mu_2}. \quad (\text{A.15})$$

Next, we define the time slice as the spatial average of the field over the lattice at each time  $t$

$$S(t) = \frac{1}{V} \sum_{\vec{x}} \phi(\vec{x}, t). \quad (\text{A.16})$$

In a similar way as discussed above, we can express  $\chi_2$  in terms of the integrated correlation function of time slices

using  $\langle S(t) \rangle = \langle S(0) \rangle = \langle M \rangle$ .

$$\begin{aligned} \chi_2 &= \frac{1}{\Omega} \sum_{x,y} \langle \phi(x+y)\phi(y) \rangle - \Omega \langle M \rangle^2 \\ &= \frac{1}{\Omega} \sum_{(t,\vec{x}),(t',\vec{y})} \langle \phi(\vec{x} + \vec{y}, t+t')\phi(\vec{y}, t') \rangle - \Omega \langle M \rangle^2 \\ &= \sum_{t,t'} \frac{V}{T} \langle S(t+t')S(t') \rangle - V \sum_t \langle S(t) \rangle \langle S(0) \rangle \\ &= V \sum_t \langle S(t)S(0) \rangle_c = V \sum_t G_c(t). \end{aligned} \quad (\text{A.17})$$

The second moment  $\mu_2$  can be expressed in form of time slices exploiting  $\langle \phi(\vec{x}, t) \rangle = \langle S(t) \rangle$  as follows

$$\begin{aligned} \mu_2 &= \sum_x x^2 G_c(x, 0) = \sum_x x^2 \langle \phi(x)\phi(0) \rangle_c \\ &= \sum_{t,\vec{x}} (t^2 + \vec{x}^2) \langle \phi(\vec{x}, t)\phi(0, 0) \rangle_c \\ &= d \sum_{t,\vec{x}} t^2 \langle \phi(\vec{x}, t)\phi(0, 0) \rangle_c \\ &= d \sum_{t,\vec{x}} t^2 \langle \phi(\vec{x}, t)\phi(0, 0) \rangle - d \sum_{t,\vec{x}} t^2 \langle \phi(\vec{x}, t) \rangle^2 \\ &= d \sum_{t,\vec{x}} t^2 \langle \phi(\vec{x}, t)S(0) \rangle - d \sum_{t,\vec{x}} t^2 \langle S(t) \rangle^2 \\ &= dV \sum_t t^2 \langle S(t)S(0) \rangle - dV \sum_t t^2 \langle S(t) \rangle^2 \\ &= dV \sum_t t^2 \langle S(t)S(0) \rangle_c. \end{aligned} \quad (\text{A.18})$$

In the step from the third to the fourth equation we have used the above premise that there is no distinguished direction on the lattice.

The corresponding formulae for a scalar field theory in  $d = 2$  read

$$\begin{aligned} \chi_2 &= \frac{1}{N^2} \sum_{x,y} \langle \phi(x+y)\phi(y) \rangle_c = N^2 \langle M^2 \rangle_c \\ &= \sum_{t,t'} \langle S(t+t')S(t') \rangle_c = N \sum_t \langle S(t)S(0) \rangle_c, \end{aligned} \quad (\text{A.19})$$

where

$$S(t) = \frac{1}{N} \sum_x \phi(x, t) \quad (\text{A.20})$$

and

$$M = \frac{1}{N^2} \sum_x \phi(x). \quad (\text{A.21})$$

For the second moment we find

$$\mu_2 = 2N \sum_t t^2 \langle S(t)S(0) \rangle_c. \quad (\text{A.22})$$

Finally, the renormalized mass can be computed from

$$m_R = \left( \frac{4\chi_2}{\mu_2} \right)^{1/2}. \quad (\text{A.23})$$

### A.3. Spacetime correlation function of colored noise

First, the spatial Fourier transform of the noise field  $\eta(x, \tau)$  is given by

$$\eta(p, \tau) = \int d^d x \eta(x, \tau) e^{-ip \cdot x}. \quad (\text{A.24})$$

The white noise correlation function in momentum space is obtained by applying the second relation from (2.25)

$$\langle \eta(p, \tau) \eta(q, \tau') \rangle = 2 (2\pi)^d \delta^{(d)}(p + q) \delta(\tau - \tau'). \quad (\text{A.25})$$

In the continuum colored noise is defined by the convolution with the sharp regulator function (3.3)

$$\eta(x, \tau)_{\text{col}} = \frac{1}{(2\pi)^d} \int d^d p \eta(p, \tau) \theta(\Lambda^2 - p^2) e^{ip \cdot x}. \quad (\text{A.26})$$

The correlation function for the colored noise field in  $d$  dimensions is derived in the following.

$$\begin{aligned} & \langle \eta_{\text{col}}(x, \tau) \eta_{\text{col}}(y, \tau') \rangle \\ &= \left\langle \frac{1}{(2\pi)^{2d}} \int d^d p d^d q e^{-ip \cdot x} e^{-iq \cdot y} \right. \\ & \quad \left. \times \theta(\Lambda - |p|) \theta(\Lambda - |q|) \eta(p, \tau) \eta(q, \tau') \right\rangle \end{aligned} \quad (\text{A.27})$$

$$\begin{aligned} &= \frac{2}{(2\pi)^d} \int d^d p d^d q e^{-ip \cdot x} e^{-iq \cdot y} \\ & \quad \times \theta(\Lambda - |p|) \theta(\Lambda - |q|) \delta^{(d)}(p + q) \delta(\tau - \tau') \end{aligned} \quad (\text{A.28})$$

$$= \frac{2}{(2\pi)^d} \int d^d p e^{-ip \cdot (x-y)} \theta(\Lambda - |p|) \delta(\tau - \tau') \quad (\text{A.29})$$

$$\begin{aligned} &= \frac{2}{(2\pi)^d} \int_0^\Lambda d|p| |p|^{d-1} \int_{\vartheta_{d-1}=0}^{2\pi} \int_{\vartheta_{d-2}=0}^\pi \cdots \int_{\vartheta_1=0}^\pi \\ & \quad \times e^{-i|p||x-y| \cos(\vartheta_{d-2})} \sin^{d-2}(\vartheta_1) \cdots \sin(\vartheta_{d-2}) \\ & \quad \times d\vartheta_1 \cdots d\vartheta_{d-2} d\vartheta_{d-1} \delta(\tau - \tau') \end{aligned} \quad (\text{A.30})$$

$$= \frac{2}{(2\pi)^d} \int_0^\Lambda d|p| |p|^{d-1} \frac{\sin(|p||x-y|)}{|x-y|} \int \Omega_d \delta(\tau - \tau') \quad (\text{A.31})$$

$$= \frac{1}{2^{d-2} \pi^{d/2} \Gamma(\frac{d}{2})} \int_0^\Lambda d|p| |p|^{d-1} J_0(|p||x-y|) \delta(\tau - \tau'). \quad (\text{A.32})$$

Here  $\Gamma(t) := \int dy e^{-y} y^{t-1}$  denotes the Euler gamma function and  $J_0(x) \equiv \sin(x)/x$  is a Bessel function of the first kind. The Bessel profile is also visible in observables such as the correlation function of time slices for sufficiently low cutoff in numerical simulations. This is discussed further in Appendix A.4.2.

## A.4. Aspects of colored noise

### A.4.1. Fokker-Planck equation

In this section, we derive the Fokker-Planck equation (FPE) with a noise kernel (3.2) which describes the evolution of the probability distribution  $P(\phi, \tau)$  in fictitious time  $\tau$ . The derivation presented in [86, 163] is worked out in more detail focusing on the important technical steps. Thereto, we consider a real one-component interacting scalar field theory in  $d$  dimensions whose Euclidean action reads

$$S = \int d^d x \left[ \frac{1}{2} \left( \sum_{\mu=1}^d (\partial_\mu \phi(x))^2 \right) + \frac{m^2}{2} \phi^2(x) + V(\phi) \right]. \quad (\text{A.33})$$

The regularized Langevin equation reads

$$\frac{\partial \phi(x, \tau)}{\partial \tau} = -\frac{\delta S}{\delta \phi(x, \tau)} + r_\Lambda(\Delta_x) \eta(x, \tau), \quad (\text{A.34})$$

where  $r_\Lambda(\Delta_x)$  denotes the regularization function which depends on the cutoff parameter  $\Lambda$  and the Laplacian  $\Delta_x$  with  $r_\Lambda(\Delta_x) \rightarrow 1$  in the limit  $\Lambda \rightarrow \infty$ . The field is evolved in Langevin time according to

$$\begin{aligned} \phi(x, \tau) &= \int_{x'} \int_{-\infty}^{\tau} d\tau' G(x - x', \tau - \tau') \\ &\quad \times \left[ r_\Lambda(\Delta_x) \eta(x, \tau') - \frac{\delta V}{\delta \phi} \phi(x', \tau) \right], \end{aligned} \quad (\text{A.35})$$

where the Langevin Green's function, see [86] for the derivation, is given by

$$G(x - x', \tau - \tau') = \theta(\tau - \tau') \int_p e^{-ip \cdot (x - x')} e^{-(\tau - \tau')(p^2 + m^2)}. \quad (\text{A.36})$$

Note, that the lower bound in the fictitious time integral is set to  $-\infty$  such that at finite (positive) Langevin times the system is in thermal equilibrium. Stochastic averages are equivalent to functional averages over a probability distribution  $P(\phi, \tau)$ . Moreover, let  $F[\phi]$  be an arbitrary functional of the field variables. To stress the explicit noise dependence of the field obtained as a solution of the Langevin equation we write  $\phi_\eta$ . Stochastic averages are written as

$$\begin{aligned} \langle F[\phi_\eta] \rangle_\eta &= \int \mathcal{D}\eta F[\phi_\eta] \exp \left[ -\frac{1}{4} \int d\tau d^d x \eta^2(x, \tau) \right] \\ &= \int \mathcal{D}\phi F[\phi] P(\phi, \tau). \end{aligned} \quad (\text{A.37})$$

Before we proceed, we derive some useful identities. First, it follows from (A.35)

$$\begin{aligned} \frac{\delta \phi(x, \tau)}{\eta(y, \tau)} &= \theta(0) \int_{x'} r_\Lambda(\Delta_x) \delta^{(d)}(x - y) \int_p e^{-ip \cdot (x - x')} \\ &= \frac{1}{2} r_\Lambda(\Delta_x) \delta^{(d)}(x - y), \end{aligned} \quad (\text{A.38})$$

where the convention  $\theta(0) = \frac{1}{2}$  is used. Finally, we note the trivial identity

$$\left( 2 \frac{\delta}{\delta \eta_{y, \tau}} + \eta_{y, \tau} \right) \exp \left[ -\frac{1}{4} \int_\tau \int_x \eta_{x, \tau}^2 \right] = 0. \quad (\text{A.39})$$

To derive the FPE we consider the derivative with respect to fictitious time  $\tau$  of the stochastic average given in (A.37). For simplicity, we drop the subscript  $\eta$ .

$$\begin{aligned}
\frac{d}{d\tau} \langle F[\phi] \rangle &= \left\langle \int_x \frac{\delta F[\phi]}{\delta \phi_{x,\tau}} \frac{\partial \phi_{x,\tau}}{\partial \tau} \right\rangle \\
&= \left\langle \int_x \frac{\delta F[\phi]}{\delta \phi_{x,\tau}} \left( -\frac{\delta S}{\delta \phi_{x,\tau}} + r_\Lambda(\Delta_x) \eta_{x,\tau} \right) \right\rangle \\
&= \int \mathcal{D}\eta \left\{ \int_x \frac{\delta F[\phi]}{\delta \phi_{x,\tau}} \left( -\frac{\delta S}{\delta \phi_{x,\tau}} + r_\Lambda(\Delta_x) \eta_{x,\tau} \right) \right. \\
&\quad \left. \times \exp \left[ -\frac{1}{4} \int_\tau \int_z \eta_{z,\tau}^2 \right] \right\} \\
&= \int \mathcal{D}\eta \int_x \frac{\delta F[\phi]}{\delta \phi_{x,\tau}} \\
&\quad \times \left( -\frac{\delta S}{\delta \phi_{x,\tau}} - 2 \int_y r_\Lambda(\Delta_x) \delta^{(d)}(x-y) \frac{\delta}{\delta \eta_{y,\tau}} \right) \\
&\quad \times \exp \left[ -\frac{1}{4} \int d\tau \int d^d z \eta_{z,\tau}^2 \right]. \tag{A.40}
\end{aligned}$$

In the second equation the Langevin equation (A.34) was inserted. The third equation follows by writing the noise average in the functional integral form. In the fourth equation the identity for the functional derivative with respect to the noise field from (A.39) was used. This can be simplified further as follows

$$\begin{aligned}
\frac{d}{d\tau} \langle F[\phi] \rangle &= \int \mathcal{D}\eta \exp \left[ -\frac{1}{4} \int_\tau \int_z \eta_{z,\tau}^2 \right] \int_x \left( -\frac{\delta S}{\delta \phi_{x,\tau}} + 2 \int_y r_\Lambda(\Delta_x) \delta^{(d)}(x-y) \frac{\delta}{\delta \eta_{y,\tau}} \right) \frac{\delta F[\phi]}{\delta \phi_{x,\tau}} \\
&= \left\langle \int_x \left( -\frac{\delta S}{\delta \phi_{x,\tau}} + 2 \int_y r_\Lambda(\Delta_x) \delta^{(d)}(x-y) \frac{\delta}{\delta \eta_{y,\tau}} \right) \frac{\delta F[\phi]}{\delta \phi_{x,\tau}} \right\rangle \\
&= \left\langle \int_x \left( -\frac{\delta S}{\delta \phi_{x,\tau}} + 2 \int_y r_\Lambda(\Delta_x) \delta^{(d)}(x-y) \int_w \frac{\delta \phi_{w,\tau}}{\delta \eta_{y,\tau}} \frac{\delta}{\delta \phi_{w,\tau}} \right) \frac{\delta F[\phi]}{\delta \phi_{x,\tau}} \right\rangle \\
&= \left\langle \int_x \left( -\frac{\delta S}{\delta \phi_{x,\tau}} + r_\Lambda^2(\Delta_x) \frac{\delta}{\delta \phi_{x,\tau}} \right) \frac{\delta F[\phi]}{\delta \phi_{x,\tau}} \right\rangle. \tag{A.41}
\end{aligned}$$

Here, the first equation follows from an integration by parts with respect to  $\eta$ . The third equation uses the chain rule to calculate the functional derivative of  $F$  with respect to  $\eta$ . The last equation is obtained by using the identity for the functional derivative of the field  $\phi$  with respect to  $\eta$  from (A.38). Moreover, it follows

$$\begin{aligned}
\frac{d}{d\tau} \langle F[\phi] \rangle &= \int \mathcal{D}\phi F[\phi] \frac{\partial P(\phi, \tau)}{\partial \tau} = \int \mathcal{D}\phi \left[ \int_x \left( -\frac{\delta S}{\delta \phi_x} + r_\Lambda^2(\Delta_x) \frac{\delta}{\delta \phi_x} \right) \frac{\delta F[\phi]}{\delta \phi_x} \right] P(\phi, \tau) \\
&= \int \mathcal{D}\phi F[\phi] \int_x \frac{\delta}{\delta \phi_x} \left( \frac{\delta S}{\delta \phi_x} + r_\Lambda^2(\Delta_x) \frac{\delta}{\delta \phi_x} \right) P(\phi, \tau). \tag{A.42}
\end{aligned}$$

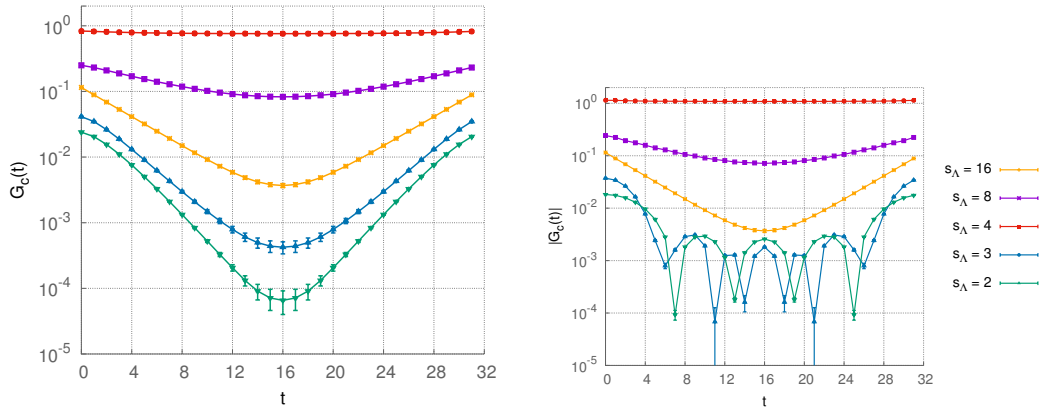


Figure A.1.: Time slice correlation functions on a  $32 \times 32$  lattice for fixed parameters  $\kappa = 0.26$  and  $\lambda = 0.02$ . The orange curve shown in both graphs is the result obtained from a Langevin simulation with white noise for cutoff  $s_\Lambda = 16$ . The full quantum theory is in the symmetric phase for the given choice of parameters. (Left) The plot shows the correlation function of time slices using a Pauli-Villars regularization function for different cutoffs. Halving the maximum lattice momentum cutoff to  $s_\Lambda = 8$  yields the violet curve showing that the mass decreases. It becomes minimal for  $s_\Lambda = 4$  where the theory is close to the critical point and the correlator is flat, see the red curve. Decreasing the cutoff further to  $s_\Lambda = 3$  and  $s_\Lambda = 2$  respectively shows that the correlator decays stronger again meaning that the mass in lattice units grows, but now with the theory being in the broken phase. (Right) The same setup as on the left is shown but here the sharp cutoff (3.3) is used. Note that for  $s_\Lambda = 2, 3$  the correlator resembles a Bessel function which is an artifact of the noise correlation (A.32).

The last equation is obtained by functional integration by parts with respect to  $\phi$ . Thus, we arrive at the Fokker-Planck equation for the stochastic process with colored noise

$$\frac{\partial}{\partial \tau} P[\phi, \tau] = \int d^d x \frac{\delta}{\delta \phi_x} \left( \frac{\delta S}{\delta \phi_x} + r_\Lambda^2(\Delta_x) \frac{\delta}{\delta \phi_x} \right) P(\phi, \tau). \quad (\text{A.43})$$

#### A.4.2. Alternative regularization functions

The regularization scheme used in [163] is a Pauli-Villars regularization with cutoff parameter  $\Lambda$ . Explicitly, the regularization function is defined as

$$r_\Lambda(\Delta_x) = \left( 1 - \frac{\Delta_x}{\Lambda^2} \right)^{-1}. \quad (\text{A.44})$$

For most purposes it suffices to use the sharp regulator introduced in (3.3). However for certain cases, smooth regularization functions such as the Pauli-Villars type cutoff (A.44) or smooth approximations to the sharp cutoff may be required. A crucial disadvantage of the sharp cutoff is that it gives rise to artifacts appearing in the noise correlation function,

as discussed for the continuum in Appendix A.3. Those are clearly visible in the correlation functions of time slices and pose difficulties, for instance to the determination of masses because standard exponential fit techniques are not applicable. The lattice version of the Pauli-Villars regularization function reads

$$r_{\tilde{s}_\Lambda}(\tilde{p}^2) := \left(1 - \frac{\tilde{p}^2}{\tilde{s}_\Lambda^2}\right)^{-m} \delta_{x,y}, \quad (\text{A.45})$$

where  $m \in \mathbb{N}$  as introduced in [163]. Here ” $\sim$ ” refers to the physical momenta introduced in (A.8). Alternatively, a smooth approximation to the sharp regulator on the lattice reads

$$r_{\tilde{s}_\Lambda}(\tilde{p}^2) := \frac{1}{2} \left(1 - \tanh \left[ \alpha \left( \frac{\tilde{p}^2}{\tilde{s}_\Lambda^2} - 1 \right) \right] \right), \quad (\text{A.46})$$

where the parameter  $\alpha \in \mathbb{R}_+$  can be tuned to vary the steepness around the cutoff momentum. Both of the regulator functions mentioned here are currently under study. They may reduce the above mentioned artifacts arising from the use of the sharp regulator. However, throughout the course of this work, we use the sharp regulator for all quantitative studies. Smooth regulators are only used in this section to illustrate a qualitatively different behaviour visible in the observables.

We discuss the effects of different choices of the regularization function by means of the two-point correlation function of time slices shown in Fig. A.1. The correlators were computed for parameters  $\kappa = 0.26$ ,  $\lambda = 0.02$  on a  $32 \times 32$  lattice, that is for the same choice as for Fig. 3.6. Note, that the curves are represented in logarithmic scaling. The orange curve visible in both plots was computed in a simulation with Gaussian white noise ( $s_\Lambda = 16$ ) and reproduces the hyperbolic cosine behaviour, typical for lattice correlators. The remaining correlators were produced in simulations with colored noise. The left plot in Fig. A.1 stems from a simulation with a smooth Pauli-Villars regularization function. The external parameters  $\kappa$  and  $\lambda$  are chosen such that by cutting off ultraviolet modes we interpolate between the phases of the theory. Close to the phase transition the mass in lattice units approaches zero. This is consistent with the flattening of the correlation functions, see the violet ( $s_\Lambda = 8$ ) and the red curve ( $s_\Lambda = 4$ ). For  $s_\Lambda = 2, 3$ , see the green and blue curve, the theory is in the broken phase and the correlator bends for small Euclidean times losing its typical exponential shape. This is a sign of an imprint of the regularization function in the correlator well visible for small  $s_\Lambda$ . This observation is also in agreement with the fact that the colored noise is correlated in Euclidean space-time. Moreover, consistently in the broken phase the mass grows again. For large Euclidean times the correlator also seems to retain the exponential behaviour. This might allow for the application of fits to extract mass values or the calculation of effective masses.

The right hand side of Fig. A.1 shows the same setup as on the left but for the sharp regularization function (3.3). For intermediate  $s_\Lambda = 4, 8$ , see the red and violet curve, the results qualitatively agree with the corresponding results obtained with the Pauli-Villars regularization. For small  $s_\Lambda = 2, 3$  however, see the green and blue curve, the correlator shapes differ. Although at small Euclidean times the correlator bends similarly, at larger times it oscillates. For illustrative reasons we show the modulus of the correlator  $|G_c(t)|$ . The sharp regularization function leaves an artifact imprinting a Bessel-like shape on the correlator, see also the discussion in Appendix A.3. The qualitative behaviour of the mass or correlation length agrees for both regularization functions used here. In Fig. A.1 we do not show the classical correlation function since it is trivially zero. This is due to the

gradient flow driving the field values into the classical minimum approaching a constant value as  $\tau \rightarrow \infty$ .

Relation to the FRG

## A.5. Stochastic regularization and the FRG

Using the sharp momentum cutoff

$$r_\Lambda(p^2) = \theta(\Lambda^2 - p^2), \quad (\text{A.47})$$

in the Fokker-Planck equation (3.2) allows for a simple relation of Stochastic Quantization with colored noise with functional renormalization group equations. To that end we write the probability distribution  $P(\phi, \tau)$  in (3.2) for  $\tau \rightarrow \infty$  as

$$P_\Lambda(\phi, \tau) = \exp(-S - \Delta S_\Lambda), \quad (\text{A.48})$$

where  $\Delta S_\Lambda$  is defined in (3.5). Inserting (A.48) with (3.5) into (3.2) leads to the fixed point equation  $\partial_\tau P_\Lambda = 0$  in momentum space with

$$\left[ (1 - r_\Lambda(p)) \frac{\delta S}{\delta \phi_p} - r_\Lambda(p) \frac{\delta \Delta S_\Lambda}{\delta \phi_p} \right] P_\Lambda(\phi, \tau) = 0. \quad (\text{A.49})$$

With  $(1 - r_\Lambda)r_\Lambda \equiv 0$  the two parts on the left hand side of (A.49) have to vanish separately. Now we use that

$$1 - r_\Lambda(p) = \theta(p^2 - \Lambda^2), \quad (\text{A.50})$$

only applies to UV modes. Accordingly we have

$$(1 - r_\Lambda(p)) \frac{\delta S}{\delta \phi_p} P_\Lambda(\phi, \tau) = 0. \quad (\text{A.51})$$

The prefactor in (A.51) does not vanish on the ultraviolet modes that do not satisfy the equations of motion,  $\delta S / \delta \phi_p \neq 0$ . For these modes (A.51) entails that the measure has to vanish,

$$P_\Lambda(\phi_p, \tau) \Big|_{|p| > \Lambda} \stackrel{!}{=} 0, \quad (\text{A.52})$$

hence the name sharp (UV) cutoff. (A.52) requires a diverging  $\Delta S_\Lambda$  for the ultraviolet modes with  $p^2 > \Lambda^2$ . In turn, the cutoff term is also constrained for  $p^2 < \Lambda^2$  by (A.49) with

$$r_\Lambda(p) \frac{\delta \Delta S_\Lambda}{\delta \phi_p} = 0, \quad (\text{A.53})$$

and  $\Delta S_\Lambda$  has to vanish for the infrared modes. A simple choice for  $\Delta S_\Lambda$  with these properties is given by

$$\Delta S_\Lambda[\phi] = \frac{1}{2} \int_p \phi_p \Lambda^2 \left( \frac{1}{r_\Lambda(p)} - 1 \right) \phi_{-p}. \quad (\text{A.54})$$

This cutoff term vanishes for momentum modes with  $p^2 < \Lambda^2$  and is infinite for  $p^2 > \Lambda^2$  leading to  $P_\Lambda(\phi, \tau) = 0$ . This entails that the UV modes satisfy the classical equation of motions and no quantum effects are taken into account.

We close this section with the remark that smooth cutoff functions  $r_\Lambda(p)$  for the noise do not lead to a measure of the type (A.48), as the related integrability relations are violated. This has been already observed in [163] in a different context.

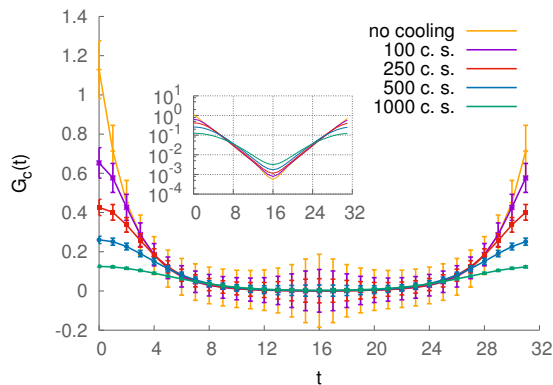


Figure A.2.: Equilibrium configurations from Langevin simulations with white noise are smoothed using the gradient flow. The correlation function of time slices  $G_c(t)$  shows a similar behaviour as the colored noise result in Fig. A.1.

## A.6. Gradient flow vs. colored noise

In this section, we briefly and qualitatively focus on the analogous behaviour of the gradient flow and the Langevin evolution with colored noise. Thereto, we consider a one-dimensional real scalar field theory and measure field configurations from a Langevin evolution with white noise. The configurations are stored and smoothed by means of the gradient flow. At each cooling step observables and corresponding errors are calculated. In Fig. A.2 the two-point correlation function of time slices is depicted. The number of configurations is of  $N_{\text{cf}} \approx O(10^4)$  for  $\kappa = 0.47$ ,  $\lambda = 0.01$  and lattice size  $N = 32$ . As configurations are smoothed by the gradient flow the errorbars shrink. To visualize this here, the errorbars are magnified by a factor  $\sqrt{N_{\text{cf}}}$ . In comparison with the result obtained using the sharp regulator in Fig. A.1 we find the same behaviour of the correlator at small Euclidean times. As the configurations are cooled the correlator bends. This signalizes the effect of a heat diffusion equation which has been investigated in [152] in the context of a massless scalar theory in  $d$  dimensions. Note that the gradient flow for a scalar theory has exactly the form of a heat diffusion equation.

## B. Lefschetz Thimbles and CLE

Here, we summarize a study on combining the Complex Langevin evolution with Lefschetz thimbles. In addition, some derivations for expressions used in Chapter 4 are carried out.

### B.1. Partition function weights

Here we give the derivation of (4.17).

$$\begin{aligned}
 \frac{Z_1^r}{Z_2^r} &= \frac{\int_a^b d\tau e^{-\text{Re}[S_1(\tau)]}}{\int_a^b d\tau e^{-\text{Re}[S_2(\tau)]}} \\
 &= \frac{\int_a^b d\tau e^{-\text{Re}[S_1(\tau)+S_2(\tau)-S_2(\tau)]}}{\int_a^b d\tau e^{-\text{Re}[S_2(\tau)]}} \\
 &= \frac{\int_a^b d\tau e^{-\text{Re}[S_2(\tau)]} e^{\text{Re}[S_2(\tau)-S_1(\tau)]}}{\int_a^b d\tau e^{-\text{Re}[S_2(\tau)]}} \\
 &= \left\langle e^{\text{Re}[S_2(\tau)-S_1(\tau)]} \right\rangle_2^r. \tag{B.1}
 \end{aligned}$$

This derivation of the case given in (B.1) requires two presuppositions

- The flow parameters on both thimbles can be identified. We normalize the steepest descent equation in order to automatically fulfill this requirement. Note that for cases where different parametrizations occur, instead of one flow parameter  $\tau$ , there will be  $\tau_1$  and  $\tau_2$  and the derivative  $d\tau_1/d\tau_2$  should be taken into account. However, for practical purposes it should be possible to normalize the steepest descent equations such that  $\tau_1 = \tau_2$ .
- The integration boundaries are the same. This can be enforced easily by variable changes in the integral, see App. B.2. Note that if the integration boundaries are the same from the beginning as for the case of (B.1), then there will be no overlap problem, since the fixed points give the main contribution on the thimbles and we chose our parametrization such that all fixed points correspond to  $\tau = 0$ . Hence the peaks of the distributions are at the same point.

### B.2. Mapping integration ranges

If different thimbles have different parameter ranges, one has to map all of them to the same interval, here we choose the interval  $[0, 1]$ . In case of an integral in the range  $[a, b]$ , a simple linear shift is enough. For an integral over  $\tau \in [-\infty, a]$ , one possible transformation is

$$x \rightarrow x' = 1 + \tanh(\xi(x - a)), \tag{B.2}$$

conversely for  $\tau \in [a, \infty]$ , the analogue is

$$x \rightarrow x' = \tanh(\xi(x - a)) , \quad (\text{B.3})$$

and for  $\tau \in [-\infty, \infty]$  the mapping becomes

$$x \rightarrow x' = \frac{1 + \tanh(\xi x)}{2} , \quad (\text{B.4})$$

where the parameter  $\xi$  can be chosen such that the overlap of the distributions in (B.1) is maximal and hence the overlap problem becomes small. The Jacobian of the transformation can then be absorbed in the action for the Monte Carlo simulation. We chose this transformation in the case of the U(1) one link model, where we chose  $\xi = 1.5$ . We only choose such transformations that have sufficiently fast falloff at the boundaries such that those regions are suppressed exponentially.

### B.3. Combining the CLE and Lefschetz thimbles

As there are many complicated steps for simulations on thimbles, it is desirable to find simpler alternatives, which at best can be applied blindly. One natural idea [125, 181, 198–200] is to combine the complex Langevin evolution with the Lefschetz thimbles. A combination of both equations is only consistent after an appropriate coordinate transformation. The latter can adaptively be generated during the combined Langevin and gradient flows. Due to its similarity to standard cooling algorithms as well as the gauge cooling we call this process *Lefschetz cooling*.

Despite its full success described below in particular for simple Gaussian models it is only partially successful in more complicated models, notably already the  $z^4$  model. While the method is not fully successful yet, in our opinion it is still a very interesting one to pursue. Its potential power is the self-adaptive *local* nature of the simulation steps. However, this also poses the biggest conceptual question: How does such a local procedure capture the global nature of the intersection numbers  $n_\sigma$  in (2.31) correctly? Note that besides its formal importance this question could be practically less important as it seems: in most models under investigation so far we have  $n_\sigma = 1$ .

Below, we list some ideas putting Lefschetz cooling to work and discuss their viability and applications. While none of those proposed ideas so far have managed to give quantitative correct results for observables, they provide useful insight into possible realizations of the approach.

#### B.3.1. Variable transformations

We aim to make the complex Langevin evolution compatible with constraints characterizing the Lefschetz thimbles by means of variable transformations. The latter have been investigated in combination with the complex Langevin evolution in a different context in [102]. There it was shown that the complex Langevin evolution including a transformation can give correct results while failing in the original formulation of the problem. Here we pursue the idea of having flow time-dependent variable transformations to transform the complex Langevin evolution towards the thimbles of the theory. This approach is natural in the sense that complex Langevin should already be able to sample the relevant fixed points [124], note that this is in a similar spirit as for the contraction algorithm [127].

By forcing the complex Langevin evolution close to thimbles the sign problem should be weakened and parameter regions that have been inaccessible so far may be reached. In the following discussion we consider again one-dimensional integrals. One rather general ansatz for such variable transformation is the Möbius transformation

$$z(u) := \frac{au + b}{cu + d}. \quad (\text{B.5})$$

This rather general ansatz has four  $\tau$ -dependent parameters that have to be determined during the simulation. This turns out to be a rather challenging task. We find that the transformation (B.5) seems to introduce repulsive structures destabilizing the evolution. Hence, we focus on a special Möbius transformation, namely a rotation

$$z(u) := ue^{i\theta}, \quad (\text{B.6})$$

where  $u$  takes the role of the (complex) field variable and  $\theta$  is a  $\tau$ -dependent parameter. Consider a point in the complex plane sufficiently close to the thimble. Then, a rotation suffices to map this point even closer to or onto the thimble. This indicates that the transformation (B.6) is both necessary and sufficient for fulfilling the constraints mentioned above. For the remaining part of this appendix we always refer to the rotation (B.6) when discussing variable transformations.

### B.3.2. Lefschetz cooling

Thimbles are curves passing through the fixed points and along them the imaginary part of the action is constant. This gives rise to various constraints which we impose onto the complex Langevin evolution by including the variable transformation (B.6).

Let  $u \in \mathbb{C}$  and  $\theta \in \mathbb{R}$ . The transformed action reads

$$S_u := S(z(u)) - \log(z'(u)). \quad (\text{B.7})$$

The procedure here is to be understood as a passive transformation, see the appendix in [102]. Hence, the complex Langevin equation in the transformed variables becomes

$$\partial_\tau u = -\frac{\partial S_u}{\partial u} + \eta, \quad (\text{B.8})$$

where  $\eta \in \mathbb{R}$ .

In the following we investigate how the  $\tau$ -dependent transformation parameter  $\theta$  evolves under the dynamics induced by different constraints.

#### Lefschetz cooling the transformed thimbles

First, we formulate the additional constraint completely in the transformed theory [198], i.e. we demand

$$\text{Im}(S_u) = \text{const}. \quad (\text{B.9})$$

This constrains the evolution close to the thimbles in the transformed theory. By taking the total  $\tau$  derivative of this equation we obtain

$$\text{Im} \left( \frac{\partial S_u}{\partial u} \dot{u} \right) + \text{Im} \left( \frac{\partial S_u}{\partial \theta} \right) \dot{\theta} = 0. \quad (\text{B.10})$$

By inserting the Langevin evolution (B.8) we get the time evolution of the angle  $\theta$

$$\frac{\partial\theta}{\partial\tau} = \frac{\text{Im}\left(\left(\frac{\partial S_u}{\partial u}\right)^2\right)}{\text{Im}\left(\frac{\partial S_u}{\partial\theta}\right)}. \quad (\text{B.11})$$

### Lefschetz cooling the original thimbles

Alternatively, we may formulate the constraint in the original theory which yields

$$\text{Im}(S_z) = \text{const}. \quad (\text{B.12})$$

Again taking the total derivative and inserting (B.8) the evolution for  $\theta$  becomes

$$\frac{\partial\theta}{\partial\tau} = \frac{\text{Im}\left(\frac{\partial S_z}{\partial z} \frac{\partial z}{\partial u} \frac{\partial S_u}{\partial u}\right)}{\text{Im}\left(\frac{\partial S_z}{\partial z} \frac{\partial z}{\partial\theta}\right)}. \quad (\text{B.13})$$

### Applicability

On both, the original and the transformed thimbles one can see that the denominator in the evolution equations for  $\theta$  in (B.11) and (B.13) introduces poles.

We analyze these in the representation of the original variable  $z$  and show the denominators of (B.11) and (B.13) for the  $z^4$  model respectively in Fig. B.1.

Those poles destabilize the numerical simulations and so far we have not found a way to resolve this. Our efforts for improvements include modifications to the noise term such that the poles are penalized, i.e. one can multiply the noise by the denominator of (B.11) or (B.13) respectively. However, this (i) leads to wrong expectation values and (ii) prohibits the Langevin evolution from jumping between the contributing thimbles. This prevents sampling of the correct thimble weights. In simple models such as the one-site Gaussian model

$$S(z) = \frac{\sigma}{2} z^2, \quad (\text{B.14})$$

(ii) is not a problem, since the model has only one thimble and (i) can be resolved by a linear rescaling. This is however due to the low complexity and high symmetry of the model and does not generalize.

### B.3.3. Advanced Lefschetz cooling

Instead of explicitly demanding the thimble constraint to be fulfilled, it is possible to directly combine the complex Langevin evolution with the steepest descent equations.

$$\begin{aligned} \frac{\partial u}{\partial\tau} &= -\frac{\partial S_u}{\partial u} + \eta \\ \frac{\partial u}{\partial\tau} &= -\overline{\frac{\partial S_u}{\partial u}}. \end{aligned} \quad (\text{B.15})$$

Here the idea is that complex Langevin already takes into account all relevant fixed points and the steepest descent equation keeps the evolution close to the thimbles, alleviating the sign problem. Taking the difference of the previous two equations implies that the

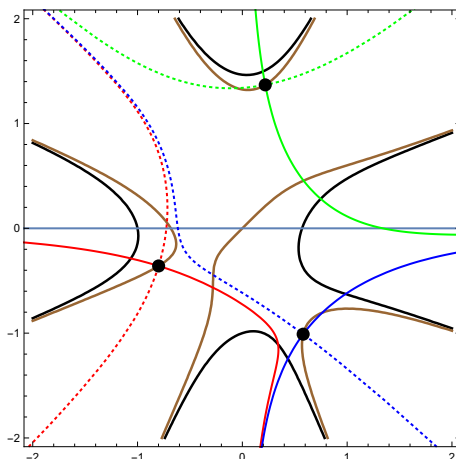


Figure B.1.: Pole and thimble structure for the  $z^4$  model enforcing the two constraints (B.9) and (B.12), each represented in the original variable  $z$ . Red, green and blue solid (dashed) lines are the (anti-)thimbles and black points denote the fixed points. The brown solid lines are the poles from the constraint  $\text{Im}[S_z] = \text{const}$ , while the black solid lines represent the poles from the constraint  $\text{Im}[S_u] = \text{const}$ .

imaginary part of  $u$  remains constant which reduces the evolution in  $u$  to real Langevin. Hence we have

$$0 = \frac{\partial S_u}{\partial u} - \overline{\frac{\partial S_u}{\partial u}} \Rightarrow \partial_\tau \text{Im}(u) = 0. \quad (\text{B.16})$$

This leads to the following evolution equation for  $u$  and conditions to the angle  $\theta$ . Thus we find by using the action as given in (B.7)

$$\partial_\tau \text{Re } u = -\text{Re} \frac{\partial S_u}{\partial u} + \eta$$

and

$$\partial_\tau \text{Im } u = -\text{Im} \frac{\partial S_u}{\partial u} = -\text{Im} \left( \frac{\partial S}{\partial z} z' - \frac{z''}{z'} \right) = 0. \quad (\text{B.17})$$

Note that here we explicitly see, why a rotation should be sufficient. We illustrate this by means of the Gaussian model (B.14). It holds that  $z' = e^{i\theta}$ ,  $z'' = 0$  leading to the following expression for the constraint in (B.17)

$$\text{Im}(\sigma z z') = \text{Im}(\sigma e^{2i\theta} u) = 0. \quad (\text{B.18})$$

Here,  $u \in \mathbb{R}$  and with  $\sigma = \sigma_r e^{i\theta_\sigma}$  the solution to (B.18) becomes

$$\theta^* = -\frac{1}{2} \theta_\sigma. \quad (\text{B.19})$$

This rotates the thimble in the original theory precisely onto the real axis of the transformed theory.

Next, we investigate how  $\theta$  changes with the flow induced by (B.16). Hence, we take the total  $\tau$  derivative of (B.16), yielding

$$\frac{d}{d\tau} \text{Im} \left( \frac{\partial S_u}{\partial u} \right) = 0. \quad (\text{B.20})$$

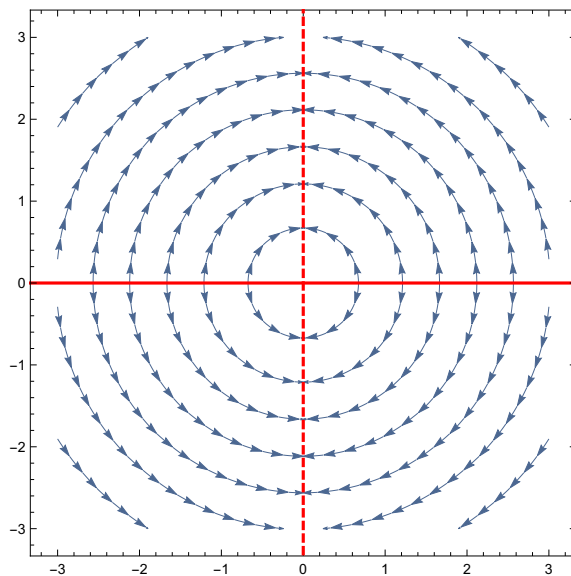


Figure B.2.: Visualization of the rotation of the complex plane for the Gaussian model with  $\sigma = 1 + i$  according to (B.23) after rotating the thimble onto the real axis. The arrows point in the direction of rotation. Here, the transformed thimble is the real axis (solid red line, repulsive), while the anti-thimble is the imaginary axis (dashed red line, attractive).

This leads to

$$\text{Im} \left( \frac{\partial^2 S_u}{\partial u^2} \dot{u} \right) + \text{Im} \left( \frac{\partial^2 S_u}{\partial u \partial \theta} \right) \dot{\theta} = 0, \quad (\text{B.21})$$

from which we find

$$\dot{\theta} = \frac{\text{Im} \left( \frac{\partial^2 S_u}{\partial u^2} \frac{\partial S_u}{\partial u} \right)}{\text{Im} \left( \frac{\partial^2 S_u}{\partial u \partial \theta} \right)}, \quad (\text{B.22})$$

upon inserting the drift term for  $\dot{u}$ . In this form, the dynamics are unstable. For instance in the Gaussian model, where the (anti-)thimble is a straight line this manifests itself by a diverging evolution along the anti-thimble to infinity. (B.19) rotates the thimble onto the real axis and transforms the anti-thimble into the imaginary axis.

Inserting the action of the Gaussian model into (B.22) we find

$$\dot{\theta} = \frac{1}{\sigma_r} \sin(\theta_\sigma + 2\theta). \quad (\text{B.23})$$

Examining the numerical solution to the previous equation we easily see that the thimble is repulsive whereas the anti-thimble is attractive, see Fig. B.2 for an illustration represented in the transformed theory.

To render the thimbles attractive we consider again (B.21). Replacing  $\dot{u}$  by the Langevin

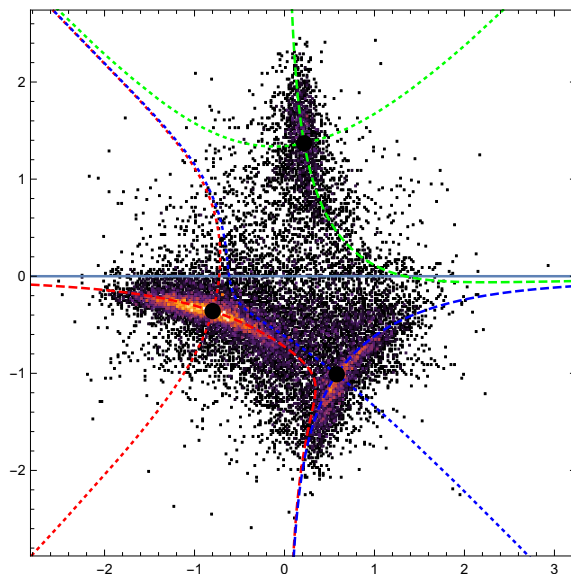


Figure B.3.: Scatter plot of the combined complex Langevin evolution and thimble constraint dynamics in  $\theta$  with the reversed sign mapping, see (B.24) and the discussion in the text. The proposed method is being applied to the  $z^4$  model and the evolution is represented in the original variable  $z$ . The scatter plot is color coded, where black corresponds to low density and yellow corresponds to high density. The mapping enforces the sampling of all relevant thimbles, as well as allowing for transitions between them and guarantees stability.

drift with a reversed sign  $+\partial S_u/\partial u$  reverses the sign in (B.22) yielding

$$\dot{\theta} = -\frac{\text{Im}\left(\frac{\partial^2 S_u}{\partial u^2} \frac{\partial S_u}{\partial u}\right)}{\text{Im}\left(\frac{\partial^2 S_u}{\partial u \partial \theta}\right)}. \quad (\text{B.24})$$

This also enables and enforces hopping between the thimbles and inverts the stability properties of the fixed points. Note that the evolution in  $u$  is still governed by the complex Langevin equation B.8).

Therefore, inserting the sign-reversed drift for  $u$  in (B.22) can be understood in the sense of a mapping with the following properties: it guarantees that the evolution stays close to the thimbles, as well as allowing for transitions between different contributing thimbles. This approach yields the correct result for the Gaussian model. However, once the thimble structure becomes slightly more complicated, the values of observables are not computed correctly. This has been tested for different actions in [181, 199]. While the procedure samples all thimbles, it does not correctly take into account their relative weights. Fig. B.3 shows a scatter plot of the  $\tau$ -evolution applied to the  $z^4$  model. Clearly, this algorithm samples all thimbles. But the contributing ones are being sampled with a higher weight, see the yellow regions in the scatter plot.

## C. Imaginary times

In this appendix we present technical details and derivations of quantities relevant for the discussion in Chapter 6.

### C.1. Quantum mechanical anharmonic oscillator

In the following we derive a non-perturbative quantum statistical expression for the two-point correlation function for the quantum mechanical anharmonic oscillator. This will be carried out by representing the system in terms of a complete set of energy eigenstates of the fully interacting Hamiltonian. From this we can extract semi-exactly<sup>1</sup> the spectral function of the theory at arbitrary couplings.

**Remark:** The following derivation stems from the author's notes compiled in April 2018 which was cross-checked and independently written down by the author's collaborator who presented the derivation also in his Master's thesis [183].

Since here we are considering explicitly quantum mechanics, we use the standard textbook conventions and work in SI-units [201, 202]. In the end of this section we will convert all expressions to natural units for a better comparison with the formulas in ch. 6 which are in field theory language.

#### C.1.1. Harmonic oscillator

We review the standard quantum mechanical harmonic oscillator the algebraic solution in the space of energy-eigenstates. The energy-eigenstate basis will then be used to write down the Hamiltonian for the anharmonic oscillator in matrix form in the next sub-section. The Hamiltonian of the harmonic oscillator reads

$$\hat{H}_0 = \frac{\hat{p}^2}{2m} + \frac{m\omega^2}{2}\hat{x}^2 \quad (\text{C.1})$$

Here,  $\omega$  denotes the (angular) frequency of the oscillator. Recall the canonical commutation relation

$$[\hat{x}, \hat{p}] = i\hbar \quad (\text{C.2})$$

The annihilation and creation operators are defined as

$$\hat{a} = \frac{1}{\sqrt{2}} \left( \sqrt{\frac{m\omega}{\hbar}} \hat{x} + i \frac{1}{\sqrt{m\hbar\omega}} \hat{p} \right) \quad (\text{C.3})$$

$$\hat{a}^\dagger = \frac{1}{\sqrt{2}} \left( \sqrt{\frac{m\omega}{\hbar}} \hat{x} - i \frac{1}{\sqrt{m\hbar\omega}} \hat{p} \right). \quad (\text{C.4})$$

---

<sup>1</sup> By semi-exactly we mean that we will rely on a truncation in the energy-eigenstate basis followed by numerical diagonalization of the Hamiltonian.

The position and momentum operator in terms of the annihilation and creation operators read

$$\hat{x} = \sqrt{\frac{\hbar}{2m\omega}}(\hat{a} + \hat{a}^\dagger) \quad (\text{C.5})$$

$$\hat{p} = i\sqrt{\frac{m\hbar\omega}{2}}(\hat{a}^\dagger - \hat{a}). \quad (\text{C.6})$$

The annihilation and creation operators fulfill the following commutation relation

$$[\hat{a}, \hat{a}^\dagger] = 1. \quad (\text{C.7})$$

Plugging the relations (C.6) into (C.1) and using (C.7) yields for the Hamiltonian

$$\hat{H}_0 = \hbar\omega \left( \frac{1}{2} + \hat{N} \right), \quad (\text{C.8})$$

where

$$\hat{N} := \hat{a}^\dagger \hat{a} \quad (\text{C.9})$$

denotes the occupation number operator. Let  $|n\rangle$  denote the eigenstate to  $\hat{N}$  with eigenvalue  $n \in \mathbb{N}_0$ . We can use the basis  $\{|n\rangle\}$  to express the energy eigenvalues and eigenstates of the Hamiltonian as follows

$$\hat{H}_0 |n\rangle = \hbar\omega \left( \hat{N} + \frac{1}{2} \right) |n\rangle = \hbar\omega \left( n + \frac{1}{2} \right) |n\rangle = E_n^{(0)} |n\rangle \quad (\text{C.10})$$

Last, we write down how the annihilation and creation operators act on the occupation number / energy eigenstates

$$\hat{a}^\dagger |n\rangle = \sqrt{n+1} |n+1\rangle \quad (\text{C.11})$$

$$\hat{a} |n\rangle = \sqrt{n} |n-1\rangle. \quad (\text{C.12})$$

### C.1.2. Anharmonic oscillator and energy eigenspace

With the toolkit introduced in the previous sub-section we can now tackle the anharmonic oscillator whose Hamiltonian is given by

$$\hat{H} = \hat{H}_0 + \hat{H}_\lambda = \frac{\hat{p}^2}{2m} + \frac{m\omega^2}{2}\hat{x}^2 + \frac{\lambda}{24}\hat{x}^4. \quad (\text{C.13})$$

We rewrite this in terms of the annihilation and creation operators. This will be useful to express the matrix elements of (C.13) in the basis  $\{|n\rangle\}$  of the harmonic oscillator described above. Here it is useful to perform the operations of products of annihilation and creation operators on the  $|n\rangle$  basis states with  $n \in \mathbb{N}_0$  analytically. That is we need to expand and simplify (C.13) as far as possible before truncating the energy eigenstate basis when diagonalizing the Hamiltonian numerically. In the end, i.e. when having received all the matrix we need to truncate the number of basis states used for the numerical diagonalization of  $\hat{H}$  to some number  $k \in \mathbb{N}$ . If one directly takes the matrix product of the  $|n\rangle$  representation of the operators  $\hat{a}, \hat{a}^\dagger$  in that truncation one ends up with a larger systematic error than if one first computes everything analytically as far as possible

without the truncation. Using the creation and annihilation operators the full Hamiltonian reads

$$\hat{H} = \hbar\omega \left( \hat{a}^\dagger \hat{a} + \frac{1}{2} \right) + \frac{\lambda}{24} \frac{\hbar^2}{4m^2\omega^2} (\hat{a} + \hat{a}^\dagger)^4. \quad (\text{C.14})$$

Now the quartic term is expanded as follows

$$\begin{aligned} (\hat{a} + \hat{a}^\dagger)^4 &= (\hat{a} + \hat{a}^\dagger)^2 (\hat{a} + \hat{a}^\dagger)^2 \\ &= (\hat{a}\hat{a} + 1 + 2\hat{N} + \hat{a}^\dagger\hat{a}^\dagger)^2 \\ &= \hat{a}\hat{a}\hat{a}\hat{a} + 2(\hat{a}\hat{a} + \hat{a}^\dagger\hat{a}^\dagger) + 4\hat{N} + 2(\hat{a}\hat{a}\hat{N} + \hat{N}\hat{a}\hat{a}) + 4\hat{N}\hat{N} \\ &\quad + 2(\hat{a}^\dagger\hat{a}^\dagger\hat{N} + \hat{N}\hat{a}^\dagger\hat{a}^\dagger) + \hat{a}\hat{a}\hat{a}^\dagger\hat{a}^\dagger + \hat{a}^\dagger\hat{a}^\dagger\hat{a}\hat{a} + \hat{a}^\dagger\hat{a}^\dagger\hat{a}^\dagger\hat{a}^\dagger + 1 \end{aligned} \quad (\text{C.15})$$

where from the first to the second equation we have used the definition of the occupation number operator (C.9) as well as the commutation relation for the annihilation and creation operator (C.7). Next, we use that

$$\hat{a}\hat{a}\hat{a}^\dagger\hat{a}^\dagger = \hat{a}(1 + \hat{a}^\dagger\hat{a})\hat{a}^\dagger = \hat{a}\hat{a}^\dagger + \hat{a}\hat{N}\hat{a}^\dagger \quad (\text{C.16})$$

$$\hat{a}^\dagger\hat{a}^\dagger\hat{a}\hat{a} = \hat{a}^\dagger\hat{N}\hat{a} \quad (\text{C.17})$$

which yields

$$\hat{a}\hat{a}\hat{a}^\dagger\hat{a}^\dagger + \hat{a}^\dagger\hat{a}^\dagger\hat{a}\hat{a} = 1 + \hat{N} + \hat{a}\hat{N}\hat{a}^\dagger + \hat{a}^\dagger\hat{N}\hat{a}. \quad (\text{C.18})$$

Plugging the latter formula into (C.15) we find

$$\begin{aligned} (\hat{a} + \hat{a}^\dagger)^4 &= \hat{a}\hat{a}\hat{a}\hat{a} + 2(\hat{a}\hat{a} + \hat{a}^\dagger\hat{a}^\dagger) + 5\hat{N} + 2 + \hat{a}\hat{N}\hat{a}^\dagger + \hat{a}^\dagger\hat{N}\hat{a} \\ &\quad + 2(\hat{a}\hat{a}\hat{N} + \hat{N}\hat{a}\hat{a}) + 4\hat{N}\hat{N} \\ &\quad + 2(\hat{a}^\dagger\hat{a}^\dagger\hat{N} + \hat{N}\hat{a}^\dagger\hat{a}^\dagger) + \hat{a}^\dagger\hat{a}^\dagger\hat{a}^\dagger\hat{a}^\dagger. \end{aligned} \quad (\text{C.19})$$

Next, we write down the matrix elements of all terms appearing in (C.19) in the  $|n\rangle$  basis. It holds

$$\langle m | \hat{a}\hat{a}\hat{a}\hat{a} | n \rangle = \sqrt{n}\sqrt{n-1}\sqrt{n-2}\sqrt{n-3}\delta_{m,n-4}, \quad (\text{C.20})$$

$$\langle m | 2(\hat{a}\hat{a} + \hat{a}^\dagger\hat{a}^\dagger) | n \rangle = 2(\sqrt{n}\sqrt{n-1}\delta_{m,n-2} + \sqrt{n+1}\sqrt{n+2}\delta_{m,n+2}), \quad (\text{C.21})$$

$$\langle m | 4\hat{N}\hat{N} + 5\hat{N} + 2 | n \rangle = (4n^2 + 5n + 2)\delta_{m,n}, \quad (\text{C.22})$$

$$\langle m | \hat{a}\hat{N}\hat{a}^\dagger + \hat{a}^\dagger\hat{N}\hat{a} | n \rangle = (2n^2 + n + 1)\delta_{m,n}, \quad (\text{C.23})$$

$$\langle m | 2(\hat{a}\hat{a}\hat{N} + \hat{N}\hat{a}\hat{a}) | n \rangle = 2(n\sqrt{n}\sqrt{n-1} + \sqrt{n}\sqrt{n-1})(n-2)\delta_{m,n-2}, \quad (\text{C.24})$$

$$\langle m | 2(\hat{a}^\dagger\hat{a}^\dagger\hat{N} + \hat{N}\hat{a}^\dagger\hat{a}^\dagger) | n \rangle = 2(n\sqrt{n+1}\sqrt{n+2} + \sqrt{n+1}\sqrt{n+2})(n+2)\delta_{m,n+2}, \quad (\text{C.25})$$

$$\langle m | \hat{a}^\dagger\hat{a}^\dagger\hat{a}^\dagger\hat{a}^\dagger | n \rangle = \sqrt{n+1}\sqrt{n+2}\sqrt{n+3}\sqrt{n+4}\delta_{m,n+4}. \quad (\text{C.26})$$

With these ingredients the matrix elements of the Hamiltonian read

$$\begin{aligned}
\langle m | \hat{H} | n \rangle &= \hbar\omega \left( n + \frac{1}{2} \right) \delta_{m,n} \\
&+ \frac{\lambda}{24} \frac{\hbar^2}{4m^2\omega^2} \left[ \left( 6n^2 + 6n + 3 \right) \delta_{m,n} + 2(2n-1)\sqrt{n}\sqrt{n-1}\delta_{m,n-2} \right. \\
&+ 2(2n+3)\sqrt{n+1}\sqrt{n+2}\delta_{m,n+2} + \sqrt{n+1}\sqrt{n+2}\sqrt{n+3}\sqrt{n+4}\delta_{m,n+4} \\
&\left. + \sqrt{n}\sqrt{n-1}\sqrt{n-2}\sqrt{n-3}\delta_{m,n-4} \right]. \tag{C.27}
\end{aligned}$$

### C.1.3. Quantum statistics for the QM-AHO

#### The retarded propagator

Let  $\{|\phi_n\rangle\}$  denote the basis of energy eigenstates that belong to the fully interacting Hamiltonian. That is they fulfill the following eigenvalue relation

$$\hat{H} |\phi_n\rangle = E_n |\phi_n\rangle. \tag{C.28}$$

The partition function reads

$$Z = \text{tr}(e^{-\beta\hat{H}}) = \sum_n \langle \phi_n | e^{-\beta E_n} | \phi_n \rangle = \sum_n e^{-\beta E_n} \tag{C.29}$$

where we have expressed the trace in terms of the energy eigenstate basis. For the two-point correlation function we compute

$$\langle \hat{x}(t_2)\hat{x}(t_1) \rangle = \frac{1}{Z} \text{tr} \left( e^{-\beta\hat{H}} \hat{x}(t_2)\hat{x}(t_1) \right) = \frac{1}{Z} \text{tr} \left( e^{-\beta\hat{H}} e^{i\hat{H}t_2} \hat{x} e^{-i\hat{H}(t_2-t_1)} \hat{x} e^{-i\hat{H}t_1} \right) \tag{C.30}$$

The completeness relation reads

$$\mathbb{1} = \sum_n |\phi_n\rangle \langle \phi_n|. \tag{C.31}$$

Now we insert a complete set of energy eigenstates of the fully interacting Hamiltonian into (C.30). Thus, we obtain

$$\begin{aligned}
\langle \hat{x}(t_2)\hat{x}(t_1) \rangle &= \frac{1}{Z} \sum_{n,k,l} \langle \phi_n | e^{-\beta\hat{H}} e^{i\hat{H}t_2} | \phi_k \rangle \langle \phi_k | \hat{x} e^{-i\hat{H}(t_2-t_1)} | \phi_l \rangle \langle \phi_l | \hat{x} e^{-i\hat{H}t_1} | \phi_n \rangle \\
&= \frac{1}{Z} \sum_{n,l} e^{-\beta E_n} e^{iE_n t_2} e^{-iE_l(t_2-t_1)} e^{-iE_n t_1} \langle \phi_n | \hat{x} | \phi_l \rangle \langle \phi_l | \hat{x} | \phi_n \rangle \\
&= \frac{1}{Z} \sum_{n,l} e^{-\beta E_n} e^{i(E_n - E_l)(t_2 - t_1)} |\langle \phi_l | \hat{x} | \phi_n \rangle|^2 \tag{C.32}
\end{aligned}$$

where in the step from the first to the second equation orthogonality of the states  $\langle \phi_n | \phi_k \rangle = \delta_{nk}$  has been used. We are interested in the retarded propagator [64]

$$\begin{aligned}
G_{\text{AHO}}^{(R)}(t_2, t_1) &:= -i\theta(t_2 - t_1) \langle [\hat{x}(t_2), \hat{x}(t_1)] \rangle \\
&= \frac{-i}{Z} \theta(t_2 - t_1) \sum_{n,l} e^{-\beta E_n} \left( e^{i(E_n - E_l)(t_2 - t_1)} - e^{i(E_n - E_l)(t_1 - t_2)} \right) |\langle \phi_l | \hat{x} | \phi_n \rangle|^2 \\
&= \frac{2}{Z} \theta(t_2 - t_1) \sum_{n,l} e^{-\beta E_n} \sin((E_n - E_l)(t_2 - t_1)) |\langle \phi_l | \hat{x} | \phi_n \rangle|^2. \tag{C.33}
\end{aligned}$$

### The spectral function

In thermal equilibrium the correlator depends only on the time difference  $|t_2 - t_1|$ . The Fourier transform of (C.33) yields the spectral function

$$\begin{aligned}
\rho_{\text{AHO}}(\mu) &:= \text{Im} \left[ \int_{-\infty}^{\infty} dt G_{\text{AHO}}(t, 0) e^{-i\mu t} \right] \\
&= \frac{2}{Z} \sum_{n,l} e^{-\beta E_n} |\langle \phi_l | \hat{x} | \phi_n \rangle|^2 \text{Im} \left[ \int_{-\infty}^{\infty} dt \theta(t) \sin((E_n - E_l)t) e^{-i\mu t} \right] \\
&= \frac{\pi}{Z} \sum_{n,l} e^{-\beta E_n} |\langle \phi_l | \hat{x} | \phi_n \rangle|^2 \left[ \delta(\mu - (E_l - E_n)) - \delta(\mu + E_l - E_n) \right]. \tag{C.34}
\end{aligned}$$

In the step from the second to the third equation we have used the following representation for the Fourier transform of the Heaviside-step function [203]

$$\int_{-\infty}^{\infty} dt \theta(t) e^{-i\mu t} = \pi \left( \delta(\mu) - \frac{i}{\pi} \mathbb{P} \left( \frac{1}{\mu} \right) \right) \tag{C.35}$$

where  $\mathbb{P}$  denotes the principal value. This can be used to evaluate

$$\begin{aligned}
\int_{-\infty}^{\infty} dt \theta(t) \sin(\zeta t) e^{-i\mu t} &= \frac{1}{2i} \int_{-\infty}^{\infty} dt \theta(t) (e^{-i(\mu - \zeta)t} - e^{-i(\mu + \zeta)t}) \\
&= \frac{-i\pi}{2} \left[ \delta(\mu - \zeta) - \delta(\mu + \zeta) \right] - \frac{1}{2} \left[ \mathbb{P} \left( \frac{1}{\mu - \zeta} \right) - \mathbb{P} \left( \frac{1}{\mu + \zeta} \right) \right] \tag{C.36}
\end{aligned}$$

which after taking the imaginary part and setting  $\zeta := E_n - E_l$  yields (C.34.)

By numerical diagonalization of the Hamiltonian (C.27) we change the basis from  $|n\rangle$  to  $\{|\phi_n\rangle\}$ . The differences of energy eigenvalues  $(E_l - E_n)$  yield the mass peaks in the spectral function. The eigenvectors can be used to determine the relative weights of the thermally excited states with respect to the vacuum state. Those weights are encoded in the matrix elements  $|\langle \phi_l | \hat{x} | \phi_n \rangle|^2$ .

### The vacuum limit

Next, we consider the  $T \rightarrow 0$  or  $\beta \rightarrow \infty$  limit.

$$\begin{aligned}
 \rho_{\text{AHO}}(\mu) &= \frac{\pi}{e^{-\beta E_0} + e^{-\beta E_1} + \dots} \left[ e^{-\beta E_0} \left( |\langle \phi_0 | \hat{x} | \phi_0 \rangle|^2 (\delta(\mu) - \delta(\mu)) \right. \right. \\
 &\quad \left. \left. + |\langle \phi_1 | \hat{x} | \phi_0 \rangle|^2 (\delta(\mu - (E_1 - E_0)) - \delta(\mu + E_1 - E_0)) + \dots \right) + e^{-\beta E_1} (\dots) + \dots \right] \\
 &\xrightarrow{\beta \rightarrow \infty} \frac{\pi}{e^{-\beta E_0}} \left[ e^{-\beta E_0} |\langle \phi_1 | \hat{x} | \phi_0 \rangle|^2 (\delta(\mu - (E_1 - E_0)) - \delta(\mu + E_1 - E_0)) \right] \\
 &= \pi |\langle \phi_1 | \hat{x} | \phi_0 \rangle|^2 (\delta(\mu - (E_1 - E_0)) - \delta(\mu + E_1 - E_0)). \tag{C.37}
 \end{aligned}$$

There we used that  $E_0 < E_1 < E_2 < \dots$  and thus in the limit  $\beta \rightarrow \infty$  only the groundstate contribution to  $Z = \text{tr}(\exp -\beta \hat{H})$  survives whereas the higher excited states are exponentially suppressed compared to it. The last equation in (C.37) confirms that in the  $\beta \rightarrow \infty$  limit a spectral function with a single peak is produced. In the language of field theory (and the convention  $\hbar = c = 1$ ) the physical mass of the particle is  $m_{\text{phys}} = E_1 - E_0$  which coincides with the energy difference between the ground state and the first excited state. This is analogous to a single particle excitation from the vacuum. Hence the limit (C.37) reproduces the correct vacuum spectral function of the theory.

### The imaginary time correlator

Another important quantity also relevant for comparisons with the lattice is the correlator in imaginary time. We proceed analogously to the real-time case (C.30) and study correlations of the position space operator at imaginary times  $0 \leq \tau_1 < \tau_2 \leq \beta$ . In imaginary time the Heisenberg picture operators are defined as follows [64]

$$\hat{O}(\tau) = e^{\hat{H}\tau} \hat{O} e^{-\hat{H}\tau}. \tag{C.38}$$

The derivation of the representation in terms of energy eigenstates and eigenvalues is as follows

$$\begin{aligned}
 G_\beta(\tau_2, \tau_1) &:= \langle \hat{x}(\tau_2) \hat{x}(\tau_1) \rangle = \frac{1}{Z} \text{tr} \left( e^{-\beta \hat{H}} \hat{x}(\tau_2) \hat{x}(\tau_1) \right) \\
 &= \frac{1}{Z} \text{tr} \left( e^{-\beta \hat{H}} e^{\hat{H}\tau_2} \hat{x} e^{-\hat{H}(\tau_2 - \tau_1)} \hat{x} e^{-\hat{H}\tau_1} \right) \\
 &= \frac{1}{Z} \sum_{n,l} \left( e^{-\beta E_n} e^{(E_n - E_l)(\tau_2 - \tau_1)} |\langle \phi_l | \hat{x} | \phi_n \rangle|^2 \right). \tag{C.39}
 \end{aligned}$$

Now, we set  $\tau_2 = \tau$  and  $\tau = 0$  which is of only interest for us. Using the KMS relation  $G_\beta(\tau, 0) = G_\beta(\tau + \beta, 0)$  we can manipulate (C.39) further

$$\begin{aligned}
G_\beta(\tau, 0) &= \frac{1}{2} \left( G_\beta(\tau, 0) + G_\beta(\tau + \beta, 0) \right) \\
&= \frac{1}{Z} \sum_{n,l} \frac{1}{2} \left[ \left( e^{-\beta E_n} e^{(E_n - E_l)\tau} + e^{-\beta E_n} e^{(E_n - E_l)(\tau + \beta)} \right) |\langle \phi_l | \hat{x} | \phi_n \rangle|^2 \right] \\
&= \frac{1}{Z} \sum_{n,l} \frac{1}{2} \left[ \left( e^{-\beta E_n} e^{(E_n - E_l)\tau} + e^{-\beta E_l} e^{-(E_l - E_n)\tau} \right) |\langle \phi_l | \hat{x} | \phi_n \rangle|^2 \right] \\
&= \frac{1}{Z} \sum_{n,l} \frac{1}{2} \left[ e^{-\beta E_n} \left( e^{(E_n - E_l)\tau} + e^{-(E_n - E_l)\tau} \right) |\langle \phi_l | \hat{x} | \phi_n \rangle|^2 \right] \\
&= \frac{1}{Z} \sum_{n,l} \left[ e^{-\beta E_n} \cosh((E_n - E_l)\tau) |\langle \phi_l | \hat{x} | \phi_n \rangle|^2 \right]. \tag{C.40}
\end{aligned}$$

# Acknowledgments

I want to thank many people who have supported me during the work of this thesis both on a personal and on a physics-related level.

First of all, I want to express my gratitude to my supervisor Jan M. Pawłowski. Uncountably many discussions have significantly enhanced my insight into physics and the progress of my work. His door has always been open and I have enjoyed a lot working with him in a constructive and motivating atmosphere. Without his support this thesis would not have been possible. Moreover, I am grateful for his support in participating in scientific exchange at various workshops and conferences.

I am grateful to Joerg Jaeckel for being my second referee.

My special thanks go to my collaborators Alexander Rothkopf and Ion-Olimpiu Stamatescu for discussions on physics and for sharing their knowledge on lattice simulations as well as for their advice and support during my time as a PhD student.

Moreover I am grateful to my collaborators, Manuel Scherzer, Christian Schmidt and Felix Ziesché for many discussions on Lefschetz Thimbles and productive stays in Bielefeld.

I also thank my collaborators Lukas Kades, Dominik Michels, Julian Urban and Sebastian Wetzel for many discussions.

I want to express my thanks to the co-organizers of the seminar Cold Quantum Coffee Laura Classen, Anton Cyrol, Bruno Faigle-Cedzich, Manuel Reichert and Nicolas Wink.

I want to thank the Physics Department at the George-Washington University, Washington D.C., USA for their hospitality during my research stay in summer 2018. I acknowledge financial support from HGS-HIRE. In particular I thank Andrei Alexandru for the enjoyable and productive atmosphere and for discussions on lattice QCD and his support.

I am indebted to Bruno Faigle-Cedzich, Jens Müller, Manuel Scherzer and Nicolas Wink for critical reading of parts of the manuscript for this thesis.

I acknowledge support from the University of Heidelberg, the DFG Collaborative Research Centre "SFB 1225 (ISOQUANT)". I also acknowledge support by the state of Baden-Württemberg through bwHPC. A part of this work was carried out on the bwUniCluster.

Also I am grateful to many friends and colleagues from the Institute for Theoretical Physics for the enjoyable PhD time. Special thanks go to Stefan Blücher, Lukas Correll, Eduardo Grossi, Markus Heller, Fabian Rennecke and Stefano Zundl.

Last but not least, I want to express my utmost gratitude to my friends and to my family, Martina Geist, Gerd and Vera Ziegler, for their constant support during all phases as a PhD student.

## Bibliography

- [1] I. Bloch, J. Dalibard, and W. Zwerger, “Many-body physics with ultracold gases,” *Rev. Mod. Phys.* **80** (2008) 885–964, [arXiv:0704.3011 \[cond-mat.other\]](#).
- [2] B. Müller, “Investigation of Hot QCD Matter: Theoretical Aspects,” *Phys. Scripta* **T158** (2013) 014004, [arXiv:1309.7616 \[nucl-th\]](#).
- [3] A. Adams, L. D. Carr, T. Schäfer, P. Steinberg, and J. E. Thomas, “Strongly Correlated Quantum Fluids: Ultracold Quantum Gases, Quantum Chromodynamic Plasmas, and Holographic Duality,” *New J. Phys.* **14** (2012) 115009, [arXiv:1205.5180 \[hep-th\]](#).
- [4] **ATLAS** Collaboration, G. Aad *et al.*, “Observation of a new particle in the search for the Standard Model Higgs boson with the ATLAS detector at the LHC,” *Phys. Lett.* **B716** (2012) 1–29, [arXiv:1207.7214 \[hep-ex\]](#).
- [5] **CMS** Collaboration, S. Chatrchyan *et al.*, “Observation of a new boson at a mass of 125 GeV with the CMS experiment at the LHC,” *Phys. Lett.* **B716** (2012) 30–61, [arXiv:1207.7235 \[hep-ex\]](#).
- [6] J. Jaeckel and A. Ringwald, “The Low-Energy Frontier of Particle Physics,” *Ann. Rev. Nucl. Part. Sci.* **60** (2010) 405–437, [arXiv:1002.0329 \[hep-ph\]](#).
- [7] C.-N. Yang and R. L. Mills, “Conservation of Isotopic Spin and Isotopic Gauge Invariance,” *Phys. Rev.* **96** (1954) 191–195. [[150\(1954\)](#)].
- [8] H. D. Politzer, “Reliable Perturbative Results for Strong Interactions?,” *Phys. Rev. Lett.* **30** (1973) 1346–1349. [[274\(1973\)](#)].
- [9] D. J. Gross and F. Wilczek, “Ultraviolet Behavior of Nonabelian Gauge Theories,” *Phys. Rev. Lett.* **30** (1973) 1343–1346. [[271\(1973\)](#)].
- [10] K. Fukushima and T. Hatsuda, “The phase diagram of dense QCD,” *Rept. Prog. Phys.* **74** (2011) 014001, [arXiv:1005.4814 \[hep-ph\]](#).
- [11] M. A. Stephanov, “QCD phase diagram: An Overview,” *PoS LAT2006* (2006) 024, [arXiv:hep-lat/0701002 \[hep-lat\]](#).
- [12] J. B. Kogut and M. A. Stephanov, “The phases of quantum chromodynamics: From confinement to extreme environments,” *Camb. Monogr. Part. Phys. Nucl. Phys. Cosmol.* **21** (2004) 1–364.
- [13] G. Boyd, J. Engels, F. Karsch, E. Laermann, C. Legeland, M. Lutgemeier, and B. Petersson, “Thermodynamics of SU(3) lattice gauge theory,” *Nucl. Phys.* **B469** (1996) 419–444, [arXiv:hep-lat/9602007 \[hep-lat\]](#).

- 
- [14] Y. Aoki, S. Borsanyi, S. Durr, Z. Fodor, S. D. Katz, S. Krieg, and K. K. Szabo, “The QCD transition temperature: results with physical masses in the continuum limit II,” *JHEP* **06** (2009) 088, arXiv:0903.4155 [hep-lat].
- [15] **Wuppertal-Budapest** Collaboration, S. Borsanyi, Z. Fodor, C. Hoelbling, S. D. Katz, S. Krieg, C. Ratti, and K. K. Szabo, “Is there still any  $T_c$  mystery in lattice QCD? Results with physical masses in the continuum limit III,” *JHEP* **09** (2010) 073, arXiv:1005.3508 [hep-lat].
- [16] A. Bazavov *et al.*, “The chiral and deconfinement aspects of the QCD transition,” *Phys. Rev.* **D85** (2012) 054503, arXiv:1111.1710 [hep-lat].
- [17] H.-T. Ding, F. Karsch, and S. Mukherjee, “Thermodynamics of strong-interaction matter from Lattice QCD,” *Int. J. Mod. Phys.* **E24** no. 10, (2015) 1530007, arXiv:1504.05274 [hep-lat].
- [18] P. Petreczky, “Lattice QCD at non-zero temperature,” *J. Phys.* **G39** (2012) 093002, arXiv:1203.5320 [hep-lat].
- [19] D. H. Rischke, “The Quark gluon plasma in equilibrium,” *Prog. Part. Nucl. Phys.* **52** (2004) 197–296, arXiv:nucl-th/0305030 [nucl-th].
- [20] **PHENIX** Collaboration, K. Adcox *et al.*, “Formation of dense partonic matter in relativistic nucleus-nucleus collisions at RHIC: Experimental evaluation by the PHENIX collaboration,” *Nucl. Phys.* **A757** (2005) 184–283, arXiv:nucl-ex/0410003 [nucl-ex].
- [21] **STAR** Collaboration, J. Adams *et al.*, “Experimental and theoretical challenges in the search for the quark gluon plasma: The STAR Collaboration’s critical assessment of the evidence from RHIC collisions,” *Nucl. Phys.* **A757** (2005) 102–183, arXiv:nucl-ex/0501009 [nucl-ex].
- [22] **ALICE** Collaboration, K. Aamodt *et al.*, “The ALICE experiment at the CERN LHC,” *JINST* **3** (2008) S08002.
- [23] N. Brambilla *et al.*, “QCD and Strongly Coupled Gauge Theories: Challenges and Perspectives,” *Eur. Phys. J.* **C74** no. 10, (2014) 2981, arXiv:1404.3723 [hep-ph].
- [24] Y. Akiba *et al.*, “The Hot QCD White Paper: Exploring the Phases of QCD at RHIC and the LHC,” arXiv:1502.02730 [nucl-ex].
- [25] Y. Aoki, G. Endrodi, Z. Fodor, S. D. Katz, and K. K. Szabo, “The Order of the quantum chromodynamics transition predicted by the standard model of particle physics,” *Nature* **443** (2006) 675–678, arXiv:hep-lat/0611014 [hep-lat].
- [26] J. Braun, L. M. Haas, F. Marhauser, and J. M. Pawłowski, “Phase Structure of Two-Flavor QCD at Finite Chemical Potential,” *Phys. Rev. Lett.* **106** (2011) 022002, arXiv:0908.0008 [hep-ph].
- [27] M. A. Stephanov, K. Rajagopal, and E. V. Shuryak, “Event-by-event fluctuations in heavy ion collisions and the QCD critical point,” *Phys. Rev.* **D60** (1999) 114028, arXiv:hep-ph/9903292 [hep-ph].

- [28] T. Schäfer, “Quark matter,” in *Mesons and quarks. Proceedings, Workshop, Mumbai, India, January 28-February 1, 2003*, pp. 185–233. 2003. arXiv:hep-ph/0304281 [hep-ph]. [,185(2003)].
- [29] P. Braun-Munzinger and J. Wambach, “The Phase Diagram of Strongly-Interacting Matter,” *Rev. Mod. Phys.* **81** (2009) 1031–1050, arXiv:0801.4256 [hep-ph].
- [30] F. J. Wegner, “Duality in Generalized Ising Models and Phase Transitions Without Local Order Parameters,” *J. Math. Phys.* **12** (1971) 2259–2272.
- [31] K. G. Wilson, “Confinement of Quarks,” *Phys. Rev.* **D10** (1974) 2445–2459.
- [32] S. Durr *et al.*, “Ab-Initio Determination of Light Hadron Masses,” *Science* **322** (2008) 1224–1227, arXiv:0906.3599 [hep-lat].
- [33] S. Borsanyi *et al.*, “Ab initio calculation of the neutron-proton mass difference,” *Science* **347** (2015) 1452–1455, arXiv:1406.4088 [hep-lat].
- [34] R. Bellwied, S. Borsanyi, Z. Fodor, J. Günther, S. D. Katz, C. Ratti, and K. K. Szabo, “The QCD phase diagram from analytic continuation,” *Phys. Lett.* **B751** (2015) 559–564, arXiv:1507.07510 [hep-lat].
- [35] A. Bazavov *et al.*, “Additional Strange Hadrons from QCD Thermodynamics and Strangeness Freezeout in Heavy Ion Collisions,” *Phys. Rev. Lett.* **113** no. 7, (2014) 072001, arXiv:1404.6511 [hep-lat].
- [36] P. de Forcrand, “Simulating QCD at finite density,” *PoS LAT2009* (2009) 010, arXiv:1005.0539 [hep-lat].
- [37] G. Aarts, “Introductory lectures on lattice QCD at nonzero baryon number,” *J. Phys. Conf. Ser.* **706** no. 2, (2016) 022004, arXiv:1512.05145 [hep-lat].
- [38] G. Aarts and I.-O. Stamatescu, “Stochastic quantization at finite chemical potential,” *JHEP* **09** (2008) 018, arXiv:0807.1597 [hep-lat].
- [39] E. Witten, “Analytic Continuation Of Chern-Simons Theory,” *AMS/IP Stud. Adv. Math.* **50** (2011) 347–446, arXiv:1001.2933 [hep-th].
- [40] **AuroraScience** Collaboration, M. Cristoforetti, F. Di Renzo, and L. Scorzato, “New approach to the sign problem in quantum field theories: High density QCD on a Lefschetz thimble,” *Phys. Rev.* **D86** (2012) 074506, arXiv:1205.3996 [hep-lat].
- [41] J. M. Pawłowski, “Aspects of the functional renormalisation group,” *Annals Phys.* **322** (2007) 2831–2915, arXiv:hep-th/0512261 [hep-th].
- [42] N. Christiansen, M. Haas, J. M. Pawłowski, and N. Strodthoff, “Transport Coefficients in Yang–Mills Theory and QCD,” *Phys. Rev. Lett.* **115** no. 11, (2015) 112002, arXiv:1411.7986 [hep-ph].
- [43] A. K. Cyrol, L. Fister, M. Mitter, J. M. Pawłowski, and N. Strodthoff, “Landau gauge Yang-Mills correlation functions,” *Phys. Rev.* **D94** no. 5, (2016) 054005, arXiv:1605.01856 [hep-ph].

- 
- [44] A. K. Cyrol, M. Mitter, J. M. Pawłowski, and N. Strodthoff, “Nonperturbative finite-temperature Yang-Mills theory,” *Phys. Rev.* **D97** no. 5, (2018) 054015, [arXiv:1708.03482 \[hep-ph\]](#).
- [45] J. M. Pawłowski, N. Strodthoff, and N. Wink, “Finite temperature spectral functions in the O(N)-model,” *Phys. Rev.* **D98** no. 7, (2018) 074008, [arXiv:1711.07444 \[hep-th\]](#).
- [46] C. S. Fischer, “QCD at finite temperature and chemical potential from Dyson–Schwinger equations,” *Prog. Part. Nucl. Phys.* **105** (2019) 1–60, [arXiv:1810.12938 \[hep-ph\]](#).
- [47] S. Borsanyi, Z. Fodor, C. Hoelbling, S. D. Katz, S. Krieg, and K. K. Szabo, “Full result for the QCD equation of state with 2+1 flavors,” *Phys. Lett.* **B730** (2014) 99–104, [arXiv:1309.5258 \[hep-lat\]](#).
- [48] **HotQCD** Collaboration, A. Bazavov *et al.*, “Equation of state in ( 2+1 )-flavor QCD,” *Phys. Rev.* **D90** (2014) 094503, [arXiv:1407.6387 \[hep-lat\]](#).
- [49] A. Bazavov *et al.*, “The QCD Equation of State to  $\mathcal{O}(\mu_B^6)$  from Lattice QCD,” *Phys. Rev.* **D95** no. 5, (2017) 054504, [arXiv:1701.04325 \[hep-lat\]](#).
- [50] H. B. Meyer, “A Calculation of the shear viscosity in SU(3) gluodynamics,” *Phys. Rev.* **D76** (2007) 101701, [arXiv:0704.1801 \[hep-lat\]](#).
- [51] R. P. Feynman, “Simulating physics with computers,” *Int. J. Theor. Phys.* **21** (1982) 467–488.
- [52] E. Zohar, J. I. Cirac, and B. Reznik, “Simulating Compact Quantum Electrodynamics with ultracold atoms: Probing confinement and nonperturbative effects,” *Phys. Rev. Lett.* **109** (2012) 125302, [arXiv:1204.6574 \[quant-ph\]](#).
- [53] E. Zohar, J. I. Cirac, and B. Reznik, “Cold-Atom Quantum Simulator for SU(2) Yang-Mills Lattice Gauge Theory,” *Phys. Rev. Lett.* **110** no. 12, (2013) 125304, [arXiv:1211.2241 \[quant-ph\]](#).
- [54] U.-J. Wiese, “Ultracold Quantum Gases and Lattice Systems: Quantum Simulation of Lattice Gauge Theories,” *Annalen Phys.* **525** (2013) 777–796, [arXiv:1305.1602 \[quant-ph\]](#).
- [55] J. M. Pawłowski, I.-O. Stamatescu, and F. P. G. Ziegler, “Cooling Stochastic Quantization with colored noise,” *Phys. Rev.* **D96** no. 11, (2017) 114505, [arXiv:1705.06231 \[hep-lat\]](#).
- [56] S. Bluecher, J. M. Pawłowski, M. Scherzer, M. Schlosser, I.-O. Stamatescu, S. Syrkowski, and F. P. G. Ziegler, “Reweighting Lefschetz Thimbles,” *SciPost Phys.* **5** no. 5, (2018) 044, [arXiv:1803.08418 \[hep-lat\]](#).
- [57] L. Kades, J. M. Pawłowski, A. Rothkopf, M. Scherzer, J. M. Urban, S. J. Wetzel, N. Wink, and F. Ziegler, “Spectral Reconstruction with Deep Neural Networks,” [arXiv:1905.04305 \[physics.comp-ph\]](#).

- [58] S. Bluecher, J. M. Pawłowski, M. Scherzer, M. Schlosser, I.-O. Stamatescu, S. Syrkowski, and F. P. G. Ziegler, “Reweighting Lefschetz Thimbles,” in *36th International Symposium on Lattice Field Theory (Lattice 2018) East Lansing, MI, United States, July 22-28, 2018*. 2019. [arXiv:1901.05187](https://arxiv.org/abs/1901.05187) [[hep-lat](#)].
- [59] J. M. Pawłowski, M. Scherzer, C. Schmidt, I.-O. Stamatescu, F. Ziegler, and F. Ziesché, *in preparation*.
- [60] J. Pawłowski and A. Rothkopf, “Thermal dynamics on the lattice with exponentially improved accuracy,” *Phys. Lett.* **B778** (2018) 221–226, [arXiv:1610.09531](https://arxiv.org/abs/1610.09531) [[hep-lat](#)].
- [61] M. E. Peskin and D. V. Schroeder, *An Introduction to quantum field theory*. Addison-Wesley, Reading, USA, 1995. <http://www.slac.stanford.edu/~mpeskin/QFT.html>.
- [62] C. Itzykson and J. B. Zuber, *Quantum Field Theory*. International Series In Pure and Applied Physics. McGraw-Hill, New York, 1980. <http://dx.doi.org/10.1063/1.2916419>.
- [63] S. Weinberg, *The quantum theory of fields. Vol. 2: Modern applications*. Cambridge University Press, 2013.
- [64] M. Laine and A. Vuorinen, *Basics of Thermal Field Theory*. Lecture notes in physics. Springer, Cham, 2016. <http://dx.doi.org/10.1007/978-3-319-31933-9>.
- [65] J. I. Kapusta and C. Gale, *Finite-temperature field theory: Principles and applications*. Cambridge Monographs on Mathematical Physics. Cambridge University Press, 2011.
- [66] A. K. Das, *Finite Temperature Field Theory*. World Scientific, New York, 1997.
- [67] T. Matsubara, “A New approach to quantum statistical mechanics,” *Prog. Theor. Phys.* **14** (1955) 351–378.
- [68] J. S. Schwinger, “Brownian motion of a quantum oscillator,” *J. Math. Phys.* **2** (1961) 407–432.
- [69] L. V. Keldysh, “Diagram technique for nonequilibrium processes,” *Zh. Eksp. Teor. Fiz.* **47** (1964) 1515–1527. [[Sov. Phys. JETP20,1018\(1965\)](#)].
- [70] J. Berges, “Nonequilibrium Quantum Fields: From Cold Atoms to Cosmology,” [arXiv:1503.02907](https://arxiv.org/abs/1503.02907) [[hep-ph](#)].
- [71] A. J. Niemi and G. W. Semenoff, “Finite Temperature Quantum Field Theory in Minkowski Space,” *Annals Phys.* **152** (1984) 105.
- [72] F. Karsch and H. W. Wyld, “Thermal Green’s Functions and Transport Coefficients on the Lattice,” *Phys. Rev.* **D35** (1987) 2518.
- [73] A. Hosoya, M.-a. Sakagami, and M. Takao, “Nonequilibrium Thermodynamics in Field Theory: Transport Coefficients,” *Annals Phys.* **154** (1984) 229.

- [74] N. Astrakhantsev, V. Braguta, and A. Kotov, “Temperature dependence of shear viscosity of  $SU(3)$ -gluodynamics within lattice simulation,” *JHEP* **04** (2017) 101, [arXiv:1701.02266 \[hep-lat\]](#).
- [75] R. Kubo, “Statistical mechanical theory of irreversible processes. 1. General theory and simple applications in magnetic and conduction problems,” *J. Phys. Soc. Jap.* **12** (1957) 570–586.
- [76] D. A. Teaney, “Viscous Hydrodynamics and the Quark Gluon Plasma,” in *Quark-gluon plasma 4*, R. C. Hwa and X.-N. Wang, eds., pp. 207–266. 2010. [arXiv:0905.2433 \[nucl-th\]](#).
- [77] P. Kovtun, D. T. Son, and A. O. Starinets, “Viscosity in strongly interacting quantum field theories from black hole physics,” *Phys. Rev. Lett.* **94** (2005) 111601, [arXiv:hep-th/0405231 \[hep-th\]](#).
- [78] H. J. Rothe, “Lattice gauge theories: An Introduction,” *World Sci. Lect. Notes Phys.* **43** (1992) 1–381. [World Sci. Lect. Notes Phys.82,1(2012)].
- [79] C. Gattringer and C. B. Lang, “Quantum chromodynamics on the lattice,” *Lect. Notes Phys.* **788** (2010) 1–343.
- [80] F. Knechtli, M. Günther, and M. Peardon, *Lattice Quantum Chromodynamics: Practical Essentials*. SpringerBriefs in Physics. Springer, 2017. [http://www.springer.com/-/0/AVjATAj-VqkG3\\_-0sK4X](http://www.springer.com/-/0/AVjATAj-VqkG3_-0sK4X).
- [81] J. Smit, “Introduction to quantum fields on a lattice: A robust mate,” *Cambridge Lect. Notes Phys.* **15** (2002) 1–271.
- [82] I. Montvay and G. Münster, *Quantum fields on a lattice*. Cambridge Monographs on Mathematical Physics. Cambridge University Press, 1997.
- [83] M. Creutz, *Quarks, gluons and lattices*. Cambridge Monographs on Mathematical Physics. Cambridge Univ. Press, Cambridge, UK, 1985. <http://www-spires.fnal.gov/spires/find/books/www?cl=QC793.3.F5C73::1983>.
- [84] N. Metropolis, A. W. Rosenbluth, M. N. Rosenbluth, A. H. Teller, and E. Teller, “Equation of state calculations by fast computing machines,” *J. Chem. Phys.* **21** (1953) 1087–1092.
- [85] A. D. Kennedy and B. J. Pendleton, “Improved Heat Bath Method for Monte Carlo Calculations in Lattice Gauge Theories,” *Phys. Lett.* **156B** (1985) 393–399.
- [86] P. H. Damgaard and H. Huffel, “Stochastic Quantization,” *Phys.Rept.* **152** (1987) 227.
- [87] M. E. J. Newman and G. T. Barkema, *Monte Carlo methods in statistical physics*. Clarendon Press, Oxford, repr. (with corr.) ed., 2004.
- [88] A. Wipf, “Statistical approach to quantum field theory,” *Lect. Notes Phys.* **864** (2013) pp.1–390.

- [89] C. B. Lang, “Computer Stochastics in scalar quantum field theory,” *NATO Sci. Ser. C* **449** (1994) 133–191, [arXiv:hep-lat/9312004](#) [[hep-lat](#)].
- [90] P. Hasenfratz and F. Karsch, “Chemical Potential on the Lattice,” *Phys. Lett.* **125B** (1983) 308–310.
- [91] J. B. Kogut, H. Matsuoka, M. Stone, H. W. Wyld, S. H. Shenker, J. Shigemitsu, and D. K. Sinclair, “Chiral Symmetry Restoration in Baryon Rich Environments,” *Nucl. Phys.* **B225** (1983) 93–122.
- [92] G. Aarts, “Complex Langevin dynamics and other approaches at finite chemical potential,” *PoS LATTICE2012* (2012) 017, [arXiv:1302.3028](#) [[hep-lat](#)].
- [93] D. Sexty, “New algorithms for finite density QCD,” *PoS LATTICE2014* (2014) 016, [arXiv:1410.8813](#) [[hep-lat](#)].
- [94] C. Gattringer, “New developments for dual methods in lattice field theory at non-zero density,” *PoS LATTICE2013* (2014) 002, [arXiv:1401.7788](#) [[hep-lat](#)].
- [95] L. Scorzato, “The Lefschetz thimble and the sign problem,” *PoS LATTICE2015* (2016) 016, [arXiv:1512.08039](#) [[hep-lat](#)].
- [96] E. Laermann and O. Philipsen, “The Status of lattice QCD at finite temperature,” *Ann. Rev. Nucl. Part. Sci.* **53** (2003) 163–198, [arXiv:hep-ph/0303042](#) [[hep-ph](#)].
- [97] C. R. Allton, S. Ejiri, S. J. Hands, O. Kaczmarek, F. Karsch, E. Laermann, C. Schmidt, and L. Scorzato, “The QCD thermal phase transition in the presence of a small chemical potential,” *Phys. Rev.* **D66** (2002) 074507, [arXiv:hep-lat/0204010](#) [[hep-lat](#)].
- [98] P. de Forcrand and O. Philipsen, “The QCD phase diagram for small densities from imaginary chemical potential,” *Nucl. Phys.* **B642** (2002) 290–306, [arXiv:hep-lat/0205016](#) [[hep-lat](#)].
- [99] M. D’Elia and M.-P. Lombardo, “Finite density QCD via imaginary chemical potential,” *Phys. Rev.* **D67** (2003) 014505, [arXiv:hep-lat/0209146](#) [[hep-lat](#)].
- [100] Z. Fodor and S. D. Katz, “A New method to study lattice QCD at finite temperature and chemical potential,” *Phys. Lett.* **B534** (2002) 87–92, [arXiv:hep-lat/0104001](#) [[hep-lat](#)].
- [101] K. Langfeld and B. Lucini, “Density of states approach to dense quantum systems,” *Phys. Rev.* **D90** no. 9, (2014) 094502, [arXiv:1404.7187](#) [[hep-lat](#)].
- [102] G. Aarts, F. A. James, J. M. Pawłowski, E. Seiler, D. Sexty, and I.-O. Stamatescu, “Stability of complex Langevin dynamics in effective models,” *JHEP* **03** (2013) 073, [arXiv:1212.5231](#) [[hep-lat](#)].
- [103] D. Sexty, “Simulating full QCD at nonzero density using the complex Langevin equation,” *Phys. Lett.* **B729** (2014) 108–111, [arXiv:1307.7748](#) [[hep-lat](#)].

- 
- [104] G. Aarts, F. Attanasio, B. Jäger, E. Seiler, D. Sexty, and I.-O. Stamatescu, “QCD at nonzero chemical potential: recent progress on the lattice,” *AIP Conf. Proc.* **1701** (2016) 020001, arXiv:1412.0847 [hep-lat].
- [105] G. Aarts, E. Seiler, D. Sexty, and I.-O. Stamatescu, “Complex Langevin dynamics and zeroes of the fermion determinant,” *JHEP* **05** (2017) 044, arXiv:1701.02322 [hep-lat].
- [106] D. K. Sinclair and J. B. Kogut, “Complex Langevin for Lattice QCD at  $T = 0$  and  $\mu \geq 0$ ,” *PoS LATTICE2016* (2016) 026, arXiv:1611.02312 [hep-lat].
- [107] K. Nagata, H. Matsufuru, J. Nishimura, and S. Shimasaki, “Gauge cooling for the singular-drift problem in the complex Langevin method — an application to finite density QCD,” *PoS LATTICE2016* (2016) 067, arXiv:1611.08077 [hep-lat].
- [108] J. Langelage, M. Neuman, and O. Philipsen, “Onset Transition to Cold Nuclear Matter from Lattice QCD with Heavy Quarks to  $\kappa^4$ ,” *PoS LATTICE2013* (2014) 141, arXiv:1311.4409 [hep-lat].
- [109] G. Aarts, F. Attanasio, B. Jäger, and D. Sexty, “The QCD phase diagram in the limit of heavy quarks using complex Langevin dynamics,” *JHEP* **09** (2016) 087, arXiv:1606.05561 [hep-lat].
- [110] M. Scherzer, E. Seiler, D. Sexty, and I.-O. Stamatescu, “Complex Langevin: Boundary terms and application to QCD,” *PoS LATTICE2018* (2019) 320, arXiv:1810.09713 [hep-lat].
- [111] G. Parisi and Y. Wu, “Perturbation Theory Without Gauge Fixing,” *Sci.Sin.* **24** (1981) 483.
- [112] M. Namiki, I. Ohba, K. Okano, Y. Yamanaka, A. K. Kapoor, H. Nakazato, and S. Tanaka, “Stochastic quantization,” *Lect. Notes Phys. Monogr.* **9** (1992) 1–217.
- [113] J. Honerkamp, *Stochastic dynamical systems*. VCH, New York, Weinheim, 1994.
- [114] K. Jacobs, *Stochastic processes for physicists*. Cambridge University Press, Cambridge, 1st ed., 2010.
- [115] G. Aarts, L. Bongiovanni, E. Seiler, D. Sexty, and I.-O. Stamatescu, “Controlling complex Langevin dynamics at finite density,” *Eur. Phys. J.* **A49** (2013) 89, arXiv:1303.6425 [hep-lat].
- [116] G. Parisi, “On Complex Probabilities,” *Phys. Lett.* **131B** (1983) 393–395.
- [117] J. R. Klauder, “Stochastic Quantization,” in *Recent Developments in High-Energy Physics*, H. Mitter and C. B. Lang, eds., pp. 251–281. Springer Vienna, Vienna, 1983.
- [118] J. R. Klauder, “A Langevin Approach to Fermion and Quantum Spin Correlation Functions,” *J. Phys.* **A16** (1983) L317.
- [119] J. R. Klauder, “Coherent State Langevin Equations for Canonical Quantum Systems With Applications to the Quantized Hall Effect,” *Phys. Rev.* **A29** (1984) 2036–2047.

- [120] G. Aarts, E. Seiler, and I.-O. Stamatescu, “The Complex Langevin method: When can it be trusted?,” *Phys. Rev.* **D81** (2010) 054508, [arXiv:0912.3360 \[hep-lat\]](#).
- [121] G. Aarts, F. A. James, E. Seiler, and I.-O. Stamatescu, “Complex Langevin: Etiology and Diagnostics of its Main Problem,” *Eur. Phys. J.* **C71** (2011) 1756, [arXiv:1101.3270 \[hep-lat\]](#).
- [122] M. Scherzer, E. Seiler, D. Sexty, and I.-O. Stamatescu, “Complex Langevin and boundary terms,” *Phys. Rev.* **D99** no. 1, (2019) 014512, [arXiv:1808.05187 \[hep-lat\]](#).
- [123] E. Seiler, D. Sexty, and I.-O. Stamatescu, “Gauge cooling in complex Langevin for QCD with heavy quarks,” *Phys. Lett.* **B723** (2013) 213–216, [arXiv:1211.3709 \[hep-lat\]](#).
- [124] G. Aarts, L. Bongiovanni, E. Seiler, and D. Sexty, “Some remarks on Lefschetz thimbles and complex Langevin dynamics,” *JHEP* **10** (2014) 159, [arXiv:1407.2090 \[hep-lat\]](#).
- [125] J. Nishimura and S. Shimasaki, “Combining the complex Langevin method and the generalized Lefschetz-thimble method,” *JHEP* **06** (2017) 023, [arXiv:1703.09409 \[hep-lat\]](#).
- [126] A. Alexandru, G. Başar, P. F. Bedaque, H. Lamm, and S. Lawrence, “Finite Density  $QED_{1+1}$  Near Lefschetz Thimbles,” *Phys. Rev.* **D98** no. 3, (2018) 034506, [arXiv:1807.02027 \[hep-lat\]](#).
- [127] A. Alexandru, G. Basar, and P. Bedaque, “Monte Carlo algorithm for simulating fermions on Lefschetz thimbles,” *Phys. Rev.* **D93** no. 1, (2016) 014504, [arXiv:1510.03258 \[hep-lat\]](#).
- [128] M. Cristoforetti, F. Di Renzo, A. Mukherjee, and L. Scorzato, “Monte Carlo simulations on the Lefschetz thimble: Taming the sign problem,” *Phys. Rev.* **D88** no. 5, (2013) 051501, [arXiv:1303.7204 \[hep-lat\]](#).
- [129] M. Cristoforetti, F. Di Renzo, G. Eruzzi, A. Mukherjee, C. Schmidt, L. Scorzato, and C. Torrero, “An efficient method to compute the residual phase on a Lefschetz thimble,” *Phys. Rev.* **D89** no. 11, (2014) 114505, [arXiv:1403.5637 \[hep-lat\]](#).
- [130] F. Di Renzo and G. Eruzzi, “One-dimensional QCD in thimble regularization,” *Phys. Rev.* **D97** no. 1, (2018) 014503, [arXiv:1709.10468 \[hep-lat\]](#).
- [131] F. Di Renzo, “Simulating lattice field theories on multiple thimbles,” in *35th International Symposium on Lattice Field Theory (Lattice 2017) Granada, Spain, June 18-24, 2017*. 2017. [arXiv:1710.06958 \[hep-lat\]](#).  
<http://inspirehep.net/record/1631649/files/arXiv:1710.06958.pdf>.
- [132] C. Schmidt and F. Ziesché, “Simulating low dimensional QCD with Lefschetz thimbles,” *PoS LATTICE2016* (2017) 076, [arXiv:1701.08959 \[hep-lat\]](#).
- [133] T. Kanazawa and Y. Tanizaki, “Structure of Lefschetz thimbles in simple fermionic systems,” *JHEP* **03** (2015) 044, [arXiv:1412.2802 \[hep-th\]](#).

- 
- [134] A. Alexandru, G. Basar, P. F. Bedaque, S. Vartak, and N. C. Warrington, “Monte Carlo Study of Real Time Dynamics on the Lattice,” *Phys. Rev. Lett.* **117** no. 8, (2016) 081602, [arXiv:1605.08040 \[hep-lat\]](#).
- [135] Y. Tanizaki, H. Nishimura, and J. J. M. Verbaarschot, “Gradient flows without blow-up for Lefschetz thimbles,” *JHEP* **10** (2017) 100, [arXiv:1706.03822 \[hep-lat\]](#).
- [136] Y. Mori, K. Kashiwa, and A. Ohnishi, “Toward solving the sign problem with path optimization method,” *Phys. Rev.* **D96** no. 11, (2017) 111501, [arXiv:1705.05605 \[hep-lat\]](#).
- [137] Y. Mori, K. Kashiwa, and A. Ohnishi, “Application of a neural network to the sign problem via the path optimization method,” *PTEP* **2018** no. 2, (2018) 023B04, [arXiv:1709.03208 \[hep-lat\]](#).
- [138] A. Alexandru, P. F. Bedaque, H. Lamm, and S. Lawrence, “Finite-Density Monte Carlo Calculations on Sign-Optimized Manifolds,” *Phys. Rev.* **D97** no. 9, (2018) 094510, [arXiv:1804.00697 \[hep-lat\]](#).
- [139] F. Bursa and M. Kroyter, “A simple approach towards the sign problem using path optimisation,” [arXiv:1805.04941 \[hep-lat\]](#).
- [140] R.-A. Tripolt, P. Gubler, M. Ulybyshev, and L. Von Smekal, “Numerical analytic continuation of Euclidean data,” *Comput. Phys. Commun.* **237** (2019) 129–142, [arXiv:1801.10348 \[hep-ph\]](#).
- [141] M. Lerch, “Sur un point de la théorie des fonctions génératrices d’abel,” *Acta Math.* **27** (1903) 339–351. <https://doi.org/10.1007/BF02421315>.
- [142] A. M. Cohen, *Inversion Formulae and Practical Results*, pp. 23–44. Springer US, Boston, MA, 2007. [https://doi.org/10.1007/978-0-387-68855-8\\_2](https://doi.org/10.1007/978-0-387-68855-8_2).
- [143] H. Gzyl, A. Tagliani, and M. Milev, “Laplace transform inversion on the real line is truly ill-conditioned,” *Applied Mathematics and Computation* **219** no. 18, (2013) 9805–9809. <http://www.sciencedirect.com/science/article/pii/S0096300313003731>.
- [144] S. Borsányi, Z. Fodor, M. Giordano, S. D. Katz, S. Mages, A. Schäfer, B. Tóth, and A. Pásztor, “Viscosity of the pure  $SU(3)$  gauge theory revisited,” *PoS LATTICE2016* (2016) 073.
- [145] S. I. Kabanikhin, “Definitions and examples of inverse and ill-posed problems,” *Journal of Inverse and Ill-posed Problems* **16** (2008) .
- [146] M. Jarrell and J. E. Gubernatis, “Bayesian inference and the analytic continuation of imaginary-time quantum Monte Carlo data,” *Phys. Rept.* **269** (1996) 133–195.
- [147] M. Asakawa and T. Hatsuda, “ $J/\psi$  and  $\eta(c)$  in the deconfined plasma from lattice QCD,” *Phys. Rev. Lett.* **92** (2004) 012001, [arXiv:hep-lat/0308034 \[hep-lat\]](#).

- [148] Y. Burnier and A. Rothkopf, “Bayesian Approach to Spectral Function Reconstruction for Euclidean Quantum Field Theories,” *Phys. Rev. Lett.* **111** (2013) 182003, [arXiv:1307.6106 \[hep-lat\]](#).
- [149] D. Dudal, O. Oliveira, M. Roelfs, and P. Silva, “Spectral representation of lattice gluon and ghost propagators at zero temperature,” [arXiv:1901.05348 \[hep-lat\]](#).
- [150] N. Yu. Astrakhantsev, V. V. Braguta, and A. Yu. Kotov, “Study of shear viscosity of SU(2)-gluodynamics within lattice simulation,” *JHEP* **09** (2015) 082, [arXiv:1507.06225 \[hep-lat\]](#).
- [151] M. Teper, “Instantons in the Quantized SU(2) Vacuum: A Lattice Monte Carlo Investigation,” *Phys. Lett.* **B162** (1985) 357–362.
- [152] C. Bonati and M. D’Elia, “Comparison of the gradient flow with cooling in SU(3) pure gauge theory,” *Phys. Rev.* **D89** no. 10, (2014) 105005, [arXiv:1401.2441 \[hep-lat\]](#).
- [153] M. Garcia Perez, O. Philipsen, and I.-O. Stamatescu, “Cooling, physical scales and topology,” *Nucl. Phys.* **B551** (1999) 293–313, [arXiv:hep-lat/9812006 \[hep-lat\]](#).
- [154] M. Lüscher, “Properties and uses of the Wilson flow in lattice QCD,” *JHEP* **08** (2010) 071, [arXiv:1006.4518 \[hep-lat\]](#). [Erratum: *JHEP*03,092(2014)].
- [155] R. Narayanan and H. Neuberger, “Infinite N phase transitions in continuum Wilson loop operators,” *JHEP* **03** (2006) 064, [arXiv:hep-th/0601210 \[hep-th\]](#).
- [156] A. Gonzalez-Arroyo and M. Okawa, “The string tension from smeared Wilson loops at large N,” *Phys. Lett.* **B718** (2013) 1524–1528, [arXiv:1206.0049 \[hep-th\]](#).
- [157] S. Datta, S. Gupta, and A. Lytle, “Using Wilson flow to study the SU(3) deconfinement transition,” *Phys. Rev.* **D94** no. 9, (2016) 094502, [arXiv:1512.04892 \[hep-lat\]](#).
- [158] F. Capponi, A. Rago, L. Del Debbio, S. Ehret, and R. Pellegrini, “Renormalisation of the energy-momentum tensor in scalar field theory using the Wilson flow,” *PoS LATTICE2015* (2016) 306, [arXiv:1512.02851 \[hep-lat\]](#).
- [159] C. Monahan, “The gradient flow in simple field theories,” *PoS LATTICE2015* (2016) 052, [arXiv:1512.00294 \[hep-lat\]](#).
- [160] A. Kagimura, A. Tomiya, and R. Yamamura, “Effective lattice action for the configurations smeared by the Wilson flow,” [arXiv:1508.04986 \[hep-lat\]](#).
- [161] V. G. Bornyakov *et al.*, “Wilson flow and scale setting from lattice QCD,” [arXiv:1508.05916 \[hep-lat\]](#).
- [162] Z. Bern, M. B. Halpern, L. Sadun, and C. H. Taubes, “Continuum Regularization of QCD,” *Phys. Lett.* **B165** (1985) 151.
- [163] Z. Bern, M. B. Halpern, L. Sadun, and C. H. Taubes, “Continuum Regularization of Quantum Field Theory. 1. Scalar Prototype,” *Nucl. Phys.* **B284** (1987) 1.

- 
- [164] Z. Bern, M. B. Halpern, L. Sadun, and C. H. Taubes, “Continuum Regularization of Quantum Field Theory. 2. Gauge Theory,” *Nucl. Phys.* **B284** (1987) 35.
- [165] Z. Bern, M. B. Halpern, and L. Sadun, “Continuum Regularization of Quantum Field Theory. 3. The QCD in Four-dimensions Beta Function,” *Nucl. Phys.* **B284** (1987) 92–117.
- [166] Z. Bern, M. B. Halpern, and N. G. Kalivas, “Heat Kernel Regularization of Gauge Theory,” *Phys. Rev.* **D35** (1987) 753.
- [167] L. P. Kadanoff, “Scaling laws for Ising models near  $T_c$ ,” *Physics* **2** (1966) 263–272.
- [168] J. Berges, N. Tetradis, and C. Wetterich, “Non-perturbative renormalization flow in quantum field theory and statistical physics,” *Phys. Rept.* **363** (2002) 223–386, [arXiv:hep-ph/0005122](#).
- [169] J. Polonyi, “Lectures on the functional renormalization group method,” *Central Eur.J.Phys.* **1** (2003) 1–71, [arXiv:hep-th/0110026](#) [[hep-th](#)].
- [170] B. Delamotte, “An Introduction to the nonperturbative renormalization group,” *Lect. Notes Phys.* **852** (2012) 49–132, [arXiv:cond-mat/0702365](#) [[cond-mat.stat-mech](#)].
- [171] O. J. Rosten, “Fundamentals of the Exact Renormalization Group,” *Phys. Rept.* **511** (2012) 177–272, [arXiv:1003.1366](#) [[hep-th](#)].
- [172] W. Metzner, M. Salmhofer, C. Honerkamp, V. Meden, and K. Schönhammer, “Functional renormalization group approach to correlated fermion systems,” *Reviews of Modern Physics* **84** (Jan., 2012) 299–352, [arXiv:1105.5289](#) [[cond-mat.str-el](#)].
- [173] G. G. Batrouni, G. R. Katz, A. S. Kronfeld, G. P. Lepage, B. Svetitsky, and K. G. Wilson, “Langevin simulations of lattice field theories,” *Phys. Rev. D* **32** (1985) 2736–2747.
- [174] A. S. Kronfeld, “Dynamics of Langevin simulations,” *Prog. Theor. Phys. Suppl.* **111** (1993) 293–312, [arXiv:hep-lat/9205008](#) [[hep-lat](#)].
- [175] K. Binder, “Finite size scaling analysis of Ising model block distribution functions,” *Zeitschrift für Physik B Condensed Matter* **43** no. 2, (1981) 119–140.
- [176] K. Huang, *Introduction to statistical physics*. CRC Press, Boca Raton, Fla. [u.a.], 2. ed. ed., 2010.
- [177] A. K. De, A. Harindranath, J. Maiti, and T. Sinha, “Investigations in 1+1 dimensional lattice  $\phi^4$  theory,” *Phys. Rev.* **D72** (2005) 094503, [arXiv:hep-lat/0506002](#) [[hep-lat](#)].
- [178] F. J. Wegner and A. Houghton, “Renormalization group equation for critical phenomena,” *Phys. Rev.* **A8** (1973) 401–412.
- [179] T. J. Hollowood, *Renormalization group and fixed points*. SpringerBriefs in Physics. Springer, Heidelberg [u.a.], 2013.

- [180] A. Alexandru, G. Basar, P. F. Bedaque, G. W. Ridgway, and N. C. Warrington, “Sign problem and Monte Carlo calculations beyond Lefschetz thimbles,” *JHEP* **05** (2016) 053, [arXiv:1512.08764 \[hep-lat\]](#).
- [181] M. Schlosser, *Langevin Dynamics on Lefschetz thimbles*. Bachelor thesis, Heidelberg University, 2017.
- [182] M. R. Spiegel and J. Liu, *Mathematical handbook of formulas and tables*. Schaum’s outline series. McGraw-Hill, New York [a.o.], 2nd ed., 1999.
- [183] D. Michels, *A novel approach to thermal quantum fields on the lattice*. Master thesis, Heidelberg University, 2018.
- [184] E. Kovacs, “Finite Volume Effects in SU(2) Lattice Gauge Theories,” *Phys. Lett.* **118B** (1982) 125–128.
- [185] J. Engels, S. Mashkevich, T. Scheideler, and G. Zinovev, “Critical behavior of SU(2) lattice gauge theory: A Complete analysis with the  $\chi^2$  method,” *Phys. Lett.* **B365** (1996) 219–224, [arXiv:hep-lat/9509091 \[hep-lat\]](#).
- [186] M. Luscher and P. Weisz, “Locality and exponential error reduction in numerical lattice gauge theory,” *JHEP* **09** (2001) 010, [arXiv:hep-lat/0108014 \[hep-lat\]](#).
- [187] H. B. Meyer, “Locality and statistical error reduction on correlation functions,” *JHEP* **01** (2003) 048, [arXiv:hep-lat/0209145 \[hep-lat\]](#).
- [188] H. B. Meyer, “The Yang-Mills spectrum from a two level algorithm,” *JHEP* **01** (2004) 030, [arXiv:hep-lat/0312034 \[hep-lat\]](#).
- [189] L. Schlessinger, “Use of analyticity in the calculation of nonrelativistic scattering amplitudes,” *Phys. Rev.* **167** (Mar, 1968) 1411–1423.  
<https://link.aps.org/doi/10.1103/PhysRev.167.1411>.
- [190] H. Kleinert, *Path integrals in quantum mechanics, statistics, polymer physics, and financial markets*. World Scientific, New Jersey [u.a.], 5. ed., 2009.
- [191] J. Berges, S. Borsanyi, D. Sexty, and I. O. Stamatescu, “Lattice simulations of real-time quantum fields,” *Phys. Rev.* **D75** (2007) 045007, [arXiv:hep-lat/0609058 \[hep-lat\]](#).
- [192] J. Berges and I. O. Stamatescu, “Simulating nonequilibrium quantum fields with stochastic quantization techniques,” *Phys. Rev. Lett.* **95** (2005) 202003, [arXiv:hep-lat/0508030 \[hep-lat\]](#).
- [193] A. Alexandru, G. Basar, P. F. Bedaque, and G. W. Ridgway, “Schwinger-Keldysh formalism on the lattice: A faster algorithm and its application to field theory,” *Phys. Rev.* **D95** no. 11, (2017) 114501, [arXiv:1704.06404 \[hep-lat\]](#).
- [194] G. Aarts, F. A. James, E. Seiler, and I.-O. Stamatescu, “Adaptive stepsize and instabilities in complex Langevin dynamics,” *Phys. Lett.* **B687** (2010) 154–159, [arXiv:0912.0617 \[hep-lat\]](#).

- 
- [195] A. Ohnishi, Y. Mori, and K. Kashiwa, “Path optimization method with use of neural network for the sign problem in field theories,” *PoS LATTICE2018* (2018) 023, [arXiv:1812.11506 \[hep-lat\]](#).
- [196] H. Sonoda and H. Suzuki, “Derivation of a gradient flow from the exact renormalization group,” *PTEP* **2019** no. 3, (2019) 033B05, [arXiv:1901.05169 \[hep-th\]](#).
- [197] A. Carosso, “Stochastic Renormalization Group and Gradient Flow,” [arXiv:1904.13057 \[hep-th\]](#).
- [198] S. Blücher, *Complex Langevin Dynamics with Lefschetz-thimble cooling*. Bachelor thesis, Heidelberg University, 2017.
- [199] S. Syrkowski, *Lefschetz cooled Stochastic Quantization*. Bachelor thesis, Heidelberg University, 2017.
- [200] D. Unverzagt, *Combining the Complex Langevin evolution with Lefschetz thimbles*. Bachelor thesis, Heidelberg University, 2017.
- [201] F. Schwabl, *Quantenmechanik*. Springer-Lehrbuch. Springer, Berlin, Heidelberg, 6 ed., 2005.
- [202] J. J. Sakurai and J. Napolitano, *Modern quantum mechanics*. Cambridge University Press, Cambridge, 2nd ed., 2017.
- [203] E. W. Weisstein, “Heaviside step function. from mathworld—a wolfram web resource..” <http://mathworld.wolfram.com/HeavisideStepFunction.html>.